

# **ACOUSTIC TRANSDUCTION – MATERIALS AND DEVICES**

**Period 1 January 1999 to 31 December 1999**

**Annual Report**

**VOLUME I**

**OFFICE OF NAVAL RESEARCH  
Contract No: N00014-96-1-1173**

**APPROVED FOR PUBLIC RELEASE –  
DISTRIBUTION UNLIMITED**

**Reproduction in whole or in part is permitted for any  
purpose of the United States Government**

**Kenji Uchino**

**PENNSTATE**



**THE MATERIALS RESEARCH LABORATORY  
UNIVERSITY PARK, PA**

**DTIC QUALITY INSPECTED 4**

**20000815 044**

REPORT DOCUMENTATION PAGE			Form Approved OMB No. 0704-0188	
<small>Public reporting burden for this collection of information is estimated to average 1 hour per response, including the time for reviewing instructions, searching existing data sources, gathering and maintaining the data needed, and completing and reviewing the collection of information. Send comments regarding this burden estimate or any other aspect of this collection of information, including suggestions for reducing this burden, to Washington Headquarters Services, Directorate for Information Operations and Reports, 1215 Jefferson Davis Highway, Suite 1204, Arlington, VA 22202-4302, and to the Office of Management and Budget, Paperwork Reduction Project (0704-0188), Washington, DC 20503.</small>				
1. AGENCY USE ONLY (Leave blank)	2. REPORT DATE 06/12/2000	3. REPORT TYPE AND DATES COVERED ANNUAL REPORT 01/01/2000-12/31/2000		
4. TITLE AND SUBTITLE  ACOUSTIC TRANSDUCTION -- MATERIALS AND DEVICES		5. FUNDING NUMBERS  ONR CONTRACT NO. N00014-96-1-11173		
6. AUTHOR(S)  KENJI UCHINO				
7. PERFORMING ORGANIZATION NAME(S) AND ADDRESS(ES)  Materials Research Laboratory The Pennsylvania State University University Park, PA 16802		8. PERFORMING ORGANIZATION REPORT NUMBER		
9. SPONSORING/MONITORING AGENCY NAME(S) AND ADDRESS(ES) Office of Naval Research    Office of Naval Research ONR 321SS                      Regional Office Chicago Ballston Centre Tower One    536 S Clark Str., RM 208 800 N Quincy Street          Chicago IL 60605-1588 Arlington VA 22217-5660		10. SPONSORING/MONITORING AGENCY REPORT NUMBER		
11. SUPPLEMENTARY NOTES				
12a. DISTRIBUTION / AVAILABILITY STATEMENT			12b. DISTRIBUTION CODE	
13. ABSTRACT (Maximum 200 words)  SEE FOLLOWING PAGE				
14. SUBJECT TERMS			15. NUMBER OF PAGES	
			16. PRICE CODE	
17. SECURITY CLASSIFICATION OF REPORT UNCLASSIFIED			18. SECURITY CLASSIFICATION OF THIS PAGE UNCLASSIFIED	19. SECURITY CLASSIFICATION OF ABSTRACT UNCLASSIFIED
20. LIMITATION OF ABSTRACT				

## GENERAL INSTRUCTIONS FOR COMPLETING SF 298

The Report Documentation Page (RDP) is used in announcing and cataloging reports. It is important that this information be consistent with the rest of the report, particularly the cover and title page. Instructions for filling in each block of the form follow. It is important to **stay within the lines** to meet optical scanning requirements.

**Block 1. Agency Use Only (Leave blank).**

**Block 2. Report Date** Full publication date including day, month, and year, if available (e.g. 1 Jan 88). Must cite at least the year.

**Block 3. Type of Report and Dates Covered.** State whether report is interim, final, etc. If applicable, enter inclusive report dates (e.g. 10 Jun 87 - 30 Jun 88).

**Block 4. Title and Subtitle.** A title is taken from the part of the report that provides the most meaningful and complete information. When a report is prepared in more than one volume, repeat the primary title, add volume number, and include subtitle for the specific volume. On classified documents enter the title classification in parentheses.

**Block 5. Funding Numbers.** To include contract and grant numbers; may include program element number(s), project number(s), task number(s), and work unit number(s). Use the following labels:

C - Contract	PR - Project
G - Grant	TA - Task
PE - Program Element	WU - Work Unit Accession No.

**Block 6. Author(s).** Name(s) of person(s) responsible for writing the report, performing the research, or credited with the content of the report. If editor or compiler, this should follow the name(s).

**Block 7. Performing Organization Name(s) and Address(es).** Self-explanatory.

**Block 8. Performing Organization Report Number.** Enter the unique alphanumeric report number(s) assigned by the organization performing the report.

**Block 9. Sponsoring/Monitoring Agency Name(s) and Address(es).** Self-explanatory.

**Block 10. Sponsoring/Monitoring Agency Report Number.** (If known)

**Block 11. Supplementary Notes.** Enter information not included elsewhere such as: Prepared in cooperation with...; Trans. of...; To be published in.... When a report is revised, include a statement whether the new report supersedes or supplements the older report.

**Block 12a. Distribution/Availability Statement.** Denotes public availability or limitations. Cite any availability to the public. Enter additional limitations or special markings in all capitals (e.g. NOFORN, REL, ITAR).

DOD - See DoDD 5230.24, "Distribution Statements on Technical Documents."

DOE - See authorities.

NASA - See Handbook NHB 2200.2.

NTIS - Leave blank.

**Block 12b. Distribution Code.**

DOD - Leave blank.

DOE - Enter DOE distribution categories from the Standard Distribution for Unclassified Scientific and Technical Reports.

NASA - Leave blank.

NTIS - Leave blank.

**Block 13. Abstract.** Include a brief (*Maximum 200 words*) factual summary of the most significant information contained in the report.

**Block 14. Subject Terms.** Keywords or phrases identifying major subjects in the report.

**Block 15. Number of Pages.** Enter the total number of pages.

**Block 16. Price Code.** Enter appropriate price code (*NTIS only*).

**Blocks 17. - 19. Security Classifications.** Self-explanatory. Enter U.S. Security Classification in accordance with U.S. Security Regulations (i.e., UNCLASSIFIED). If form contains classified information, stamp classification on the top and bottom of the page.

**Block 20. Limitation of Abstract.** This block must be completed to assign a limitation to the abstract. Enter either UL (unlimited) or SAR (same as report). An entry in this block is necessary if the abstract is to be limited. If blank, the abstract is assumed to be unlimited.

## ABSTRACT

This report describes the research performed over the period of 1 January 1999 to 31 December 1999 on a MURI under Office of Naval Research contract N00014-96-1-1173 on the topic "Acoustic Transduction: Materials and Devices" brings together work from the Materials Research Laboratory (MRL), the Applied Research Laboratory (ARL), and the Center for Acoustics and Vibrations (CAV) at The Pennsylvania State University. As has become customary over many years research on the program is described in detail in the 87 technical appendices to this report and only a brief narrative description connecting this research is given in the text.

Perhaps the most outstanding accomplishment of the year is a "spin on" from our earlier single crystal studies now involving Brookhaven National Laboratory and Professor Gonzalo's group in Madrid, Spain. Using exceptionally homogeneous polycrystal lead zirconate titanate samples prepared in MRL, precise synchrotron x-ray analysis has confirmed a new monoclinic phase at lower temperature in composition close to the important morphotropic phase boundary. This work demands a re-thinking of both intrinsic and extrinsic contributions to response in this most important practical transducer material family. Domain Engineering/Domain Averaging in lead zinc niobate:lead titanate (PZN:PT) in lead magnesium niobate:lead titanate (PMN:PT) and in barium titanate ( $\text{BaTiO}_3$ ) continues to offer single crystal systems with outstanding transducer and actuator properties and new insights into the field induced strain mechanisms in all perovskite type piezoelectrics. Excellent progress with the new high strain irradiated P(VDF:TrFE) relaxor ferroelectric copolymer system has helped catalyze a new DARPA initiative in this area and a re-awakening of interest in the whole area of electrostrictive polymer systems.

A primary objective of this MURI grouping was to help shorten the time constant for new materials and device concepts to be applied in practical Navy Systems. We believe this has now been realized in joint work on the composite cymbal type flexensional arrays for large area projectors, and in the progress made towards a micro-tonpils array system.

Original work on new step and repeat piezoelectric high strain systems continues to make good progress now using commercial motion rectifiers to produce both linear and rotary systems with high torque capability. New composite designs are pushing toward 1 mm diameter motors in the size regimen where there are real difficulties for conventional electromagnetic designs.

A new area of activity this year is in piezoelectric transformers where a circular symmetry design in conjunction with controlled inhomogeneous poling is shown to offer capabilities which are of real interest for energy recovery actuator power systems. Basic studies have evolved a new environmental SEM technique for high resolution domain wall studies without changing problems. Work is continuing on reliable measurements of electrostrictive constants in simple solids confirming by both direct and converse methods and permitting the first generalization of trends in these fundamentally important coupling constants.

# **ACOUSTIC TRANSDUCTION – MATERIALS AND DEVICES**

**Period 1 January 1999 to 31 December 1999**

**Annual Report**

**VOLUME I**

**OFFICE OF NAVAL RESEARCH  
Contract No: N00014-96-1-1173**

**APPROVED FOR PUBLIC RELEASE –  
DISTRIBUTION UNLIMITED**

**Reproduction in whole or in part is permitted for any  
purpose of the United States Government**

**Kenji Uchino**

## TABLE OF CONTENTS

APPENDICES LISTING .....	2
ABSTRACT .....	9
INTRODUCTION .....	9
1.0 GENERAL SUMMARY PAPERS .....	10
2.0 MATERIALS STUDIES .....	11
2.1 Polycrystal Perovskite Ceramics .....	11
2.2 Relaxor Ferroelectric Single Crystal Systems .....	11
2.3 High Strain Polymers. ....	12
3.0 TRANSDUCER STUDIES .....	12
3.1 Composite Structures .....	12
3.2 3-Dimensional Acoustic Intensity Probes .....	12
3.3 Piezoelectric Transformers .....	12
4.0 ACTUATOR STUDIES .....	13
4.1 Materials and Designs .....	13
4.2 Photostriction. ....	13
4.3 High Force Torsional Actuators. ....	13
4.4 Piezoelectric Mini Motors .....	13
5.0 MODELING and CHARACTERIZATION .....	13
5.1 Simulation. ....	13
5.2 Thin and Thick Films. ....	14
5.4 Domain Studies .....	14
5.5 Electrostriction .....	15
6.0 GRADUATE STUDENTS IN THE PROGRAM .....	15
7.0 HONORS and AWARDS .....	15
8.0 PAPERS PUBLISHED IN REFEREED JOURNALS .....	15
9.0 PAPERS SUBMITTED FOR PUBLICATION. ....	20
10.0 PAPERS APPEARING IN NON REFERRED PROCEEDINGS .....	23
11.0 INVITED PAPERS PRESENTATIONS AT NATIONAL AND INTERNATIONAL MEETINGS .....	25
12.0 INVITED PAPERS PRESENTED AT UNIVERSITY, INDUSTRY, AND GOVERNMENT LABORATORIES .....	27
13.0 CONTRIBUTED PAPERS AT NATIONAL AND INTERNATIONAL MEETINGS .....	29
14.0 BOOKS (AND SECTIONS THERE OF) .....	35
15.0 PATENTS .....	35

## APPENDICES

### VOLUME I

#### GENERAL SUMMARY PAPERS

1. Cross, L.E., "Newnham Festschrift Introduction." Guest Editorial, Mat. Res. Innovations **2**, 251 (1999).
2. Newnham, R.E., "Ceramics into the Next Millennium," *British Ceramic Transactions* **98**(5), 251-255 (1999).
3. Uchino, K. and S. Takahashi, "New Trend in Multilayer Ceramic Actuators," Proc. Int'l Symp. Dielectric Ceramics, Amer. Ceram. Soc. '98; Ceramic Trans., Vol. 100, Dielectric Ceramic Materials, p.455 - 468 (1999).
4. Uchino, K., "Smart Composite Materials," Chap.5.19, Comprehensive Composite Materials, Elsevier Science, Oxford, UK (2000). [in press]
5. Kelly, A., R. Davidson, and K. Uchino "Smart Composite Materials Systems," Chap.5.20, Comprehensive Composite Materials, Elsevier Science, Oxford, UK (2000). [in press]
6. Fousek, J., L.E. Cross, and D.B. Litvin, "Possible Piezoelectric Composites Based on the Flexoelectric Effect." Materials Letters **39**, 287-291 (1999).

#### 2.0 MATERIALS STUDIES

##### 2.1 Polycrystal Perovskite Ceramics

7. Noheda, B., D.E. Cox, G. Shirane, J.A. Gonzalo, L.E. Cross, and S.-E. Park, "A Monoclinic Ferroelectric Phase in the  $\text{Pb}(\text{Zr}_{1-x}\text{Ti}_x)\text{O}_3$  Solid Solution." Applied Physics Letters **74**(14), 2059-2061 (1999).
8. Noheda, B., J.A. Gonzalo, R. Guo, S.-E. Park, L.E. Cross, D.E. Cox, and G. Shirane, "The monoclinic phase in PZT: new light on morphotropic phase boundaries," Proceedings of the Workshop on Fundamental Physical of Ferroelectrics, Aspen, CO (February 2000).
9. Noheda, B., J.A. Gonzalo, L.E. Cross, R. Guo, S.-E. Park, D.E. Cox, and G. Shirane, "Tetragonal-to-monoclinic phase transition in a ferroelectric perovskite: The structure of  $\text{PbZr}_{0.52}\text{Ti}_{0.48}\text{O}_3$ ," *Physical Review B* **61**(13), 8687 (April 2000).
10. Guo, R., L.E. Cross, S.-E. Park, B. Noheda, D.E. Cox, and G. Shirane, "Origin of the high piezoelectric response in  $\text{PbZr}_{1-x}\text{Ti}_x\text{O}_3$ ," *Physical Review Letters* **84**(23) (June 2000).
11. Zhang, Q.M., "Electromechanical Properties of Lead Zirconate Titanate Piezoceramics Under the Influence of Mechanical Stresses," IEEE Transactions on Ultrasonics, Ferroelectrics, and Frequency Control **46**(6) (November 1999).
12. Wang, H., W. Jiang, and W. Cao, "Characterization of Lead Zirconate Titanate Piezoceramic Using High Frequency Ultrasonic Spectroscopy," J. Appl. Phys. **85**, 8083-8091 (1999).
13. Zhao, J., V. Mueller, and Q.M. Zhang, "The Influence of External Stress on the Electromechanical Response of Electrostrictive 0.9PMN-0.1PT in the DC Field Biased State," J. Mater. Res. **14**, 948-956 (1999).

## 2.0 MATERIALS STUDIES

### 2.1 Polycrystal Perovskite Ceramics (continued)

14. Zhao, J., A.E. Glazounov, and Q.M. Zhang, "Change in Electromechanical Properties of 0.9PMN-0.1PT Relaxor Ferroelectric Induced by Uniaxial Compressive Stress Directed Perpendicular to the Electric Field," *Appl. Phys. Lett.* **74**, 436-438 (1999).
15. Albert, E.F., A.S. Bhalla, and T. Takenaka, "Large Hydrostatic Piezoelectric Constant and Temperature Dependence of the Piezoelectric Properties  $\text{Bi}(\text{Ni}_{1/2}\text{Ti}_{1/2})\text{O}_3\text{:PbTiO}_3$  Ceramics," *Ferroelectrics Letters* **25**, 45-52 (1999).
16. Alberta, E.F. and A.S. Bhalla, "Investigation of the Lead Indium Niobate-Lead Magnesium Niobate Solid Solution," *Materials Letters* **40**, 114-117 (1999).
17. Alberta, E.F. and A.S. Bhalla, "Electrical Properties of the Morphotropic Phase Boundary in  $\text{Pb}(\text{In}_{1/2}\text{Ta}_{1/2})\text{O}_3\text{-PbTiO}_3$  Ceramics," *Ferroelectrics Letters* **26**, 117-123 (1999).
18. Kim, J.S., S.J. Kim, H.G. Kim, D.C. Lee, and K. Uchino, "Piezoelectric and Dielectric Properties of  $\text{Fe}_2\text{O}_3$ -Doped  $0.57\text{Pb}(\text{Sc}_{1/2}\text{Nb}_{1/2})\text{O}_3\text{-}0.43\text{PbTiO}_3$  Ceramic Materials," *Jpn. J. Appl. Phys.* **38**(Part 1, No. 3A), 1433-1437 (1999).

## VOLUME II

19. Liu, S.F., I.R. Abothu, S. Komarneni, P. Poosanaas, D.S. Paik, Y. Ito, and K. Uchino, "PLZT Ceramics Prepared from Conventional and Microwave Hydrothermal Powders," *Ferroelectrics* **231**, 179-185 (1999).
20. Chen, Y. H., S. Hirose, D. Viehland, S. Takahashi, and K. Uchino, "Mn-Modified  $\text{Pb}(\text{Mg}_{1/3}\text{Nb}_{2/3})\text{O}_3\text{-PbTiO}_3$  Ceramics: Improved Mechanical Quality Factors for High Power Transduction Applications," *Jpn. J. Appl. Phys.* (1999). [accepted].
21. Chen, Y.H., S. Hirose, D. Viehland, and K. Uchino, "Doping Effects in  $\text{Pb}(\text{Mg}_{1/3}\text{Nb}_{2/3})\text{O}_3\text{-PbTiO}_3$  Ceramics for High Power Transduction Applications," *Mater. Res. Soc. Fall Mtg. '99*, LL.5.9, Boston (Nov. 29-Dec.3, 1999).
22. Du, X.H., Q.M. Wang, U. Belegundu, and K. Uchino, "Piezoelectric Property Enhancement in Polycrystalline Lead Zirconate Titanate by Changing Cutting Angle," *J. Ceram. Soc. Jpn.* **107**(2), 190-191 (1999).

### 2.2 Single Crystal Systems

23. Wada, S., S.E. Park, L.E. Cross, and T.R. Shrout, "Engineered Domain Configuration in Rhombohedral PZN-PT Single Crystals and their Ferroelectric Related Properties," *Ferroelectrics* **221**, 147-155 (1999).
24. Liu, S.-F., S.E. Park, T.R. Shrout, and L.E. Cross. "Electric Field Dependence of Piezoelectric Properties for Rhombohedral  $0.955\text{Pb}(\text{Zn}_{1/3}\text{Nb}_{2/3})\text{O}_3\text{-}0.045\text{PbTiO}_3$  Single Crystals," *Journal of Applied Physics* **85** (5), 2810-2814 (1999).
25. Erhart, J. and W. Cao, "Effective Material Properties in Twinned Ferroelectric Crystals," *J. Appl. Phys.* **86**, 1073- 1081 (1999).

## 2.0 MATERIALS STUDIES

### 2.2 *Single Crystal Systems (continued)*

26. Yin, J., B. Jiang, and W. Cao, "Elastic, Piezoelectric and Dielectric Properties of  $0.955\text{Pb}(\text{Zn}_{1/3}\text{Nb}_{2/3})\text{O}_3$ - $0.045\text{PbTiO}_3$  Single Crystal with Designed Multidomains," *IEEE Transactions UFFC* **47**, 285-291 (2000).
27. Wada, S., S.E. Park, L.E. Cross, and T.R. Shrout, "Defect-induced Domain Configuratrion in Relaxor PZN Single Crystal and Its Origin." *Trans. of the Mat. Res. Soc. Of Japan* **24**(1), 19-22 (1999).
28. Belegundu, U., X. Du, and K. Uchino, "Switching Current In  $\text{Pb}(\text{Zn}_{1/3}\text{Nb}_{2/3})\text{O}_3$ - $\text{PbTiO}_3$  Single Crystals, MRS Meeting, Boston (November 1999).
29. Park, S.-E., S. Wada, L.E. Cross, and T.R. Shrout, "Crystallographically Engineered  $\text{BaTiO}_3$  Single Crystals for High-Performance Piezoelectrics." *Journal of Applied Physics* **86**(5), 2746-2750 (1999).
30. Du, X.H., Q.M. Wang, U. Belegundu, A. Bhalla, and K. Uchino, "Crystal Orientation Dependence of Piezoelectric Properties of Single Crystal Barium Titanate," *Mater. Lett.* **40**, 109-113 (1999).
31. Lu, .Y., Z.-Y. Cheng, E. Park, S.F. Liu and Q.M. Zhang, "Linear Electro-optic Effect of  $0.88\text{Pb}(\text{Zn}_{1/3}\text{Nb}_{2/3})$ - $0.12\text{PbTiO}_3$  Single Crystal," *Jpn. J. Appl. Phys.* **39**, 141-145 (2000).

### 2.3 *High Strain Polymers*

32. Bharti, V., H.S. Xu, G. Shanthi, Q.M. Zhang, and K. Liang, "Polarization and Structural Properties of High Energy Electron Irradiated P(VDF-TrFE) Copolymer Films," *J. Appl. Phys.* **87**, 452-461 (2000).
33. Cheng, Z.-Y., T.-B. Xu, V. Bharti, S. Wang, and Q.M. Zhang, "Transverse Strain Response in the Electrostrictive P(VDF-TrFE) Copolymer," *Appl. Phys. Lett.* **74**, 1901-1903 (1999).
34. Cheng, Z.-Y., V. Bharti, T.B. Xu, S. Wang, Q.M. Zhang, T. Ramotowski, F. Tito, and R. Ting, "Transverse Strain Responses in Electrostrictive P(VDF-TrFE) Films and Development of a Dilatometer for the Measurement," *J. Appl. Phys.* **86**, 2208-2214 (1999).
35. Bharti, V., Z-Y Cheng, S. Gross, T.B. Xu, and Q.M. Zhang, "High Electrostrictive Strain under High Mechanical Stress in High Energy Electron Irradiated Poly(vinylidene fluoride-trifluoroethylene) Copolymer Films," *Appl. Phys. Lett.* **75**, 2653-2655 (1999).

## 3.0 TRANSDUCER STUDIES

### 3.1 *Composite Structures*

36. Geng, X. and Q.M. Zhang, "Resonance Modes and Losses in 1-3 Composites for Ultrasonic Transducer Applications," *J. Appl. Phys.* **85**, 1342-1350 (1999).
37. Tressler, J. and K. Uchino, "Piezoelectric Composite Sensors," Chap.5.25, *Comprehensive Composite Materials*, Elsevier Science, Oxford, UK (2000). [in press]
38. Tressler, J.F., S. Alkoy, A. Dogan, and R.E. Newnham, "Functional Composites for Sensors, Actuators and Transducers," *Composites Part A: Applied Science & Manufacturing* **30**, 477-482 (1999).

3.0 TRANSDUCER STUDIES

3.1 *Composite Structures (continued)*

39. Tressler, J.F. and R.E. Newnham, "Capped Ceramic Underwater Sound Projector: The "Cymbal" Transducer," J. of Acoustical Soc. America **105**(2), part 1, 591-600 (1999).

**VOLUME III**

40. Zhang, J., W.J. Hughes, P. Bouchilloux, R. Meyer Jr., K. Uchino, and R.E. Newnham, "A Class V Flexensional Transducer: The Cymbal," Ultrasonics **37**, 387-393 (1999).

41. Zhang, J., W.J. Hughes, R.J. Meyer Jr., K. Uchino, and R.E. Newnham, "Cymbal Array: A Broad Band Sound Projector," Ultrasonics **37**, 523-529 (2000).

3.0 TRANSDUCER STUDIES

3.1 *Composite Structures (continued)*

42. Zhang, J., W.J. Hughes, A.C. Hladky-Hennion and R.E. Newnham, "Concave Cymbal Transducers," Materials Research Innovations **2** (5), 252-255 (1999).

43. Alkoy, S., R.E. Newnham, A.C. Hladky, A. Dogan, and J.K. Cochran, Jr., "Piezoelectric Hollow Spheres for Microprobe Hydrophones," Ferroelectrics **226**, 11-25 (1999).

44. Carlson, W.B., R.E. Newnham and D.P. Williams, "Piezotensegritic Structures for Transducer Applications," Materials Research Innovations **3**, 175-178 (1999).

45. Newnham, R.E. and A. Amin, "Smart Systems: Microphones, Fish Farming, and Beyond," Chemtech **29**(12), 38-47 (1999).

3.2 *3-Dimensional Acoustic Intensity Probes*

46. Bastyr, K.J., G.C. Lauchle, and J.A. McConnell, "Development of a Velocity Gradient Underwater Acoustic Intensity Sensor," J. Acoust. Soc. Am. **106**, 3178-3188 (1999).

47. Lauchle, G.C. and W.A. Kargus, IV, "Scaling of Turbulent Wall Pressure Fluctuations Downstream of a Rearward Facing Step," J. Acoust. Soc. Am. **107**, L1-L6 (2000).

3.3 *Piezoelectric Transformers*

48. Koc, B., S. Alkoy, and K. Uchino, "A Circular Piezoelectric Transformer with Crescent Shape Input Electrodes," Proc. IEEE Ultrasonic Symp., Lake Tahoe, Nevada, Oct. 17-21 (1999).

49. Koc, B. and K. Uchino, "Disk Type Piezoelectric Transformer with Crescent Shape Input Electrodes," Proc. NATO- Advanced Research Workshop: Piezoelectric Materials, Advance in Science, Technology and Applications, Predeal, Romania (May 24-27, 1999).

#### 4.0 ACTUATOR STUDIES

##### 4.1 *Materials and Designs*

50. Uchino, K., "Recent Trend of Piezoelectric Actuator Developments," Proc. Int'l Symp. Micromechatronics and Human Science '99, p.3-9, Nagoya, Japan (Nov. 23-26, 1999).
51. Yao, K., W. Zhu, K. Uchino, Z. Zhang and L.C. Lim, "Design and Fabrication of a High Performance Multilayer Piezoelectric Actuator with Bending Deformation," **46** (4), 1020-1027 (1999).
52. Wang, Q.-M., X.-H. Du, B. Xu, and L.E. Cross, "Electromechanical Coupling and Output Efficiency of Piezoelectric Bending Actuators," IEEE Transactions on Ultrasonics, Ferroelectrics, and Frequency Control **46** (3), 638-646 (1999).
53. Wang, Q.-M. and L.E. Cross, "Analysis of High Temperature Reduction Processing of RAINBOW Actuator," Materials Chemistry and Physics **58**, 20-25 (1999).
54. Glazounov, A.E., Q.M. Zhang, and C. Kim, "Torsional Actuator Based on Mechanically Amplified Shear Piezoelectric Response," Sensors and Actuators A79, 22-30 (2000).
55. Yoo, J.-H., J.-I Hong, and W. Cao, "Piezoelectric Ceramic Bimorph Coupled to Thin Metal Plat as Cooling Fan for Electronic Devices," Sensors and Actuators **79**, 8-12 (1999).

##### 4.2 *Photostriction*

56. Poosanaas, P., K. Tonooka and K. Uchino, "Photostrictive Actuators," J. Mechatronics (1999) [in press].
57. Poosanaas, P. and K. Uchino, "Photostrictive Effect in Lanthanum-Modified Lead Zirconate Titanate Ceramics near the Morphotropic Phase Boundary," J. Mater. Chem. and Phys. **61**, 36-41 (1999).

### VOLUME IV

##### 4.3 *High Force Torsional Actuators*

58. Frank, J.E., G.H. Koopmann, W. Chen, and G.A. Lesieutre, "Design and Performance of a High Force Piezoelectric Inchworm Actuator," Proceedings of SPIE 6<sup>th</sup> Annual International Symposium on Smart Structures and Materials, 1999.
59. Koopmann, G.H., G.A. Lesieutre, J. Frank, and W. Chen, "Design and Performance of a Linear Piezoelectric Wedgeworm Actuator," Piezoelectric Materials: Advances in Science, Technology and Applications, 383-390 (2000).
60. Frank, J. E.M. Mockensturm, W. Chen, G.H. Koopmann, and G.A. Lesieutre, "Roller-Wedgeworm: A Piezoelectrically-Driven Rotary Motor," 10<sup>th</sup> International Conference on Adaptive Structures and Technologies, Paris (October 1999).

#### 4.4 Piezoelectric Mini Motors

61. Glazounov, A.E., S. Wang, Q.M. Zhang, and C. Kim, "High Efficiency Piezoelectric Motor Combining Continuous Rotation with Precise Control Over Angular Positioning," *Appl. Phys. Lett.* **75**, 862-864 (1999).
62. Uchino, K. and B. Koc, "Compact Piezoelectric Ultrasonic Motors," *Ferroelectrics* **230**, 73-86 (1999).
63. Kim, J.S., M.J. Park, and K. Uchino, "Composite Ultrasonic Motors Using a Piezoelectric Disk and an Elastic Body of "Windmill" Type," *Ferroelectrics* **232**, 185-190 (1999).
64. Koc, B., P. Bouchilloux, and K. Uchino, "Piezoelectric Micromotor Using A Metal-Ceramic Composite Structure," *IEEE Trans. Ultrasonic, Ferroelectrics, and Frequency Control* (1999).

#### 5.0 MODELING and CHARACTERIZATION

##### 5.1 Simulation

65. Cao, W., S. Tavener, and S. Xie, "Simulation of Boundary Condition Influence in a Second-Order Ferroelectric Phase Transition," *J. Appl. Phys.* **86**, 5739-5746 (1999).
66. Shen, M. and W. Cao, "Acoustic Band-Gap Engineering Using Finite Size Layered Structures of Multiple Periodicity," *Appl. Phys. Lett.* **75**, 3713-3715 (1999).
67. Uchino, K., and H. Aburatani, "Field Induced Acoustic Emission in Ferroelectric Ceramics," *Proc. 101st Annual Mtg. of Amer. Ceram. Soc., Symp. Dielectric Materials and Devices*, SE-56, Indianapolis, April 25 - 28 (1999). [accepted]
68. Uchino, K., J. Zheng, Y.H. Chen, X. Du, S. Hirose, and S. Takahashi, "Loss Mechanisms in Piezoelectrics—Extrinsic and Intrinsic Losses." *Mater. Res. Soc. Fall Mtg. '99*, LL.1.6, Boston, Nov. 29-Dec.3 (1999).
69. Uchino, K. and S. Hirose, "Loss Mechanisms in Piezoelectrics," submitted to *IEEE UFFC Transactions* (1999).

#### VOLUME V

70. Uchino, K., J. Zheng, Y.H. Chen, X. Du, and S. Hirose, "Loss Mechanisms in Piezoelectrics," *Mater. Res. Soc. Fall Mtg. '99*, Boston (Nov. 29-Dec.3, 1999).

##### 5.2 Thin and Thick Films

71. Abothu, I.R., Y. Ito, P. Poosanaas, S. Kalpat, S. Komarneni, and K. Uchino, "Sol-Gel Processing of Piezoelectric Thin Films," *Ferroelectrics* **232**, 191-195 (1999).
72. Kalpat, S., I.R. Abothu, A. Akiba, H. Goto, S. Trolier-McKinstry, and K. Uchino, "Dielectric and Piezoelectric Property Dependence on Highly Textured (100), (111) and Random Thin Films Grown by RF Sputtering," *Symp. LL Proc., Mater. Res. Soc. Fall Mtg. '99*, LL.1.3, Boston, Nov. 29-Dec.3 (1999).
73. Xu, F., F. Chu, and S. Trolier-McKinstry, "Longitudinal Piezoelectric Coefficient Measurement for Bulk Ceramics and Thin Films Using Pneumatic Pressure Rig," *J. Appl. Phys.* **86** (1) 588 -594 (1999).

## 5.0 MODELING and CHARACTERIZATION

### 5.2 *Thin and Thick Films (continued)*

- 74. Shepard, J. F., Jr., F. Chu, I. Kanno, and S. Trolier-McKinstry, "Characterization and Aging Response of the  $d_{31}$  Piezoelectric Coefficient of Lead Zirconate Titanate Thin Films," J. Appl. Phys. **85**(9), 6711-6716 (1999).
- 75. Xu, B., Y. Ye, L.E. Cross, J.J. Bernstein, and R. Miller, "Dielectric Hysteresis from Transverse Electric Fields in Lead Zirconate Titanate Thin Films." Applied Physics Letters **74** (23), 3549-3551 (1999).
- 76. Xu, B., R.G. Polcawich, S. Trolier-McKinstry, Y. Ye, L.E. Cross, J.J. Bernstein, and R. Miller, "Sensing Characteristics of In-Plane Polarized Lead Zirconate Titanate Thin Films," Applied Physics Letter **75** (26), 4180 (December 1999).
- 77. Xu, B., L.E. Cross, and D. Ravichandran, "Synthesis of Lead Zirconate Titanate Stannate Antiferroelectric Thick Films by Sol-Gel Processing." J. Am. Ceramic Soc. **82** (2), 306-312 (1999).
- 78. Xu, B., Y. Ye, Q.-M. Wang, and L.E. Cross, "Dependence of Electrical Properties on Film Thickness in Lanthanum-Doped Lead Zirconate Titanate Stannate Antiferroelectric Thin Films." Journal of Applied Physics **85** (7), 3753-3758 (1999).

### 5.3 *Domain Studies*

- 79. Belegundu, U., X.H. Du, A. Bhalla, and K. Uchino, "Effect of Electric Field on Domain Formation in Relaxor Based  $\text{Pb}(\text{Zn}_{1/3}\text{Nb}_{2/3})\text{O}_3$ - $\text{PbTiO}_3$  Single Crystals," Ferroelectrics Letters **26** (5-6), 107-116 (1999).
- 80. Belegundu, U., X.H. Du, L.E. Cross and K. Uchino, "In Situ Observation of Domains in  $0.9\text{Pb}(\text{Zn}_{1/3}\text{Nb}_{2/3})\text{O}_3$ - $0.1\text{PbTiO}_3$  Single Crystals," Ferroelectrics **221**, 67-71 (1999). (First Author Supervised by Candidate).
- 81. Hatch, D.M. and W. Cao, "Determination of Domain and Domain Wall Formation at Ferroic Transitions," Ferroelectrics **222**, 1-10 (1999).
- 82. Cao, W. and S.N. Zhu, "Observation of Ferroelectric Domains in  $\text{LiTaO}_3$ ," Ferroelectrics **226**, 27-35 (1999).
- 83. Zhu, S.N. and W. Cao, "Imaging of 180 Ferroelectric Domains in  $\text{LiTaO}_3$  by Scanning Electron Microscopy," Phys. Stat. Sol. (a) **173**, 495-502 (1999).
- 84. Mueller, V., H. Beige, and Q.M. Zhang, "Nonlinear Ferroelectric Domain Wall Response," Ferroelectrics **222**, 295-302 (1999).
- 85. Liu, R., R. Guo, A.S. Bhalla, L.E. Cross, M. Levy, and R.M. Osgood Jr., "Optical Observation of Dynamic Ferroelectric Phase Transition and Static Domain Structures in Crystal Ion Sliced (CIS)  $\text{LiNbO}_3$  Film." Materials Letters **39**, 264-267 (1999).

### 5.4 *Electrostriction*

- 86. Eury, S., R. Yimnirun, V. Sundar, P.J. Moses, S.J. Jang, and R.E. Newnham, "Converse Electrostriction in Polymers and Composites," Mat. Chem. and Phys. **61**, 18-23 (1999).
- 87. Yimnirun, R., S.M.-L. Eury, V. Sundar, P.J. Moses, S. Jang, and R.E. Newnham, "Electrostriction Measurement on Low Permittivity Dielectric Materials," Journal of European Ceramics Society **19**, 1269-1273 (1999).

## ABSTRACT

This report describes the research performed over the period of 1 January 1999 to 31 December 1999 on a MURI under Office of Naval Research contract N00014-96-1-1173 on the topic "Acoustic Transduction: Materials and Devices" brings together work from the Materials Research Laboratory (MRL), the Applied Research Laboratory (ARL), and the Center for Acoustics and Vibrations (CAV) at The Pennsylvania State University. As has become customary over many years research on the program is described in detail in the 87 technical appendices to this report and only a brief narrative description connecting this research is given in the text.

Perhaps the most outstanding accomplishment of the year is a "spin on" from our earlier single crystal studies now involving Brookhaven National Laboratory and Professor Gonzalo's group in Madrid, Spain. Using exceptionally homogeneous polycrystal lead zirconate titanate samples prepared in MRL, precise synchrotron x-ray analysis has confirmed a new monoclinic phase at lower temperature in composition close to the important morphotropic phase boundary. This work demands a re-thinking of both intrinsic and extrinsic contributions to response in this most important practical transducer material family. Domain Engineering/Domain Averaging in lead zinc niobate:lead titanate (PZN:PT) in lead magnesium niobate:lead titanate (PMN:PT) and in barium titanate ( $\text{BaTiO}_3$ ) continues to offer single crystal systems with outstanding transducer and actuator properties and new insights into the field induced strain mechanisms in all perovskite type piezoelectrics. Excellent progress with the new high strain irradiated P(VDF:TrFE) relaxor ferroelectric copolymer system has helped catalyze a new DARPA initiative in this area and a re-awakening of interest in the whole area of electrostrictive polymer systems.

A primary objective of this MURI grouping was to help shorten the time constant for new materials and device concepts to be applied in practical Navy Systems. We believe this has now been realized in joint work on the composite cymbal type flextensional arrays for large area projectors, and in the progress made towards a micro-tonpils array system.

Original work on new step and repeat piezoelectric high strain systems continues to make good progress now using commercial motion rectifiers to produce both linear and rotary systems with high torque capability. New composite designs are pushing toward 1 mm diameter motors in the size regimen where there are real difficulties for conventional electromagnetic designs.

A new area of activity this year is in piezoelectric transformers where a circular symmetry design in conjunction with controlled inhomogeneous poling is shown to offer capabilities which are of real interest for energy recovery actuator power systems. Basic studies have evolved a new environmental SEM technique for high resolution domain wall studies without changing problems. Work is continuing on reliable measurements of electrostrictive constants in simple solids confirming by both direct and converse methods and permitting the first generalization of trends in these fundamentally important coupling constants.

## INTRODUCTION

This report describes research performed over the period of 1 January 1999 to 31 December 1999 on a MURI under Office of Naval Research contract N00014-96-1173 on the topic "Acoustic Transduction Materials and Devices." This program commenced on 31 July 1996 and brings together activities in the Materials Research Laboratory (MRL), the Applied Research Laboratory (ARL), and the Center for Acoustics and Vibrations (CAV) at The Pennsylvania State University. The principal investigator on this program is

Dr. Kenji Uchino, Professor of Electrical Engineering at Penn State. The program officer for the Office of Naval Research is Dr. Jan Lindberg.

The overall objective of the program is the development of acoustic transduction materials and devices of direct relevance to U.S. Navy needs, but also with relevant application capability in commercial sector products. A continuing emphasis is upon high performance high sensitivity sensors and upon high authority high strain actuators for transducing functions. New materials and improved material systems are being developed on the program. These studies are affording new insights into the strain mechanisms in already widely used ceramics and polymers and are developing needs for new device structures and improved drive and control strategies. There is a proper emphasis upon performance and reliability under the wide range of operating conditions consonant with Navy needs.

Responsibility for the program elements are assigned as follows:

MATERIAL STUDIES	A.S. Bhalla
COMPOSITE SYSTEMS	R.E. Newnham
DEVICE STRUCTURES	T.R. Shrout
MODELING	W. Cao
DEVICE FABRICATION and TESTING	W.J. Hughes
AIR ACOUSTICS: STEP and REPEAT SYSTEMS	G. Lesieutre

Layout of the report follows long established precedent drawing upon the 87 published papers that are included as appendices with a very brief narrative summary to interconnect the different studies. In this report the topics are clustered as follows:

- 1.0 GENERAL SUMMARY PAPERS
- 2.0 MATERIALS STUDIES
  - 2.1 Polycrystal Perovskite Ceramics
  - 2.2 Single Crystal Systems
  - 2.3 High Strain Polymers
- 3.0 TRANSDUCER STUDIES
  - 3.1 Composite Transducers
  - 3.2 3 Dimensional Acoustic Intensity Probes
  - 3.3 Piezoelectric Transformers
- 4.0 ACTUATOR STUDIES
  - 4.1 Materials and Designs
  - 4.2 Photostriction
  - 4.3 High Force Torsional Actuators
  - 4.4 Piezoelectric Mini Motors
- 5.0 MODELING and CHARACTERIZATION
  - 5.1 Simulation
  - 5.2 Thin and Thick Films
  - 5.3 Domain Studies
  - 5.4 Electrostriction

#### 1.0 GENERAL SUMMARY PAPERS

In December of 1998, Dr. Robert E. Newnham retired taking Emeritus status at Penn State. There is certainly no better way to start this 1999 year report than a brief tribute to his long highly productive career as exemplified at the Newnham Festschrift Session of the innovations in Materials Conference in Washington, DC, July 1999 (1). His insights and true

social concerns are further evidenced in the European Ceramic Society Plenary Address (2). New trends in Ceramic Actuators (3) and their broadening use in smart composite materials (4,5) are well described by Uchino and co-authors. The possibilities for a very different charge separation mechanism in insulators, flexoelectricity is discussed in (6).

## 2.0 MATERIALS STUDIES

### 2.1 *Polycrystal Perovskite Ceramics*

A most exciting new discovery in the phase behavior of the widely used lead zirconate titanate PZT family materials is delineated in (7,8,9,10). Very careful, precise x-ray analysis using the synchrotron facility at Brookhaven on highly homogeneous samples prepared at Penn State has shown unequivocal evidence of a monoclinic symmetry phase just at the critical 52:48 composition of the Morphotropic Phase Boundary (MPB) on the rhombohedral side of the boundary. No doubt this phase plays an important role in the continuity of  $D$  in the poled PZT and offers the possibility of a completely new extrinsic contribution to weak field response. Influence of external applied stress on hard and soft PZTs is explored in (11), results agree well with the expectation from defect dipole hardening in the hard materials. High frequency characterization is discussed in (12) for the range 20-60 MHz. The effects of stress on the ceramic 0.9 PMN:0.1 PT are examined in (13,14) and provide an interesting indirect assessment of the scale of the micropolar regions responsible for the relaxor behavior.

Several different solid solution systems are considered in (15,16,17,18). For  $\text{Bi}(\text{NiTi})_{1/2}\text{O}_3\text{:PbTiO}_3$  compositions with high hydrostatic  $d_h$  are demonstrated (15) giving figure of merit  $d_{hg} \cong 1055 \cdot 10^{-5} \text{ m}^2/\text{N}$  lead indium niobate:lead titanate at the high PIN end (16) shows typical relaxor behavior, with low hysteresis in field induced  $x_{33}$  and correspondingly low  $P_r$ . In  $\text{Pb}(\text{In}_{1/2}\text{Ta}_{1/2})\text{O}_3\text{:PbTiO}_3$  MPB compositions (17) are explored at 38 mole% PT with  $T_c \sim 248^\circ\text{C}$  and  $d_{33} \sim 302 \text{ pC/N}$ . Iron doped  $\text{Pb}(\text{Sc}_{1/2}\text{Nb}_{1/2})\text{O}_3\text{:PbTiO}_3$  at the MPB composition (18) is examined for high power applications and shown to have quality factor  $Q_m = 297$  with 0.3 wt%  $\text{Fe}_2\text{O}_3$  added. Properties of hydrothermal PLZT powders are discussed in (19) that compares traditional and microwave assisted synthesis. A second avenue to explore "hardening" mechanisms is in the PMN:PT family at compositions close to the MPB using different doping schemes (20,21). Following from the massive anisotropy observed in single crystals, measurements have been carried out of induced anisotropy in poled polycrystal PZT (22). It is gratifying to find that in the rhombohedral phase a weak peak occurs for a  $45^\circ$  tilt to  $P_r$  whilst in the tetragonal phase  $d_{33}$  effective continuously decreases with tilt angle.

### 2.2 *Single Crystal Systems*

The domain configuration engineering in 001 field poled rhombohedral PZN:PT crystals is discussed in (23-28). Stability of the polydomain 001 poled structure is contrasted in (23) with the lower stability of the 111 poled state. Weak field measurements are shown to give equivalent values of  $d_h$  in both 111 and 001 poled PZN 4.5% PT in (24). The more general problem of twinned ferroelectric crystals is discussed in (25) and symmetries derived for twinned  $\text{LiNbO}_3$  and  $\text{BaTiO}_3$ . Elastic, Dielectric, and Piezoelectric properties for 001 poled PZN 4.5 PT are examined in (26) and a very soft 110 directed shear mode identified. Defect induced domain like properties are described in (27) for PZN single crystals and suggested to be defect related. Domain switching is examined in (28) for both PZN 4.5 %PT and PZN 9%PT. Under these high fields evidence for the co-existence of both tetragonal and rhombohedral phases is adduced. Crystallographically engineered  $\text{BaTiO}_3$  crystals are discussed in (29,30) where very high values of  $d_{33}$  and  $k_{33}$  are observed in 001 oriented crystals near

the ferroelectric:ferroelectric phase transitions (29) and at room temperature canted cuts are shown both experimentally and theoretically to have enhanced effective  $d_{33}$  up to a tilt angle  $\sim 50^\circ$  (30).

In an important paper, the fully panoply of electro-optic constants for 88% PZN:12% PT are measured (31) and the expected high values of  $r_{51}$  delineated

### 2.3 *High Strain Polymers*

Evidence is presented for the very useful high electrostrictive strain capability in high energy electron irradiated P(VDF:TrFE) copolymers. In (32) structural and polarization properties are discussed. Relaxor behavior is confirmed in the dielectric response by close agreement with Vogel:Fulcher law. Transverse strain that is the most important parameter in polymers is shown to be enhanced by drawing (33) and a very neat cantilever beam dilatometer for such transverse strain measurement is explored in (34). That high strain can even be generated at high mechanical stress levels is confirmed in (35).

## 3.0 TRANSDUCER STUDIES

### 3.1 *Composite Transducers*

One of the earliest structures evolved in the Penn State composite transducer program was the 1:3 composite. It has proven to be most effective and versatile in both Navy and commercial systems, however only recently has the theory developed to the state of being able to properly describe the resonant modes and losses (36). Current status in both polymer:ceramic and metal:ceramic composites is summarized in (37,38) covering both sensing and actuation functions.

Larger area projectors using cymbal type composites have been assembled and tested (39) with most encouraging results for shallow water applications. Tests on single cymbals are discussed in (40), and the requirements for the planar  $3 \times 3$  cymbal array in (41). A new design that has been tested up to much higher pressure uses a ring transducer with concave cymbal caps (42). It has been shown to stand 6MPa pressure and to be amenable to high sensitivity array construction. For piezoelectric hollow mini spheres resonant performance has been examined for both radial and transverse poling. Hydrostatic charge coefficients  $d_h$  from 600 to 1,800 pC/N have been measured (43).

A new type of piezoelectric tensegrity structure is discussed in (44) and shown to yield hydrostatic response of 700 pC/N. Applications of piezoelectrics and composites as both sensors and actuators forming smart structures are discussed in (45) and possible application in fish farming and beyond underscored.

### 3.2 *3 Dimensional Acoustic Intensity Probes*

A most interesting displacement, displacement (u,u) sensing intensity probe is discussed in (46) where a new theoretical approach is used to compute acoustic intensity from particle velocity at two closely spaced locations.

The problem of turbulent wall pressure fluctuations downstream from a rearward facing profile step is considered in (47) where a new form for the non dimensional point wall pressure auto-frequency spectrum is proposed that includes the statistical variation of the reattachment locations.

### 3.3 *Piezoelectric Transformers*

A new type of circular piezoelectric transformer is discussed in (48). To make use of the higher shear mode constants of PZT, crescent shaped electrodes at the input side and focused poling direction at the output is designed so that planar and shear mode coupling

factors became effective rather than the lower transverse mode coupling. A prototype three-layer disk type operating at a frequency of 153 kHz is discussed in (49).

#### 4.0 ACTUATOR STUDIES

##### 4.1 *Materials and Designs*

Recent trends in actuator development are summarized in (50) with a focus on high coupling piezoelectrics. A new type of bending mode device is discussed in (51) using a transverse rather than thickness mode in a multilayer structure. The more conventional bending mode bimorph and unimorph are discussed in (52) which gives four detailed examples of derivations for unimorph structures. A more complete analysis of the reduction process involved in fabricating RAINBOW bending mode actuators is given in (53) that determines both the diffusion rate constant and activation energy for the oxygen vacancy dominated process. An interesting new type of amplified torsional vibrator is discussed in (54) where increased gain is not at the expense of torque. The application of bimorphs as cooling element drivers for electron devices is discussed in (55).

##### 4.2 *Photostriction*

Photostriction in tungsten modified PLZT compositions is examined in (56,57). Light driven relays and walking devices have been demonstrated in bimorph configuration (56) and it is shown that maximum photo current and maximum photo voltage occur with slightly different La concentration. Material figures of merit are given that include both magnitude of strain and response speed (57).

##### 4.3 *High Force Torsional Actuators*

Work on the program has continued to make major improvements in step and repeat inchworm type actuators. A new design for the classic inchworm is discussed in (58) that yields force ~150N, unlimited displacement, holding force of 350N and precise sub-micron positioning precision. An alternative wedge worm device is described in (59) with a much simplified structure yielding force ~250N throw of 25mm and a speed of 8mm/sec. A rotary form of the wedgeworm, using roller clutches is examined in (60) with demonstrated steady torque of 05Nm and speed of 450 RPM.

##### 4.4 *Piezoelectric Mini Motors*

The whole area of piezoelectric motor development appears poised for major advance with high torque (60), high efficiency (61) and new very compact motor types now under development. The torsional amplifier discussed earlier (54) has been adapted using a roller clutch to develop (61) a highly efficient rotary stepping motor with high angular precision. A more general discussion of motor principles is given in (62) with emphasis upon the possibility of very compact motors. The composite "Windmill" type small motor is discussed in (63) and a very compact simple to construct miniature variant is considered in (64). This very simple structure provides a starting torque of 17 $\mu$ Nm for a driving voltage of 20 V rms.

#### 5.0 MODELING and CHARACTERIZATION STUDIES

##### 5.1 *Simulation*

Using a two-dimensional Ginsburg-Landau model with finite element computation stable domain structures are calculated for the state resulting from a second order ferroelectric phase change (65). Acoustic band gap engineering (66) is explored for finite size layer structures. It is found that very sharp pass bands and broad stop bands can be engineering

using only 3-4 cells of a two-phase layer structure. Field induced acoustic emission in ferroelectric ceramics is discussed in (67). For bipolar fields it is suggested that both domain reorientation and piezoelectric deformation can contribute.

The important topic of loss mechanisms in piezoelectrics is examined in (68,69,70). These papers set up the phenomenological relations to separate and measure the dielectric, mechanical, and piezoelectric contributions to loss. It is shown that off resonance at high drives, heat generation is mostly through electrical loss  $\tan \delta$  (P-E hysteresis loss). Based on these works, it is suggested that for high power applications antiresonant mode may be more effective since the  $Q$  is larger than at resonance.

### 5.2 *Thin and Thick Films*

Sol-gel processing has been used to produce 001 oriented PZT thin films in the rhombohedral phase (71) with 80/20 Zr/Ti films showing  $28 \mu\text{C}/\text{cm}^2$   $P_r$  and  $E_c \sim 17 \text{ kV}/\text{cm}$ .

Both 001 and 111 oriented films of PZT have been produced by reactive sputtering (72) and it is shown that the 001 oriented films show lower coercivity and squarer hysteresis. Using a newly designed pneumatic test rig (73) piezoelectric  $d_{33}$  constants have been measured for both bulk and thin films PZTs. For the bulk samples pneumatic, Berlincourt meter and optical dilatometer measurements yield consistent results. Aging of  $d_{31}$  has been measured in both sputtered and sol-gel films (74) and shown to be a strong function of film thickness with very high rates in the thinner films.

To exploit the higher  $d_{33}$  in thin film bending mode devices bilayer PZT:ZrO<sub>2</sub> films have been produced by sol-gel processing (75). Excellent hysteresis is observed for fields applied with interdigitated electrodes. Very high sensor sensitivity can be achieved in the bilayer diaphragm (76) since thickness and electrode spacing on the PZT can now be controlled separately. Both square and slanted double hysteresis effects have been generated in lanthanum and in niobium modified lead zirconate titanate stannate antiferroelectric films (77). Polarization in the range  $35\text{-}40 \mu\text{C}/\text{cm}$  with zero remanence can be generated (78) where both thin and thick films have been examined.

### 5.3 *Domain Studies*

Domain switching has been observed in 0.9 PZN:0.1 PT crystals under the influence of both 001 and 111 oriented fields (79). For 001 orientation a single domain tetragonal phase can be achieved at higher field levels. Temperature studies on a similar composition in (80) where it was observed that single phase rhombohedral symmetry was not obtained even at  $-100^\circ\text{C}$ . More general determination of domain and domain wall formation is discussed in (81) using group theory and a Landau Ginsburg expansion. Dependence of the wall profile on the expansion coefficients in the energy is discussed. The interesting environmental scanning electron microscope (ESEM) technique for exploring ferroelectric domain structure on insulating surfaces without surfaces charging is described in (82). The images observed in a conventional SEM are discussed in (83) and the differences between pyroelectric and piezoelectric contrast are described.

Nonlinear ferroelectric wall response in an incommensurate Rb<sub>2</sub>ZnCl<sub>4</sub> crystal is analyzed in (84) and compared to response in PZTs. Similarities between these very different systems are suggested to stem from a universal model for the nonlinearity.

Intriguing optical microscopy of the surfaces of ion sliced LiNbO<sub>3</sub> crystals show complex surface domain structures, but the ferroelectric phase change at  $1163^\circ\text{C}$  is unaffected by the ion slicing process (85).

#### 5.4 Electrostriction

Electrostriction is the fundamental coupling between electric polarization and elastic strain in all insulating crystals. It is almost scandalous that no Standards organization in the world has ever made any effort to make reliable measurements of electrostriction in simple solids and until the Penn State work there were no reliable constants in the literature. Using both the converse effect (86) and combinations of direct and converse measurements (87) it is shown that reliable data can be achieved and the general relation governing electrostriction in simple solids can be explored.

#### 6.0 GRADUATE STUDENTS IN THE PROGRAM

Student	Advisor	Student	Advisor
E. Alberta	A.S. Bhalla	J. Frank	G.H. Koopmann
K. Kang	G.C. Lauchle	J. Jiang	G.H. Koopmann
J.A. McConnell	G.C. Lauchle	W. Ren	S. Trolier-McKinstry
K.J. Bastyr	G.C. Lauchle	A. Foulk	W.J. Hughes
J. Zhang	R.E. Newnham	D. VanTol	W.J. Hughes
B. Yi	Q. Zhang	V. Desai	R. Tutwiler
Y.H. Chen	K. Uchino	J.S. Sabarad	R. Tutwiler
B. Koc	K. Uchino	R. Dave	R. Tutwiler

#### 7.0 HONORS and AWARDS

Robert E. Newnham

ASME Adaptive Structures & Materials Systems Prize, 1999.  
International Award, European Ceramic Society, 1999.  
International Prize, Japan Fine Ceramics Center, 1999.

Susan Trolier-McKinstry

Incoming Vice-President of the IEEE Ferroelectrics Committee.  
Robert Coble Award of the American Ceramic Society, 1999,  
Achieving Women at Penn State, 1999.

#### 8.0 PAPERS PUBLISHED IN REFEREED JOURNALS

1. Cross, L.E., "Newnham Festschrift Introduction," Guest Editorial, Mat. Res. Innovations **2**, 251 (1999).
2. Fousek, J., L.E. Cross, and D.B. Litvin, "Possible Piezoelectric Composites Based on the Flexoelectric Effect," Materials Letters **39**, 287-291 (1999).
3. Liu, R., R. Guo, A.S. Bhalla, L.E. Cross, M. Levy, and R.M. Osgood Jr., "Optical Observation of Dynamic Ferroelectric Phase Transition and Static Domain Structures in Crystal Ion Sliced (CIS) LiNbO<sub>3</sub> Film," Materials Letters **39**, 264-267 (1999).
4. Liu, S.-F., S.E. Park, T.R. Shrout, and L.E. Cross. "Electric Field Dependence of Piezoelectric Properties for Rhombohedral 0.955Pb(Zn<sub>1/3</sub>Nb<sub>2/3</sub>)O<sub>3</sub>-0.045PbTiO<sub>3</sub> Single Crystals," Journal of Applied Physics **85**(5), 2810-2814 (1999).
5. Noheda, B., D.E. Cox, G. Shirane, J.A. Gonzalo, L.E. Cross, and S.-E. Park, "A Monoclinic Ferroelectric Phase in the Pb(Zr<sub>1-x</sub>Ti<sub>x</sub>)O<sub>3</sub> Solid Solution," Applied Physics Letters **74**(14), 2059-2061 (1999).

6. Park, S.-E., S. Wada, L.E. Cross, and T.R. Shrout, "Crystallographically Engineered BaTiO<sub>3</sub> Single Crystals for High-Performance Piezoelectrics," Journal of Applied Physics **86**(5), 2746-2750 (1999).
7. Wada, S., S.E. Park, L.E. Cross, and T.R. Shrout, "Engineered Domain Configuration in Rhombohedral PZN-PT Single Crystals and their Ferroelectric Related Properties," Ferroelectrics **221**, 147-155 (1999).
8. Wada, S., S.E. Park, L.E. Cross, and T.R. Shrout, "Defect-induced Domain Configuratrion in Relaxor PZN Single Crystal and Its Origin," Trans. of the Mat. Res. Soc. Of Japan **24**(1), 19-22 (1999).
9. Wang, Q.-M. and L.E. Cross, "Analysis of High Temperature Reduction Processing of RAINBOW Actuator." Materials Chemistry and Physics **58**, 20-25 (1999).
10. Wang, Q.-M., X.-H. Du, B. Xu, and L.E. Cross, "Electromechanical Coupling and Output Efficiency of Piezoelectric Bending Actuators." IEEE Transactions on Ultrasonics, Ferroelectrics, and Frequency Control **46**(3), 638-646 (1999).
11. Xu, B, L.E. Cross, and D. Ravichandran, "Synthesis of Lead Zirconate Titanate Stannate Antiferroelectric Thick Films by Sol-Gel Processing." J. Am. Ceramic Soc. **82**(2), 306-312 (1999).
12. Xu, B., Y. Ye, Q.-M. Wang, and L.E. Cross, "Dependence of Electrical Properties on Film Thickness in Lanthanum-Doped Lead Zirconate Titanate Stannate Antiferroelectric Thin Films." Journal of Applied Physics **85**(7), 3753-3758 (1999).
13. Xu, B., Y. Ye, L.E. Cross, J.J. Bernstein, and R. Miller, "Dielectric Hysteresis from Transverse Electric Fields in Lead Zirconate Titanate Thin Films." Applied Physics Letters **74**(23), 3549-3551 (1999).
14. Tressler, J.F., S. Alkoy, A. Dogan, and R.E. Newnham, "Functional Composites for Sensors, Actuators and Transducers," Composites Part A: Applied Science & Manufacturing **30**, 477-482 (1999).
15. Tressler, J.F. and R.E. Newnham, "Capped Ceramic Underwater Sound Projector: the cymbal transducer," J. of Acoustical Soc. America **105**(2), part 1, 591-600 (1999).
16. Zhang, J., W.J. Hughes, A.C. Hladky-Hennion and R.E. Newnham, "Concave Cymbal Transducers," Materials Research Innovations **2**(5), 252-255 (1999).
17. Eury, S., R. Yimnirun, V. Sundar, P.J. Moses, S.J. Jang, and R.E. Newnham, "Converse Electrostriction in Polymers and Composites," Mat. Chem. and Phys. **61**, 18-23 (1999).
18. Yimnirun, R., S.M.-L. Eury, V. Sundar, P.J. Moses, S. Jang, and R.E. Newnham, "Electrostriction Measurement on Low Permittivity Dielectric Materials," Journal of European Ceramics Society **19**, 1269-1273 (1999).
19. Alkoy, S., R.E. Newnham, A.C. Hladky, A. Dogan, and J.K. Cochran, Jr., "Piezoelectric Hollow Spheres for Microprobe Hydrophones," Ferroelectrics **226**, 11-25 (1999).
20. Zhang, J., W.J. Hughes., P. Bouchilloux, R. Meyer Jr., K. Uchino, and R.E. Newnham, "A Class V Flexensional Transducer: The Cymbal," Ultrasonics **37**, 387-393 (1999).
21. Newnham, R.E., "Ceramics into the Next Millennium," British Ceramic Transactions, **98**(5), 251-255 (1999).
22. Carlson, W.B., R.E. Newnham and D.P. Williams, "Piezotensegritic Structures for Transducer Applications," Materials Research Innovations **3**, 175-178 (1999).

23. Newnham, R.E. and A. Amin, "Smart Systems: Microphones, Fish Farming, and Beyond," Chemtech **29**(12), 38-47 (1999).
24. Zhao, J., A.E. Glazounov, and Q.M. Zhang, "Change in Electromechanical Properties of 0.9PMN-0.1PT Relaxor Ferroelectric Induced by Uniaxial Compressive Stress Directed Perpendicular to the Electric Field," Appl. Phys. Lett. **74**, 436-438 (1999).
25. Geng, X. and Q.M. Zhang, "Resonance Modes and Losses in 1-3 Composites for Ultrasonic Transducer Applications," J. Appl. Phys. **85**, 1342-1350 (1999).
26. Zhao, J., V. Mueller, and Q.M. Zhang, "The Influence of External Stress on the Electromechanical Response of Electrostrictive 0.9PMN-0.1PT in the DC Field Biased State," J. Mater. Res. **14**, 948-956 (1999).
27. Liu, R., Q. Wang, Q.M. Zhang, and L.E. Cross, "Piezoelectric Pseudo-Shear Universal Actuator Made by L-Shape Joint Bonding," J. Mat. Sci: Mat. in Electro. **9**, 453-456 (1999).
28. Cheng, Z.-Y., T.-B. Xu, V. Bharti, S. Wang, and Q.M. Zhang, "Transverse Strain Response in the Electrostrictive P(VDF-TrFE) Copolymer," Appl. Phys. Lett. **74**, 1901-1903 (1999).
29. Cheng, Z.-Y., S. Gross, J. Su, and Q.M. Zhang, "Pressure-Temperature Phase Diagram for a Polyurethane Elastomer," J. Polym. Sci. **37**, 983-990 (1999).
30. Glazounov, A.E., S. Wang, Q.M. Zhang, and C. Kim, "High Efficiency Piezoelectric Motor Combining Continuous Rotation with Precise Control Over Angular Positioning," Appl. Phys. Lett. **75**, 862-864 (1999).
31. Cheng, Z.-Y., V. Bharti, T.B. Xu, S. Wang, Q.M. Zhang, T. Ramotowski, F. Tito, and R. Ting, "Transverse Strain Responses in Electrostrictive P(VDF-TrFE) Films and Development of a Dilatometer for the Measurement," J. Appl. Phys. **86**, 2208-2214 (1999).
32. Liu, R., Q.M. Zhang, and L.E. Cross, "Experimental Investigation of Field Induced Direct Piezoelectric Properties in Polyurethane Elastomer Under Quasistatic Condition," J. Appl. Polym. Sci. **73**, 2603-2609 (1999).
33. Mueller, V., H. Beige, and Q.M. Zhang, "Nonlinear Ferroelectric Domain Wall Response," Ferroelectrics **222**, 295-302 (1999).
34. Bharti, V., Z-Y Cheng, S. Gross, T.B. Xu, and Q.M. Zhang, "High Electrostrictive Strain under High Mechanical Stress in High Energy Electron Irradiated Poly(vinylidene fluoride-trifluoroethylene) Copolymer Films," Appl. Phys. Lett. **75**, 2653-2655 (1999).
35. Zhang, Q.M. and J. Zhao, "Electromechanical Responses of Lead Zirconate Titanate Piezoceramics Under the Influence of Mechanical Stresses. IEEE Trans. UFFC **46**, 1518-1526 (1999).
36. Wang, Q.-M., Q.M. Zhang, B. Xu, R. Liu, and L.E. Cross, "Nonlinear Piezoelectric Behavior of Ceramic Bending Mode Actuators Under Strong Electric Fields," J. Appl. Phys. **86**, 3352-3360 (1999).
37. Bharti, V., H.S. Xu, G. Shanthi, Q.M. Zhang, and K. Liang, "Polarization and Structural Properties of High Energy Electron Irradiated P(VDF-TrFE) Copolymer Films," J. Appl. Phys. **87**, 452-461 (2000).
38. Glazounov, A.E., Q.M. Zhang, and C. Kim, "Torsional Actuator Based on Mechanically Amplified Shear Piezoelectric Response," Sensors and Actuators A79, 22-30 (2000).

39. Lu, .Y., Z.-Y. Cheng, E. Park, S.F. Liu and Q.M. Zhang, "Linear Electro-optic Effect of  $0.88\text{Pb}(\text{Zn}_{1/3}\text{Nb}_{2/3})\text{-}0.12\text{PbTiO}_3$  Single Crystal," Jpn. J. Appl. Phys. 141-145 (2000).
40. Cao, W. and S.N. Zhu, "Observation of Ferroelectric Domains in  $\text{LiTaO}_3$ ," Ferroelectrics **226**, 27-35 (1999).
41. Zhu, S.N. and W. Cao, "Imaging of 180 Ferroelectric Domains in  $\text{LiTaO}_3$  by Scanning Electron Microscopy," Phys. Stat. Sol. (a) **173**, 495-502 (1999).
42. Hatch, D.M. and W. Cao, "Determination of Domain and Domain Wall Formation at Ferroic Transitions," Ferroelectrics **222**, 1-10 (1999).
43. Cao, W., S. Tavener, and S. Xie, "Simulation of Boundary Condition Influence in a Second-Order Ferroelectric Phase Transition," J. Appl. Phys. **86**, 5739-5746 (1999).
44. Erhart, J. and W. Cao, "Effective Material Properties in Twinned Ferroelectric Crystals," J. Appl. Phys. **86**, 1073-1081 (1999).
45. Yin, J., B. Jiang, and W. Cao, "Elastic, Piezoelectric and Dielectric Properties of  $0.955\text{Pb}(\text{Zn}_{1/3}\text{Nb}_{2/3})\text{O}_3\text{-}0.045\text{PbTiO}_3$  Single Crystal with Designed Multidomains," IEEE Transactions UFFC **47**, 285-291 (2000).
46. Wang, H., W. Jiang, and W. Cao, " Characterization of Lead Zirconate Titanate Piezoceramic Using High Frequency Ultrasonic Spectroscopy," J. Appl. Phys. **85**, 8083-8091 (1999).
47. Xu, F., F. Chu, and S. Trolier-McKinstry, "Longitudinal Piezoelectric Coefficient Measurement for Bulk Ceramics and Thin Films Using Pneumatic Pressure Rig," J. Appl. Phys. **86**(1) 588 -594 (1999).
48. Shepard, J. F., Jr., F. Chu, I. Kanno, and S. Trolier-McKinstry, "Characterization and Aging Response of the  $d_{31}$  Piezoelectric Coefficient of Lead Zirconate Titanate Thin Films," J. Appl. Phys. **85**(9), 6711-6716 (1999).
49. Shen, M. and W. Cao, "Acoustic Band-Gap Engineering Using Finite Size Layered Structures of Multiple Periodicity," Appl. Phys. Lett. **75**, 3713-3715 (1999).
50. Yoo, J.-H., J.-I Hong, and W. Cao, "Piezoelectric Ceramic Bimorph Coupled to Thin Metal Plat as Cooling Fan for Electronic Devices," Sensors and Actuators **79**, 8-12 (1999).
51. Brungart, T.A., G.C. Lauchle, S. Deutsch, and E. Riggs, "Outer Flow Modifications on Turbulent Boundary Layer Wall Pressure Fluctuations," J. Acoust. Soc. Am. **105**, 2097-2106 (1999).
52. Brungart, T.A., G.C. Lauchle, and R.K. Ramanujam, "Installation Effects on Fan Acoustic and Aerodynamic Performance," Noise Control Eng. J. **47**, 3-7 (1999).
53. Bastyr, K.J., G.C. Lauchle, and J.A. McConnell, "Development of a Velocity Gradient Underwater Acoustic Intensity Sensor," J. Acoust. Soc. Am. **106**, 3178-3188 (1999).
54. Lauchle, G.C. and W.A. Kargus, IV, "Scaling of Turbulent Wall Pressure Fluctuations Downstream of a Rearward Facing Step," J. Acoust. Soc. Am. **107**, L1-L6 (2000).
55. Albert, E.F., A.S. Bhalla, and T. Takenaka, "Large Hydrostatic Piezoelectric Constant and Temperature Dependence of the Piezoelectric Properties  $\text{Bi}(\text{Ni}_{1/2}\text{Ti}_{1/2})\text{O}_3\text{:PbTiO}_3$  Ceramics," Ferroelectrics Letters **25**, 45-52 (1999).
56. Alberta, E.F. and A.S. Bhalla, "Investigation of the Lead Indium Niobate-Lead Magnesium Niobate Solit Solution," Materials Letters **40**, 114-117 (1999).

57. Alberta, E.F. and A.S. Bhalla, "Electrical Properties of the Morphotropic Phase Boundary in  $\text{Pb}(\text{In}_{1/2}\text{Ta}_{1/2})\text{O}_3\text{-PbTiO}_3$  Ceramics," Ferroelectrics Letters **26**, 117-123 (1999).
58. Bernard, J., G. Lesieutre, and G.H. Koopmann, "Active Broadband Force Isolation Using Flexural Piezoelectric Inertial Actuators," Journal of the American Institute of Aeronautics and Astronautics, 99-1532 (1999).
59. Constans, E.W., A.D. Belegundu, and G.H. Koopmann, "Optimally Designed Shell Enclosures with Tuned Absorbers for Minimizing Sound Power," Optimization and Engineering (in print), Kluwer, 1999.
60. Frank, J.E., G.H. Koopmann, W. Chen, and G.A. Lesieutre, "Design and Performance of a High Force Piezoelectric Inchworm Actuator," Proceedings of SPIE 6<sup>th</sup> Annual International Symposium on Smart Structures and Materials, 1999.
61. Canfield, S., B. Peterson, M. Frecker, and G.H. Koopmann, "Design of Piezoelectric Inchworm Actuator and Compliant End-Effector for Minimally Invasive Surgery," Proceedings of SPIE 6<sup>th</sup> Annual International Symposium on Smart Structures and Materials, 1999.
62. Frank, J.E., G.H. Koopmann, W. Chen, and G.A. Lesieutre, "Design and Performance of a High-Force, High-Displacement Piezoelectric Wedgeworm Actuators," NATO Advanced Research Workshop, Predeal, Rumania, 1999.
63. Lesieutre, G.A. and G.H. Koopmann, "Roller Wedgeworm: A Piezoelectrically Driven Rotary Motor," 10<sup>th</sup> International Conference on Adaptive Structures and Technologies, Paris, France, October 1999.
64. Kim, J.S., S.J. Kim, H.G. Kim, D.C. Lee, and K. Uchino, "Piezoelectric and Dielectric Properties of  $\text{Fe}_2\text{O}_3$ -Doped  $0.57\text{Pb}(\text{Sc}_{1/2}\text{Nb}_{1/2})\text{O}_3\text{-}0.43\text{PbTiO}_3$  Ceramic Materials," Jpn. J. Appl. Phys. **38**(Part 1, No. 3A), 1433-1437 (1999).
65. Du, X.H., Q.M. Wang, U. Belegundu, and K. Uchino, "Piezoelectric Property Enhancement in Polycrystalline Lead Zirconate Titanate by Changing Cutting Angle," J. Ceram. Soc. Jpn. **107**(2), 190-191 (1999).
66. Du, X.H., Q.M. Wang, U. Belegundu, A. Bhalla, and K. Uchino, "Crystal Orientation Dependence of Piezoelectric Properties of Single Crystal Barium Titanate," Mater. Lett. **40**, 109-113 (1999).
67. Yao, K., W. Zhu, K. Uchino, Z. Zhang and L.C. Lim, "Design and Fabrication of a High Performance Multilayer Piezoelectric Actuator with Bending Deformation," **46**(4), 1020-1027 (1999).
68. Zhang, J., W.J. Hughes, P. Bouchilloux, R.J. Meyer, Jr., K. Uchino, and R.E. Newnham, "A Class V Flexensional Transducer: The Cymbal," Ultrasonics **37**, 387-393 (1999).
69. Uchino, K. and Y. Ito, "Trends in Electromechanical Transduction," (authored by I.J. Busch-Vishniac) Translation, Parity, **14**(6), p. 29 - 37 (1999).
70. Uchino, K., "Ultra-Small Ultrasonic Motors," Ultrasonic Techno. **11**(4), 72-76 (1999).
71. Poosanaas, P. and K. Uchino, "Photostrictive Effect in Lanthanum-Modified Lead Zirconate Titanate Ceramics near the Morphotropic Phase Boundary," J. Mater. Chem. and Phys. **61**, 36-41 (1999).
72. Zhang, J., W.J. Hughes, R.J. Meyer Jr., K. Uchino, and R.E. Newnham, "Cymbal Array: A Broad Band Sound Projector," Ultrasonics **37**, 523-529 (2000).

73. Belegundu, U., X.H. Du, L.E. Cross and K. Uchino, "In Situ Observation of Domains in  $0.9\text{Pb}(\text{Zn}_{1/3}\text{Nb}_{2/3})\text{O}_3$ - $0.1\text{PbTiO}_3$  Single Crystals," *Ferroelectrics* **221**, 67-71 (1999).
74. Uchino, K. and B. Koc, "Compact Piezoelectric Ultrasonic Motors," *Ferroelectrics* **230**, 73-86 (1999).
75. Kim, J.S., M.J. Park, and K. Uchino, "Composite Ultrasonic Motors Using a Piezoelectric Disk and an Elastic Body of "Windmill" Type," *Ferroelectrics* **232**, 185-190 (1999).
76. Abothu, I.R., Y. Ito, P. Poosanaas, S. Kalpat, S. Komarneni, and K. Uchino, "Sol-Gel Processing of Piezoelectric Thin Films," *Ferroelectrics* **232**, 191-195 (1999).
77. Liu, S.F., I.R. Abothu, S. Komarneni, P. Poosanaas, D.S. Paik, Y. Ito, and K. Uchino, "PLZT Ceramics Prepared from Conventional and Microwave Hydrothermal Powders," *Ferroelectrics* **231**, 179-185 (1999).
78. Yu, H. and C.A. Randall, "Dendritic Domain Structures in PZN-PT Crystals," *J. Appl. Phys.* **86**, 5733 (1999).
- 9.0. PAPERS SUBMITTED FOR PUBLICATIONS
1. Newnham, R.E., "Ceramics into the Next Millennium," *Materials World*, pp. 16-18 (Jan. 2000).
2. Villegas, M., A.C. Caballero, C. Moure, P. Duran, J.F. Fernandez, and R.E. Newnham, "Influence of Processing Method on Sintering and Electrical Properties of  $\text{Pb}(\text{Zn}_{1/3}\text{Nb}_{2/3})\text{O}_3$ -Based Ceramics," *J. Amer. Ceram. Soc.* **83**(1), 141-146 (2000).
3. Zhang, J., W. J. Hughes, R.J. Meyer, Jr., K. Uchino, and R.E. Newnham, "Cymbal Array: A Broad Band Sound Projector," *Ultrasonics* **37**(8), 523-529 (2000).
4. Witham, J.P., P. Ravindranathan, R.E. Newnham, and J.P. Dougherty, "Hydrothermal Preparation and Fabrication of Lead Zirconate-Titanate (PZT) Ceramics," re-submitted to *J. Amer. Ceram. Soc.* (1997)
5. Meyer, R.J., Jr., S. Alkoy, J. Cochran, and R.E. Newnham, "Development of Materials and Composites for  $> 25$  MHz Single Element Transducers," in *Proc. IEEE UFFC* (October 1999).
6. Meyer, R.J., Jr., S. Alkoy, J. Cochran, T. Ritter, and R.E. Newnham, "Pro-focused Very High Frequency Lead Titanate Single Element Transducers from Hollow Spheres," submitted to *IEEE Transactions* (December 1999).
7. Meyer, R.J., Jr. and R.E. Newnham, "Flextensional Transducers with Shape Memory Caps for Tunable Devices," submitted to *J. of Int. Systems & Structures* (January 2000).
8. Meyer, R.J., Jr., A. Dogan, C. Yoon, S. Pilgrim, and R.E. Newnham, "Displacement Amplification of Electroactive Materials Using the Cymbal Flextensional Transducer," submitted to *Sensors & Actuators* (February 2000).
9. Bharti, V., G. Shanthi, H. Xu, Q.M. Zhang, and K. Liang, "Evolution of Transitional Behavior and Structure of Electron Irradiated P(VDF-TrFE) Copolymer Films," *Mater. Lett.* (1999).
10. Zhang, Q.M., Z.Y. Cheng, and V. Bharti, "Relaxor Ferroelectric Behavior in High Energy Electron Irradiated P(VDF-TrFE) Copolymers," *Appl. Phys. A*, in print (2000).

11. Cheng, Z.Y., V. Bharti, T. Mai, T.B. Xu, Q.M. Zhang, K. Hamilton, T. Ramotowski, K.A. Wright, and R. Ting, "Effect of High Energy Electron Irradiation on the Electromechanical Properties of Poly(vinylidene fluoride-trifluoroethylene) 50/50 and 65/35 Copolymers," *IEEE Trans. UFFC* (2000).
12. Glazounov, A.E., S. Wang, Q.M. Zhang, and C. Kim, "Piezoelectric Stepper Motor with Direct Coupling Mechanism to Achieve High Efficiency and Precise Control of Motor. Submitted to *IEEE Trans. UFFC* (1999).
13. Xu, H., G. Shanthi, V. Bharti, Q.M. Zhang, and T. Ramatowski, "Structural, Conformational, and Polarization Changes of P(VDF-TrFE) Copolymer Induced by High Energy Electron Irradiation," submitted to *Macromolecules* (1999).
14. Bharti, V, Z.-Y. Cheng, T. Mai, Q.M. Zhang, T. Ramotowski, K.A. Wright," High Electromechanical Coupling Factor and Electrostrictive Strain over a Broad Frequency Range in Electrostrictive Poly(vinylidene fluoride-trifluoroethylene) Copolymer. submitted to *J. Appl. Phys.* (2000).
15. Xu, T.B., Z-Y. Cheng, Q.M. Zhang, R. Baughman, C. Cui, A. Zakhidov, and J. Su, "Fabrication and Characterization of 3-Dimensional Periodic Ferroelectric Polymer-Silica Opal Composites and Inverse Opal," submitted to *J. Appl. Phys.* (2000).
16. Bai, Y, Z.Y. Cheng, V. Bharti, H.S. Xu, and Q.M. Zhang, "High Dielectric Constant Ceramic Powder Polymer Composites," submitted to *Appl. Phys. Lett.* (2000).
17. Brungart, T.A., G.C. Lauchle, S. Deutsch, and E. Riggs, "Wall Pressure Fluctuations Induced by Non-Equilibrium Turbulent Boundary Layer Flow," submitted to *J. Sound and Vib.* (December 1998); being revised.
18. Brungart, T.A., G.C. Lauchle, S. Deutsch, and E. Riggs, "Effect of a Moving Wall on a Fully-Developed, Equilibrium Turbulent Boundary Layer," submitted to *Exp. Fluids* (May 1999); revisions in process.
19. Howe, M.S., G.C. Lauchle, and J. Wang, "Aerodynamic Lift and Drag Fluctuations of a Sphere," submitted to *J. Fluid Mechanics* (May 1999).
20. Capone, D.E. and G.C. Lauchle, "Modeling the Unsteady Lift and Drag on a Finite-Length Circular Cylinder in Cross-Flow," accepted for publication in *J. Fluids and Structures* (September 24, 1999).
21. Wang, J., G.C. Lauchle, and M.S. Howe, "Hydrodynamic Lift and Drag Fluctuations on a Sphere in Uniform Flow," in preparation for submittal to *J. Acoust. Soc. Am.*
22. Gavin, J.R. and G.C. Lauchle, "The Effects of Blade Sweep on Low Frequency Pump Noise," in preparation for *Proc. ASME Winter Annual Meeting* (2000).
23. Gavin, J.R. and G.C. Lauchle, "A Two-Point Anisotropic Turbulence Model for Predicting Low Frequency Pump Noise," in preparation for *ASME Winter Annual Meeting* (2000).
24. Brungart, T.A. and G.C. Lauchle, "Modifications of a Handheld Vacuum Cleaner for Noise Control," submitted to *Noise Control Eng. J* (February 2000).
25. Lauchle, G.C. and T.A. Brungart, "Handheld Vacuum Cleaner Noise Control," invited paper for InterNoise 2000 to be held in August 2000 in Nice, France.
26. Alberta, E.F., A.S. Bhalla, and M. Adachi, "Temperature Dependence of the Piezoelectric and Dielectric Coefficients of Niobium-doped  $\text{Pb}(\text{Sc}_{1/2}\text{Nb}_{1/2})_{0.575}\text{Ti}_{0.425}\text{O}_3$  Ceramics," accepted for publication in *Ferroelectrics*.
27. Alberta, E.F., R. Guo, and A.S. Bhalla, "Structure-Property Diagrams of Ferroic Solid Solutions. Part I: Perovskite Relaxor Ferroelectrics with Morphotropic Phase Boundaries," accepted for publication in *Ferroelectrics Review*.

28. Frank, J.E., G.H. Koopmann, W. Chen, and G.A. Lesieutre, "Design and Performance of a High Force Piezoelectric Inchworm Motor," *Journal of Intelligent Structures* (April 1999).
29. Poosanaas, P., K. Tonooka, I.R. Abothu, S. Komarneni, and K. Uchino, "Influence of Composition and Dopant on Photostriction in Lanthanum-Modified Lead Zirconate Titanate Ceramics," submitted to *J. Intelligent Mater. Systems and Structures* (1999). (First Author Supervised by Candidate).
30. Poosanaas, P., A. Dogan,, A.V. Prasadaraao, S. Komarneni, and K. Uchino, "Effect of Ceramic Processing Methods on Photostrictive Ceramics," submitted to *J. Advanced Performance Mater.* (1997).
31. Uchino, K. and S. Hirose, "Loss Mechanisms in Piezoelectrics," submitted to *IEEEUFFC Transactions* (1999). (Principal Author)
32. Belegundu, U., X.H. Du, and K. Uchino, "Switching Current Dependence on Crystal Orientation for Relaxor Based Ferroelectric Single Crystals," submitted to *Electroceramics* (1999).
33. Yao, K., K. Uchino, Y. Xu, S. Dong, and L.C. Lim, "Compact Piezoelectric Stacked Actuators for High Power Applications," submitted to *IEEE Trans. UFFC* (1999).
34. Chen, Y.H., D. Viehland, and K. Uchino, "Substituent Effects in 0.65Pb(Mg<sub>1/3</sub>Nb<sub>2/3</sub>)O<sub>3</sub>-0.35PbTiO<sub>3</sub> Piezoelectric Ceramics," submitted to *Jpn. J. Appl. Phys.* (2000).
35. Du, X.H., Q.M. Wang, and K. Uchino, "Accurate Determination of Complex Dielectric, Elastic, and Piezoelectric Coefficients of Piezoelectric Materials," submitted to *IEEE Trans. UFFC* (2000).
36. Zheng, J., Y.H. Cheng, and K. Uchino, "Pulse Drive Method for Determining High Electric-Field Electromechanical Coupling Parameters," submitted to *J. Electroceramics* (2000).
37. Kalpat, S., I.R. Abothu, A. Akiba, H. Goto, S. Trolier-McKinstry, and K. Uchino, "Dielectric and Piezoelectric Property Dependence on Highly Textured (100), (111) and Random Thin Films Grown by RF Sputtering," Symp. LL Proc., Mater. Res. Soc. Fall Mtg. '99, LL.1.3, Boston, Nov. 29-Dec.3 (1999).
38. Uchino, K., J. Zheng, Y.H. Chen, X. Du, and S. Hirose, "Loss Mechanisms in Piezoelectrics," Mater. Res. Soc. Fall Mtg. '99, LL.1.6, Boston (Nov. 29-Dec.3, 1999).
39. Belegundu, U., H. Aburatani, and K. Uchino, "Studies on Switching Current in Relaxor Based (1-x)PZN-xPT Single Crystals," Symp. LL Proc., Mater. Res. Soc. Fall Mtg. '99, LL.1.9, Boston (Nov. 29-Dec.3, 1999).
40. Bouchilloux, P., K. Craig, B. Koc and K. Uchino, "Design and Construction of a Rotary and a Linear Ultrasonic Motors with Free Stators," Symp. LL Proc., Mater. Res. Soc. Fall Mtg. '99, LL.2.10, Boston (Nov. 29-Dec.3, 1999).
41. Koc, B., Y. Gao, and K. Uchino, "Disk Type Piezoelectric Transformer Design Employing High Power Piezoelectric Ceramic Material," Mater. Res. Soc. Fall Mtg. '99, LL.5.8, Boston (Nov. 29-Dec.3, 1999).
42. Koc, B., S. Alkoy, and K. Uchino, "A Circular Piezoelectric Transformer with Crescent Shape Input Electrodes," Proc. IEEE Ultrasonic Symp., Lake Tahoe, Nevada (Oct. 17-21, 1999).
43. Poosanaas, P., K. Tonooka and K. Uchino, "Photostrictive Actuators," *J. Mechatronics* (1999) [in press].

44. Koc, B., P. Bouchilloux, and K. Uchino, "Piezoelectric Micromotor Using A Metal-Ceramic Composite Structure," IEEE Trans. Ultrasonic, Ferroelectrics, and Frequency Control (1999). [in press].
45. Chen, Y. H., S. Hirose, D. Viehland, S. Takahashi, and K. Uchino, "Mn-Modified  $\text{Pb}(\text{Mg}_{1/3}\text{Nb}_{2/3})\text{O}_3\text{-PbTiO}_3$  Ceramics: Improved Mechanical Quality Factors for High Power Transduction Applications," *Jpn. J. Appl. Phys.* (1999). [accepted].
46. Uchino, K., and J. Zheng, Y.H. Chen, X. Du and S. Hirose, "Loss Mechanisms in Piezoelectrics and Resonance/ Antiresonance," Proc. 101st Annual Mtg. of Amer. Ceram. Soc., Symp. Dielectric Materials and Devices, SE-27, Indianapolis (April 25 - 28, 1999). [accepted]
47. Uchino, K., and H. Aburatani, "Field Induced Acoustic Emission in Ferroelectric Ceramics," Proc. 101st Annual Mtg. of Amer. Ceram. Soc., Symp. Dielectric Materials and Devices, SE-56, Indianapolis, April 25 - 28 (1999). [accepted]
48. Uchino, K., "Smart Composite Materials," Chap.5.19, Comprehensive Composite Materials, Elsevier Science, Oxford, UK (2000). [in press]
49. Kelly, A., R. Davidson, and K. Uchino "Smart Composite Materials Systems," Chap.5.20, Comprehensive Composite Materials, Elsevier Science, Oxford, UK (2000). [in press]
50. Tressler, J. and K. Uchino, "Piezoelectric Composite Sensors," Chap.5.25, Comprehensive Composite Materials, Elsevier Science, Oxford, UK (2000). [in press]
51. Uchino, K., "Piezoelectric Actuators," Chap.6.1, Comprehensive Composite Materials, Elsevier Science, Oxford, UK (2000). [in press]
52. Koc, B. and K. Uchino, "Ultrasonic Motors," Chap.6.2, Comprehensive Composite Materials, Elsevier Science, Oxford, UK (2000). [in press]
53. Yu, H., V. Goplan, J. Sindel, and C.A. Randall, "Domain Switching and Electromechanical Properties of Pulse Poled PZN-PT Crystals," accepted *J. Appl. Physics.* (1999).

#### 10.0 PAPERS APPEARING IN NON REFEREED PUBLICATIONS

1. Yimnirun, R., S. Eury, V. Sundar, P.J. Moses and R.E. Newnham, "Compressometer Based Method for Measuring Converse Electrostriction in Polymers," 1999 *Annual Report Conference on Electrical Insulation and Dielectric Phenomena (IEEE-CEIDP 99)*, pp. 338-341 (1999).
2. Zhang, Q.M., V. Bharti, Z.Y. Cheng, X.Z. Zhao, F. Tito, T. Ramotowski, and R. Ting, "Electromechanical Behavior of Electrostrictive P(VDF-TrFE) Copolymers," *Proc.1999 SPIE Conf. Smart Structures and Materials*, Vol. 3669, 134-144 (Newport Beach, CA, 1999).
3. Cheng, Z.Y., J. Su, Q.M. Zhang, P.C. Wang, and A. MacDiarmid, "High Performance All Polymer Electrostrictive Systems," *Proc.1999 SPIE Conf. Smart Structures and Materials*, Vol. 3669, 140-147 (Newport Beach, CA, 1999).
4. Kim, C., A. Glazounov, L. Flippen, A. Pattnaik, and Q.M. Zhang, "Piezoelectric Ceramic Assembly Tubes for Torsional Actuators," *Proc.1999 SPIE Conf. Smart Structures and Materials*, Vol. 3675, 53-60 (Newport Beach, CA, 1999).

5. Kim, C., A. Glazounov, and Q.M. Zhang, "Development of Piezoelectric Ceramic Torsional Actuators Based on Shear Piezoelectric Response and Their Potential Applications," *Proc. 9<sup>th</sup> US-Japan Meeting on Dielectric and Piezoelectric Ceramics*, (Okinawa, Japan 1999).
6. Zhang, Q.M. and A. Glazounov, "Torsional Inchworm Ultrasonic Piezomotor Compining Continuous Rotation with Precise Control Over Angular Positions and High Torque Output," *Proc. 1999 IEEE Inter. Symp. Ultrasonics* (Lake Tahoe, NE, 1999).
7. Gross, S.J., V. Bharti, Z-Y. Cheng, and Q.M. Zhang, "Mechanical Load Effects on the Electrostrictive Strain of P(VDF-TrFE) Copolymer," *Proc. 1999 IEEE Inter. Symp. Ultrasonics*, (Lake Tahoe, NE, 1999).
8. Bai, Y., V. Bharti, Z.Y. Cheng, H. Xu, Q.M. Zhang, "High Dielectric Constant Polymer Ceramic Composites," *Proc. MRS Boston Meeting*, Vol. 600 (1999).
9. Bharti, V., Z.Y. Cheng, H. Xu, G. Shanthi, T.B. Xu, and Q.M. Zhang, "Effect of Processing and High Energy Irradiation Conditions on the Electro-Mechanical and Structural Properties of P(VDF-TrFE) Copolymers," *Proc. MRS Boston Meeting*, Vol. 600 (1999).
10. Cheng, Z.Y., S. Gross, V. Bharti, T.B. Xu, and Q.M. Zhang, "Electromechanical Properties of Electron Irradiated P(VDF-TrFE) Copolymers," *Proc. MRS Boston Meeting*, Vol. 600 (1999).
11. Xu, H., Z.Y. Cheng, Q.M. Zhang, P. Wang, and A. MacDiarmid, "Conduction Behavior of Doped Polyaniline under High Current Density and the Performance of an All Polymer Electromechanical System," *Proc. MRS Boston Meeting*, Vol. 600 (1999).
12. Zhang, Q.M., Z.Y. Cheng, V. Bharti, T.B. Xu, H.S. Xu, T. Mia, and S. Gross, "Piezoelectric and Electrostrictive Polymer Based Actuator Materials," *Proc. of SPIE's 7<sup>th</sup> Ann. International Symp. on Smart Struct. and Mater.*, Vol. 3987 (Newport Beach, CA 2000)
13. Cheng, Z.Y., T.B. Xu, V. Bharti, and Q.M. Zhang, "Characterization of Electrostrictive P(VDF-TrFE) Copolymer Films for High-frequency and High-load Applications," *Proc. of SPIE's 7<sup>th</sup> Ann. International Symp. on Smart Struct. and Mater.*, Vol. 3987 (Newport Beach, CA 2000)
14. Cao, W. and J. Erhart, "Effective Material Properties of Multi-domain Ferroelectric Crystals," *Proceedings of the 9<sup>th</sup> US-Japan Seminar on Dielectric and Piezoelectric Ceramics*, pp. 95-98 (1999).
15. Cao, W., "Characterization of Elastic, Dielectric and Piezoelectric Properties of Piezoelectric Materials," *Proceedings of the 1999 Fall Conference of the Korean Institute of Electrical and Electronic Material Engineering*, pp. 13-22 (1999).
16. Lesieutre, G.A. and G.H. Koopmann, "High Force Piezoelectric Motors," *UEF Conference on Adaptive Structures II*, Barga, Italy, May 1999
17. Uchino, K. and S. Takahashi, "New Trend in Multilayer Ceramic Actuators," *Proc. Int'l Symp. Multilayer Electronic Ceramic Devices*, Amer. Ceram. Soc. '98; *Ceramic Trans.* Vol. 97, Multilayer Electronic Ceramic Devices, p.305 - 318 (1999).
18. Uchino, K. and S. Takahashi, "New Trend in Multilayer Ceramic Actuators," *Proc. Int'l Symp. Dielectric Ceramics*, Amer. Ceram. Soc. '98; *Ceramic Trans.* Vol. 100, Dielectric Ceramic materials, p.455 - 468 (1999).
19. Koc, B. and K. Uchino, "Disk Type Piezoelectric Transformer with Crescent Shape Input Electrodes," *Proc. NATO- Advanced Research Workshop: Piezoelectric Materials, Advance in Science, Technology and Applications*, Predeal, Romania (May 24-27, 1999).

20. Uchino, K. and B. Koc, "Compact Piezoelectric Ultrasonic Motors," *Proc. NATO-Advanced Research Workshop: Piezoelectric Materials, Advance in Science, Technology and Applications*, Predeal, Romania (May 24-27, 1999).
21. Uchino, K., "Recent Trend of Piezoelectric Actuator Developments," *Proc. Int'l Symp. Micromechatronics and Human Science '99*, p.3-9, Nagoya, Japan (Nov. 23-26, 1999).

#### 11.0 INVITED PAPERS PRESENTATIONS AT NATIONAL AND INTERNATIONAL MEETINGS

1. Cross, L.E., S. Park, and S. Liu, "Simple Phenomenological Analysis of the Strain Behavior in Relaxor Ferroelectric Lead Zinc Niobate:Lead Titanate Single Crystals," *SPIE 6<sup>th</sup> Annual International Symposium on Smart Structures and Materials*, Newport Beach, California (3-5 March 1999).
2. Xu, B., Yaohong Ye, and L.E. Cross, "Dielectric Hysteresis Under Transverse Electric Fields in Sol-Gel Lead Zirconate Titanate Films Deposited on ZrO<sub>2</sub> Passivated Silicon," *ISIF 99*, Colorado Springs, Colorado (7-10 March 1999).
3. Cross, L.E., "High Strain Actuator Materials Current Status and Future Prospects," *U.S. Navy Workshop on Acoustic Transduction Materials and Devices*, State College, Pennsylvania (13-15 April 1999).
4. Cross, L.E., "Phenomenology of the Elasto-Dielectric Response in the Field Forced Ferroelectric Phases of Lead Zinc Niobate : Lead Titanate (PZN:PT) Relaxor Ferroelectric Single Crystals," *Ferroelectric Workshop in Puerto Rico*, Guanica, Puerto Rico (12-14 May 1999).
5. Cross, L.E., "Electronic Ceramics: Current Progress and Prospects for the 21<sup>st</sup> Century," *IUMRS-ICAM 99*, Beijing China (13-19 June 1999).
6. Cross, L.E., "Piezoelectricity in Single Crystal Relaxor Ferroelectrics with Morphotropic Phase Boundaries Properties: Processing and Future Prospects," *1999 Annual Conference of British Association for Crystal Growth*, Cambridge, England (16-17 September 1999).
7. Cross, L.E., "New Materials for Smart Applications Progress in the USA," *US:Japan 2<sup>nd</sup> Collaboration Meeting*, Penn State, University Park, Pennsylvania (23 September 1999).
8. Cross, L.E., "New Relaxor Ferroelectric Piezoelectric and Electrostrictive Actuators and Sensors for Smart Materials," *Euromat 99*, Munich, Germany (27-30 September 1999).
9. Cross, L.E., "Current and Potential Future Developments in Electrostrictive Actuator Materials," *ICAST 99*, Paris, France (11-13 October 1999).
10. Newnham, R.E., "Biomimetic Sensors and Actuators," *ASME Adaptive Structures and Materials Systems Prize Lecture*, American Institute of Aeronautics and Astronautics Conference, St. Louis (April 13, 1999).
11. Newnham, R.E., "Domains in Smart Materials," plenary lecture at *the Workshop on Dynamics of Interfaces*, held at Los Alamos National Laboratory (April 23, 1999).
12. Newnham, R.E., "Biomimetic Ceramic Sensors," invited lecture at *the 101<sup>st</sup> Annual Meeting of the American Ceramic Society*, April, Indianapolis, IN (April 26, 1999).
13. Newnham, R.E., "Future of Ceramics," invited lecture at student forum, *American Ceramic Society Meeting*, Indianapolis, IN (April 27, 1999).

14. Newnham, R.E., "Ceramics into the Next Millennium," plenary lecture at the *European Ceramic Society*, Brighton, England (June 22, 1999).
15. Newnham, R.E., "Ceramic Engineering in the 21<sup>st</sup> Century: Scaling Up and Scaling Down," *International Symposium on Current Global Status of Ceramics*, Tokyo, Japan (July 22, 1999).
16. Newnham, R.E., "Ferroic Engineering in Ferroic Valley," invited lecture at *Fourth ARO Smart Structures Workshop*, Penn State (August 17, 1999).
17. Newnham, R.E., "Functional Composites for Sensors, Actuators, and Transducers," Plenary lecture at *Second International Meeting on Composites*, Lake Louise, Alberta, Canada (November 3, 1999).
18. Newnham, R.E., "Materials Science and Engineering in the 21<sup>st</sup> Century: Scaling Up and Scaling Down," Plenary lecture at *Swiss Materials Science Meeting*, Interlaken (November 12, 1999).
19. Cross, L.E., "High Strain High Coupling Piezoelectric Ferroelectric Single Crystals: Current Status and Future Prospects," *IEEE International Ultrasonics Meeting*, Lake Tahoe, Nevada (October 1999).
20. Cross, L.E. and P. Hana, "Phenomenology of the Elasto-Dielectric Response in the Field-Forced Ferroelectric Phases of Lead Zinc Niobate: Lead Titanate (PZN:PT) Relaxor Ferroelectric," *9<sup>th</sup> US:Japan Meeting on Dielectric and Piezoelectric Ceramics*, Okinawa, Japan (2-5 November 1999).
21. Cross, L.E., "Materials Issues in Electric Field Tunable RF and Microwave Dielectrics," *MRS Fall Meeting*, Boston, Massachusetts (29 November-3 December 1999).
22. Zhang, Q.M., "Novel Electrostrictive P(VDF-TrFE) Copolymer Actuators," *137<sup>th</sup> Meeting of the Acoustic Society of America*, Berlin, Germany (March 1999).
23. Zhang, Q.M. and V. Bharti, "Ferroelectric Relaxor P(VDF-TrFE) for Electromechanical and Dielectric Applications," *Symposium of Utilization of Electroactive Polymers*, Coronado, CA (October 1999).
24. Zhang, Q.M., "Electrostrictive P(VDF-TrFE) Copolymer," *MRS 1999 Fall Meeting*, Boston (November 30, 1999).
25. Zhang, Q.M., "Electroactive P(VDF-TrFE) Copolymer Based High Strain Actuators," *SPIE's 7<sup>th</sup> International Meeting on Smart Structures and Materials*, California (March 6, 2000).
26. Zhang, Q.M., "Electrostrictive Polymers," *Materials Congress 2000*, UK (April 12, 1999).
27. Cao, W., "Review on Finite Element Design Modeling of Medical Ultrasonic Transducers," *Medical Imaging 1999*, San Diego, CA (Feb. 20-26, 1999).
28. Cao, W., "Effective Properties of a Multi-Domain Ferroelectric Material," *9<sup>th</sup> US-Japan Seminar on Dielectric and Piezoelectric Ceramics* (Nov. 3-5, 1999).
29. Cao, W., "Characterization of Elastic, Dielectric and Piezoelectric Properties of Piezoelectric Single Crystals and Ceramics," *1999 Fall Conference of the Korean Institute of Electrical and Electronic Material Engineers* (Nov. 12, 1999).
30. Trolier-McKinstry, S., J-P. Maria, V. Bornand, and J.H. Park, "Epitaxial and Oriented Relaxor Ferroelectric-PbTiO<sub>3</sub> Films," Invited Presentation at *American Conference on Crystal Growth-II*, Tempe Arizona (August 1-4, 1999).

31. Frank, J.E. and G.H. Koopmann, "Design and Performance of a High-Force High-Displacement Piezoelectric Wedgeworm Actuators," *1999 U.S. Navy Workshop on Acoustic Transduction Materials and Devices*, University Park, Pennsylvania (April 1999).
32. Frank, J.E. and G.H. Koopmann, "Design and Performance of a High-Force High-Displacement Piezoelectric Wedgeworm Actuators," *1999 NATO Advanced Research Workshop*, Predeal, Romania (May 1999).
33. Lesieutre, G.A. and G.H. Koopmann, "High Force Piezoelectric Motors," *UEF Conference on Adaptive Structures II*, Barga, Italy (May 1999).
34. Lesieutre, G.A. and G.H. Koopmann, "Roller Wedgeworm: A Piezoelectrically Driven Rotary Motor," *10<sup>th</sup> International Conference on Adaptive Structures and Technologies*, Paris, France (October 1999).
35. Uchino, K. and J. H. Zheng, "Loss Mechanisms in Piezoelectrics and Resonance/Antiresonance," *101st Annual Mtg. of Amer. Ceram. Soc., Symp. Dielectric Materials and Devices*, SE-27, Indianapolis (April 25 - 28, 1999).
36. Uchino, K. and H. Aburatani, "Field Induced Acoustic Emission in Ferroelectric Ceramics," *101<sup>st</sup> Annual Mtg. of Amer. Ceram. Soc., Symp. Dielectric Materials and Devices*, SE-56, Indianapolis (April 25 - 28, 1999).
37. Uchino, K., "High Electromechanical Coupling in  $\text{Pb}(\text{Zn}_{1/3}\text{Nb}_{2/3})\text{O}_3\text{-PbTiO}_3$  Single Crystals - How High Energy Conversion Rate is Possible?," *NATO- Advanced Research Workshop: Piezoelectric Materials, Advance in Science, Technology and Applications*, Predeal, Romania (May 24-27, 1999).
38. Uchino, K. and B. Koc, "Compact Piezoelectric Ultrasonic Motors," *NATO- Advanced Research Workshop: Piezoelectric Materials, Advance in Science, Technology and Applications*, Predeal, Romania (May 24-27, 1999).
39. Uchino, K. and B. Koc, "Compact Piezoelectric Ultrasonic Motors," *Unite Engineering Foundation Conference on Engineered Adaptive Structures for Noise and Vibration Control II*, Barga, Italy (May 16-21, 1999).
40. Uchino, K., "Recent Trend of Piezoelectric Actuator Developments," *Int'l Symp. Micro-Mechatronics and Human Science '99*, Nagoya, Japan (Nov. 23-26, 1999).
41. Uchino, K., "Loss Mechanisms in Piezoelectrics and Heat Generation," *Fundamental Physics Workshop on Ferroelectrics*, Aspen, CO (Feb. 13-19, 2000).
42. Uchino, K., "Crystal Orientation Dependence of Piezoelectricity in Perovskites and Related Materials," *Fundamental Physics Workshop on Ferroelectrics*, Aspen, CO (Feb. 13-19, 2000).

#### 12.0 INVITED PAPERS PRESENTED AT UNIVERSITY, INDUSTRY, AND GOVERNMENT LABORATORIES

1. Newnham, R.E., "Smart Materials and Smart Structures," *Second Reunion de Invierno Symposium on New Horizons in Materials Science*, Queretaro, Mexico (January 19, 1999).
2. Newnham, R.E., "Structure Property Relations in Smart Materials," *Materials Science Department, University of Michigan*, Ann Arbor, MI (March 19, 1999).
3. Newnham, R.E., "Smart Materials and Smart Systems," *Materials Dept. Seminar*, Oak Ridge National Laboratory, TN (March 23, 1999).
4. Newnham, R.E., "Electrostriction," *Materials Science Seminar*, Los Alamos National Laboratory, NM (April 20, 1999).

5. Newnham, R.E., "Electrostriction," Applied Physics Dept., Hong Kong Polytechnic Univ., China (July 16, 1999).
6. Newnham, R.E., "Future of Ceramic Engineering," Applied Physics Dept., Hong Kong Polytechnic Univ., China (July 19, 1999).
7. Newnham, R.E., "Smart Materials," Applied Physics Dept., Hong Kong Polytechnic Univ., China (July 20, 1999).
8. Newnham, R.E., "Predicting Electrostriction Coefficients," Seminar at Murata Manufacturing Co., Kyoto, Japan (July 24, 1999).
9. Newnham, R.E., J. Zhang and W.J. Hughes, "Cymbal Transducers," MURI Review Meeting, Penn State (November 18, 1999).
10. Zhang, Q.M., "Relaxor ferroelectric polymers-high energy electron irradiated P(VDF-TrFE) copolymers," Raychem, CA (April 23, 1999).
11. Zhang, Q.M., "Novel electrostrictive P(VDF-TrFE) Actuators," Center for Acoustic and Vibration, Penn State (April 2, 1999).
12. Zhang, Q.M., "Electromechanical properties of electron irradiated P(VDF-TrFE) copolymer," NIH National Resource for Medical Transducer Technology, Penn State (April 6, 1999).
13. Zhang, Q.M., "High Dielectric Constant Polymers," Center for Dielectric Study Spring Meeting, Penn State University (March 1999).
14. Zhang, Q.M., "Relaxor ferroelectric polymers – opportunities and challenges," University of Nebraska at Lincoln (March 9, 1999).
15. Trolrier-McKinstry, S., "Piezoelectric Thin Films for Microelectromechanical Systems," seminar at Cornell University (Fall 1999).
16. Trolrier-McKinstry, S., "Piezoelectric Thin Films for Microelectromechanical Systems," seminar at Harvard University (Spring 2000).
17. Cao, W., "Review on Finite Element Design Modeling of Medical Ultrasonic Transducers," Medical Imaging 1999, San Diego, CA. (Feb. 20-26, 1999).
18. Cao, W., "Effective Properties of a Multi-Domain Ferroelectric Material," 9<sup>th</sup> US-Japan Seminar on Dielectric and Piezoelectric Ceramics (Nov. 3-5, 1999).
19. Cao, W., "Characterization of Elastic, Dielectric and Piezoelectric Properties of Piezoelectric Single Crystals and Ceramics," 1999 Fall Conference of the Korean Institute of Electrical and Electronic Material Engineers (Nov. 12, 1999).
20. Frank, J.E. and G.H. Koopmann, "Design and Performance of a High-Force High-Displacement Piezoelectric Wedgeworm Actuators," 1999 U.S. Navy Workshop on Acoustic Transduction Materials and Devices, University Park, Pennsylvania (April 1999).
21. Frank, J.E. and G.H. Koopmann, "Design and Performance of a High-Force High-Displacement Piezoelectric Wedgeworm Actuators," 1999 NATO Advanced Research Workshop, Predeal, Romania (May 1999).
22. Lauchle, G.C., "TBL Noise Modeling, invited speaker at 1999 ONR Stealth Technology for Torpedoes Workshop (March 29-30, 1999).
23. Lauchle, G.C., K.J. Bastyr, and J.A. McConnell, "A Velocity Gradient Underwater Acoustic Intensity Sensor," 1999 U.S. Navy Workshop on Acoustic Transduction Materials and Devices, The Penn State Conference Center (April 13-15, 1999).

24. Lauchle, G.C., "Acoustics of Ventilated Gas Cavities Underwater," 1999 ONR Workshop on Supercavitating High Speed Bodies (September 16-17, 1999).
25. Lauchle, G.C., "Modeling of Sensor Flow-Induced Noise," invited speaker at the 1999 ONR Workshop on Stealth Torpedoes (September 28, 1999).
26. Uchino, K., "New Trends in Ceramic Actuators," Denso Corp., Nagoya, Japan (March 2, 1999).
27. Uchino, K., "Single Crystal Piezoelectric Transducers," Hitachi Medical, Japan (March 3, 1999).
28. Uchino, K., "New Trends in Ceramic Actuators," Toshiba, Kawasaki, Japan (March 4, 1999).
29. Uchino, K., "Introduction to Actuators," Chongwon Univ., Chongwon, Korea (March 8, 1999).
30. Uchino, K., "Reliability of Piezoelectric Actuators," Siemens, Munich, Germany (May 21, 1999).
31. Uchino, K., "Introduction to Piezoelectric Actuators," Honda Electronics, Nagoya, Japan (July 13, 1999).
32. Uchino, K., "Composite Piezoelectric Transducers," Aloka, Tokyo, Japan (July 15, 1999).
33. Uchino, K., "High Power Piezoelectrics," Taiheiyo Cement, Tokyo, Japan (Sept. 6, 1999).
34. Uchino, K., "Flexensional Piezoelectric Actuators," Honda Electronics, Nagoya, Japan (Sept. 7-8, 1999).
35. Uchino, K., "Loss in Piezoelectrics," Mitsubishi Materials, Saitama, Japan (Oct. 4, 1999).
36. Uchino, K., "Polymer Piezoelectrics," Mitsui Chemical, Chiba, Japan (Oct. 5, 1999).
37. Uchino, K., "Loss Mechanisms in Piezoelectrics," Murata Manufacturing, Kyoto, Japan (Oct. 6, 1999).
38. Uchino, K., "Flexensional Piezoelectric Actuators," Time Engineering, Nagoya, Japan (Nov. 25, 1999).
39. Uchino, K., "Recent Development of Piezoelectric Actuators," Massachusetts Institute of Technology, Boston (Dec. 3, 1999).
40. Uchino, K., "Micromechatronics," Tohoku University, Sendai, Japan (March 6, 2000).
41. Uchino, K., "Micromechatronics," University of Tokyo, Tokyo, Japan (March 8, 2000).
42. Uchino, K., "Introduction to Micromechatronics," NAIR, Tsukuba, Japan (March 10, 2000).
43. Uchino, K., "Micromechatronics," Rutgers Univ., Piscataway, NJ (April 5, 2000).
44. Uchino, K., "Introduction to Micromechatronics," ETH, Zurich (May 8, 2000).

#### 13.0 CONTRIBUTED PAPERS AT NATIONAL AND INTERNATIONAL MEETINGS

1. R. Yimnirun, S. Eury, V. Sundar, P.J. Moses, and R.E. Newnham, "Measurements of Electrostrictive Effects in Low Permittivity Dielectrics," The 1999 Centennial American Physical Society Meeting, Atlanta, GA (March 19-25, 1999).
2. Eury, S., R. Yimnirun, V. Sundar, P.J. Moses, and R.E. Newnham, "Converse Electrostriction in Polymers and Composites," The 1999 Centennial American Physical Society Meeting, Atlanta, GA (March 19-25, 1999).

3. Yimnirun, R., S. Eury, V. Sundar, P.J. Moses, and R.E. Newnham, "Measurements of Electrostrictive Effects in Low Dielectric Constant Materials," The 1999 Materials Research Society Spring Meeting, San Francisco, CA (April 4-8, 1999).
4. Alkoy, S., R. Meyer, R.E. Newnham; A.C. Hladky-Hennion, and J.K. Cochran "Omni-directional Miniature Transducers and Directional Arrays from Piezoelectric Hollow Spheres," 101<sup>st</sup> Annual Meeting of the American Ceramic Society, Indianapolis, IN (April 25-28, 1999).
5. J. Zhang, R. E. Newnham, A. C. Hladky-Hennion, W. J. Hughes, "A Class V Flextensional Underwater Transducer: The Cymbal," 101<sup>st</sup> Annual Meeting of the American Ceramic Society, Indianapolis, IN (April 25-28, 1999).
6. R. Yimnirun, R. J. Meyer, R. E. Newnham, V. Sundar, "Anisotropy in Electrostriction and Elasticity of Low Permittivity Dielectrics," 101<sup>st</sup> Annual Meeting of the American Ceramic Society, Indianapolis, IN (April 25-28, 1999).
7. Yimnirun, R., S. Eury, V. Sundar, P.J. Moses, and R.E. Newnham, "Compressometer Based Method for Measuring Converse Electrostriction in Polymers," IEEE Conference on Electrical Insulation and Dielectric Phenomena (CEIDP) Annual Meeting, Austin, TX (October 17-21, 1999).
8. Alkoy, S., R.J. Meyer, A.C. Hladky-Hennion, W.J. Hughes, J.K. Cochran and R.E. Newnham, "Hydrophone Arrays and 1-3 Composites from Hollow Piezoelectric Spheres", IEEE International Ultrasonic Symposium, Lake Tahoe, NV (October 20, 1999).
9. Meyer, R.J., S. Alkoy, R.E. Newnham, J. Cannata, T. Ritter, J. Cochran, "Development of Materials and Composites for 30-100 MHz Single Element Transducer," IEEE International Ultrasonic Symposium, Lake Tahoe, NV (October 20, 1999).
10. Zhang, Q.M., V. Bharti, Z.-Y. Cheng, X.Z. Zhao, F. Tito, T. Ramotowski, and R. Ting, "Electromechanical Behavior of Electrostrictive P(VDF-TrFE) Copolymers," 1999 SPIE Conf. Smart Structures and Materials, Newport Beach, CA (March 1999).
11. Cheng, Z.-Y., J. Su, Q.M. Zhang, P.C. Wang, and A. MacDiarmid, "High Performance all Polymer Electrostrictive Systems," 1999 SPIE Conf. Smart Structures and Materials, Newport Beach, CA (March 1999).
12. Kim, C., A. Glazounov, L. Flippen, A. Pattnaik, and Q.M. Zhang, "Piezoelectric Ceramic Assembly Tubes for Torsional Actuators," 1999 SPIE Conf. Smart Structures and Materials, Newport Beach, CA, (March 1999).
13. Bharti, V., Z.-Y. Cheng, and Q.M. Zhang, "Electrstrictive P(VDF-TrFE) Copolymers," APS March Annual Meeting, Atlanta, GA (March 1999).
14. Glazounov, A.E., and Q.M. Zhang, "Changes in Electromechanical Properties of 0.9PMN-0.1 PT Induced by Uniaxial Stress," APS March Annual Meeting, Atlanta, GA (March 1999).
15. Bharti, V., Z.-Y. Cheng, H.S. Xu, T.B. Xu, S. Wang, G. Shanthi, and Q.M. Zhang, "Structural and Transitional Analysis of Relaxor Ferroelectric P(VDF-TrFE) Copolymer Films," ONR Workshop on Transducers and transducer Materials (April 1999).

16. Hamilton, K., T. Ramotowski, G. Kavarnos, Q.M. Zhang, V. Bharti, "Electron Irradiated P(VDF-TrFE) Copolymers for use in Naval Transducer Applications," ONR Workshop on Transducers and Transducer Materials (April 1999).
17. Cheng, Z.-Y., V. Bharti, T.B. Xu, S. Wang, Q.M. Zhang, and R. Ting, "Development of a Dilatometer for Measuring Transverse Strain Response and the Results in Electrostrictive P(VDF-TrFE) Films," ONR Workshop on Transducers and Transducer Materials (April 1999).
18. Liu, R. B., T. Karaki, S. Wang, Q.M. Zhang, and L.E. Cross, "Electrical and Electrostrictive Properties of Various Soft and Hard Polymers," ONR Workshop on Transducers and Transducer Materials (April 1999).
19. Xu, H.S., Z.-Y. Cheng, V. Bharti, S. Wang, and Q.M. Zhang, "All-Polymer Electromechanical Systems," ONR Workshop on Transducers and Transducer Materials (April 1999).
20. Zhang, Q.M., V. Bharti, Z.-Y. Cheng, H. Xu, T. Ramotowski, F. Tito, R. Ting, and K. Liang, "Electrostrictive P(VDF-TrFE) Copolymers," ONR Workshop on Transducers and Transducer Materials (April 1999).
21. Kim, C., A. Glazounov, and Q.M. Zhang, "Torsional Actuator and Torsional Inch-Worm Motor Based on Amplified Shear Piezoelectric Strain," DARPA Actuator Program Meeting, NASA -Langley, VA (June 1999).
22. Zhang, Q.M., A. Glazounov, and C. Kim, "Torsional Actuator and Motor Based on Mechanically Amplified Shear Piezoelectric Response," Fourth ARO Workshop on Smart Structures, University Park, PA (August 16, 1999).
23. Bai, Y., V. Bharti, Z.Y. Cheng, H. Xu, and Q.M. Zhang, "High Dielectric Constant Polymer Ceramic Composites," MRS 1999 Fall Meeting, Boston (November 29, 1999).
24. Bharti, V., Z.Y. Cheng, H. Xu, G. Shanthi, T.B. Xu, and Q. M. Zhang, "Effect of Processing and High Energy Electron Irradiation Conditions on the Electromechanical Properties of P(VDF-TrFE) Copolymer Films," MRS 1999 Fall Meeting, Boston (November 29, 1999).
25. Cheng, Z.Y., S. Gross, V. Bharti, T.B. Xu, and Q.M. Zhang, "Electromechanical Properties of Relaxor P(VDF-TrFE) Copolymers," MRS 1999 Fall Meeting, Boston (November 29, 1999).
26. Hamilton, K., T. Ramotowski, G. Kavarnos, Q.M. Zhang, and V. Bharti, "Electron Irradiated P(VDF-TrFE) Copolymers for Use in Naval Transducer Applications," MRS 1999 Fall Meeting, Boston (November 29, 1999).
27. Xu, H., Z.Y. Cheng, Q.M. Zhang, P.C. Wang, and A. MacDiarmid, "Conduction Behavior of Doped Polyaniline Under High Current Density and the Properties of an All Polymer Electromechanical System," MRS 1999 Fall Meeting, Boston (December 1, 1999).
28. Cheng, Z.-Y., T.B. Xu, V. Bharti, Q.M. Zhang, T. Ramotowski, and R. Ting, "Characterization of Electrostrictive P(VDF-TrFE) Copolymers for High Frequency and High-load Applications," SPIE's 7<sup>th</sup> International Meeting on Smart Structures and Materials, CA (March 6, 2000).
29. Bharti, V., Z-Y. Cheng, G. Shanthi, and Q.M. Zhang, "Dielectric Response of Relaxor Ferroelectric P(VDF-TrFE) Copolymers," America Phys. Society March Meeting, Minnesota (March 2000).

30. Xu, T.B., Z.Y. Cheng, Q.M. Zhang, and R. Baughman, "Fabrication and Characterization of 3-D Periodic Ferroelectric Polymer-Silica Opal Composites and Inverse Opal for Photonic Crystals," America Phys. Society March Meeting, Minnesota (March 2000).
31. Xu, F., W. Ren, and S. Trolier-McKinstry, "Domain Wall Contributions to the Dielectric and Piezoelectric Properties of PZT Thin Films," poster presentation at the Fall 1999 MRS Meeting, Boston, MA (Nov. 29- Dec. 2, 1999).
32. Wang, H., T. A. Ritter, W. Cao, and K. Shung, "Passive Materials for High-Frequency Ultrasonic Transducers," Medical Imaging 1999, San Diego, CA (Feb. 20-26, 1999).
33. Yin, J. H., B. Jiang, and W. Cao, "Elastic, Piezoelectric and Dielectric Properties of PZN-PT Single Crystals," Medical Imaging 1999, San Diego, CA. (Feb. 20-26, 1999).
34. Cao, W., A. Saxena, D. Hatch, and G. Barsch, "Theory of Domain Walls in Improper Ferroelastic Phase Transition Driven by Zone Boundary Phonon," APS March Meeting, Atlanta, GA (March 1999).
35. Alberta, E.F., K. Williams, and A.S. Bhalla, "Hydrostatic Piezoelectric Properties of Various MPB Systems," presented at the 1999 U.S. Navy Workshop on Acoustic Transduction Materials and Devices, University Park, PA (April 13-15, 1999).
36. Alberta, E.F. and A.S. Bhalla, "Dielectric and Piezoelectric Properties of  $(1-x)\text{Pb}(\text{In}_{1/2}\text{Ta}_{1/2})\text{O}_3\text{:PbTiO}_3$ ," Presented at the 1999 U.S. Navy Workshop on Acoustic Transduction Materials and Devices, University Park, PA (April 13-15, 1999).
37. McConnell, J.A. and G.C. Lauchle, "Comparative Study: Flow-Induced Noise on Underwater Acoustic Pressure, Particle Velocity, and Intensity Sensors," Joint Meeting 137<sup>th</sup> Regular Meeting of the Acoust. Soc. Am. and 2<sup>nd</sup> Convention of the European Acoust. Assoc. Technical University of Berlin, Berlin, Germany [*J. Acoust. Soc. Am.* **105**, Pt. 2, 1120 (1999)].
38. McConnell, J.A., K.J. Bastyr, and G.C. Lauchle, "Sound-Speed Determination in a Fluid-Filled Elastic Waveguide," Joint Meeting 137<sup>th</sup> Regular Meeting of the Acoust. Soc. Am. and 2<sup>nd</sup> Convention of the European Acoust. Assoc. Technical University of Berlin, Berlin, Germany [*J. Acoust. Soc. Am.* **105**, Pt. 2, 1143 (1999)].
39. Bastyr, K.J. and G.C. Lauchle, "Bias Error Due to Flow-Induced Noise on a Velocity Gradient Underwater Acoustic Intensity Sensor," Joint Meeting 137<sup>th</sup> Regular Meeting of the Acoust. Soc. Am. and 2<sup>nd</sup> Convention of the European Acoust. Assoc. Technical University of Berlin, Berlin, Germany [*J. Acoust. Soc. Am.* **105**, Pt. 2, 1121 (1999)].
40. Lauchle, G.C. and T.A. Brungart, "Modification of a Handheld Vacuum Cleaner for Noise Control," 138<sup>th</sup> Meeting of Acoust. Soc. Am., Columbus, OH [*J. Acoust. Soc. Am.* **106**, Pt. 2, 2171 (1999)].
41. Kim, K., G.C. Lauchle, and T.B. Gabrielson, "Pressure-Particule Acceleration Underwater Acoustic Intensity Sensor," 138<sup>th</sup> Meeting of Acoust. Soc. Am., Columbus, OH [*J. Acoust. Soc. Am.* **106**, Pt. 2, 2297 (1999)].
42. Capone, D.E. and G.C. Lauchle, "Modeling the Unsteady Forces on a Finite-Length Circular Cylinder in Cross-Flow," 138<sup>th</sup> Meeting of Acoust. Soc. Am., Columbus, OH [*J. Acoust. Soc. Am.* **106**, Pt. 2, 2297 (1999)].

43. Lauchle, G.C. and W.A. Kargus IV, "Scaling of Turbulent Wall Pressure Fluctuations Downstream of a Rearward Facing Step," Inter-Noise 99, Fort Lauderdale, FL (December 6-8, 1999).
44. Canfield, S., B. Peterson, M. Frecker, and G.H. Koopmann, "Design of Piezoelectric Inchworm Actuator and Compliant End-Effector for Minimally Invasive Surgery," Proceedings of SPIE 6<sup>th</sup> Annual International Symposium on Smart Structures and Materials, California (March 1999).
45. Frank, J.E. and G.H. Koopmann, "Design and Performance of a High-Force Piezoelectric Inchworm Actuator," Proceedings of SPIE 6<sup>th</sup> Annual International Symposium on Smart Structures and Materials, California (March 1999).
46. Lesieutre, G.A. and G.H. Koopmann, "Roller Wedgeworm: A Piezoelectrically Driven Rotary Motor," 10<sup>th</sup> International Conference on Adaptive Structures and Technologies, Paris, France (October 1999).
47. Belegundu, U., X.H. Du, and K. Uchino, "Comparison of Domain Formation in Rhombohedral and Tetragonal Crystals of  $(1-x)\text{Pb}(\text{Zn}_{1/3}\text{Nb}_{2/3})\text{O}_3$ - $x\text{PbTiO}_3$  Single Crystals," ONR Transducer Workshop, University Park, PA, (April 1999).
48. Koc, B., P. Bouchilloux, and K. Uchino, "Piezoelectric Motor Array for Micro Air Vehicles," ONR Transducer Workshop, University Park, PA (April 1999).
49. Chen, Y.H., S. Hirose, and K. Uchino, "Effects of Processing and Doping on PMN-PT Based Ceramics for High-Power Applications," ONR Transducer Workshop, University Park, PA (April 1999).
50. Du, X.H., U. Belegundu, and K. Uchino, "Crystal Orientation Dependence of Piezoelectric Properties in Ferroelectric Crystals (Part II)," ONR Transducer Workshop, University Park, PA (April 1999).
51. Du, X.H., U. Belegundu, and K. Uchino, "Crystal Orientation Dependence of Piezoelectric Properties in Perovskite Ferroelectrics," 27<sup>th</sup> ICAT Smart Actuator Symposium, State College (April 1999).
52. Chen, Y.H., S. Hirose, and K. Uchino, "Dielectric and Electromechanical Properties of PMN-PT Based Ceramics for High-Power Applications," 27<sup>th</sup> ICAT Smart Actuator Symposium, State College (April 1999).
53. Koc, B., P. Bouchilloux, and K. Uchino, "Tiny Piezoelectric Ultrasonic Motor," 27<sup>th</sup> ICAT Smart Actuator Symposium, State College (April 1999).
54. Yao, K., Y.H. Chen, P. Bouchilloux, and K. Uchino, "Compact Langevin Vibrators with Increased Number of the Piezoelectric Layers," 27<sup>th</sup> ICAT Smart Actuator Symposium, State College (April 22-23, 1999).
55. Zheng, J. and K. Uchino, "Loss Mechanisms in Piezoelectric Actuators," 27<sup>th</sup> ICAT Smart Actuator Symposium, State College (April 22-23, 1999).
56. Kalpat, S., Y. Ito, X. Du, I.R. Abothu, and K. Uchino, "Dielectric and Piezoelectric Property Dependence of PZT Thin Films," 27<sup>th</sup> ICAT Smart Actuator Symposium, State College (April 22-23, 1999).
57. Belegundu, U., H. Aburatani, X.H. Du, and K. Uchino, "Switching Current Dependence on Crystal Orientation for Relaxor Based Ferroelectric Single Crystals," 101<sup>st</sup> Annual Mtg. of Amer. Ceram. Soc., Symp. Dielectric Materials and Devices, SE-76, Indianapolis (April 25 - 28, 1999).

58. Poosanaas, P., A.I. Robin, S. Komarneni, and K. Uchino, "Nanocomposite PLZT Ceramics for Photostrictive Materials," 101st Annual Mtg. of Amer. Ceram. Soc., Symp. Dielectric Materials and Devices, SEP-24, Indianapolis (April 25-28, 1999).
59. Du, X.H., U. Belegundu, S.S. Kalpat, and K. Uchino, "Crystal Orientation Dependence of Piezoelectric Properties in Some Single Crystals," 101st Annual Mtg. of Amer. Ceram. Soc., Symp. Dielectric Materials and Devices, SEP-38, Indianapolis (April 25-28, 1999).
60. Kalpat, S.S., Y. Ito, X.H. Du, I.R. Abothu, and K. Uchino, "Dielectric and Piezoelectric Property Dependence of PZT Thin Films," 101st Annual Mtg. of Amer. Ceram. Soc., Symp. Dielectric Materials and Devices, SEP-46, Indianapolis (April 25 - 28, 1999).
61. Yao, K., S.X. Dong, L.C. Lim, and K. Uchino, "Compact Hollow Multilayer Actuators Prepared from Hard Piezoelectric Materials," 101st Annual Mtg. of Amer. Ceram. Soc., Symp. Dielectric Materials and Devices, SEP-58, Indianapolis (April 25 - 28, 1999).
62. Chen, Y.H., S. Hirose, and K. Uchino, "Doping and Processing Effects on PMN-PT Based Ceramics for High-Power Application," 101st Annual Mtg. of Amer. Ceram. Soc., Symp. Dielectric Materials and Devices, SEP-59, Indianapolis (April 25 - 28, 1999).
63. Zheng, J.H., B. Sugg, and K. Uchino, "Heat Generation in Piezoelectric Actuators under Different Driving Conditions," 101st Annual Mtg. of Amer. Ceram. Soc., Symp. Dielectric Materials and Devices, SEP-60, Indianapolis (April 25-28, 1999).
64. Koc, B., A. Amin, P. Bouchiloux, and K. Uchino, "Design of Circular Type Piezoelectric Transformer with Off-Centered Input Electrodes," 101st Annual Mtg. of Amer. Ceram. Soc., Symp. Dielectric Materials and Devices, SEP-65, Indianapolis (April 25 - 28, 1999).
65. Abothu, I.R., Y. Ito, S. Komarneni, and K. Uchino, "Processing  $\text{Pb}(\text{Co}_{1/3}\text{Nb}_{2/3})\text{O}_3$  Ceramics by Sol-Gel Method," 101st Annual Mtg. of Amer. Ceram. Soc., Symp. Innovative Processing and Synthesis of Ceramics, SN-79, Indianapolis (April 25-28, 1999).
66. Koc, B. and K. Uchino, "Disk Type Piezoelectric Transformer with Crescent Shape Input Electrodes," NATO- Advanced Research Workshop: Piezoelectric Materials, Advance in Science, Technology and Applications, Predeal, Romania (May 24-27, 1999).
67. Kalpat, S., I.R. Abothu, A. Akiba, H. Goto, S. Trolrier-McKinstry, and K. Uchino, "Dielectric and Piezoelectric Property Dependence on Highly Textured (100), (111) and Random Thin Films Grown by RF Sputtering," Mater. Res. Soc. Fall Mtg. '99, LL.1.3, Boston (Nov. 29-Dec.3, 1999).
68. Uchino, K., J. Zheng, Y.H. Chen, X. Du, and S. Hirose, "Loss Mechanisms in Piezoelectrics," Mater. Res. Soc. Fall Mtg. '99, LL.1.6, Boston (Nov. 29-Dec.3, 1999).
69. Belegundu, U., H. Aburatani, and K. Uchino, "Studies on Switching Current in Relaxor Based (1-x)PZN-xPT Single Crystals," Mater. Res. Soc. Fall Mtg. '99, LL.1.9, Boston (Nov. 29-Dec.3, 1999).
70. Bouchilloux, P., K. Craig, B. Koc, and K. Uchino, "Design and Construction of a Rotary and a Linear Ultrasonic Motors with Free Stators," Mater. Res. Soc. Fall Mtg. '99, LL.2.10, Boston (Nov. 29-Dec.3, 1999).

71. Zheng, J. and K. Uchino, "Determination of Energy Loss in Piezoelectric Actuators under Off-Resonance Driving," Mater. Res. Soc. Fall Mtg. '99, LL.5.7, Boston (Nov. 29-Dec.3, 1999).
72. Koc, B., Y. Gao, and K. Uchino, "Disk Type Piezoelectric Transformer Design Employing High Power Piezoelectric Ceramic Material," Mater. Res. Soc. Fall Mtg. '99, LL.5.8, Boston (Nov. 29-Dec.3, 1999).
73. Chen, Y.H., S. Hirose, D. Viehland, and K. Uchino, "Doping Effects in  $\text{Pb}(\text{Mg}_{1/3}\text{Nb}_{2/3})\text{O}_3\text{-PbTiO}_3$  Ceramics for High Power Transduction Applications," Mater. Res. Soc. Fall Mtg. '99, LL.5.9, Boston (Nov. 29-Dec.3, 1999).

#### 14.0 BOOKS (AND SECTIONS THERE OF)

1. Newnham, R.E., "Smart Electroceramics," Chapter in Ceramic Innovations, edited by J. B. Watchman, pp. 185-187, American Ceramic Society Press (1999).
2. Newnham, R. E., "Ceramics Engineering in the 21st Century: Age of Aquarius," Chapter in Ceramics as a Global Enterprise, edited by Margaret Rasmussen and W. David Kingery, pp. 187-195 (1999).
3. Uchino, K., Wiley Encyclopedia of Electrical and Electronics Engineering, J.G. Webster, Edit., (Partial Charge "Piezoelectric Actuators"), John Wiley & Sons (1999).
4. Ito, Y. and K. Uchino, Wiley Encyclopedia of Electrical and Electronics Engineering, J.G. Webster, Edit., (Partial Charge "Piezoelectricity"), John Wiley & Sons (1999).
5. Uchino, K., How to Polish Up Scientific English Papers - Second Edition - (Partial Charge: Chapter 3 - Common Mistakes by Japanese Scientists). Edit. Jpn. Phys. Soc., Maruzen Pub. Co., Tokyo (1999).
6. Uchino, K., Ferroelectric Devices, Marcel Dekker, NY (1999).
7. Koopmann, G.H., McGraw Hill Science Encyclopedia 2000 article on "Acoustic Equivalent Source Methods."
8. Q. M. Zhang, T. Furukawa, Y. Bar-Cohen, and J. Scheinbeim. Editors, Electroactive Polymers, Proceedings of Materials Research Society 600, 1999.

#### 15.0 PATENTS

1. Robert E. Newnham and Jindong Zhang, "Flexensional Metal-Ceramic Composite Transducer," US patent application No. 09/376,259.
2. B. Koc and K. Uchino, "Ultrasonic Motor," US Patent (05955820) (September 21, 1999).
3. K. Uchino and B. Koc, "Micro Air/Underwater Vehicle Powered by Piezoelectric Motor of Motor Array," US Patent (PSU Invention Disclosure No. 99-2090).

# **GENERAL SUMMARY PAPERS**

# **APPENDIX 1**

## GUEST EDITORIAL

L.E. Cross

## Newnham Festschrift introduction

It is both a privilege and a real pleasure to write this short introduction to the report of the Newnham Festschrift Session that was held at the *Innovations in Materials Conference* in Washington, DC on Monday, July 20th, 1998. Robert and I go back a long way together, not just for the thirty-two (32) years we have worked closely together in MRL at Penn State, but also from a surprising commonality of early instructors. Bob took his first Ph.D. under Professor G.W. Brindley, a world leader in Clay Mineralogy research at Penn State. Dr. Brindley was my undergraduate tutor in Physics at Leeds University before he came to the USA. Bob's second Ph.D. was with Helen Megaw in Cambridge, England. I was a frequency visitor to Helen whilst on an ICI fellowship at Leeds.

Over the years, Bob has maintained close interest and made outstanding contributions to progress in Ferroelectrics, Piezoelectrics, Secondary Ferroics, Pyroelectrics, Composites, Sensors, Actuators, and Smart Systems. Not surprisingly, contributors to this Festschrift issue picked up on several of these strong threads of Prof. Newnham's professional interest.

In electroactive composites, Ahmad Safari and D.C. Danforth at Rutgers use solid free form fabrication to architect a wide range of piezoceramic and ceramic-polymer composite structures, including rod, tube, dome shaped and concentric ring arrays. Geometries which would be difficult or impossible to realize with other methods. An alternative realization of the 1:3 fiber:polymer composite on an exceptionally fine scale is discussed by D. Sporn and A. Schönecker from Fraunhofer Institute in Würzburg, Germany. The preparation of  $\text{PbZrO}_3\text{:PbTiO}_3$  (PZT) piezoelectric fibers by sol-gel processing with final fired diameter less than 30  $\mu\text{m}$  is certainly a processing "tour de force" and makes possible exciting high frequency transducers not accessible by other methods. An extension from Newnham's own

moonie and cymbal actuators are the important large area light weight cymbal arrays now under development by Tom Howarth and Jim Tressler at the Naval Research Laboratory. These arrays look to have outstanding sonar properties in both send and receive modes.

Polarization switching is the key distinguishing property of ferroelectrics, yet it is not fully understood either in bulk or in thin film ferroelectrics. Seshu Desu from VPI, Blacksburg, Virginia presents interesting new data on fatigue effects which dog the non-volatile memory efforts in ferroelectric thin films. Clearly however now there is light at the end of this tunnel in the form of non-fatiguing oxide metal electrodes for PZTs or the alternative non-fatiguing bismuth oxide layer structure ferroelectrics.

For frequency agile materials which maintain high Q at microwave frequencies Louise and Somnath Sengupta from Pratek Corporation in Maryland have certainly made an important breakthrough with the  $\text{Ba}_x\text{Sr}_{1-x}\text{TiO}_3\text{:MgO}$  composites which by their processing achieve adequate tunability and loss properties for application up to 20 GHz. An interesting alkali-metal free sol-gel process for  $\text{BaTiO}_3$  is discussed by K.M.S. Khalil from Egypt. Well crystallized  $\text{BaTiO}_3$  is obtained at 600°C.

Higher order ferroic properties of TGS Monocrystals are discussed by E.F. Dudnik, A.I. Kushnerev, and V.M. Duba from Dniepropetrovsk in Ukraine. Here the effects of elastic stress on switching are traced to the ferroelastoelectric interaction with the opposing piezoelectric constants in the antipolar domains. The Atomic Force Microscope is proving to be an excellent tool for ferroelectricians to study local surface effects. S. Balakumar and H.C. Zeng use the microscope to study humidity effects upon the switching in TGS crystals.

Fittingly, Newnham's own contribution in this volume deals with the latest developments in cymbal transducers. One of the permanent impacts Bob Newnham has left on the field is the scientific design of electroactive *composites*. More recently he has moved on to devices incorporating some of his composites.

I believe this session in Washington was a signal success, and a fitting tribute to the interests and achievements of Professor R.E. Newnham.

L.E. Cross

Evan Pugh Professor of Electrical Engineering,  
112B Research Unit A, Materials Research Laboratory,  
The Pennsylvania State University,  
University Park, PA 16802, USA  
Fax: +1-814-863-7846, e-mail: LEC3@PSU.EDU

# **APPENDIX 2**

# ECerS Plenary Address Ceramics into next millennium

R. E. Newnham

*Overpopulation is the overriding problem of the twenty-first century, and water is key to human survival. Irrigation, desalination, filtration, and aquaculture are the key technologies and, given the natural abundance of oxides, ceramics are the key materials. High strength saline cements, semipermeable membranes, antibacterial coatings, limestone farming, accretion chemistry, and sonar systems for massive fish farms are concepts worthy of consideration in the twenty-first century. All will involve the use of vast amounts of oxide materials, mainly cement, concrete, synthetic coral, together with ceramic membranes and transducers. The scaling up process for engineering megaworks will be matched by equally interesting scaling down processes in which ceramic, electronic, and optical components are made smaller and smaller until they disappear inside integrated inorganic systems which rival biological systems both in scale and complexity. The age of engineering microworks is upon us, and in the coming century a global system will evolve which involves the integration of human and machine intelligence.*

*The author is in the Materials Research Laboratory, Pennsylvania State University, University Park, PA 16802, USA. Presented at the Sixth Conference and Exhibition of the European Ceramic Society, Brighton, UK, 20–24 June 1999.*

© 1999 IoM Communications Ltd.

## INTRODUCTION

In a speech several years ago at the National Academy of Engineering, incoming President Norm Augustine spoke of the need for a new public image for engineers. His suggestion was *L. A. Engineer*, a new TV series with episodes about 'thought decoders', 'irrigating the Sahara', 'spacecraft on the moons of Jupiter', 'college implants', and 'the bridge over Gibraltar' to provide some much needed excitement to our profession. 'Engineers' like Brooke Shields and Arnold Schwarzenegger could easily match the exploits of the lawyers, medical doctors, and policemen populating today's television, and stimulate interest in the engineering profession.

Throughout history, engineers have been 'pilots of change' though we seldom see ourselves as affecting society in any meaningful way. But in the new millennia of fast paced technological change with instant global impact, engineers must view their work in a larger context. As Jonas Salk once remarked, we must be 'good ancestors' to our planet and to future generations.

One problem stands above all others as the world population doubles during the next century. According to a United Nations estimate, the population will level off at 11.5bn in the year 2150. Other estimates range from 15 to 30bn with 90% of the increase occurring in the Third World. A population explosion such as this will inevitably

lead to malnutrition, famine, deforestation, pollution, epidemics, drought, political crises, revolutions, homeless refugees, and war. Or, as Woody Allen once remarked, 'The world is at a crossroads: one road leads to famine, disease, and despair ... the other leads to total oblivion'.

Birth control is desperately needed to limit population growth, but there are economic, political, and religious reasons why this is a slow and difficult process. As engineers, we naturally lean toward technical fixes, which will mitigate the crisis, and water is one of the key factors.

## WATER AND IRRIGATION

The availability of fresh water varies widely in different parts of the world. In water rich countries like Canada more than 10<sup>6</sup> L of fresh water is available annually per capita. In Malta, Libya, and other water poor countries, only about 100 L per year is available, barely enough to fill a large bathtub. Even in the United States there are major water problems because of the imbalance in supply and demand. The southwestern states from California to Texas have only 6% of the water but 31% of the population and a very rapid growth rate. Water table levels are dropping at an alarming rate in Arizona and New Mexico.

Where will the water come from to feed the burgeoning world population? Irrigation is one answer. Diversion of the Yangtze River into a grand canal is underway in China. Egypt has a plan to create 1.3m acres of new farmland by creating a new delta using waters from Lake Nasser. And in North America, Canadian engineer T. W. Kierans has proposed a vast irrigation system in which Hudson's Bay, James Bay, and the Great Lakes are used as reservoirs to feed a vast network of irrigation canals in Canada, the US, and Mexico. In the more distant future, one can imagine a world in which the Caribbean, Mediterranean, and other shallow seas are converted to fresh water reservoirs. The deserts of Mexico, North Africa, and the Near East could then be converted to farmland.

With regard to ceramics, vast tonnages of cement will be required to bring about engineering megaworks. Calcium aluminate cements have been implicated in hydration failures, often leading to structural failures. Superior saline resistance has been obtained from calcium aluminosilicate cements recrystallised from glasses to form stratlingite or hydrogarnet.<sup>1</sup>

Macrodefect-free (MDF) cements<sup>2</sup> are far stronger than normal cements. Hydraulic cement and water soluble polymers are mixed at high shear rates, calendared, and cured under pressure in the process developed by ICI. Repeated extrusion helps to eliminate the critical flaws responsible for mechanical failure. Polymer chains cross-linked by metal ions impart tensile strength to the cement.

Cement and concrete have more influence on people's lives than ever before. As the world's premier building materials, they are a tremendous challenge to the industries concerned, and to the ceramic and civil engineering professions. During the past 20 years, global consumption of cement has risen from 172 to 257 kg per capita with most of the increase taking place in China and other parts of Asia. This has led to predictions of future depletions of

source materials for concrete, especially aggregates, but innovative solutions are available.<sup>3</sup>

- new methods for compacting fresh cement and for monitoring the curing process
- techniques for improving the workability of fresh concrete with greatly reduced amounts of water
- increased utilisation of fly ash and other recycled light-weight aggregates
- composite technology, especially fibre reinforcement
- impregnated concrete with polymerised organics or molten sulphur.

The global production is  $\times 10$  larger than competitive building and construction materials. It is time that cement, concrete, and other low temperature ceramics received increased attention from the research community.

## DESALINATION

But irrigation is unlikely to solve the water problem for very long. It is an ironic fact of nature that two-thirds of our planet is covered with unusable salt water. Desalination is the ultimate solution to our dilemma. To bring this about, the cost of desalination, presently about 0.1 cents  $L^{-1}$ , needs to be reduced by an order of magnitude.

Seawater contains 3.5% dissolved ions, mostly  $Na^+$  and  $Cl^-$ . Until a decade ago, the dominant desalination methods were based on multistage distillation, but reverse osmosis is now the leading technique. Osmosis involves the transmission of fluids through a semipermeable membrane. If the membrane separates fresh water and seawater, fresh water would normally pass through the membrane because of the concentration gradient. If, however, a pressure greater than the so-called osmotic pressure is applied to the seawater, then water from the seawater side diffuses through the membrane. There is a preferential sorption layer on the membrane, which determines the critical pore diameter of the membrane.<sup>4</sup> This is a key problem in membrane science, which is crucial to desalination technology.

Ceramic membranes have a number of advantages over polymers.<sup>5</sup> Their mechanical strength prevents membrane compression and subsequent pore closure. Superior thermal stability is an advantage for high temperature separation processes, and for many cleaning operations. Ceramics also have remarkable chemical stability in a large number of solvents and can easily be steam cleaned. They are also immune to microbe and bacterial attack.

Asymmetric membranes consisting of a thin dense skin mounted on a porous substructure have proved useful in desalting by hyperfiltration. The structures resemble the extruded honeycomb structures developed by Corning Inc. for catalytic substrates.<sup>6</sup> By blocking alternate channels a gas or fluid can be forced through the porous ceramic walls to filter out the waste product. The honeycomb substrates are commonly made from cordierite ceramics with low thermal expansion coefficients. The structure of cordierite resembles that of beryl with open channels along the *c*-crystallographic axes. In natural cordierite crystals, the channels are often occupied by water molecules forming strong hydrogen bonds to the oxygen ions lining the walls of the channels. The  $H_2O$  vibration modes of the trapped molecules are shifted dramatically from those in liquid water, ice, and water vapour<sup>7</sup> indicating a reduced level of bonding between water molecules. This is a key idea in desalination and other water purification process. As pointed out in the series of papers by W. A. P. Luck, water can be separated into two phases in which the dissolved ions are segregated into the newly formed secondary phase. The primary hydration water does not dissolve ions, and suggests the following working hypothesis for water purification: 'Desalination membranes should contain mainly primary hydrate water, the structure of which weakens ion solubility. The existence of secondary hydration shells with

ion solubility should be prevented by steric effects'.<sup>8</sup> Infrared spectroscopy appears to be an excellent characterisation tool in understanding the molecular structure of water.

Nature is another splendid source of ideas. Glasswort (*salicornia bigelovii*) is a saltwater crop grown commercially for animal fodder and seed oil. The roots of the glasswort plant have a composite structure with a wax-like film capable of rejecting the dissolved salts in seawater. Synthetic membranes based on similar composite geometries could be of great value.

## SANITARYWARE

In addition to desalination, there are a number of other applications for ceramic and polymeric membranes including water purification, kidney dialysis, gas separation, and the eradication of water borne disease. These techniques include microporous filtration, ultrafiltration, dialysis, electrodialysis, semipermeable gas membranes, and support liquid membranes.

It is time for a new generation of sanitaryware since only recently ceramists celebrated the great achievements of Thomas Crapper (1837–1910) the great Victorian sanitary engineer. One hundred years ago, Crapper developed the record-setting 'super flush' toilet that is still in use today. In the widely publicised Health Exhibition competition, ten  $1\frac{1}{2}$  in apples, a flat  $4\frac{1}{2}$  in sponge, three hollow paper cones, and four pieces of tissue paper covered with a thick layer of plumber's smudge all went down in a single super flush.

A century later there is a new competition called The Great Public Toilet Contest. Sponsored by the Chinese government, the new contest involves designing sanitary systems for the Third World. The standard western commode – virtually unchanged since the time of Thomas Crapper – does not meet the needs of an overpopulated world with severe water shortages. In addition to water conservation, several other interesting concepts are under development. Smart toilets capable of rapid urine analysis provide rapid screening for diabetes and other health problems. 'Johnny on the spot' is a portable commode with self-adjustable seats that fit all sizes and temperature preferences. Magnetic filtration systems remove many of the particulates in polluted waters and have been successfully tested on the River Ganges.

One of the most fascinating ideas is the development of antibacterial tiles that eradicate *e-coli* through a photocatalytic process. Methicillin resistant, *staphylococcus aureus* (MRSA) bacteria are responsible for many infectious diseases. Ceramic tiles coated with a thin layer of titania and a metal catalyst are capable of attacking bacterial cell membranes.<sup>9</sup> The ultraviolet component of sunlight excites electrons across the narrow band gap (3 eV) of  $TiO_2$ , creating holes and free electrons. These, in turn, react with oxygen molecules and hydroxyl ions to form very reactive superoxide and hydroxide radicals that attack the bacteria. Antibacterial tiles are used in hospitals, food processing factories, toilets, swimming pools, and home kitchens.

My own interests are in the application of ferroelectric ceramics and composite transducers to the water problem. It is interesting to speculate on reverse osmosis systems in which the membranes are rhythmically driven to open and close the nanometre scale pore system. The hope is to develop a family of smart membranes capable of cleaning fouled passages by mechanical, electrical, or chemical means.

A second goal is drop by drop irrigation using piezoelectric pumps, based on ink jet designs. Ferroelectric titanates might also be worthy candidates for antibacterial photocatalysis, similar to the anatase-coated tiles used in bathroom sanitaryware. Sonochemical cavitation combining acoustically driven phase changes and chemical reactions are other possibilities.

## AQUACULTURE

Especially close to my heart are the biomimetic piezoelectric transducers we have investigated during the past 20 years.<sup>10</sup> The subsonic sonar systems developed for navy needs hold great promise for sonobuoy fish schooling and deep ocean geophysical mapping.

As the earth's population continues to increase, the human race must continue to search for new and efficient sources of food and nutrition. The world's oceans will provide a partial solution to this problem through aquaculture and the use of new and varied saltwater vegetation that can provide an abundant source of food for countries in which poor soil and harsh climates limit conventional farming.

The burgeoning population of the Third World obtains most of its protein from fish, but fisheries and fishermen are in trouble throughout the world's oceans. Statistics released by the Worldwatch Institute<sup>11</sup> have spotlighted an alarming decrease in fish populations in most of the world's oceans. Large scale aquaculture is a major goal for an overpopulated world.

Fish catches are down nearly everywhere from the North Atlantic to the Indian Ocean. The only bright spot is fish farming which is growing at a rapid rate, but the number of suitable fresh water ponds is limited. Oceanic fish farming may be the answer.<sup>12</sup>

In his book, 'The millennial project', Michael Savage describes the next century as the Age of Aquarius in which huge fisheries are grown - literally grown - in tropical oceans.<sup>13</sup> Floating colonies miles across can be formed by the electrodeposition of  $\text{CaCO}_3$  on a wire frame. The procedure is described in several patents filed by W. Hilbertz more than a decade ago.<sup>14</sup> The accretion chemistry involves the deposition of  $\text{CaCO}_3$ ,  $\text{Mg}(\text{OH})_2$ ,  $\text{SiO}_2$ ,  $\text{NaCl}$ , and other salts on a metal cathode. Approximately 2 kg of sea cement is formed for each  $\text{kW h}^{-1}$  of electrical energy. Energy would be supplied from solar panels or by an ocean thermal energy converter (OTEC) utilising the temperature gradient in the ocean. By taking advantage of the saturated salts in the world's oceans, millions of limestone farms can be constructed around the equator. Aquaculture can then be carried out on a grand scale.

By converting the Mediterranean sea and the Caribbean sea into giant fishponds, aquaculture could be carried out on an even grander scale. The scale of such fish farming would be comparable to cattle ranching in the Wild West where cows ranged free over hundreds of miles of pasture. In such a setting, 'fish boys' would herd schools of fish like cowboys herded cattle in the old west. Artificial reefs made of stone, cement, and coral would provide shelter and food for the fish, and the fences could be made from woven glass fibres. Sonar transmitters could be used to guide the schools using the appropriate fish language.

In recent years great advances have been made in recording and translating fish talk, largely through the development of PZT hydrophone arrays and high speed spectrum analysis. Low frequency sound waves function in a variety of ways for fish, both in offence and defence, for warning and intimidation.<sup>15</sup> Fish speak differently during the breeding season using coded repetition rates. Our ability to 'farm the oceans' could be greatly enhanced by learning to talk to fish and control their movements and feeding habits. Smart ceramic transceivers could receive and transmit fish talk and monitor the growth of underwater vegetation.

## SCALING DOWN: INORGANIC EVOLUTION

The field of high tech ceramics is dominated by electroceramics, which account for about 90% of the commercial market. Capacitors, resistors, transducers, and other ceramic components are undergoing rapid changes. Integration

and miniaturisation is taking place as information and control systems grow smaller and more complex. By incorporating sensors, actuators, and evolvable chips into these systems, it becomes possible to emulate biological behaviour. Smaller electronic and optical subsystems are capable of evolving into more complex systems with the ability to sense and respond to changes in their surroundings. At the same time biochemists are making major advances in understanding how the human brain functions and what it means to be alive. In the coming century there will be confluence of organic and inorganic life into some type of composite life form, perhaps an immortal life form, with a common consciousness that transcends individual beings. Internet and the World Wide Web seem to be leading us in that direction. The evolution of machine technology into a global intelligence is the theme of a major new book by George Dyson.<sup>16</sup>

More relevant to ceramists is the miniaturisation of ceramic electronic components and their integration with silicon based circuitry in the form of thick or thin films. Billions of multilayer ceramic capacitors are manufactured annually with lateral dimensions less than a millimetre and layer thickness approaching  $1 \mu\text{m}$ . Grain sizes are being pushed down to  $0.1 \mu\text{m}$  with all the incumbent problems in powder processing and densification. Barium strontium titanate thin film DRAMs and lead zirconate titanate FeRAMs are being deposited on silicon for enhanced capacitance and non-volatile memories.

Following Moore's law, microcircuit complexity doubles every 18 months with dynamic random access memories approaching 1 Gb and microprocessor elements approaching 10m per chip. Extrapolating ahead, memories may reach 1 Tb by the year 2020 and 1 Pb later in the century. By way of comparison, the genetic information in the human brain is about 10 Tb. All cultural information in the form of books and pictures would require about 1 Pb.

Semiconductor technology is not the only industry experiencing exponential growth. Multilayer capacitors and other packaging components also follow Moore's law, doubling at the same rate as the IC chip market. Even faster growth is taking place in the communications industry. Optical fibre capacity doubles every 12 months, and microwave wireless production every 9 months. It is interesting to speculate on the underlying causes of this exponential growth.

Is it fashion? Do people buy these products and services to keep up with their neighbours? Or is it a self-fulfilling prophecy that we are somehow programmed by our culture to continually look for something new? Or even more interesting, is our universe structured in such a way that life continually evolves into more complex forms with technological advances augmenting the biological process?

## SMART SYSTEMS

Sensors and actuators are needed to connect computers to the outer world, and bring them to life. Many modern day electroceramics have been cleverly designed to perform useful functions, and we feel justified in calling them smart because they combine sensing and actuation in one material. Smart materials are capable of coupling cyberspace to the real world.

The concept of a smart material is exemplified by a videotape-head positioner made from PZT piezoceramic bimorphs. The positioner has large actuator electrodes that move the material, as well as smaller electrodes to sense the position and orientation of the tape head. This combination of sensing and actuating mimics two of the functions of a living system - namely being aware of the surroundings and being able to respond to that signal with a useful response, usually in the form of a motion. A smart material is not simply a sensor. A sensor receives a stimulus and

responds with a signal. A smart material is not simply an actuator either. An actuator produces a useful motion or action. Smart materials function as both sensors and actuators.

Smart materials sometimes have a control system and sometimes not. Some function like our spinal cord in that they are passively smart and respond without thought – or signal processing. They are analogous to the reflex responses of the human body. In other cases, smart materials analyse the sensed signal, perhaps for its frequency components, and then make a choice as to what type of response to make. We call that an actively smart system. We have also been developing a family of very smart materials – I am not willing to call them intelligent – which have a learning or tuning function, making it possible for them to get slightly smarter with age. Non-linear properties like electrostriction or higher order elastic constants are used in these materials.

Looking ahead to the use of thin film microelectromechanical systems (MEMS), more intelligent materials are coming on the scene that integrate the control system with the sensors and actuators, all in one common piece of material.<sup>17</sup> At this stage, I think the system deserves the name intelligent. Perhaps some day we will manufacture wise materials that make correct moral decisions and maybe evolve in some way like living systems. A few short range forecasts by World Future Society for smart systems in the coming decade:

- cash will disappear (smart cards)
- electronic immigration (lone eagles)
- robots smarter than humans (inorganic evolution)
- prisons outmoded by implants (automated paroles)
- voice drive furniture (smart chairs)
- population shifts north (smart houses)
- defective gene replacement (nanosensors and nanoactuators)
- collision avoidance systems (smart automobiles)
- older generation families (smart medical delivery system)
- automatic gardens (just-in-time farming).

Several involve the use of smart materials with sensing and actuating capabilities.

### SMART MATERIALS

With regard to the choice of materials, several common themes emerge. Two transformations are involved in most of these smart materials, often a primary ferroic (ferroelastic, ferroelectric, or ferromagnetic) with domain-wall motions that assist in the sensing and actuating processes. The ferroics are operated near an instability to make these domain walls with their associated dipoles and strains movable. We have identified several types among the commonly used actuator materials, and others appear to be possible too. In one type, a high Curie temperature exists as in PZT or terfenol, and the actuator is operated near an orientational change of the electric or the magnetic dipole moment. The second type involves a partially ordered phase, as in electrostrictive PMN or the shape-memory alloys. These materials are operated near a diffuse phase transition with two coexisting phases, the high temperature or austenite-like phase and the low temperature or martensitic type phase. A third type involves composite materials with coupled phase transformations.

The underlying strategies to optimise smart materials are fairly obvious. Why primary ferroic? These materials provide a handle for external fields or forces, whether it is a strain or an electric dipole or magnetic dipole. Why a cubic prototype phase? The answer is that it gives many equivalent orientation states and makes it possible then to use polycrystalline materials without the necessity of growing single crystals. Why partial ordering? This structure provides many nucleation sites for generating a diffuse phase transformation. Why a morphotropic transition? This insta-

bility ensures persistent disequilibrium over quite a wide range. In his recent book, 'Out of control',<sup>18</sup> author Kevin Kelly describes how biological systems evolve into more complex life forms: neither constancy nor relentless change will support a complex dynamic system. Equilibrium is death, and complete chaos leads to explosive behaviour, also followed by death. On the other hand, persistent disequilibrium optimises dynamic behaviour by staying on the hairy edge of rapid response. The behaviour of the sensor and actuator materials used in smart systems appears to be consistent with this idea.

As we look to the future, many new types of smart system will be developed. Aerospace engineers are interested in smart airfoils to control drag and turbulence. Diabetics need medical systems to sense sugar level and deliver insulin. Architects are designing smart buildings that incorporate self-adjusting windows to control the flow of energy into houses. Tennis players will want smart racquets to make overhead smashes and delicate drop shots. Smart systems will identify burglars and other dishonest people, and control their movements. Smart toilets are capable of analysing urine to identify health problems. Smart irrigation systems are needed to optimise the world's food supply. Fish are the leading source of protein in many parts of the world. We can farm the oceans using smart transducers to talk to the fish and herd them like cattle. Thus there will be a convergence of the 'scaling up' and the 'scaling down' process in the next century.

### OPTICAL FIBRES AND FUTURE OF MANKIND

Silicon and oxygen – the two most common elements in the earth's crust – are the key components in both microelectronic circuitry and optical communications systems where Internet traffic doubles every 3 or 4 months. Optical fibre transmission capacity has moved even faster than the processing power and memory capabilities of silicon devices. The operating speed of integrated circuits has risen by a factor of 60 over the past decade while the capacity of silica fibre systems grew by a factor of 200 over the same period. The tiny 8  $\mu\text{m}$  core of a single mode fibre can now transmit about 1 Tb s<sup>-1</sup>, an information rate equivalent to all the voice traffic in the world.

Where will it end? In the prologue to his novel '3001, The final Odyssey', Arthur C. Clarke discusses the future of mankind.<sup>19</sup> During the coming millennium, evolution will drive us to new goals, and soon we will reach the limits of flesh and blood. Our machines will surpass the capabilities of our biological bodies, and we will transfer our minds to new homes made of metals and silicon. In this form we can explore our galaxy, but later, as we seek answers to the origins of life and secrets of the universe, Clarke predicts that we will pass through yet another transformation as our thoughts and very existence are transferred into pure waveform. As light we can explore the universe, freed from tyranny of matter.

Is this science fiction or are we now witnessing the beginnings of new life forms in IC chips and optical fibres? Time will tell, I only wish I could be there to witness these breathtaking phase transformations. It will be an exciting time to be alive.

### SUMMARY

Aquaculture, desalination, and irrigation and microelectronic projects will all utilise the talents of ceramic engineers, but there are many more. In his book, 'Ceramic houses: how to build your own', Nader Khalili writes: 'Now is the time to create a new scale in the ceramic world, to walk out of the womb of the potter's kiln, to the space of a room. Now the time has come to create a ceramic glaze, a china,

a stoneware, not in the scale of our hands, but in the scale of our lives'.

The time for scaling up has arrived. It is time for computer designed adobe structures glazed and fired in place.<sup>20</sup> It is time for intercontinental tunnels made from concrete and steel, ceramic pontoons, and smart support structures.<sup>21</sup> In short, it is time for ceramic engineers to think big.

It is also time for scaling down. Electroceramic components and devices are being miniaturised and integrated with silicon based circuitry and with silica based optical systems at an almost exponential rate. Our materials are part of an inorganic evolution, which will soon rival biology in scale and in complexity. How these submicron smart systems will integrate with human culture will be one of the exciting engineering adventures of the coming century, perhaps leading to some kind of hybrid immortality.

Will any of this come true? When I was a teenager in high school, our English teacher assigned a book report on Edward Bellamy's 'Looking backward', a Victorian Utopian fantasy. The hero, Julian West was a Bostonian gentleman who was mesmerised and then awakened a century later to witness the 'perfect society' of the year 2000. Here are some of Edward Bellamy's predictions:

- full employment with workers retiring at age 45
- money replaced by credit cards
- no crime, no jails, and no lawyers
- splendid cultural achievements in the arts and music
- war and poverty abolished.

Some of these predictions have come true, and others not. It is obvious that we have a long way to go in achieving the perfect society. The challenge is great but so are the opportunities.

## REFERENCES

1. J. E. MACDOWELL: *Mater. Res. Soc. Symp. Proc.*, 1991, 159-179.
2. J. D. BIRCHALL: *Nature*, 1981, **28/29**, 388-390.

3. G. IDORN: 'Concrete progress from antiquity to the third millennium'; 1997, London, Thomas Telford.
4. S. SOURIRAJAN: *Am. Chem. Soc. Symp.*, 1981, **153**, 11.
5. R. BHAVE: 'Inorganic membranes'; 1991, New York, Van Nostrand Reinhold.
6. R. BAGLEY, I. LACHMAN, and R. LEWIS: in 'Role of ceramics in a self sustaining environment', (ed. R. Pampuch and K. Hoberko); 1997, Faenza, Italy, Techna.
7. E. FARRILL and R. E. NEWNHAM: *Am. Min.*, 1967, **52**, 380.
8. W. LUCK, D. SCHROBERG, and U. SIEMANN: *Chem. Soc. Faraday Trans.*, 1980, **76**, 179.
9. M. MACHIDA: Japan Fine Ceramic Association annual report, 1995, 10.
10. R. E. NEWNHAM: *Mater. Res. Soc. Bull.*, 1997, **22**, 20.
11. L. BROWN and H. KANE: 'Full house'; 1996, Washington, DC, Worldwatch Institute.
12. C. SHEPHERD and N. BROMAGE: 'Intensive fish farming'; 1988, Oxford, BSP Professional Books.
13. M. T. SAVAGE: 'The millennial project'; 1994, New York, Little Brown.
14. W. HILBERTZ: 'Mineral accretion of large structures', US patent 4 440 605, 1984.
15. M. P. FISH and W. H. MOWBRAY: 'Sounds of western north Atlantic fishes'; 1970, Baltimore, MD, John Hopkins Press.
16. G. DYSON: 'Darwin among the machines'; 1997, Reading, MA, Perseus Books.
17. R. MULLER: 'Microelectromechanical systems'; 1997, Washington, DC, National Academy Press.
18. K. KELLY: 'Out of control'; 1994, Reading, MA, Addison Wesley, Longman.
19. A. C. CLARKE: '3001. The final Odyssey'; 1997, New York, Balantine.
20. N. KHAILILI: 'Ceramic houses: building your own'; 1986, New York, Harper and Son.
21. W. GRANTZ: *Invent. Technol.*, 1996, **12**, 10.

# **APPENDIX 3**

# NEW TREND IN MULTILAYER CERAMIC ACTUATORS

**Kenji Uchino**

International Center for Actuators and Transducers  
Materials Research Laboratory, The Pennsylvania State University  
University Park, PA 16802, USA

and

**Sadayuki Takahashi**

Research & Development Group, NEC Corporation  
Miyazaki, Miyamae, Kawasaki 216, Japan

## ABSTRACT

During the past few years, piezoelectric and electrostrictive ceramic materials have become key components in smart actuator/sensor systems for use as precision positioners, miniature ultrasonic motors and adaptive mechanical dampers. In particular, multilayer structures have been intensively investigated in order to improve their reliability and to expand their applications. Recent developments in USA, Japan and Europe will be compared.

## INTRODUCTION

Piezoelectric actuators are forming a new field midway between electronic and structural ceramics [1-4]. Application fields are classified into three categories: positioners, motors and vibration suppressors. The manufacturing precision of optical instruments such as lasers and cameras, and the positioning accuracy for fabricating semiconductor chips, which are adjusted using solid-state actuators, is of the order of 0.1  $\mu\text{m}$ . Regarding conventional electromagnetic motors, tiny motors smaller than 1  $\text{cm}^3$  are often required in office or factory automation equipment, and are rather difficult to produce with sufficient energy efficiency. Ultrasonic motors whose efficiency is insensitive to size are superior in the mini-motor area. Vibration suppression in space structures and military vehicles using piezoelectric actuators is also a promising technology.

Multilayer structures are mainly used for practical applications, because of their low drive voltage, high energy density, quick response and long lifetime [5,6]. Figure 1 illustrates multilayer, multimorph and multilayer-moonie structures, which will be covered in this article. Recent investigations have focused on the improvement of reliability and durability in multilayer actuators.

---

To the extent authorized under the laws of the United States of America, all copyright interests in this publication are the property of The American Ceramic Society. Any duplication, reproduction, or republication of this publication or any part thereof, without the express written consent of The American Ceramic Society or fee paid to the Copyright Clearance Center, is prohibited.

This article reviews the investigations of device structures, reliability issues, and recent applications of multilayer actuators, comparing the developments in USA, Japan and Europe.

## MULTILAYER STRUCTURES

Two preparation processes are possible for multilayer ceramic devices: one is a cut-and-bond method and the other is a tape-casting method. The tape-casting method requires expensive fabrication facilities and sophisticated techniques, but is suitable for the mass-production of thousands of pieces per month. Tape-casting also provides thin dielectric layers, leading to low drive voltages of 40 - 100 V [7,8].

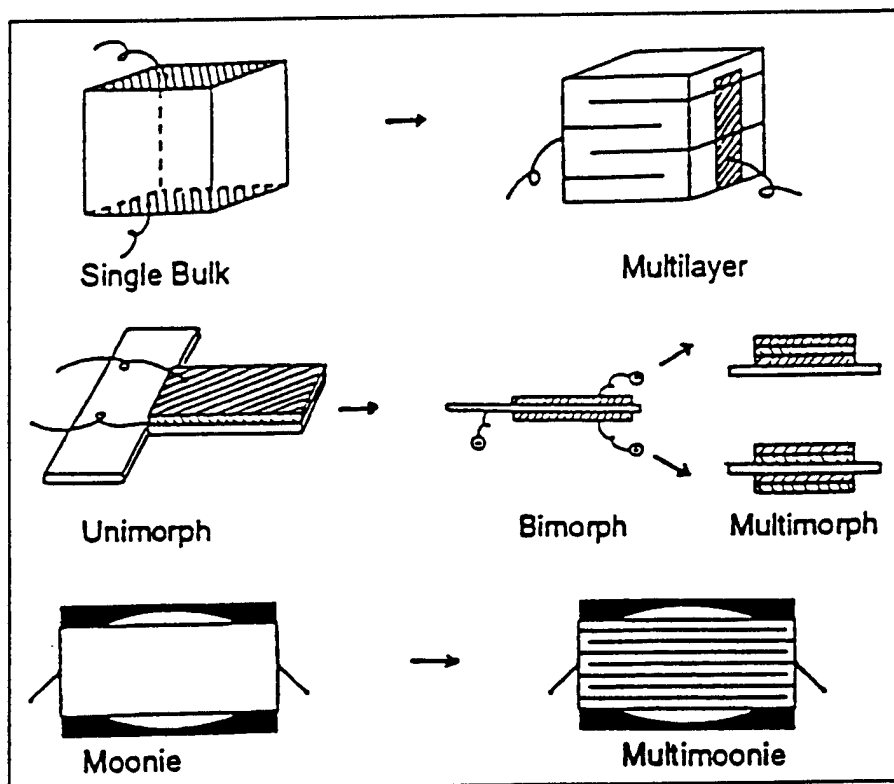


Fig.1 Examples of multilayer, multimorph and multilayer-moonie structures.

A multilayer actuator with interdigital internal electrodes has been developed by Tokin [9,10]. In contrast to the conventional electrode configuration in Fig. 1, line electrodes are printed on piezoelectric ceramic green sheets, and are stacked in such a way that alternating electrode lines are displaced by one-half pitch (see Fig. 2). This actuator generates motions at right angles to the stacking direction using the longitudinal piezoelectric effect. Long ceramic actuators up to 74 mm in length are manufactured.

A three-dimensional positioning actuator with a stacked structure has been proposed by PI Ceramic (Fig.3), in which shear strain is utilized to generate x and y displacements [11].

Composite actuator structures called "moonies" and "cymbals" have been developed at Penn State University to provide characteristics intermediate between the multilayer and bimorph actuators. These transducers exhibit an order of magnitude larger displacement than the multilayer, and much larger generative force with quicker response than the bimorph [12,13]. The device consists of a thin multilayer piezoelectric element and two metal plates with narrow moon-shaped cavities bonded together as shown in Fig. 1. A moonie  $5 \times 5 \times 2.5 \text{ mm}^3$  in size can generate a  $20\mu\text{m}$  displacement under 60V, eight times as large as the displacement of a multilayer of the same size [14]. This new compact actuator has been used to make a miniaturized laser beam scanner [14]. Moonie/cymbal characteristics have been investigated for various constituent materials and sizes [15,16].

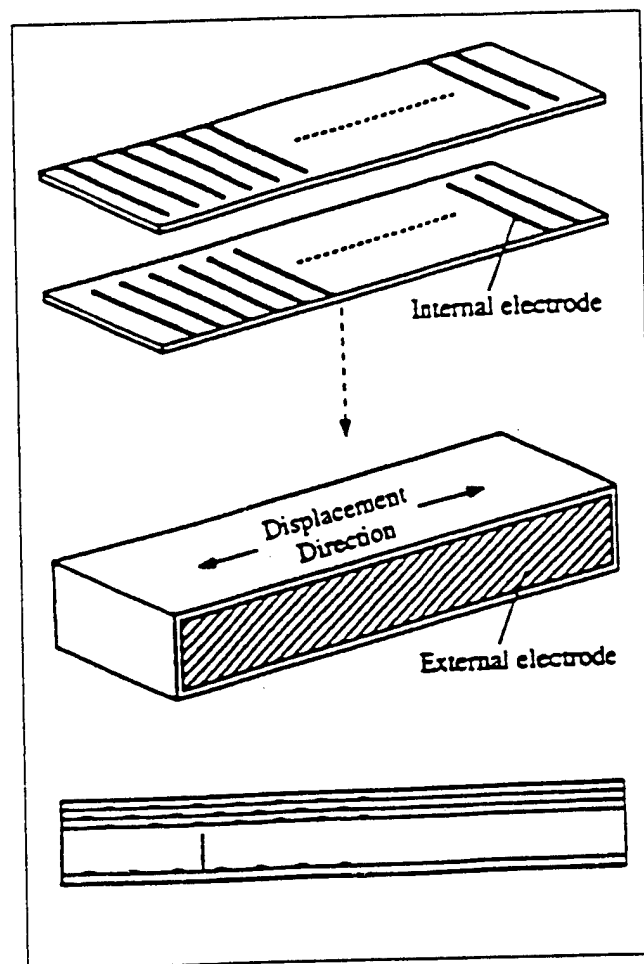


Fig.2 Structure of an internal interdigital electrode actuator.

## RELIABILITY OF MULTILAYER ACTUATORS

As the application fields expand, the reliability and durability issues of multilayer actuators become increasingly important. The reliability of ceramic actuators depends on a number of complex factors, which can be divided into three major categories: reliability of the ceramic itself, reliability of the device design, and drive technique.

Compositional changes of actuator ceramics and the effect of doping are primary issues used in stabilizing the temperature and stress dependence of the induced strains. A multilayer piezo-actuator for use at high temperatures ( $150^{\circ}\text{C}$ ) has been developed by Hitachi Metal, using  $\text{Sb}_2\text{O}_3$  doped  $(\text{Pb},\text{Sr})(\text{Zr},\text{Ti})\text{O}_3$  ceramics [17]. Systematic data on uniaxial stress dependence of piezoelectric characteristics have been collected on various Navy PZT materials [18]. Grain size and porosity control of the ceramics are also important in controlling the reproducibility of actuators [19]. Aging phenomena, especially the degradation of strain response, are, in general, strongly dependent on the applied electric field as well as on temperature, humidity and mechanical bias stress [20].

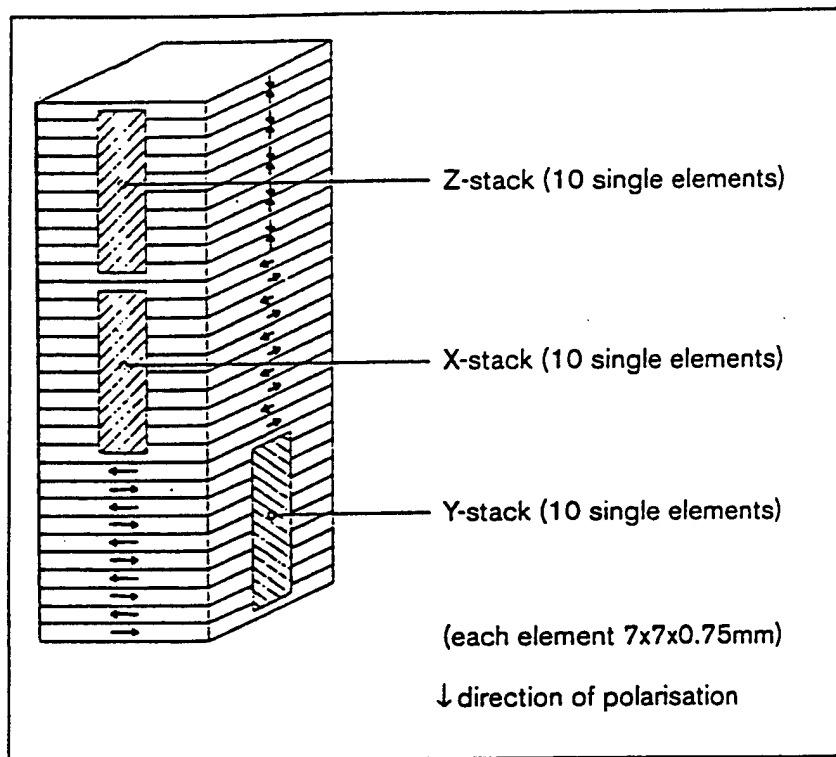
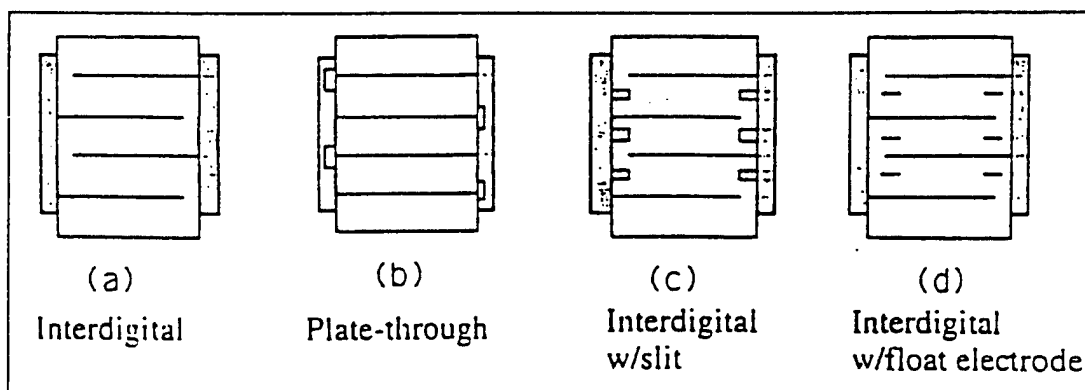


Fig.3 3-D controllable multilayer piezoelectric actuator.

The device design strongly affects its durability and lifetime. Silver electrode metal tends to migrate into the piezoceramic under a high electric field in high humidity. Silver:palladium alloys suppress this behavior effectively. Resistive coatings of the device should also be taken into account [21]. To overcome electrode delamination, improved adhesion can be realized by using a mesh-type electrode or an electrode material with mixed metal and ceramic (the matrix composition!) powders. Pure ceramic electrode materials have also been developed using semiconductive perovskite oxides (barium titanate-based PTCR ceramics) [22]. The lifetime characteristics of a multilayer actuator with applied DC or unipolar AC voltage at various temperatures [23,24] and at various humidities [25] were investigated by Nagata et al. The relationship between the logarithm of the lifetime and the reciprocal of absolute temperature showed linear characteristics similar to Arrhenius type. Nevertheless, the degradation mechanism remains a critical problem.

In multilayer actuators, reduction of the tensile stress concentration around the internal electrode edge of the conventional interdigital configuration is the central problem. Regarding the destruction mechanism of multilayer ceramic actuators, systematic data collection and analysis have led to considerable progress [26-33]. Two typical crack patterns are generated in a conventional interdigital multilayer device: one is a Y-shaped crack located on the edge of an internal electrode, and the other is a vertical crack located in a layer adjacent to the top or bottom inactive layer, connecting a pair of internal electrode.

To overcome this crack problem, three electrode configurations have been proposed as illustrated in Fig. 4: plate-through, interdigital and slit, and interdigital and float electrode types. The "float electrode" type is an especially promising design which can be fabricated using almost the same process as the conventional multilayer actuator, and lead to much longer lifetimes [34]. An empirical rule "the thinner the layer, the tougher the device" [27,28] is also very intriguing, and will be more theoretically investigated in the near future.



**Fig.4 Various internal electrode configurations in multilayer actuators.**  
 (a) Interdigital, (b) Plate-through, (c) Slit-insert, and (d) Float electrode.

Failure detection or lifetime prediction methods are expected to remarkably increase the reliability of multilayer actuators. Acoustic emission and surface potential monitoring are promising methods [35]. Penn State has developed a modified multilayer actuator containing a strain gauge as an internal electrode [36]. This internal strain gauge electrode can detect the crack initiation sensitively and monitor the field-induced strain [37].

Regarding drive techniques for ceramic actuators, pulse drive and AC drive require special attention; the vibration overshoot associated with a sharp-rise step/pulse voltage causes a large tensile force, leading to delamination of the multi-stacked structure, while long-term application of AC voltage generates considerable heat. A special pulse drive technique using a mechanical bias stress are required in the first case, and heat generation can be suppressed by changing the device design. An analytical approach to the heat generation mechanism in multilayer actuators has been reported, indicating the importance of larger surface area [38]. Heat generation in piezoelectric ceramics is mainly attributed to the P-E hysteresis loss under large electric field drive [39,40]. For ultrasonic motors, antiresonance drive is preferable to resonance drive because of higher efficiency and lower heat generation for the same vibration level [41].

## APPLICATIONS OF MULTILAYER ACTUATORS

Table I compares a variety of ceramic actuator developments in the USA, Japan and Europe. Additional details will be described in this section.

**Table I Ceramic actuator developments in the USA, Japan and Europe.**

	US	Japan	Europe
TARGET	Military-oriented products	Mass-consumer products	Laboratory equipment
CATEGORY	Vibration suppressor	Mini-motor Positioner	Mini-motor Positioner Vibration suppressor
APPLICATION FIELD	Space structure Military vehicle	Office equipment Cameras Precision machines Automobiles	Lab stage-stepper Airplanes Automobiles Hydraulic systems
ACTUATOR SIZE	Up-sizing (30 cm)	Down-sizing (1 cm)	Intermediate size (10 cm)
MAJOR MANUFACTURER	AVX/Kyocera Morgan Matroc Itek Opt. Systems Burleigh AlliedSignal	Tokin Corp. NEC Hitachi Metal Mitsui-Sekka Canon Seiko Instruments	Philips Siemens Hoechst Ceram Tec. Ferroperm Physik Instrumente

## USA

The principal target is military-oriented applications such as vibration suppression in space structures and military vehicles. Substantial up-sizing of the actuators is required for these purposes.

A typical example is found in the aircraft wing proposed by NASA [42]. A piezoelectric actuator was installed near the support of the wing, allowing immediate suppression of unwanted mechanical vibrations. Several papers have been reported on damper and noise cancellation applications [43,44].

Passive dampers constitute another important application of piezoelectrics, where mechanical noise vibration is radically suppressed by the converted electric energy dissipation through Joule heat when a suitable resistance, equal to an impedance of the piezoelectric element  $1/\omega C$ , is connected to the piezo-element [45].

A widely-publicized application took place with the repair of the Hubble telescope launched by the Space Shuttle. Multilayer PMN electrostrictive actuators corrected the image by adjusting the phase of the incident light wave (Fig.5) [46]. PMN electrostrictors provided superior adjustment of the telescope image because of negligible strain hysteresis.

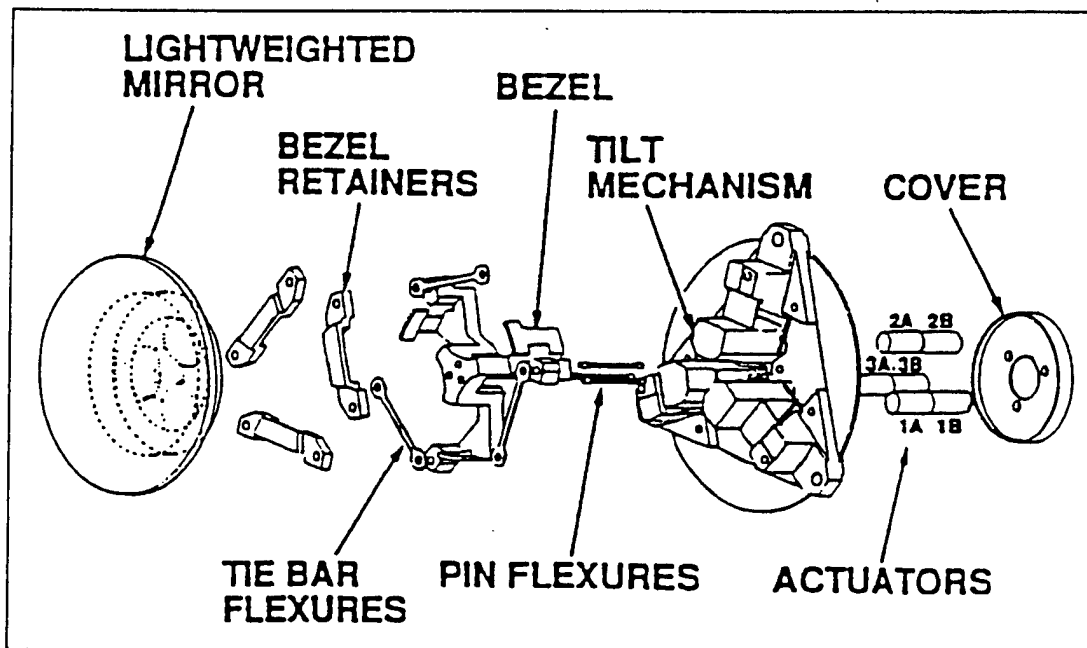


Fig.5 Articulating fold mirror using PMN multilayer actuators.

## JAPAN

Japanese industries seek to develop mass-consumer products, especially mini-motors and micro positioners, aiming at applications such as office equipment and cameras/video cameras. Tiny actuators smaller than  $1\text{cm}^3$  are the main focus in these products.

A dot matrix printer was the first widely-commercialized product using multilayer ceramic actuators [47]. Each character formed by such a printer was composed of a  $24 \times 24$  dot matrix in which a printing ribbon was impacted by a multiwire array. The printing element was composed of a multilayer piezoelectric device with a sophisticated hinge lever magnification mechanism. The magnification by a factor of 30 resulted in an amplified displacement of 0.5 mm and an energy transfer efficiency greater than 50%. A modified impact printer head has been developed by Tokin, using new interdigital internal electrode type actuators, which have lowered production cost [48]. A color ink-jet printer has also been commercialized by Seiko Epson, using multilayer piezo-actuators [49].

Automotive applications by Toyota Motor have been accelerated recently. Multilayer actuators have been introduced to an electronically controlled suspension [50] and a pilot injection system for diesel engines [51].

Efforts have been made to develop high-power ultrasonic vibrators as replacements for conventional electromagnetic motors. The ultrasonic motor is characterized by "low speed and high torque," which is contrasted with the "high speed and low torque" of the electromagnetic motors. After the invention of -shaped linear motors [52], various modifications have been reported [53,54]. The Mitsui Petrochemical model is of particular interest because the motor body is composed of only one component prepared by a cofiring method as illustrated in Fig. 6 [54]. A maximum speed of 200 mm/s and a maximum thrust of 60 gf were reported for this motor.

Camera motors utilize a traveling elastic wave induced by a thin piezoelectric ring. A ring-type slider in contact with the "rippled" surface of the elastic body bonded onto the piezoelectric can be driven in both directions by exchanging the sine and cosine voltage inputs. Another advantage is its thin design, making it suitable for installation in cameras as an automatic focusing device. Nearly 80 % of the exchange lenses in Canon's "EOS" camera series have been replaced by ultrasonic motor mechanisms [55].

Intriguing research programs are underway in Japan on the vibration damping of earthquakes, using piezoelectric actuators [56,57]. Active damping of a multilayer piezo-actuator was tested using an actual size H-type steel girder, and was verified to be effective during earthquakes.

## EUROPE

Ceramic actuator development has begun relatively recently in Europe with a wide range of research topics. A current focus of several major manufacturers is on laboratory equipment products such as laboratory stages and steppers with rather sophisticated structures.

Figure 7 shows a walking piezo motor with 4 multilayer actuators by Philips [58]. Two short actuators function as claspers while the longer two provide a proceeding distance in an inchworm mechanism. Physik Instrumente has developed more complicated two-leg type walkers [59].

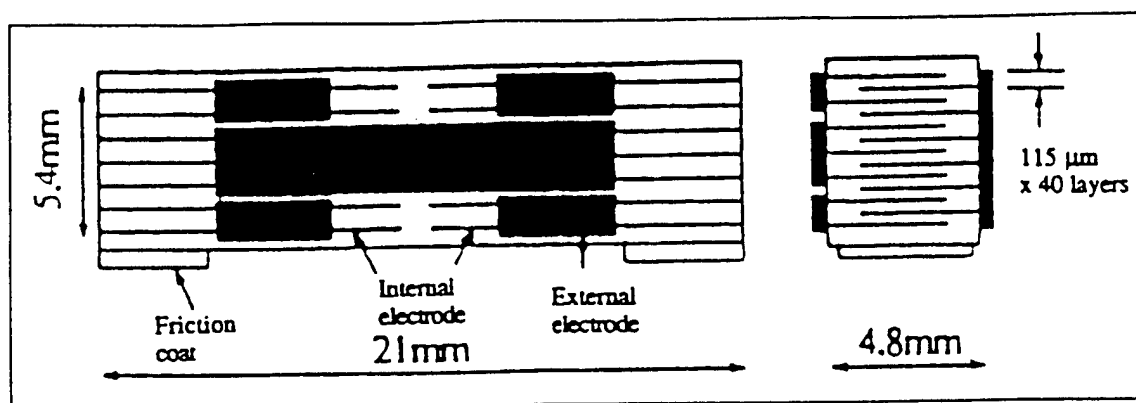


Fig.6 Monolithic multilayer piezoelectric linear motor.

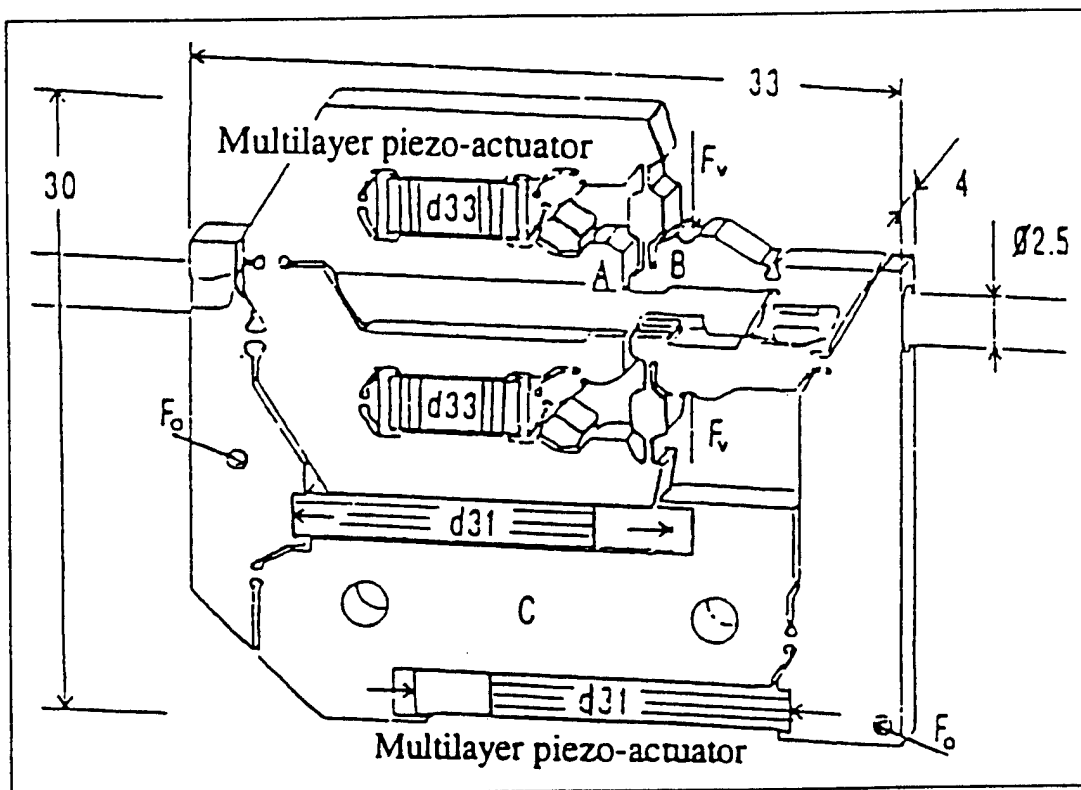


Fig.7 An inchworm using multilayer piezoelectric actuators.

## CONCLUSIONS

Twenty years have passed since the intensive development of piezoelectric actuators began in Japan, then spread worldwide. Presently, the focus has been shifted to practical device applications. This article has reviewed several reliability issues of the multilayer ceramic actuators as well as new actuator structures, and compared the developments of recent applications among USA, Japan and Europe.

The markets in USA are chiefly limited to military and defense applications, and it is difficult to estimate the amount of sales. The current Navy needs include smart submarine skins, hydrophone actuators, and prop noise cancellation. Smart aircraft skins are an Air Force objective, while Army requires helicopter rotor twisting, aeroservoelastic control and cabin noise/seat vibration cancellation.

Meanwhile in Japan, piezoelectric shutters (Minolta Camera) and automatic focusing mechanisms in cameras (Canon), dot-matrix printers (NEC) and part-feeders (Sanki) are now commercialized and mass-produced by tens of thousands of pieces per month. During the commercialization, new designs and drive-control techniques of the ceramic actuators have been mainly developed over the past few years. A number of patent disclosures have been generated by NEC, TOTO Corporation, Matsushita Electric, Brother Industry, Toyota Motors, Tokin, Hitachi Metal and Toshiba.

If we estimate the annual sales in 2001 (neglecting the current economic recession in Japan), ceramic actuator units, camera-related devices and ultrasonic motors are expected to reach \$500 million, \$300 million and \$150 million, respectively. Regarding the final actuator-related products, \$10 billion is a realistic goal [55].

Future research trends can be divided in two ways: up-sizing in space structures and down-sizing in office equipment. Further down-sizing will also be required in medical diagnostic applications such as blood test kits and surgical catheters.

Key words for the future of multilayer ceramic actuators are "miniaturization" and "hybridization." Layers thinner than 10  $\mu\text{m}$ , corresponding to current multilayer capacitor technology, will also be introduced in actuator devices replacing the present 100  $\mu\text{m}$  sheets. Piezoelectric thin films compatible with silicon technology are a focus in micro-electromechanical systems. Ultrasonic rotary motors as small as 2 mm in diameter [60] and two-dimensional micro-optical-scanner [61], both of which were fabricated on a silicon membrane are good examples.

Non-uniform configurations or hetero-structures of different materials, layer thickness, or electrode patterns will be adopted for practical devices. Functionally gradient piezoelectric actuators now being prototyped indicate a new trend [62].

## REFERENCES

1. Uchino K: Piezoelectric Actuators/Ultrasonic Motors. Kluwer Academic Pub., MA 1996.
2. Uchino K: Ceramic Actuators: Principles and Applications. MRS Bull. 1993, 18: 42 - 48.
3. Uchino K: Materials Update: Advances in Ceramic Actuator Materials. Mater. Lett. 1995, 22: 1 - 4.

4. Uchino K: New Piezoelectric Devices for Smart Actuator/Sensor Systems. Proc. 4th Int'l Conf. Electronic Ceramics & Appl. 1994, 179 -191.
5. Yoshikawa S, Shrout T: Multilayer Piezoelectric Actuators -- Structures and Reliability. AIAA/ASME/ASCE/AHS/ASC Struct. Struct. Dyn. Mater. Conf. 1993, 34: 3581-3586.
6. Uchino K: Manufacturing Technology of Multilayered Transducers. Proc. Amer. Ceram. Soc., Manufacture of Ceramic Components 1995, 81-93.
7. Dibern U: Piezoelectric Actuators in Multilayer Technique. Proc. 4th Int'l Conf. New Actuators (Actuator '94), Germany 1995, 114 - 118.
8. Takada S, Inoue Y, Oya K, Inagawa M: 100 V DC Driving Type Multilayer Piezoelectric Actuator. NEC Giho 1994, 47: 98 -102.
9. Ohashi J, Fuda Y, Ohno T: Multilayer Piezoelectric Ceramic Actuator with Interdigital Internal Electrodes. Jpn. J. Appl. Phys. 1993, 32: 2412 - 2414.
10. Ohashi J, Fuda Y, Ohno T: Multilayer Piezoelectric Ceramic Actuator with Interdigital Internal Electrodes. Tokin Tech. Rev. 1993, 19: 55 - 60.
11. Bauer A, Moller F: Piezo Actuator Special Design. Proc. 4th Int'l Conf. New Actuators (Actuator '94), Germany 1995, 128 - 132.
12. Sugawara Y, Onitsuka K, Yoshikawa S, Xu QC, Newnham RE, Uchino K: Metal-Ceramic Composite Actuators. J. Amer. Ceram. Soc. 1992, 75: 996 - 998.
13. Onitsuka K, Dogan A, Tressler JF, Xu QC, Yoshikawa S, Newnham RE: Metal-Ceramic Composite Transducer, The "Moonie". J. Intelligent Mater. Systems and Struct. 1995, 6: 447 - 455.
14. Goto H, Imanaka K, Uchino K: Piezoelectric Actuators for Light Beam Scanners. Ultrasonic Techno 1992, 5: 48 -51.
15. Tressler JF, Xu QC, Yoshikawa S, Uchino K, Newnham RE: Composite Flexensional Transducers for Sensing and Actuating. Ferroelectrics 1994, 156 (Proc. 8th Int'l Mtg. Ferroelectricity): 67 - 72.
16. Dogan A, Fernandez JF, Uchino K, Newnham RE: New Piezoelectric Composite Actuator Designs for Displacement Amplification. Proc. 4th Euro Ceramics 1994, 5: 127 - 132.
17. Watanabe J, Sometsugu T, Watanabe Y, Johmura S, Kurihara K, Kazama Y: Multilayer Piezoelectric Ceramic Actuator for High Temperature Use. Hitachi Metal Giho 1993, 9: 59 - 64.
18. Zhang QM, Zhao JZ, Uchino K, Zheng JH: Change of the Weak Field Properties of  $\text{Pb}(\text{Zr,Ti})\text{O}_3$  Piezoceramics with Compressive Uniaxial Stresses and Its Links to the Effect of Dopants on the Stability of the Polarizations in the Materials. J. Mater. Res. 1996, [in press].
19. Okada N, Ishikawa K, Murakami K, Nomura T, Ogino M: Improving Hysteresis of Piezoelectric PZT Actuator. Bull. Shizuoka Univ. Electron. Sci. Grad. School 1993, 14: 7 -13.
20. Sakai T, Ishikiriya M, Terai Y, Shimazaki R: Improvement in the Durability of PZT Ceramics for an Actuator. Toyota Tech. Rev. 1992, 42: 52 -59.
21. Takada S: Quality Improvement of Multilayer Piezoelectric Actuator. NEC Giho 1992, 45: 109 -113.
22. Abe K, Uchino K, Nomura Late S: Barium Titanate-Based Actuator with Ceramic Internal Electrodes. Ferroelectrics 1986, 68: 215 - 223.

23. Nagata K, Kinoshita S: Life Time of Multilayer Ceramic Actuator at High Temperature. *J. Powder and Metallurgy* 1994, 41: 975 - 979.
24. Nagata K, Kinoshita S: Relationship between Lifetime of Multilayer Ceramic Actuator and Temperature. *Jpn. J. Appl. Phys.* 1995, 34: 5266 -5269.
25. Nagata K, Kinoshita S: Effect of Humidity on Life Time of Multilayer Ceramic Actuator. *J. Powder and Metallurgy* 1995, 42: 623 - 627.
26. Furuta A, Uchino K: Dynamic Observation of Crack Propagation in Piezoelectric Multilayer Actuators. *J. Amer. Ceram. Soc.* 1993, 76: 1615 - 1617.
27. Aburatani H, Harada S, Uchino K, Furuta A, Fuda Y: Destruction Mechanisms in Ceramic Multilayer Actuators. *Jpn. J. Appl. Phys.* 1994, 33: 3091 - 3094.
28. Furuta A, Uchino K: Destruction Mechanism of Multilayer Ceramic Actuators: Case of Antiferroelectrics. *Ferroelectrics* 1994, 160: 277 - 285.
29. Wang H, Singh RN: Electric Field Effects on the Crack Propagation in a Electro-strictive PMN-PT Ceramic. *Ferroelectrics* 1995, 168: 281 - 291.
30. Cao HC, Evans AG: Electric-Field-Induced Fatigue Crack Growth in Piezoelectrics. *J. Amer. Ceram. Soc.* 1994, 77: 1783 - 1786.
31. Schneider GA, Rostek A, Zickgraf B, Aldinger F: Crack Growth in Ferroelectric Ceramics under Mechanical and Electrical Loading. *Proc. 4th Int'l Conf. Electronic Ceram. and Appl.*, Germany, 1994, 1211 - 1216.
32. Suo Z: Models for Breakdown Resistant Dielectric and Ferroelectric Ceramics. *J. Mech. Phys. Solids* 1993, 41: 1155 - 1176.
33. Hao TH, Gong X, Suo Z: Fracture Mechanics for the Design of Ceramic Multilayer Actuators. *J. Mech. Phys. Solids* 1996, [in press].
34. Aburatani H, Uchino K, Furuta A and Fuda Y: Destruction Mechanism and Destruction Detection Technique for Multilayer Ceramic Actuators. *Proc. 9th Int'l Symp. Appl. Ferroelectrics* 1995, 750 - 752.
35. Uchino K, Aburatani H: Destruction Detection Techniques for Safety Piezoelectric Actuator Systems. *Proc. 2nd Int'l conf. Intelligent Materials* 1994, 1248 - 1256.
36. Sano M, Ohya K, Hamada K, Inoue Y, Kajino Y: Multilayer Piezoelectric Actuator with Strain Gauge. *NEC Giho* 1993, 46 (10): 100 - 103.
37. Aburatani H, Uchino K: Stress and Fatigue Estimation in Multilayer Ceramic Actuators Using an Internal Strain Gauge. *Abstract Annual Mtg. & Expo. Amer. Ceram. Soc., Int'l Symp. Solid-State Sensors and Actuators* 1996, SXIX-37-96: 191.
38. Zheng JH, Takahashi S, Yoshikawa S, Uchino K: Heat Generation in Multilayer Piezoelectric Actuators. *J. Amer. Ceram. Soc.* 1996, [in press].
39. Hirose S, Takahashi S, Uchino K, Aoyagi M, Tomikawa Y: Measuring Methods for High-Power Characteristics of Piezoelectric Materials. *Proc. Mater. Res. Soc., '94 Fall Mtg.* 1995, 360: 15 - 20.
40. Takahashi S, Sakaki Y, Hirose S, Uchino K: Stability of  $\text{PbZrO}_3\text{-PbTiO}_3\text{-Pb}(\text{Mn}_{1/3}\text{Sb}_{2/3})\text{O}_3$  Piezoelectric Ceramics under Vibration-Level Change. *Jpn. J. Appl. Phys.* 1995, 34: 5328 - 5331.
41. Hirose S, Aoyagi M, Tomikawa Y, Takahashi S, Uchino K: High-Power Characteristics at Antiresonance Frequency of Piezoelectric Transducers. *Proc. Ultrasonic Int'l* 1995, 1 - 4.

42. Heeg J: Analytical and Experimental Investigation of Flutter Suppression by Piezoelectric Actuation. NASA Tech. Pap., NASA-TP-3241 1993, 47.
43. Mather GP, Tran BN: Aircraft Cabin Noise Reduction Tests Using Active Structural Acoustic Control. Pap. Amer. Inst. Aeronaut Astronaut 1993, AIAA-93-4437: 7.
44. Agrawal BN, Bang H: Active Vibration Control of Flexible Space Structures by Using Piezoelectric Sensors and Actuators. Amer. Soc. Mech. Eng. Des. Eng. Div. 1993, 61:169 - 179.
45. Uchino K, Ishii T: Mechanical Damper Using Piezoelectric ceramics. J. Jpn. Ceram. Soc. 1988, 96: 863 - 867.
46. Wada B: Summary of Precision Actuators for Space Application. JPL Document D-10659, 1993.
47. Yano T, Fukui I, Sato E, Inui O, Miyazaki Y: Impact Dot-Matrix Printer Head Using Multilayer Piezoelectric Actuators. Proc. Electr. & Commun. Soc. (Spring) 1984, 1: 156.
48. Ono Y, Fuda Y: Multilayer Piezoelectric Ceramic Actuator with Interdigital Internal Electrodes for Impact Dot-Matrix Printers. Proc. Symp. on Electro-Magnetic Related Dynamics 1994, 6th: 135 - 138.
49. Yonekubo S: Color Inkjet Printer by Multi-Layer Piezoelectric Actuator. J. Electron. Photo Soc. 1995, 34: 226 - 228.
50. Fukami A, Yano M, Tokuda H, Ohki M, Kizu R: Development of Piezo-electric Actuators and Sensors for Electronically Controlled Suspension. Int. J. Veh. Des. 1994, 15: 348 - 357.
51. Abe S, Igashira T, Sakakibara Y, Kobayashi F: Development of Pilot Injection System Equipped with Piezoelectric Actuator for Diesel Engine. JSAE Rev. (Soc. Automot. Eng. Jpn.) 1994, 15: 201 - 208.
52. Tohda M, Ichikawa S, Uchino K, Kato K: Ultrasonic Linear Motor Using a Multilayered Piezoelectric Actuator. Ferroelectrics (Proc. ECAPD-1/ISAF '88) 1989, 93: 287 - 294.
53. Funakubo T, Tsubata T, Taniguchi Y, Kumei K, Fujumura T, Abe C: Ultrasonic Linear Motor Using Multilayer Piezoelectric Actuators. Jpn. J. Appl. Phys. 1995, 34: 2756 - 2759.
54. Saigoh H, Kawasaki M, Maruko N, Kanayama K: Multilayer Piezoelectric Motor Using the First Longitudinal and the Second Bending Vibrations. Jpn. J. Appl. Phys. 1995, 34: 2760 - 2764.
55. Uchino K: Piezoelectric Actuators/Ultrasonic Motors - Their Developments and Markets. Proc. 9th Int'l Symp. Appl. Ferroelectrics 1995, 319 - 324.
56. Shimoda H, Ohmata J, Okamoto F: Seismic Response Control of a Piping System by a Semiactive Damper with Piezoelectric Actuators. J. Precision Engr. Jpn. 1992, 58: 2111 - 2117.
57. Fujita T: Can Piezoelectric Actuators Control Vibrations of Buildings? New Ceramics 1994, 7 (12): 52 - 55.
58. Koster MP: A Walking Piezo Motor. Proc. 4th Int'l Conf. New Actuators, Germany 1994, 144 - 148.
59. Gross R: A High Resolution Piezo Walk Drive. Proc. 4th Int'l Conf. New Actuators, Germany 1994, 190 - 192.

60. Flynn AM, Tavrow LS, Bart SF, Brooks RA, Ehrlich DJ, Udayakumar KR, Cross LE: Piezoelectric Micromotors for Microrobots. IEEE J. Microelectromechanical Systems 1992, 1: 44 - 51.
61. Goto H: Miniature 2D Optical Scanner and Its Application to an Optical Sensor. J. Opt. Tech. Contact 1994, 32: 322 - 330.
62. Kim HS, Choi SC, Lee JK, Jung HJ: Fabrication and Piezoelectric Strain Characteristics of PLZT Functionally Gradient Piezoelectric Actuator by Doctor Blade Process. J. Korean Ceram. Soc. 1992, 29: 695 - 704.

# **APPENDIX 4**

< Proofs Correction >

To : Helen Collins / Comprehensive Composite Materials

From : Kenji Uchino

## 5.19

# Smart Composite Materials

KENJI UCHINO

Pennsylvania State University, University Park PA, USA

5.19.1 INTRODUCTION	1
5.19.2 CONNECTIVITY	1
5.19.3 COMPOSITE EFFECTS	2
5.19.3.1 Sum Effects	2
5.19.3.2 Combination Effects	2
5.19.3.3 Product Effects	2
5.19.4 PZT-POLYMER COMPOSITES	3
5.19.4.1 Piezoelectric Composite Materials	3
5.19.4.2 Principle of PZT-Polymer Composites	3
5.19.4.3 Theoretical Models for 0-3 Composites	4
5.19.4.4 Advanced PZT-Polymer Composites	4
5.19.5 PZT COMPOSITE DAMPERS	5
5.19.6 REFERENCES	5

### 5.19.1 INTRODUCTION

Composite materials sometimes exhibit improved properties and/or new functions compared with single-phase materials. We will consider the principles of composite effects and their typical applications in this chapter, taking particularly piezocomposites as typical examples, which composed of a piezoelectric ceramic and polymer are promising materials because of their excellent tailorable properties. The geometry for two-phase composites can be classified according to the connectivity of each phase (1, 2, or 3 dimensionally) into 10 structures: 0-0, 0-1, 0-2, 0-3, 1-1, 1-2, 1-3, 2-2, 2-3, and 3-3. In particular, a 1-3 piezocomposite, or PZT-rod/polymer-matrix composite, is considered most useful. The advantages of this composite are high coupling factors, low acoustic impedance, good matching to water or human tissue, mechanical flexibility, broad bandwidth in combination with a low mechanical quality factor, and the possibility of making undiced arrays by simply patterning the electrodes. The

acoustic match to tissue or water (1.5 Mrayls) of the typical piezoceramics (20-30 Mrayls) is significantly improved when it is incorporated into such a composite structure, that is, by replacing some of the dense and stiff ceramic with a less dense, more pliant polymer. Piezoelectric composite materials are especially useful for underwater sonar and medical diagnostic ultrasonic transducer applications.

Another type of composite comprised of a magnetostrictive ceramic and a piezoelectric ceramic produces an intriguing product effect, the magnetoelectric effect, in which an electric field is produced in the material in response to an applied magnetic field.

### 5.19.2 CONNECTIVITY

Newnham *et al.* (1978) introduced the concept of "connectivity" for classifying the various PZT:polymer composite structures. When considering a two-phase composite, the connec-

(negative temperature coefficient  
- positive temperature coefficient  
of resistivity)

tivity of each phase is identified; e.g., if a phase is self-connected in all  $x$ ,  $y$ , and  $z$  directions, it is called "3"; if a phase is self-connected only in the  $z$  direction, it is called "1." A diphasic composite is identified with this notation with two numbers  $m$ - $n$ , where  $m$  stands for the connectivity of an active phase (such as PZT) and  $n$  for an inactive phase (such as a polymer). In general, there are 10 types of diphasic composites: 0-0, 1-0, 2-0, ..., 3-2, 3-3, as illustrated in Figure 1.

A 0-0 composite, for example, is depicted as two alternating hatched and unhatched cubes, while a 1-0 composite has Phase 1 connected along the  $z$  direction. A 1-3 composite has a structure in which PZT rods (one-dimensionally connected) are arranged in a three-dimensionally connected polymer matrix, and in a 3-1 composite, a honeycomb-shaped PZT contains the one-dimensionally connected polymer phase. A 2-2 composite indicates a structure in which ceramic and polymer sheets are stacked alternately, and a 3-3 composite is composed of a jungle-gym-like PZT frame embedded in a three-dimensionally connecting polymer.

### 5.19.3 COMPOSITE EFFECTS

There are three types of composite effects (Figure 2): the *sum effect*, the *combination effect*, and the *product effect*.

#### 5.19.3.1 Sum Effects

Let us discuss a composite function in a diphasic system to convert an input  $X$  to an output  $Y$ . Assuming  $Y_1$  and  $Y_2$  are the outputs from Phase 1 and 2, respectively, the output  $Y^*$  of a composite of Phases 1 and 2 could be an intermediate value between  $Y_1$  and  $Y_2$ . Figure 2(a) shows the  $Y^*$  variation with volume fraction of Phase 2 for a case of  $Y_1 > Y_2$ . The variation may exhibit a concave or a convex shape, but the averaged value in a composite does not exceed  $Y_1$  nor is it less than  $Y_2$ . This effect is called a *sum effect*.

An example is a fishing rod, i.e., a lightweight/tough material, where carbon fibers are mixed in a polymer matrix (between 3-1 and 3-0). The density of a composite should be an average value with respect to volume fraction, if no chemical reaction occurs at the interface between the carbon fibers and the polymer, following the linear trend depicted in Figure 2(a). A dramatic enhancement in the mechanical strength of the rod is achieved by

adding carbon fibers in a special orientation, i.e., along a rod (showing a convex relation as depicted in Figure 2(a)).

Another interesting example is an NTC-PTC material (Uchino, 1986).  $V_2O_3$  powders are mixed in epoxy with a relatively high packing rate (3-3), as illustrated in Figure 3. Since  $V_2O_3$  exhibits a semiconductor-metal phase transition at 160 K, a drastic resistivity change is observed with increasing temperature. A further increase in temperature results in a larger thermal expansion for epoxy than for the ceramic, leading to a separation of each particle and the structure becomes a 0-3 composite. The  $V_2O_3$  particle separation increases the resistivity significantly at around 100 °C. Thus, the conductivity of this composite is rather high only over a limited temperature range (around -100 to 100 °C), which is sometimes called the *conductivity window*.

#### 5.19.3.2 Combination Effects

In certain cases, the average value of the output,  $Y^*$ , of a composite does exceed  $Y_1$  and  $Y_2$ . This enhanced output refers to an effect  $Y/Z$  which depends on two parameters  $Y$  and  $Z$ . Suppose that  $Y$  and  $Z$  follow convex and concave type sum effects, respectively, as illustrated in Figure 2(b), the combination value  $Y/Z$  will exhibit a maximum at an intermediate ratio of phases. This is called a *combination effect*.

Certain piezoelectric ceramic-polymer composites exhibit a combination property of  $g$  (the *piezoelectric voltage constant*) which is provided by  $d/\epsilon$  ( $d$  = piezoelectric strain constant and  $\epsilon$  = permittivity). The details of these materials will be described in the next section.

#### 5.19.3.3 Product Effects

When Phase 1 exhibits an output  $Y$  with an input  $X$ , and Phase 2 exhibits an output  $Z$  with an input  $Y$ , we can expect for the composite an output  $Z$  with an input  $X$ . A completely new function is created for the composite structure, called a *product effect*.

Philips developed a *magnetoelectric material* based on this concept (Uchino, 1986). This material is composed of magnetostrictive  $CoFe_2O_4$  and piezoelectric  $BaTiO_3$  mixed and sintered together. Figure 4 shows a micrograph of a transverse section of a unidirectionally solidified rod of the materials with an excess of  $TiO_2$  (1.5 wt.%). Four finned spinel dendrites are observed in cells (x100). Figure 5 shows the magnetic field dependence of the

magnetoelectric effect in an arbitrary unit measured at room temperature. When a magnetic field is applied on this composite, cobalt ferrite generates magnetostriction, which is transferred to barium titanate as stress, finally leading to the generation of a charge/voltage via the piezoelectric effect in BaTiO<sub>3</sub>.

Since the magnetoelectric effect in a single-phase material such as Cr<sub>2</sub>O<sub>3</sub> can be observed only at a very low temperature (liquid helium temperature), observation of this effect at room temperature is really a breakthrough. Inexpensive sensors for monitoring magnetic field at room temperature or at elevated temperature can be produced from these composite materials.

#### 5.19.4 PZT-POLYMER COMPOSITES

##### 5.19.4.1 Piezoelectric Composite Materials

Polymer piezoelectric materials such as PVDF are very suitable for sensor applications. However, because of its small piezoelectric  $d$  constants and very small elastic stiffness, PVDF cannot be used by itself in fabricating actuators or high-power transducers. PZT-polymer composites, however, play a key role in the design of transducers, for applications such as sonar, which have both actuator and sensor functions (Uchino *et al.*, 1982).

The representative data for several composite piezoelectric materials are listed in Table 1 (Uchino *et al.*, 1982), with data for some single-phase piezoelectric polymer and PZT materials. The piezoelectric  $d$  constant of PVDF, which indicates the strain per unit electric field (actuator applications!), is 1/10 smaller than that of PZT, however, because of its small dielectric constant, the piezoelectric  $g$  constant of PVDF, which indicates the voltage per unit stress (sensor applications!), is 10 times larger than that of PZT. PZT-polymer composites exhibit a wide range of piezoelectric response, but in general  $d$  is slightly smaller than PZT and  $g$  is slightly smaller than PVDF. Thus, particularly for underwater transducers, which perform both actuation and sensing and have a figure of merit of  $d_h \cdot g_h$ , the composite materials are found to be far superior to single-phase materials like PZT or PVDF.

##### 5.19.4.2 Principle of PZT-Polymer Composites

Here, in order to illustrate the principle, let us take a 1-3 composite which is composed of PZT fibers embedded in a polymer matrix as shown

in Figure 6. The original fabrication process involves the injection of epoxy resin into an array of PZT fibers assembled with a special rack (Klicker *et al.*, 1981). After the epoxy is cured, the sample is cut, polished, electroded on the top and bottom, and finally electrically poled. The die casting technique has recently been employed to make rod arrays from a PZT slurry (Materials Systems Inc. Catalog, 1994).

The effective piezoelectric coefficients  $d^*$  and  $g^*$  of the composite can be interpreted as follows: when an electric field  $E_3$  is applied to this composite, the piezoceramic rods extend easily because the polymer is elastically very soft (assuming that the electrode plates which are bonded to its top and bottom are rigid enough). Thus,  $d_{33}^*$  is almost the same as  $d_{33}$  of the PZT itself,

$$d_{33}^* = d_{33} \quad (1)$$

Similarly,

$$d_{31}^* = {}^1V d_{31} \quad (2)$$

where  ${}^1V$  is the volume fraction of phase 1 (piezoelectric). On the other hand, when an external stress is applied to the composite, the elastically stiff piezoceramic rods will support most of the load, and the effective stress is drastically enhanced and inversely proportional to the volume fraction. Thus, larger induced electric fields and larger  $g^*$  constants are expected:

$$g_{33}^* = d_{33}^* / \epsilon_0 \epsilon_3^* = {}^1d_{33} / {}^1V \epsilon_0 {}^1\epsilon_3 = {}^1g_{33} / {}^1V \quad (3)$$

Figure 7 shows the piezoelectric coefficients for a PZT-Spurs epoxy composite with 1-3 connectivity, measured with a Berlincourt  $d_{33}$  meter. As predicted by the model for this composite, the measured  $d_{33}^*$  values are independent of volume fraction, but are only about 75% of the  $d_{33}$  value of the PZT 501A ceramic. This discrepancy may be due to incomplete poling of the rods. A linear relation between the permittivity and the volume fraction  ${}^1V$  is almost satisfied, resulting in a dramatic increase in  $g_{33}^*$  with decreasing fraction of PZT. The piezoelectric coefficients for the 1-3 composite are listed in Table 1, together with those of a PZT-silicone composite with 3-3 connectivity. In conclusion, for the composites, the piezoelectric  $g$  coefficient can be enhanced by two orders of magnitude with decreasing volume fraction of PZT, while the  $d$  coefficient remains constant.

The advantages of this composite are high coupling factors, low acoustic impedance, good

matching to water or human tissue, mechanical flexibility, broad bandwidth in combination with a low mechanical quality factor, and the possibility of making undiced arrays by simply patterning the electrodes. The thickness-mode electromechanical coupling of the composite can exceed the  $k_t$  (0.40–0.50) of the constituent ceramic, approaching almost the value of the rod-mode electromechanical coupling,  $k_{33}$  (0.70–0.80), of that ceramic (Smith, 1989). The acoustic match to tissue or water (1.5 Mrayls) of the typical piezoceramics (20–30 Mrayls) is significantly improved when they are incorporated in forming a composite structure, that is, by replacing the dense, stiff ceramic with a low density, soft polymer. Piezoelectric composite materials are especially useful for underwater sonar and medical diagnostic ultrasonic transducer applications.

Although the PZT composites are very useful for acoustic transducer applications, care must be taken when using them in actuator applications. Under an applied d.c. field, the field-induced strain exhibits large hysteresis and creep due to the viscoelastic property of the polymer matrix. More serious problems are found when they are driven under a high a.c. field, related to the generation of heat. The heat generated by ferroelectric hysteresis in the piezoceramic cannot be dissipated easily due to the very low thermal conductivity of the polymer matrix, which results in rapid degradation of piezoelectricity.

#### 5.19.4.3 Theoretical Models for 0-3 Composites

Various models have been proposed to predict the electromechanical properties of a composite material. Pauer (1973) developed a 0-3 composite material comprised of PZT powder and polyurethane rubber, and predicted its permittivity values by means of a cubes model. Figure 8 shows the relative permittivity plotted as a function of volume fraction of PZT powder, in comparison with theoretical values calculated on the basis of the cubes model (cubic PZT particles), the sphere model (spherical PZT particles), and the parallel and series models. None of the models provided a close fit to the experimental data.

Banno (1985) proposed a "modified cubes model," which took into account the anisotropic distribution of cubes in  $x$ ,  $y$ , and  $z$  directions. The unit cell of this model is shown in Figure 9. The following formulas can be derived for a uniaxially anisotropic case (i.e.,  $l = m = 1, n \neq 1$ ):

$$\epsilon_{33}^* = [a^2(a + (1-a)n)^{2.1}\epsilon_{33}^2\epsilon_{33}]/[a^2\epsilon_{33} + (1-a)n^1\epsilon_{33}] + [1 - a^2(a + (1-a)n)^2\epsilon_{33}] \quad (4)$$

$$d_{33}^* = {}^1d_{33} [a^3(a + (1-a)n)]/[a + (1-a)n({}^1\epsilon_{33}/{}^2\epsilon_{33})]/[(1-a)n/(a + (1-a)n) + a^3] \quad (5)$$

$$d_{31}^* = {}^1d_{31}[a^2(a + (1-a)n)]/[a + (1-a)n({}^1\epsilon_{33}/{}^2\epsilon_{33})].a/[1-a(a + (1-a)n)^{1/2} + a^3] \quad (6)$$

The volume fraction of phase 1 is given by

$${}^1V = a^3/(a + (1-a)n) \quad (7)$$

The case  $n = 1$  corresponds to the cubes model, and a general case  $0 < n < 1$  corresponds to a configuration more dense along the  $z$  direction. Figure 10 shows the experimentally determined permittivity and piezoelectric  $d_h^*$  ( $= d_{33}^* + 2d_{31}^*$ ) coefficient for PbTiO<sub>3</sub>-chloroprene rubber composites, with the theoretical curves (Banno and Tsunooka, 1987. When the volume fraction of PbTiO<sub>3</sub> ( ${}^1V$ ) is small,  $n$  seems to be less than 1 (that is, the rubber thickness around a PbTiO<sub>3</sub> ceramic cube is thinner along the  $z$  direction and thicker along the  $x$  and  $y$  directions) and by increasing the volume fraction,  $n$  approaches 1 (that is, the rubber thickness becomes equal in all three dimensions). This configuration change may be caused by the method of fabrication, which typically involves rolling and calendering.

#### 5.19.4.4 Advanced PZT-Polymer Composites

3-3 composites were first fabricated by the replamine method. A negative replica of a natural coral structure with 3-3 connectivity was made of wax. Then, a positive replica of the negative structure was prepared by introducing a PZT slurry into the porous network of the negative template, drying, burning out the wax, and finally sintering the PZT ceramic (Skinner *et al.*, 1978). In order to make highly porous PZT skeletons, the BURPS (BURned-out Plastic Spheres) method was proposed (Shrout *et al.*, 1979), where PZT powders and plastic spheres are mixed in a binder solution, and the mixture is sintered. Miyashita *et al.* (1980) reported an alternative method that involves piling up thin PZT rods in a three-dimensionally connected array.

3-1 and 3-2 composites can be fabricated by drilling holes in a PZT block, and back-filling with epoxy. In addition to this drilling method, an extrusion method has also been used to fabricate a PZT honeycomb. The 3-1 and 3-2 composites show large  $d_h$  and  $g_h$  values (Safari *et al.*, 1982). As shown in Figure 11, there are

12 Smith W. A.  
sx0125

sx0130

sx0135

8 L. A. Pauer,

sx0140  
F008

sx0145  
2 BannoH.

sx0150

F010

3 BannoH.

11 SkinnerD. P.

10 ShroutT. R.

6 MiyashitaM.

sx0160

9 SafariA.

F011

two types of electrode configurations commonly applied to these composites: parallel [P] and series [S]. In general, S types exhibit larger  $d_h$  and  $g_h$  values than P types.

$$(1 - k^2/2)^{1/T_0} = \exp(-t/\tau) \quad (9)$$

or

$$\tau = -T_0 \ln(1 - k^2/2) \quad (10)$$

In conclusion, the higher the  $k$  value, the quicker the vibration suppression.

Being brittle and hard, ceramics are difficult to assemble directly into a mechanical system. Hence, flexible composites can be useful in practice. When a composite of polymer, piezoceramic powder, and carbon black is fabricated (Figure 12), the electrical conductivity of the composite is greatly changed by the addition of small amounts of carbon black (Suzuki *et al.*, 1991). Figure 13 illustrates the fabrication process. By properly selecting the electrical conductivity of the composite, the ceramic powder effectively forms a series circuit with the carbon black, so that the vibrational energy is dissipated. The conductivity changes by more than 10 orders of magnitude around a certain carbon fraction called the percolation threshold, where the carbon powder link start to be generated. This eliminates the use of external resistors.

Figure 14 shows the relation between the damping time constant and the volume percentage of carbon black in the PLZT-PVDF and PZT-PVDF composites. A volume percentage of about 7% carbon black exhibited the minimum damping time constant and therefore the most rapid vibrational damping. Note that the PLZT with a higher electromechanical coupling  $k$  shows a larger dip (more effective) in the damping time constant curve.

### 5.19.5 PZT COMPOSITE DAMPERS

Another intriguing application of PZT composites is a passive mechanical damper. Consider a piezoelectric material attached to an object whose vibration is to be damped. When vibration is transmitted to the piezoelectric material, the vibrational energy is converted into electrical energy by the piezoelectric effect, and an a.c. voltage is generated. If the piezoelectric material is in an open- or short-circuit condition, the generated electrical energy changes back into vibrational energy without loss. The repetition of this process provides continuous vibration. If a proper resistor is connected, however, the energy converted into electricity is consumed in joule heating of the resistor, and the amount of energy converted back into mechanical energy is reduced, so that the vibration can be rapidly damped. Taking the series resistance as  $R$ , the capacitance of the piezoelectric material as  $C$ , the vibration frequency as  $f$ , damping takes place most rapidly when the series resistor is selected in such a manner that the *impedance matching* condition,  $R = 1/2\pi fC$ , is satisfied (Uchino and Ishii, 1988). Using this technique, in collaboration with ACX Company, K2 developed ski blades with PZT patches to suppress unnecessary vibration during sliding (ACX Company Catalog).

The electric energy  $U_E$  generated can be expressed by using the electromechanical coupling factor  $k$  and the mechanical energy  $U_M$ .

$$U_E = U_M \times k^2 \quad (8)$$

The piezoelectric damper transforms electrical energy into heat energy when a resistor is connected, and the transforming efficiency of the damper can be raised to a level of up to 50%. Accordingly, the vibration energy is decreased at a rate of  $(1 - k^2/2)$  times for a vibration cycle, since  $k^2/2$  multiplied by the amount of mechanical vibration energy is dissipated as heat energy. As the square of the amplitude is equivalent to the amount of vibrational energy, the amplitude decreases at a rate of  $(1 - k^2/2)^{1/2}$  times with every vibration cycle. If the resonance period is taken to be  $T_0$ , the number of vibrations for  $t$  seconds is  $2t/T_0$ . Consequently, the amplitude in  $t$  seconds is  $(1 - k^2/2)^{t/T_0}$ . Thus, the damping in the amplitude of vibration in  $t$  seconds can be expressed as follows:

### 5.19.6 REFERENCES

- ACX Company Catalogue: Passive Damping Ski Damper, QA3 1
- H. Banno, in 'Proceedings of the 6th International Meeting on Ferroelectricity, IMF-6', Kobe and 1985, *Jpn. J. Appl. Phys.*, 1985, 24(Suppl. 24-2), 445. 2
- H. Banno and T. Tsunooka, in 'Ceramic Data Book 87', Industrial Product Technology Society, 1987, p. 328. QA4 3
- K. A. Klicker, J. V. Biggers and R. E. Newnham, *J. Am. Ceram. Soc.*, 1981, 64, 5. Chiyoda-ku, Tokyo, JAPAN (Concord, MA) 8
- Materials Systems Inc. Catalog, 1994. QA3 6
- M. Miyashita *et al.*, *Ferroelectrics*, 1980, 27, 397. 7
- R. E. Newnham *et al.*, *Mater. Res. Bull.*, 1978, 13, 525. 7
- L. A. Pauer, IEEE International Convention Record, 1973, 1-5. (Piscataway, NJ) QA5 8
- A. Safari, R. E. Newnham, L. E. Cross and W. A. Schulze, *Ferroelectrics*, 1982, 41, 197. 9
- T. R. Shrout, W. A. Schulze and J. V. Biggers, *Mater. Res. Bull.*, 1979, 14, 1553. 10
- D. P. Skinner, R. E. Newnham and L. E. Cross, *Mater. Res. Bull.*, 1978, 13, 599. 11
- W. A. Smith, in 'Proceedings of the IEEE Ultrasonic Symposium 89', 1989, p. 755. QA5 12
- Y. Suzuki, K. Uchino, H. Gouda, M. Sumita, R. E. 13

(Piscataway, NJ) 10

ex0165

ex0170

ex0175

15 UchinoK.

1 ACX Company

ex0180

ex0185

ex0190

F012

13 SuzukiY.  
F013  
ex0195ex0200  
F014

5 (Lanthanum-doped PZT)

6

(Cambridge, MA)

QA3

2

QA4

3

QA3

6

7

8

QA5

9

10

11

12

13

Newnham and A. R. Ramachandran, *J. Ceram. Soc. Jpn., Int. Edn.*, 1991, **99**, 1096.

863.

14

K. Uchino, *Solid State Phys.*, 1986, **21**, 27.

15

K. Uchino and T. Ishii, *J. Ceram. Soc. Jpn.*, 1988, **96**,

K. Uchino, S. Nomura and R. E. Newnham, *Sensor Technology*, 1982, **2**, 81.

16

**Table 1** Comparison of the piezoelectric response of PZT-polymer composites, with the single-phase materials PVDF and PZT.

Connectivity	Material	Density $\rho$ ( $10^3 \text{ kg m}^{-3}$ )	Elastic constant $c_{33}$ (GPa)	Dielectric constant $\epsilon_3$ (GPa)	Piezoelectric constants		
					$d_{33}$ ( $10^{-12} \text{ C N}^{-1}$ )	$g_{33}$ ( $10^{-3} \text{ m V N}^{-1}$ )	$g_h$ ( $10^{-3} \text{ m V N}^{-1}$ )
	PZT(501A) single phase	7.9	81	2000	400	20	3
3-1	PZT-Epoxy	3.0	19	400	300	75	40
3-3	PZT-Silicone rubber (Replica type)	3.3	3	40	110	280	80
	PZT-Silicone rubber (Ladder type)	4.5	19	400	250	60	
3-0	PZT-PVDF	5.5	2.6	120	90	85	
	PZT-Rubber	6.2	0.08	73	52	140	30
	PZT-Chloroprene rubber		40			90	
	Extended PVDF	1.8	3	13	20	160	80

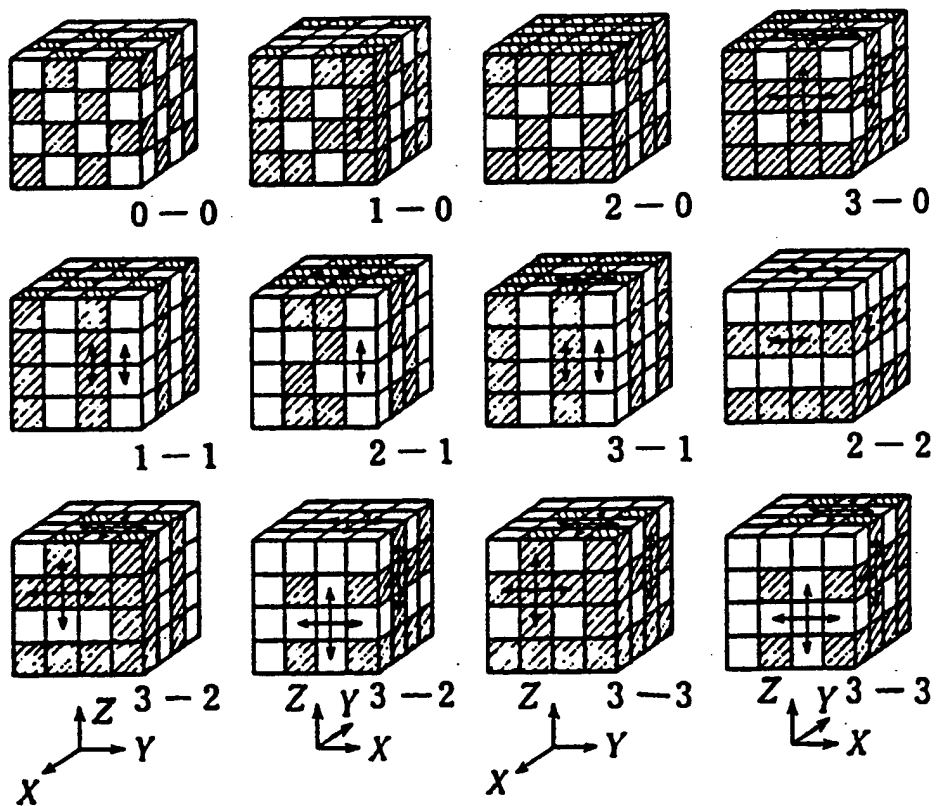
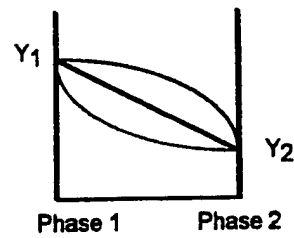


Figure 1 Classification of two-phase composites with respect to connectivity (after Newnham *et al.*, <7> 1978).

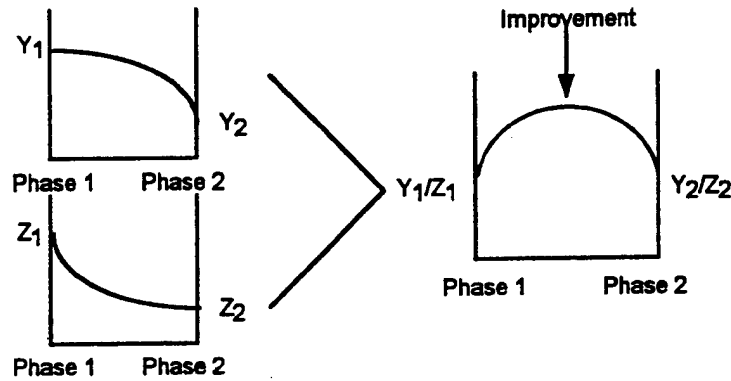
## (a) Sum Effect

Phase 1 :  $X \rightarrow Y_1$   
 Phase 2 :  $X \rightarrow Y_2$  ]  $X \rightarrow Y^*$



## (b) Combination Effect

Phase 1 :  $X \rightarrow Y_1/Z_1$   
 Phase 2 :  $X \rightarrow Y_2/Z_2$  ]  $X \rightarrow (Y/Z)^*$



## (c) Product Effect

Phase 1 :  $X \rightarrow Y$   
 Phase 2 :  $Y \rightarrow Z$  ]  $X \rightarrow Z$  New Function

Figure 2 Composite effects: sum, combination, and product effect.

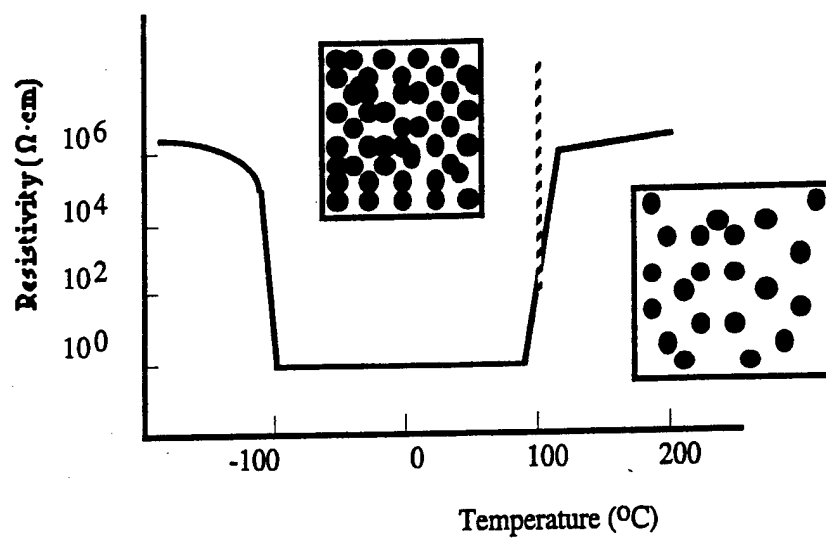
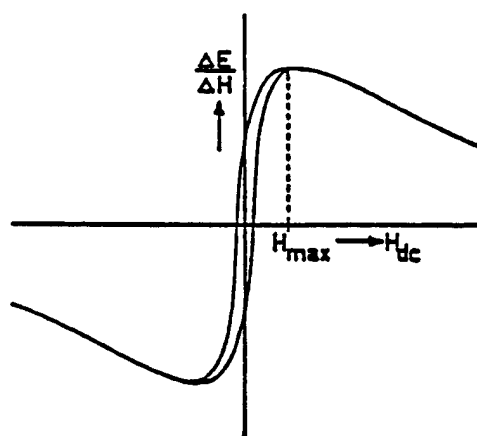


Figure 3 NTC-PTC effect observed in a  $\text{V}_2\text{O}_5$ -epoxy composite (after Uchino, <14> 1986).



Figure 4 Micrograph of a transverse section of a unidirectionally solidified rod of mixture of magnetostrictive  $\text{CoFe}_2\text{O}_4$  and piezoelectric  $\text{BaTiO}_3$ , with an excess of  $\text{TiO}_2$  (1.5 wt.%) (after Uchino, <14> 1986). <QA:6>



**Figure 5** Magnetic field dependence of the magnetoelectric effect in a  $\text{CoFe}_2\text{O}_4\text{-BaTiO}_3$  composite (arbitrary unit measured at room temperature).

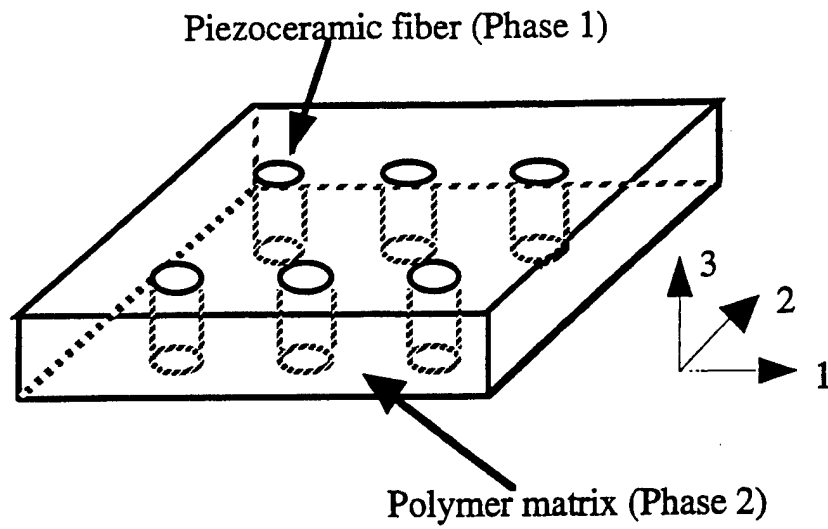


Figure 6 A 1-3 composite of PZT rods and polymer. The top and bottom planes are rigid electrodes.

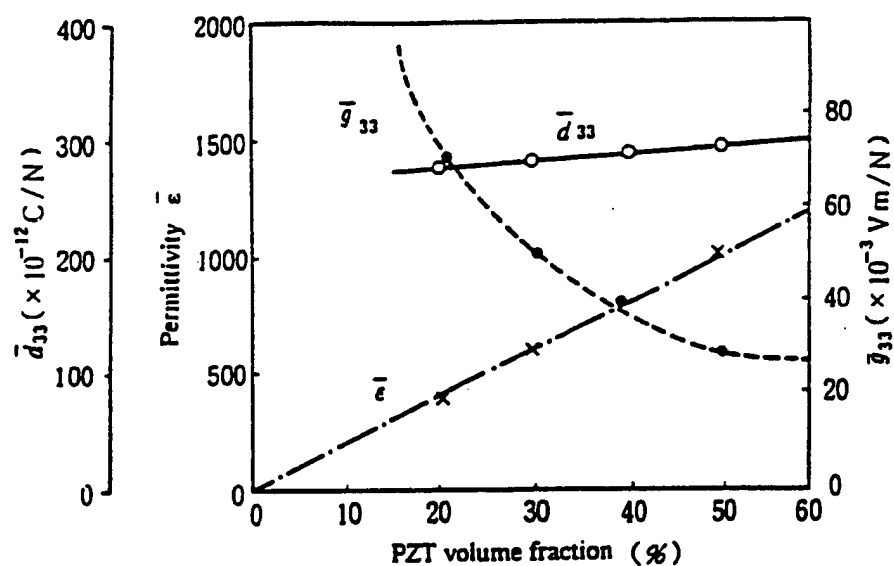


Figure 7 Volume fraction dependence of the permittivity  $\epsilon$  and the piezoelectric constants  $d_{33}$  and  $g_{33}$  in a 1-3 PZT-polymer composite.

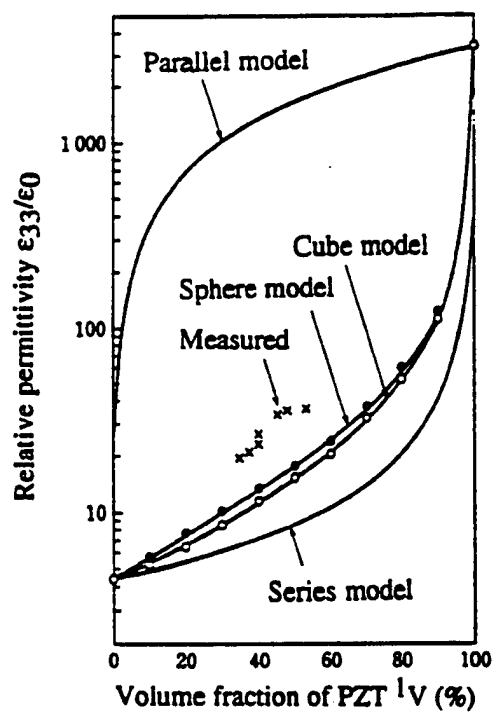
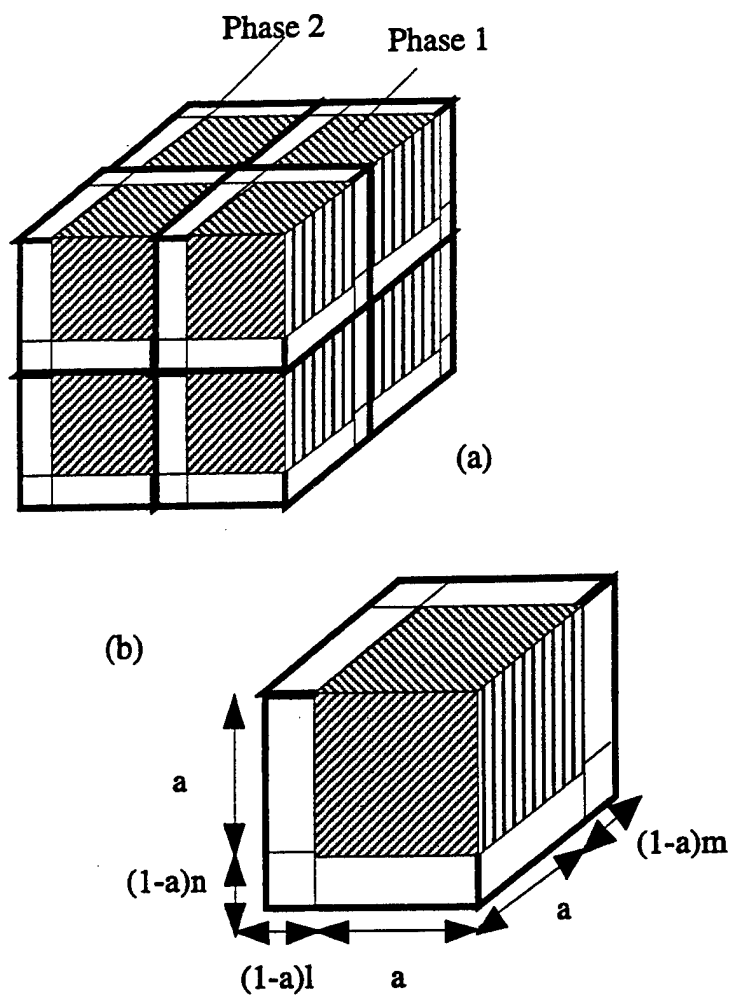


Figure 8 Relative permittivity plotted as a function of volume fraction of PZT in PZT powder-polyurethane rubber composites. Comparisons were made for the cube model, sphere model, parallel and series models.



**Figure 9** Unit cell configuration for a 0-3 composite according to Banno's modified cubes model.

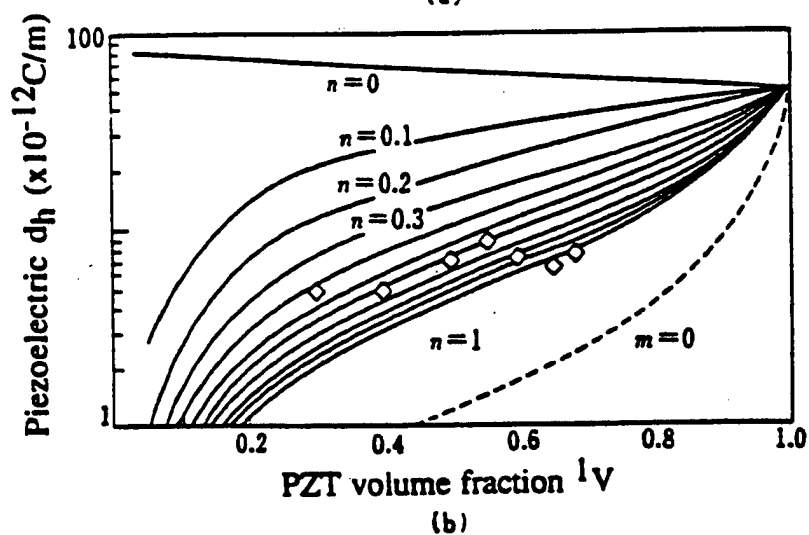
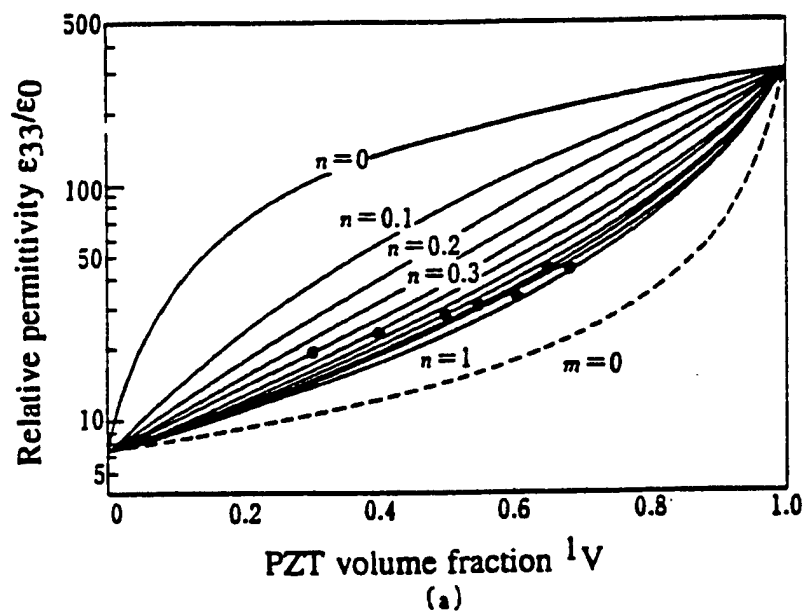


Figure 10 Experimental values of the permittivity (a) and the piezoelectric  $d_h^* (= d_{33}^* + 2d_{31}^*)$  coefficient (b) for  $\text{PbTiO}_3$ -chloroprene rubber 0-3 composites, shown with theoretical curves based on the modified cubes model.

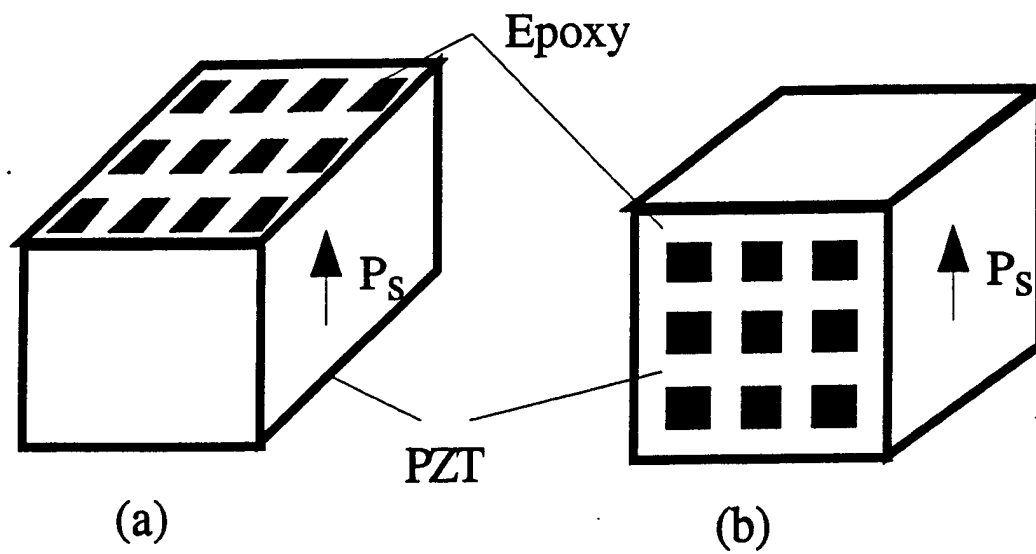


Figure 11 3-1 composites with (a) parallel and (b) series electrode configurations.

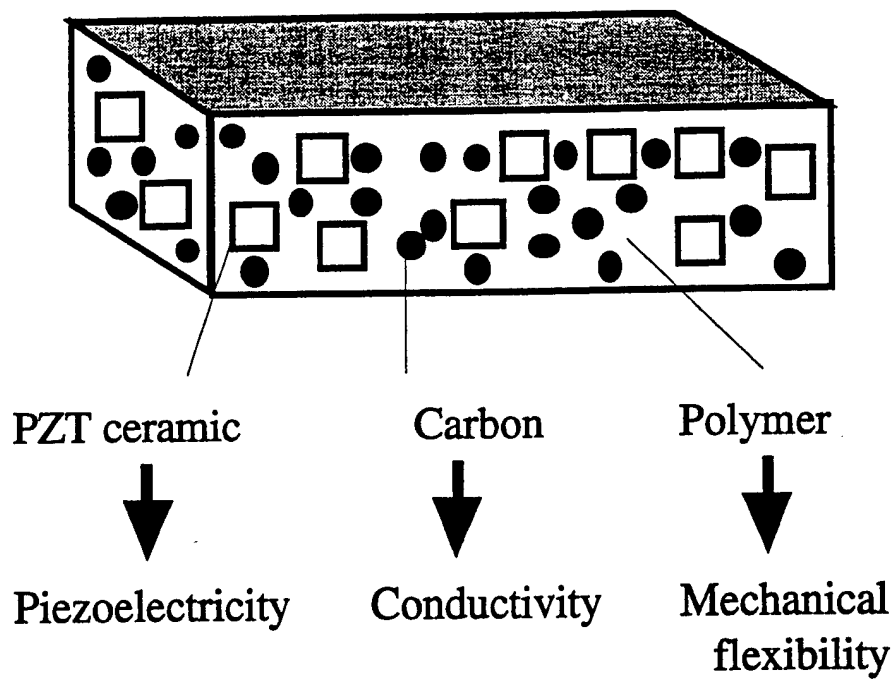


Figure 12 Piezoceramic-polymer-carbon black composite for vibration damping.

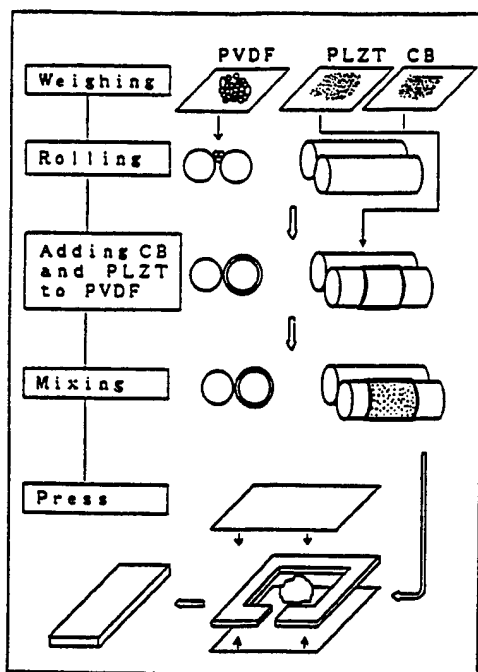
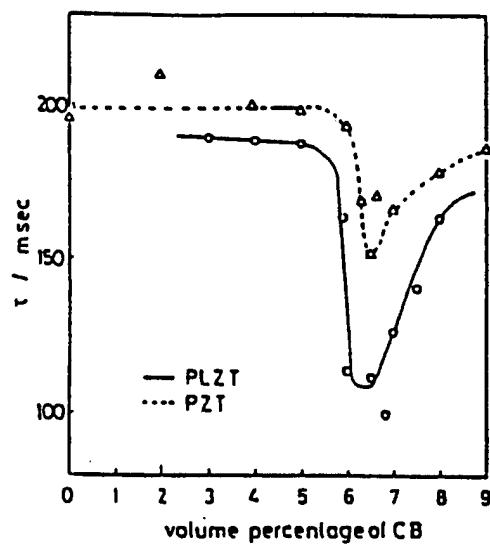


Figure 13 Fabrication process of carbon black containing PLZT-PVDF composites.



**Figure 14** Damping time constant vs. volume percentage of carbon black in the PLZT-PVDF composite. The minimum time constant (quickest damping) is obtained at the percolation threshold.

# **APPENDIX 5**

## 5.20

# Smart Composite Materials Systems

A. KELLY

*University of Cambridge, UK*

R. DAVIDSON

*AEA Technology, Harwell, UK*

and

K. UCHINO

*Pennsylvania State University, University Park, PA, , USA*

5.20.1 INTRODUCTION	1
5.20.2 SENSOR SYSTEMS	2
5.20.3 ACTUATION MECHANISMS	2
5.20.3.1 Shape Memory Alloys	2
5.20.3.2 Piezoelectric Actuators	3
5.20.3.3 Electrostrictive Materials	3
5.20.3.4 Magnetostrictive Materials	4
5.20.3.5 Electrorheological and Magnetorheological Fluids	4
5.20.4 CONTROL SYSTEMS	4
5.20.5 APPLICATION OF SMART MATERIALS	4
5.20.6 REFERENCES	5

### 5.20.1 INTRODUCTION

"Smart materials" (also described as intelligent, sense-able, multifunctional, or adaptive materials) can be thought of as material systems which manifest their own functions intelligently depending on sensed environmental changes. They are modeled on biological systems with:

(i) sensors acting as a nervous system (right-hand full circle in Figure 1),

(ii) actuators acting like muscles (left-hand full circle in Figure 1), and

(iii) real-time processors acting as a brain to control the system (lowest full circle in Figure 1).

The different classes of structures relating to the technology are given in Figure 1. Of particular interest are the following:

(i) *Type I: passive/sensory structures*, which possess a structurally integrated microsensor system for determining the state of the structure and possibly the environment in which it is operating;

(ii) *Type II: reactive smart structures*, which

have a nervous system and an actuator control loop to effect a change in some aspects (stiffness, shape, position, orientation, or velocity); and

(iii) *Type III*: intelligent structures, which are capable of adaptive learning.

## 5.20.2 SENSOR SYSTEMS

It is possible to embed sensors into composite components during manufacture to allow internal interrogation of the material. Sensors can be based on acoustic waveguide wires, piezoelectric, or optical fibers. Fiber-optic based sensors offer the greatest scope at present. They are compatible with the fabrication process and are capable of withstanding strains of the same magnitude as the composite itself. The dielectric nature of the material is maintained while the optical fibers provide their own signal paths for sensing the interior of the composite. They offer the prospect of continuously monitoring the composite structure at all stages of its life through fabrication, test qualification, and service. The successful development of a passive smart structure is reliant upon devising and adapting appropriate fiber-optic sensors, sensing techniques, and multiplexing techniques; and upon the establishment of appropriate fabrication schemes to include the embedded sensors. Fiber-optic sensors rely on the interaction of a physical parameter in the vicinity of a fiber to produce modulation of the transmitted signal. This may take the form of modulation of either amplitude, phase, polarization, or mode interactions. Optical fiber sensors can be designed to detect a whole range of physical parameters including temperature, strain, pressure, electric fields, and magnetic fields. Distributed and quasidistributed measurements have been demonstrated using optical time domain reflectometry (OTDR) techniques by monitoring reflected signals. In sensor applications the system must demodulate the fiber sensor signal and relate the demodulated output to the physical parameters under investigation. The basic optical sensor types for use in composites are described in Chapter 5.28, this volume.

Piezoelectric materials may also be used as sensors. Their use as sensors is described in Chapter 5.25, this volume, paying particular attention to sensors which are themselves composites, consisting of a piezoelectric materials, often a ceramic, e.g., lead zirconate titanate (PZT), incorporated into say a rubber. The composite overcomes the difficulty of the brittleness of the ceramic. The lower density of the rubber also improves acoustic impedance

matching.

Metal-ceramic composite sensors are also used by incorporating PZT into a metal. Tressler and Uchino deal with these in Chapter 5.25, this volume and also with the general characteristics of a piezoelectric sensor.

## 5.20.3 ACTUATION MECHANISMS

To produce controlled or reactive smart structures, actuators are necessary. These can be either retrofitted onto any material by surface bonding or embedded within a composite material. The ideal actuator does not yet exist. A range of candidate systems is being studied, because industrial and military interest in reactive smart structures is high. The main systems under investigation are described in Article Ref Chapters 5.XX-5.XX.

### 5.20.3.1 Shape Memory Alloys

Shape memory alloy (SMA) based on NiTi (53-57 wt.% Ni), Nitinol, when plastically deformed in the low-temperature martensitic phase, can be restored to its original shape or configuration by heating above a characteristic temperature. Plastic strains of 8% can be completely recovered by heat transformation from the deformed martensitic phase to the austenitic phase. However, for cyclic applications a level of <2% is recommended. If the material is restrained from regaining its memory shape, high stresses of up to 700 MPa can be induced. This compares with a yield strength of the martensitic phase of 80 MPa. On transformation to the austenitic form the Young's modulus increases by a factor of four and the yield strength by a factor of 10. SMAs have the ability of changing material properties almost reversibly. SMAs used as embedded actuators take the form of 200-400  $\mu$ m plastically elongated wires constrained from recovering their normal memorized length during fabrication. The plastically deformed fibers become an integrated part of the composite material structure. When the fibers are resistively heated, they are restrained from recovering to their memorized length by the composite and generate a uniformly distributed shear load along the entire length of the fiber. If the fibers are offset from the neutral axis the structure will deform in a predictable manner.

Chapter 5.22, this volume by Roytburd, Slutsker, and Wuttig deals with SMAs and (in analogy with piezoelectrics) points out how an SMA composite may be superior to a mono-

xx0040

Vol Ed: x-ref.  
OK?

xx0045

???: x-ref. OK?

QA1

xx0050

xx0055

xx0060

Vol Ed: x-ref.  
OK?

xx0020

xx0025

xx0030

Vol Ed: x-ref.  
OK?  
xx0035

Vol Ed: x-ref.  
OK?

lithic material and will also, in this case introduce new effects.

SMA systems have been used to control vibrations in large flexible composite structures. An alternative method of use is to place the SMA fibers in or on the structure in such a way that when actuated there are no resulting large deformations but instead the structure is placed in a residual state of strain, and the modal response of the structure is changed. Using such techniques, the ability to change the effective stiffness, natural frequencies, and mode shapes of composite plates has been demonstrated. SMAs are high-force, high-stroke, low-frequency actuators, not suitable for damping high-frequency vibrations since cooling is governed by conduction and radiation loss. All of these effects are dealt with in Chapter 5.22, this volume.

Vol Ed: x-ref.  
OK?

xx0065

### 5.20.3.2 Piezoelectric Actuators

When stress is applied to piezoelectric materials they develop polarization whose magnitude is proportional to the applied stress (Nye, 1985). This is a consequence of the direct piezoelectric effect, and the constant of proportionality  $d_{ijk}$  (a third-rank tensor) defines the piezoelectric moduli. When an electric field is applied, the dimensions of a piezoelectric material change slightly as a result of the converse piezoelectric effect. The same  $d$ -tensor relates the resultant strain to the electric field. Materials in film form can be bonded externally or embedded internally into composite structures to act as actuators. The crystalline subdomains in the films are first aligned (poled) by the application of a large coercive field of  $\sim 2 \text{ kV mm}^{-1}$  across their thickness. This causes the piezoelectric to grow in the field direction and shrink laterally. The domains remain stable at temperatures less than the Curie temperature. Subsequent application of a field in the poling direction also causes growth in that direction and generates longitudinal extension and transverse contraction strains. Application of reverse field causes a shrinkage in thickness until a negative coercive field level is reached, after which the poling reverses and the thickness expands again. Piezoelectrics are available in polycrystalline ceramic or polymer single crystal form, and the properties of several systems are given in Table 1. The effectiveness of the piezoelectric in the bending of a substrate beam is given by:

6 Nye J. F.

xx0070

T001

$$\text{Effectiveness} = E_{\text{max}} d/31 \{6/[6 + (E_b t_b/E_c t_c)]\}$$

where  $E_b$  and  $E_c$  are the elastic moduli of the beam and the piezoelectric ceramic, respectively, and  $t_b$  and  $t_c$  are the respective thicknesses.

The effectiveness data in Table 1 are obtained assuming  $t_b/t_c = 10$  and  $E_b = 70 \text{ GPa}$ . If the voltage available is limited then the effectiveness per field becomes important and ceramics are much more efficient than polymers. PZT piezoelectric ceramics are solid solutions of lead zirconate and lead titanate in a perovskite structure, with the ratio determining the phase transition boundaries and resulting properties. For embedding applications the actuator thickness must either be less than the ply thickness or plies must be cut to accommodate the sensor; also the Curie temperature must be higher than the processing temperature of the composite. It is clear that ceramics offer a wider operating temperature range and higher effectiveness per field than polymeric poly(vinylidene fluoride) (PVDF)-based films. The piezoelectric actuators also have the potential to act as dynamic strain sensors (as we have noted) since a dynamic load applied to the piezoelectric results in an electric charge which may be monitored. Hence, if the voltages generated are sufficiently high to be monitored and if the loads generated can be made large enough to cause displacements, piezoelectrics may act as both actuator and sensor.

xx0075

xx0080

Piezoelectric composites are described in Chapter 5.19, this volume. Here, as with SMA the use of a composite increases the range of possible property combinations. Optimizing the properties of a composite specifically for transducer applications is dealt with by Safari, Jadian, and Akdogan in Chapter 4.11, this volume. In all piezoelectric composites the continuity throughout the piece (?) of the two phases must be considered. The patterns of connectivity discovered and enunciated by Newnham (1986) are essential to understanding and using piezoelectric composites. All three chapters, 5.XX, 5.XX, and 5.XX use these concepts.

xx0085

Vol Ed: x-ref.  
OK?

Vol Ed: x-ref.  
OK?

5 Newnham R. E.  
QA2

### 5.20.3.3 Electrostrictive Materials

xx0090

One disadvantage of piezoelectric actuators is that the material response is both nonlinear and hysteretic, particularly at high a.c. voltages where electrostrictive contributions are significant. All materials are electrostrictive but few have a large coefficient. The electrostrictive properties result from a quadratic dependence of permittivity with electric field, in contrast to the true converse piezoelectric effect caused by

a linear dependence. Pure electrostrictive materials typified by lead magnesium niobate (PMN) show no piezoelectric effect; they are nonhysteretic but are nonlinear. The perovskite type crystal expands longitudinally and shrinks laterally on the application of an electric field. The strain effect is quadratic in voltage and decreases with temperature. The low hysteresis makes the actuator suitable for open-loop shape control. No poling is necessary but for vibration damping a bias voltage is required. Little work is available in the open literature on the use of electrostrictors in smart composites.

sx0095

#### 5.20.3.4 Magnetostrictive Materials

Recent advances in the production of Terfenol-D magnetostrictive alloys of terbium, dysprosium, and iron ( $\sim \text{Tb}_{0.3}\text{Dy}_{0.7}\text{Fe}_{1.9}$ ) offer high-strain ( $\sim 0.1\%$ ) and high-energy-density ( $\sim 20 \text{ kJ m}^{-3}$ ) materials, suitable for magnetic actuation of structures (Hathaway and Clark, 1993). Work relating to active space struts using this material is ongoing. Composites based on these materials are described in Article Ref Chapter 5.21, this volume.

4 Hathaway K. B.

???: x-ref. OK?

#### 5.20.3.5 Electrorheological and Magnetorheological Fluids

Some initial proof-of-concept work has been carried out to demonstrate that dynamically tunable smart composites can be produced using electrorheological fluid-based actuators (Winslow, 1947, 1949; Gandhi and Thompson, 1989). These fluids undergo significant instantaneous reversible changes in materials characteristics, most notably in their bulk viscosity, when subjected to electrostatic potentials. A variety of electrorheological (ER) fluids exist based on micrometer-sized hydrophilic particles suspended in a suitable hydrophobic carrier liquid. It is this type of fluid which has the most potential to modify the damping properties of composite materials. On the application of electric fields across the thickness of an ER fluid layer, the rheological characteristics are dramatically changed and the inherent molecular structure of the ER fluid creates solid-like characteristics as the particles in the suspension orient themselves in relatively regular chain-like columns. These columnar structures increase the energy dissipation characteristics of the suspension and cause a redistribution of mass in the suspension. On removal of the electrostatic field the particles return to a state of random orientation with fluid viscosities.

8 W. M. Winslow  
9 Winslow W. M.  
2 Gandhi M. V.

sx0110

The natural frequencies can be actively changed throughout the frequency spectrum by controlling the voltage imposed on the fluid domains and in this way resonances can be avoided. The problems with this technology relate to the means of adequately incorporating and confining the ER fluid into composites and being able to activate the fluid with high voltages. The fluid adds weight and does not enhance the structural performance of the composite.

sx0115

Somewhat similar effects are obtained by applying magnetic fields to magnetorheological fluids (Rabinow, 1948). Electrorheological and magnetorheological fluids are dealt with comprehensively in Chapter 5.23, this volume by Jolly and Carlson. Such materials are by definition two phase and hence are composites.

7 Rabinow J.

Vol Ed: x-ref.  
OK?

Relative properties of a variety of actuator materials are given in Table 2.

T002

#### 5.20.4 CONTROL SYSTEMS

sx0120

For type III structures, Figure 1, containing both embedded sensors and actuators, signals from the sensors will be received and interpreted by microprocessor-based controllers which will communicate with and trigger the actuators to alter the material response. Parallel processing using neural networks is receiving much attention for use in real-time controllers. The concepts are inspired by biological systems where a large number of nerve cells that individually function rather slowly and imperfectly learn collectively to perform complex tasks. Neural networks are made of layers of relatively simple nonlinear elements and are capable of adaptive learning and rapid processing and decision making. If and when sensors are developed to give strain and temperature information from critical areas of say an aircraft, then if the structural integrity is to be assessed, at the very least some comparative reference values will be necessary. Probably the best way to get a baseline would be to fly the aircraft and learn. Neural networks with self-adaptive processing are potentially well suited to handle such high volumes of data (Grossman and Thursby, 1989). Although neural network-based controllers do not yet exist in suitable forms to act as the "brain" in a fully intelligent material, it is an area where rapid advances are expected.

sx0125

3 Grossman B. G.

#### 5.20.5 APPLICATION OF SMART MATERIALS

sx0130

Composite materials with embedded sensors

and actuators will only gain acceptance if the structural integrity of the composite is not significantly reduced by the presence of the inclusions, which are presently significantly larger in diameter than the carbon, aramid, or glass-reinforcing fibers which are typically  $\sim 8\text{--}10\text{ }\mu\text{m}$  in diameter. When optical-fiber sensors, typically  $100\text{--}300\text{ }\mu\text{m}$  in diameter, are embedded in composite laminates there is an inevitable disruption of the reinforcing fibers in the vicinity of the fiber optic. The nature of this disruption is dependent on both the diameter of the embedded sensor and the relative orientation of the fiber optic with respect to neighboring reinforcing plies. For example, sensing fibers lying parallel to the local reinforcement cause a minimum disruption provided the diameter is less than half the ply thickness. Reinforcing fibers laying orthogonally to the sensors are locally deformed, creating a resin-rich region around the sensor. In order to be acceptable the fiber sensor must:

(i) produce a minimum perturbation in the distribution of reinforcing fibers;

(ii) not significantly reduce the mechanical properties of the composite;

(iii) not suffer from excessive attenuation or damage from the embedding process, such that the sensing technique cannot be applied; and

(iv) include a suitable means to input and output the laser light into the system, through pigtails or connectors. Such systems must be robust and compatible with the fabrication process.

These effects are dealt with in Chapter 5.30, this volume by Davidson and Roberts.

Many factors remain to be fully investigated before sensing technology can be applied in real structures (e.g., naval, aircraft, or space structures).

(i) Materials considerations include how the fiber affects the composite strength characteristics, and whether the sensors are resistant to the composite environment.

(ii) Fabrication aspects include determining the best deposition of the sensors in the composite; how to retain accurate positioning during manufacture; how to monitor and automate the fabrication process and deal with connec-

tion problems; and how to make cost-effective structures and make repairs.

(iii) Sensing/multiplexing techniques include the kind of sensor to use; how to differentiate important variables; how to make distributed measurements to the required resolutions; and how to design reliable connect schemes and miniaturized systems.

(iv) System aspects include how the strain sensing relates to scheduled maintenance; which necessary developments in artificial intelligence techniques are required to interpret the data; and how redundancy can be built into the system.

Many of the above factors are equally important as far as actuation is concerned. The actuator developments are at a less advanced stage than for sensors. Nonetheless there is considerable success being achieved. Furuya in Chapter 5.29, this volume deals with a number of suggestions for actuator integration and in Chapter 5.38, this volume, Baz shows how active shape control may be realized using shape memory and electrical effects.

## ACKNOWLEDGMENTS

This chapter is based on an article by Davidson (1994).

I DavidsonR.

## 5.20.6 REFERENCES

- 1 R. Davidson, in 'Concise Encyclopedia of Composite Materials', ed. A. Kelly, Pergamon, Oxford, 1994, pp. 259-265.
- 2 M. V. Gandhi and B. S. Thompson, *Proc. Soc. Photo-Opt. Instrum. Eng.*, 1989, 1170, 294-304.
- 3 B. G. Grossman and M. H. Thursby, *Proc. Soc. Photo-Opt. Instrum. Eng.*, 1989, 1170, 316-325.
- 4 K. B. Hathaway and A. E. Clark, *MRS Bull.*, 1993, (1993), 34-41.
- 5 R. E. Newnham, *Ann. Res. Mater. Sci.*, 1986, 16, 47-68.
- 6 J. F. Nye, 'Physical Properties of Crystals', Clarendon Press, Oxford, UK, 1985.
- 7 J. Rabinow, *National Bureau of Standards. Technical News Bulletin*, 1948, 32(4), 54-60.
- 8 W. M. Winslow, *US Pat.* + 2 417 850 (1947).
- 9 W. M. Winslow, *J. Appl. Phys.*, 1949, 20, 1137-1140.

xx0140

xx0145

Vol Ed: x-ref.  
OK?

Vol Ed: x-ref.  
OK?

Vol Ed: x-ref.  
OK?

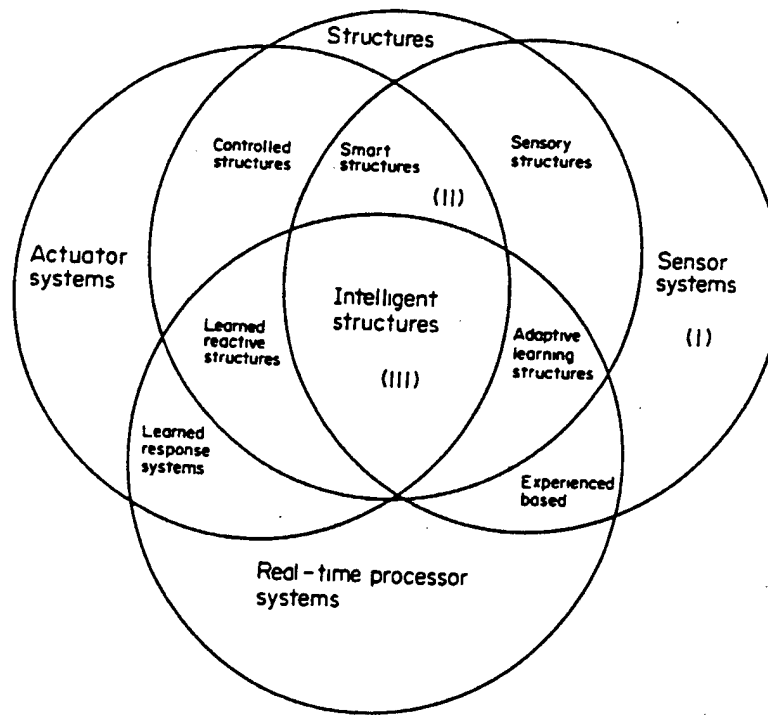


Figure 1 Smart materials classification

Table 1 Comparison of piezoelectric materials..

Material	PZT	PZT	PVDF
	G1195	G1278	
Curie temperature ( $^{\circ}\text{C}$ )	360	190	100
Electric field $E_{\text{max}}$ ( $\text{kV m}^{-1}$ )	600	600	40000
$d_{31}^a$ ( $\text{pm V}^{-1}$ )	190	250	23
Modulus (GPa)	63	60	2
Effectiveness ( $\times 10^{-6}$ )	40	51	16
Effectiveness/field ( $\text{pm V}^{-1}$ )	67	85	0.39

<sup>a</sup>  $d_{33} \approx 2.5d_{31}$  (units:  $\text{m V}^{-1} = \text{C N}^{-1}$ ).

Table 2 A comparison of actuator materials.

	<i>PZT G1195</i>	<i>PVDF</i>	<i>PMN-BA</i>	<i>Terfanol</i>	<i>Nitinol</i>
Actuation mechanism	Piezoceramic	Piezofilm	Electrostrictor	Magnetostrictor	SMA
$\epsilon_{\max}^a$ ( $\mu$ strain)	1300	230 d.c. 690 d.c.	1300	> 2000	80000 d.c.
$E$ (GPa)	63	2	121	48	30(m), 89(a) <sup>c</sup>
$T_{\max}^b$ ( $^{\circ}\text{C}$ )	360	80–120	> 500	380	~ 50
Linearity	good	good	fair	fair	poor
Hysteresis (%)	10	> 10	< 1	2	5
Temperature sensitivity ( $\% ^{\circ}\text{C}^{-1}$ )	0.05	0.8	0.9	high	
Bandwidth	high	high	high	moderate	low

<sup>a</sup> Maximum strain capability. <sup>b</sup> m = martensitic phase, a = austenitic phase. <sup>c</sup> Maximum operating temperature.

# **APPENDIX 6**

# Possible piezoelectric composites based on the flexoelectric effect

J. Fousek <sup>a,1</sup>, L.E. Cross <sup>a,\*</sup>, D.B. Litvin <sup>b</sup>

<sup>a</sup> Materials Research Laboratory, The Pennsylvania State University, University Park, PA 16802, USA

<sup>b</sup> Department of Physics, The Pennsylvania State University, Berks Campus, Reading, PA 19610, USA

Received 30 November 1998; accepted 2 December 1998

## Abstract

Current piezoelectric composite materials contain two or more phases out of which at least one reveals piezoelectric properties in itself. We show that this is in fact not a necessary condition. The mechanism of the linear stress-polarization response averaged over a composite sample can be also based on flexoelectric properties of one or more constituents. Proper shaping of the composite constituents is required, such that the system as a whole acquires a symmetry allowing for nonzero piezoelectric coefficients even if none of the components is piezoelectric. Externally applied stress is transformed, due to proper geometry of the constituents with different elastic properties, into a strongly nonhomogeneous distribution of induced strain. Flexoelectric properties which are, by symmetry, allowed in all materials, transform the strain gradient into polarization. The proposed piezoelectric composite falls into the category of composites with product properties since it involves different assets of the phases (elastic, flexoelectric and dielectric) and the interaction between the phases, determining the inhomogeneous distribution of stress, is essential. © 1999 Elsevier Science B.V. All rights reserved.

PACS: 77.34 – s; 77.90 – k

Keywords: Piezoelectric materials; Composites; Flexoelectric effect

## 1. Introduction

Composites are multiple-phase solids which combine materials of different chemical composition and macroscopic properties with the aim to produce samples with the desired average response. Figures of merit of the final composite can be tuned by choosing component phases with the right properties and coupling them in an optimum manner. Newnham et al. [1] offered a classification of composites based on

three criteria. The most important aspects are the macroscopic properties of the constituents, e.g., their response to electric, magnetic and elastic fields. This determines the final assets of the composite. The second, connectivity, indicates the way in which each phase connects to itself. It is essential for the magnitude and symmetry of the composite's response. The third is scale, which determines the response of the composite when wavelengths of propagating waves become comparable with the characteristic dimensions of any of the constituents.

Many composites have been considered in connection with their piezoelectric properties [1,2]. To discuss or model the piezoelectric response of a composite, it was generally assumed that at least one

\* Corresponding author. Tel.: +1-814-865-1181; Fax: +1-814-863-7846

<sup>1</sup> On leave from the Department of Physics, University of Technology, CZ-46117 Liberec, Czech Republic.

of the components was piezoelectric. In this paper we reconsider this assumption.

## 2. Discussion

For a system to be piezoelectric, it has to fulfill certain symmetry criteria. If it has a crystalline structure, the material must, by symmetry, belong to one of 20 crystal classes. The remaining 12 classes do not show piezoelectric properties; these are the 11 centrosymmetric classes and the class 432 in which piezoelectricity is forbidden by the combined symmetry elements.

In Nye's widely used overview of the equilibrium properties of the 32 crystal classes [3], the properties of an isotropic medium are also included. The symmetry of an isotropic medium is primarily characterized by the presence of arbitrarily oriented symmetry axes of infinite order. Depending on whether its symmetry elements do or do not include arbitrarily oriented mirror planes, the isotropic medium represents one of the Curie symmetry groups (limiting groups), namely,  $\infty$ ,  $\infty/m$  or  $\infty 2$ , respectively. In

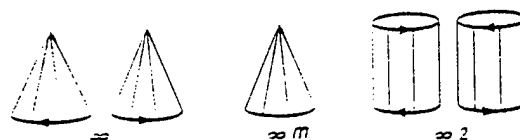


Fig. 1. Characteristic forms representing symmetry of the Curie groups which allow for piezoelectricity [4].

both these groups no nonzero piezoelectric coefficients are possible.

In addition to these two groups, however, we may consider systems representing the remaining Curie groups, namely  $\infty$ ,  $\infty/m$ ,  $\infty 2$ ,  $\infty m$  and  $\infty/mm$ . Out of these,  $\infty/m$  and  $\infty/mm$  do not allow for the existence of nonzero components of a third-rank polar tensor  $d_{ijk}$  of symmetry  $V [V^+]$ , i.e., of the piezoelectric tensor. In the remaining groups nonzero components are possible, as shown in Table 1. It is useful to illustrate symmetry properties of these point groups by characteristic forms [4]; these are shown in Fig. 1. We realize that systems revealing the symmetries  $\infty$  or  $\infty 2$  can exist in two forms, left- and right-handed.

Thus, for instance, a composite with connectivity 0-3, in which the phase '0' is represented by cone-shaped particles whose  $\infty$ -axes are parallel to each other but which are randomly distributed in the phase '3', has the symmetry  $\infty m$ . Next we can imagine that the cones are subject to helical deformations so that spiral-shaped particles result. This lowers the symmetry to  $\infty$ . The system can exist in two forms, right- or left-handed. The third piezoelectric Curie group can be visualized starting again with a composite of connectivity 0-3 in which the phase '0' is represented by cylinders; its symmetry is nonpiezoelectric  $\infty/mm$ . If now all cylinders are subject to a helical deformation, the symmetry is reduced to  $\infty 2$ , which again can exist in two forms differing in handedness. Fig. 2 shows such composites schematically. These particular models are based on the 0-3 connectivity but similar considerations can be made for other connectivities as well.

It thus appears easily possible to manufacture composites whose symmetry properties allow for the existence of piezoelectric tensor although they consist of components which by themselves need not be made of piezoelectric materials.

Table 1  
Matrices of  $d_{ijk}$  in Curie groups which are piezoelectric

$\infty$						
0	0	0	$d_{14}$	$d_{15}$	0	0
0	0	0	$d_{15}$	$-d_{14}$	0	0
$d_{31}$	$d_{31}$	$d_{33}$	0	0	0	0
$\infty 2$						
0	0	0	$d_{14}$	0	0	0
0	0	0	0	$-d_{14}$	0	0
0	0	0	0	0	0	0
$\infty m$						
0	0	0	0	$d_{15}$	0	0
0	0	0	$d_{15}$	0	0	0
$d_{31}$	$d_{31}$	$d_{33}$	0	0	0	0

In all groups the  $\infty$  axis is taken as  $x_3$ ; the axes  $x_1$ ,  $x_2$  are perpendicular to  $x_3$  and to each other, otherwise their orientation is arbitrary.

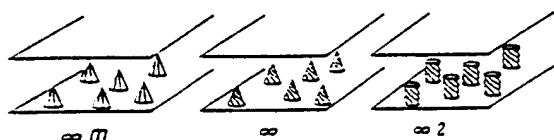


Fig. 2. Simple models of 0–3 composites allowing for piezoelectricity. There is an infinite number of shapes of the 0-constituent that could be tested for a maximum response of flexoelectric polarization.

A long time ago, Shubnikov et al. introduced the concept of *piezoelectric textures*; see Ref. [5] and the first chapter of Ref. [6]. This notion denotes systems composed of crystallites which show piezoelectric properties, some crystal axes of which are chaotically oriented in a given way, leading to specific averaging of properties characterizing the piezoelectric effect. In the subsequent parts of Ref. [6], two specific kinds of materials are discussed as examples. Plate-like samples containing crystallites of Rochelle salt separated by amorphous layers (chapter 2 by Konstantinova and Sil'vestrova) could indeed be considered a 0–3 composite. Polarized ceramic samples of barium titanate (chapter 3 by Zheludev), on the other hand, whose symmetry is  $\infty m$ , represent a piezoelectric texture by Shubnikov's definition but could only be included into the family of composites if the grain boundaries had an appreciable volume.

In both these cases basic components are piezoelectric by themselves (point symmetries 2 for Rochelle salt and  $4mm$  for  $\text{BaTiO}_3$ ). On the other hand, in the general symmetry approach this is not a specific requirement. As shown above, the possibility of a piezoelectric response in a 0–3 composite is assured, from the point of view of symmetry, already by shaping the particles of zero connectivity. We thus have to look for alternative mechanisms which would lead to formation of an average polarization proportional to an applied stress for a 0–3 composite made of nonpiezoelectric materials, with properly shaped particles.

For several decades, the effect of inducing polarization by imposing spatially nonuniform strain was repeatedly discussed in the literature. Originally discovered experimentally in centrosymmetric (and therefore nonpiezoelectric) liquid crystals, it was

termed the flexoelectric effect and described by the equation

$$P_i = \mu_{ijkl} \frac{\partial \varepsilon_{ij}}{\partial x_k} \quad (1)$$

from which it is obvious that the tensor  $\mu$  has the general symmetry  $[V^2] V^2$ , i.e.,  $\mu_{ijkl} = \mu_{jikl}$  is the only requirement imposed by symmetry. A tensor of this symmetry has nonzero components in all crystal classes. The first attempt to observe the flexoelectric effect in a solid crystal of point symmetry  $4/m$ , namely  $\text{CaWO}_4$  was made by Zheludev et al. [7]. As shown by Tagantsev [8], the static effect includes a bulk and a surface contribution. The bulk part is due to the fact that the crystal lattice which has been nonhomogeneously deformed in accordance with the laws of the theory of elasticity is not in equilibrium from the point of view of displacements in the unit cell. The displacements that are necessary to reach true equilibrium give rise to a dipole moment of the cell, i.e., to polarization. In addition, the deformation of the surface of a finite sample, whose electrical neutrality in the original state was achieved by compensating free charges, leads to a surface contribution which can be expected to be of the same order of magnitude as the bulk part of the effect. The simplest estimates [8] for a common insulator indicate that both contributions to the value of  $\mu$  are of the order of the ratio of the electron charge to the lattice constant.

We now have in mind a 0–3 composite made of nonpiezoelectric constituents, in which the 0-elements are shaped and oriented in such a way that the overall symmetry is one of the Curie groups  $\infty$ ,  $\infty m$  and  $\infty 2$ . As an example, consider a plate-like sample of composite of symmetry  $\infty m$  in which the orientation of the 0-constituents is such that the  $\infty$  axis is perpendicular to the major plane. Since the tensor  $\mu_{ijkl}$  has nonzero components even for continuous groups  $\infty$  and  $\infty m$  [4], one can imagine that both the 0-component and 3-components are made of isotropic materials. Their shaping is such that when a load  $\sigma_{33\text{appl}}$  is applied, the spatial distribution of stress will be nonhomogeneous, leading to gradients of strain in both constituents. To be concrete, we can imagine that a plate-like sample of thickness  $d$  is

divided into a regular system of cubes of linear size  $d_0$ , each cube containing one particle of the component with zero connectivity and only this component is assumed to have nonzero flexoelectric properties. The dipole moment of each 0-particle within one cube will be given by

$$P_{3\text{flex}} = \int_{(d_0^3)} \mu_{3ijk} \frac{\partial \varepsilon_{ij}(\mathbf{r})}{\partial x_k} d\mathbf{r} \quad (2)$$

where the strain gradient will be determined by a factor  $a_{ijk}$  which reflects the shape of the components 0 of the composite and depends on elastic compliances of both constituents:

$$\frac{\partial \varepsilon_{ij}(\mathbf{r})}{\partial x_k} = a_{ijk}(\mathbf{r}) \sigma_{33\text{appl}} \quad (3)$$

The induced charge density on the electrode of the plate will be

$$Q = \frac{P_{3\text{flex}}}{d_0^3} \quad (4)$$

so that the effective polarization of the sample  $P_3 = Q$  will be given by

$$P_3 = d_{33\text{flex}} \sigma_{33\text{appl}} \quad (5)$$

where

$$d_{33\text{flex}} = \frac{1}{d_0^3} \int_{(d_0^3)} a_{ijk}(\mathbf{r}) \mu_{3ij3} d\mathbf{r} \quad (6)$$

A piezoelectric composite based on flexoelectricity will be useful if a reasonably high value of  $d_{33\text{flex}}$  could be reached, e.g., 100 pC/N. It follows from the preceding formulae that the latter can be influenced by a proper tuning of several independent factors: selecting materials with high values of those components of  $\mu_{ijkl}$  which are involved in a particular geometry of the constituents, choosing a high density of the constituents 0, but also by achieving large factors  $a_{ijk}$  which depend on the shape of the 0-components and on the elastic tensors of both 0 and 3 constituents.

Newnham [2] classified properties of composite materials into three groups: sum properties (the composite property coefficient depends on the corresponding coefficients of its constituent phases), combination properties (the composite property coefficient depends on two or more corresponding coefficients

of its constituent phases) and product properties. In the latter case the composite property coefficient involves different properties of the constituent phases with interactions between them. It appears that piezoelectric composites based on flexoelectricity fall into this last category and the effect might be referred to as a 'shape-controlled product property'; indeed the combined effect involves different properties of the constituent phases (elastic, flexoelectric and dielectric) and the interaction between the phases is essential: here it is the nonhomogeneous distribution of stress which depends primarily on the shapes of constituents and on their elastic tensors. The following sequence of phenomena describes the combined effect: homogeneous applied stress  $\rightarrow$  inhomogeneous stress in the 0-constituents  $\rightarrow$  polarization in the 0-constituents due to flexoelectric effect  $\rightarrow$  nonhomogeneous distribution of polarization in the sample depending also on spatial distribution of permittivity  $\rightarrow$  nonhomogeneous surface bound charge  $\rightarrow$  averaged surface bound charge density defining effective polarization. Considering a stress  $\sigma_{zz}$  applied perpendicularly to a plate-like composite sample, we have the sequence

$$\begin{aligned} \sigma_{zz,\text{appl}} &\rightarrow \text{grad } \sigma_{ij,\text{sample}}(\mathbf{r}) \rightarrow P(\mathbf{r}) \rightarrow q(x,y)_{\text{surf}} \\ &\rightarrow \bar{q}_{\text{surf}} \propto P_{z,\text{surf}} \propto \sigma_{zz,\text{appl}} \end{aligned}$$

At this stage very few data on the tensor  $\mu_{ijkl}$  in solids seem to be available. A fairly strong flexoelectric response was reported for crystals of  $\text{Cd}_2\text{WO}_4$  [7]. Marvan and Havránek [9] studied the flexoelectric effect in elastomers of isotropic symmetry. Samples in the form of truncated pyramids were deformed by axial pressure along the axis 3. Then for constant volume of the sample the only active coefficient is  $\mu_{3333}$  which was estimated to be of the order  $10^{-11}$  to  $10^{-10}$  C/m. Experiments with 0–3 composites in which the 0-constituent or both components of the composite would be a polymer might be worthwhile.

We may also note that such composite samples might be interesting to investigate in which one of the constituents is piezoelectric: due to flexoelectricity, its induced dipole moment could be considerably enhanced by proper shaping to optimize the nonhomogeneous distribution of strain.

### Acknowledgements

J. Fousek: This work was supported in part through grants VS 96006 and 202/96/0722 of the Ministry of Education and of the Grant Agency of the Czech Republic, respectively. D.B. Litvin: This work was supported in part by the National Science Foundation through grant No. DMR-9722799.

### References

- [1] R.E. Newnham, D.P. Skinner, L.E. Cross, *Mater. Res. Bull.* 13 (1978) 525.
- [2] R.E. Newnham, *Jpn. J. Appl. Phys.* 25 (1986) 9, Suppl. 25-1.
- [3] J.F. Nye, *Physical Properties of Crystals*, Clarendon Press, Oxford, 1993.
- [4] Yu.I. Sirotn, M.P. Shaskolskaya, *Fundamentals of Crystal Physics*, Mir Publishers, Moscow, 1982.
- [5] A.V. Shubnikov, *Piezoelectric Textures* (in Russian), Publishing House of the Academy of Sciences of USSR, Moscow–Leningrad, 1946.
- [6] A.V. Shubnikov, I.S. Zheludev, V.P. Konstantinova, I.M. Sil'vestrova, *Investigation of Piezoelectric Textures* (in Russian), Publishing House of the Academy of Sciences of USSR, Moscow–Leningrad, 1955.
- [7] I.S. Zheludev, Yu.S. Likhacheva, N.A. Lileeva, *Sov. Phys. Crystallogr.* 14 (1969) 425.
- [8] A.K. Tagantsev, *Sov. Phys. JETP* 61 (1985) 1246.
- [9] M. Marvan, A. Havránek, *Progr. Colloid Polym. Sci.* 78 (1988) 33.

# **MATERIALS STUDIES**

***Polycrystal Perovskite Ceramics***

# **APPENDIX 7**

# A monoclinic ferroelectric phase in the $\text{Pb}(\text{Zr}_{1-x}\text{Ti}_x)\text{O}_3$ solid solution

B. Noheda,<sup>a)</sup> D. E. Cox, and G. Shirane

Physics Department, Brookhaven National Laboratory, Upton, New York 11973-5000

J. A. Gonzalo

Dept. Física de Materiales, U.A.M., Cantoblanco, 28049-Madrid, Spain

L. E. Cross and S.-E. Park

Materials Research Laboratory, The Pennsylvania State University, Pennsylvania 16802-4800

(Received 14 December 1998; accepted for publication 8 February 1999)

A previously unreported ferroelectric phase has been discovered in a highly homogeneous sample of  $\text{PbZr}_{0.52}\text{Ti}_{0.48}\text{O}_3$  by high-resolution synchrotron x-ray powder diffraction measurements. At ambient temperature the sample has tetragonal symmetry ( $a_t=4.037\text{ \AA}$ ,  $c_t=4.138\text{ \AA}$ ), and transforms below  $\sim 250\text{ K}$  into a phase which, unexpectedly, has monoclinic symmetry ( $a_m=5.717\text{ \AA}$ ,  $b_m=5.703\text{ \AA}$ ,  $c_m=4.143\text{ \AA}$ ,  $\beta=90.53^\circ$ , at  $20\text{ K}$ ). The intensity data strongly indicate that the polar axis lies in the monoclinic  $ac$  plane close to the pseudocubic  $[111]$  direction, which would be an example of the species  $m3m(12)A2Fm$  predicted on symmetry grounds by Shuvalov.

© 1999 American Institute of Physics. [S0003-6951(99)00714-7]

The solid solution system  $\text{Pb}(\text{Zr}_{1-x}\text{Ti}_x)\text{O}_3$  (PZT) has a complex phase diagram containing a number of materials which exhibit useful ferroelectric and piezoelectric properties. In particular, compositions near the morphotropic phase boundary (MPB) around  $x\approx 0.45\text{--}0.5$  have attracted considerable interest for many years due to their high piezoelectric response. The PZT phase diagram as now accepted, was determined by Jaffe *et al.*<sup>1</sup> (Fig. 1), and nearly four decades of study on the physical and structural properties of PZT have made possible the development of a phenomenological theory to explain the stability of the phases and the properties of PZT over the entire range of the phase diagram.<sup>2</sup> Nevertheless, many questions still remain. It is generally accepted that for ferroelectric compositions with rhombohedral and tetragonal symmetry on the two sides of the MPB the polar axis are  $[111]$  and  $[001]$ , respectively. However, very recently, based on neutron powder diffraction data for several ferroelectric rhombohedral compositions in the range of  $x\approx 0.12\text{--}0.40$ , Corker *et al.*<sup>3</sup> have proposed a model in which random  $\langle 100 \rangle$  Pb displacements are superimposed on those along the  $[111]$  polar axis, which allows a much better structure refinement than achieved with a normal long-range order model incorporating anisotropic temperature factors.

The MPB which separates rhombohedral Zr-rich from tetragonal Ti-rich PZT is nearly vertical along the temperature scale, and many x-ray diffraction studies have been reported over this region.<sup>4-9</sup> This boundary is not well defined since it appears to be associated with a phase coexistence region whose width depends on the compositional homogeneity and on the sample processing conditions.<sup>7-10</sup> Cao and Cross<sup>11</sup> have modeled the width of this region based on the free energy differences between the tetragonal and rhombohedral phases, obtaining an inverse dependence with particle size in a polycrystalline sample.

In the present work we have utilized high-resolution synchrotron x-ray powder techniques to study the structure of a composition close to the MPB ( $x=0.48$ ) as a function of temperature, and we report the observation of a low temperature monoclinic phase in the PZT system.

A PZT composition with  $x=0.48$  was prepared by conventional solid-state reaction techniques using appropriate amounts of reagent-grade powders of lead carbonate, zirconium oxide, and titanium oxide, with chemical purities better than 99%. Pellets were pressed and heated to  $1250^\circ\text{C}$  at a ramp rate of  $10^\circ\text{C/min}$ , and held at this temperature for 2 h. During sintering,  $\text{PbZrO}_3$  was used as a lead source in the crucible to minimize volatilization of lead. The product was found to be a single phase within a detection limit of  $<2\%$  by conventional x-ray techniques.

High-resolution synchrotron x-ray powder diffraction measurements were made at beam line X7A at the Brookhaven National Synchrotron Light Source. An incident beam of wavelength  $0.6896\text{ \AA}$  from a  $\text{Ge}(111)$  double-crystal monochromator was used in combination with a  $\text{Ge}(220)$

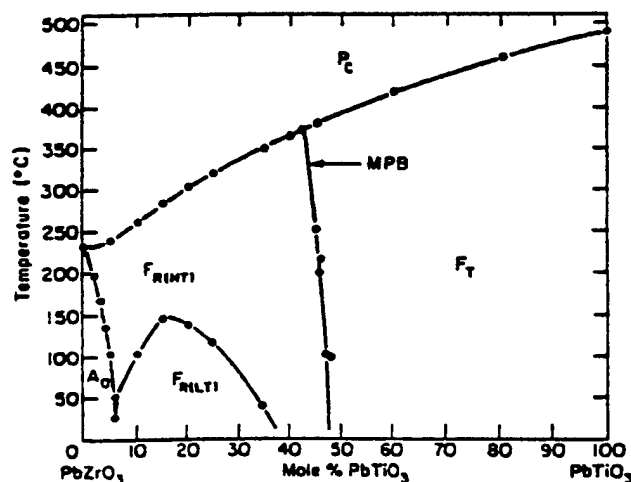


FIG. 1. PZT phase diagram after Jaffe *et al.* (Ref. 1).

<sup>a)</sup>Permanent address: Dept. Física de Materiales, U.A.M., Cantoblanco, 28049-Madrid, Spain. Electronic mail: beatriz.noheda@uam.es

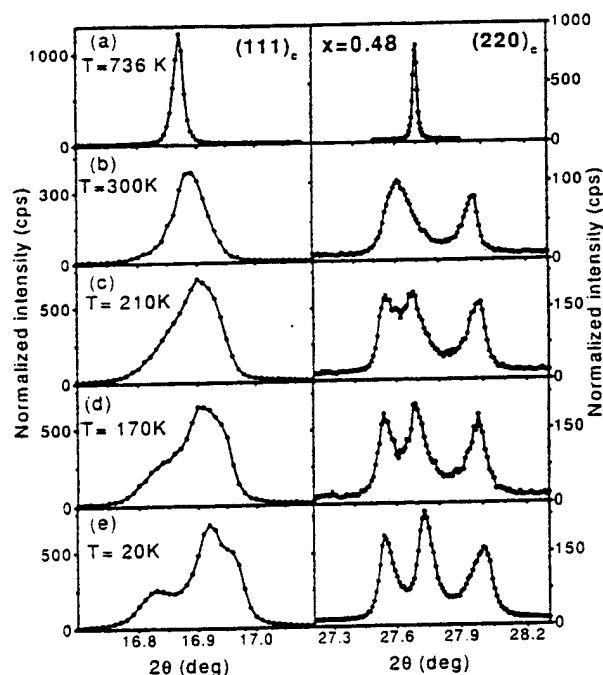


FIG. 2. Evolution of the pseudocubic reflections (111) and (220) for  $x = 0.48$  from  $T = 736$  (a) to 20 K (e).

crystal and scintillation detector in the diffraction path. The resulting instrumental resolution is about  $0.01^\circ$  on the  $2\theta$  scale, an order-of-magnitude better than that of a laboratory instrument. For measurements above room temperature, the pellet was mounted on a BN sample pedestal inside a wire-wound BN tube furnace. The furnace temperature scale was calibrated with a sample of  $\text{CaF}_2$ . The accuracy of the temperature was estimated to be within 10 K, and the temperature stability was  $\sim 2$  K. For measurements below room temperature, the pellet was mounted on a Cu sample holder and loaded in a closed-cycle He cryostat, with an estimated temperature accuracy of 1 K and stability of 0.1 K. Coupled  $\theta$ - $2\theta$  scans were performed over selected angular regions with a  $2\theta$  step interval of  $0.005^\circ$  or  $0.01^\circ$  depending on the peak widths. The sample was rocked  $1^\circ$ - $2^\circ$  during data collection to improve powder averaging. The diffracted intensities were normalized with respect to the incident beam monitor.

The evolution of the (111) and (220) reflections is shown as a function of temperature in Fig. 2. At the highest temperature reached (736 K), the material is cubic and the sharpness of the peaks [full-width at half-maximum (FWHM)  $\sim 0.02^\circ$ ] demonstrates the excellent quality of the sample [Fig. 2(a)]. From a Williamson-Hall plot,<sup>12</sup> we estimate a particle size of  $\sim 0.7 \mu\text{m}$  and a  $\Delta d/d$  of about  $3 \times 10^{-4}$ , corresponding to a compositional inhomogeneity,  $\Delta x$ , better than  $\pm 0.5\%$ .

On cooling, the symmetry changes to tetragonal at  $\sim 660$  K and remains tetragonal down to 300 K. There is no sign of any rhombohedral component as shown by the absence of a Bragg peak at the rhombohedral (200) position. However, some of the tetragonal peaks broaden as the temperature is lowered, especially the (111) and (202) reflections [Fig. 2(b)]. Below room temperature these reflections become distinctly asymmetric, and at 210 K the latter is clearly split into

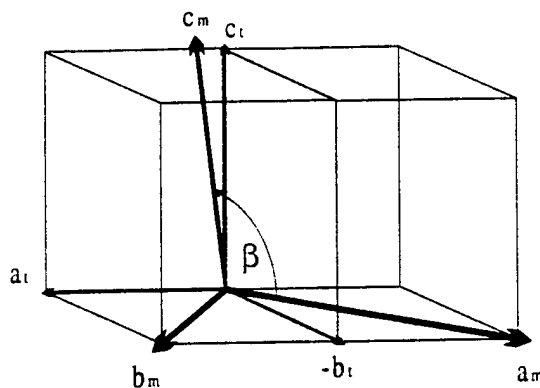


FIG. 3. Tetragonal and monoclinic unit cell representations.

two roughly equal peaks, while the (111) peak has a low angle shoulder [Fig. 2(c)]. As the temperature is lowered further the splitting increases [Fig. 2(d)] until at 20 K the (202) is well resolved into two peaks, and the (111) is seen to consist of a central stronger peak with weaker shoulders on both low-and-high-angle sides [Fig. 2(e)]. The positions and intensity ratios of the peaks are very well described by a monoclinic cell in which  $a_m$  and  $b_m$  lie along the tetragonal  $[\bar{1}\bar{1}0]$  and  $[1\bar{1}0]$  directions ( $a_m \approx b_m \approx a_t/\sqrt{2}$ ), and  $c_m$  is close to the  $[001]$  axis ( $c_m \approx c_t$ ), as illustrated in Fig. 3. The monoclinic cell has  $b_m$  as the unique axis, and the angle between  $a_m$  and  $c_m$  is  $\sim 90.5^\circ$  at 20 K.

The lattice parameters are plotted in Fig. 4 over the entire temperature range. At the low-temperature phase transition,  $a_m$  is slightly elongated with respect to tetragonal  $a_t/\sqrt{2}$ , whereas  $b_m \approx a_t/\sqrt{2}$  continues to decrease as the temperature is lowered, and  $c_m \approx c_t$  appears to reach a broad maximum around the transition.

A direct phase transition from a tetragonal to monoclinic phase is rather uncommon, and the existence of the latter is likely to be a direct consequence of the proximity of the MPB. Consequently, one might expect the monoclinic phase to exist over a relatively narrow composition region. However, because of the asymmetrical peak broadening, which

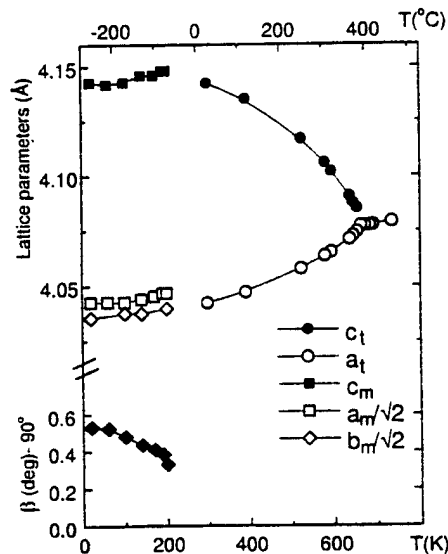


FIG. 4. Lattice parameters of PZT with a composition  $x = 0.48$  as a function of temperature.

occurs between 300 and 210 K, we cannot altogether rule out the possibility of an orthorhombic phase in this region, although we feel this is unlikely.

In the tetragonal region of PZT the space group is  $P4mm$ , with the polar axis along  $[001]$ , while in the rhombohedral region, with space group  $R3m$ , the polar axis is along the pseudocubic  $[111]$ . The most plausible space group for the new monoclinic phase is  $Cm$ , which is a subgroup of  $P4mm$  and  $R3m$  and allows the polar axis to lie anywhere between the  $[001]$  and the  $[111]$  axes. A preliminary check of the peak intensities indicates that the cation displacements lie close to the monoclinic  $[201]$  direction, i.e., close to the rhombohedral  $[111]$  axis. If this is the case, monoclinic PZT would be the first example of the ferroelectric species with  $P_x^2 = P_y^2 \neq P_z^2, P_x^2, P_y^2, P_z^2 \neq 0, m3m(12)A2Fm$  predicted from symmetry by Shuvalov.<sup>13</sup> A more detailed investigation of the structure is currently in progress, and the extent of the monoclinic region will be investigated with additional samples containing slightly different amounts of Ti.

We thank E. Sawaguchi for his efforts trying to locate his 1953 sample for this work, and Evagelia Moshopoulou

for her helpful comments. Support by NATO (R.C.G.0037), Spanish CICyT (PB96-0037), and U.S. Department of Energy, Division of Materials Science (Contract No. DE-AC02-98CH10886) is also acknowledged.

- <sup>1</sup>B. Jaffe, W. R. Cook, and H. Jaffe, *Piezoelectric Ceramics* (Academic, London, 1971), p. 136.
- <sup>2</sup>M. J. Haun, E. Furman, S. J. Jang, and L. E. Cross, *Ferroelectrics* **99**, 13 (1989).
- <sup>3</sup>D. L. Corker, A. M. Glazer, R. W. Whatmore, A. Stallard, and F. Fauth, *J. Phys.: Condens. Matter* **10**, 6251 (1998).
- <sup>4</sup>G. Shirane and K. Suzuki, *J. Phys. Soc. Jpn.* **7**, 333 (1952).
- <sup>5</sup>E. Sawaguchi, *J. Phys. Soc. Jpn.* **8**, 615 (1953).
- <sup>6</sup>P. Ari-Gur and L. Benguigui, *Solid State Commun.* **15**, 1077 (1974).
- <sup>7</sup>K. Kakewaga, O. Matsunaga, T. Kato, and Y. Sasaki, *J. Am. Ceram. Soc.* **78**, 1071 (1995).
- <sup>8</sup>J. C. Fernandes, D. A. Hall, M. R. Cockburn, and G. N. Greaves, *Nucl. Instrum. Methods Phys. Res. B* **97**, 137 (1995).
- <sup>9</sup>M. Hammer, C. Montry, A. Endriss, and Michel J. Hoffmann, *J. Am. Ceram. Soc.* **81**, 721 (1998).
- <sup>10</sup>A. P. Wilkinson, J. Xu, S. Pattanaik, and J. L. Billinge, *Chem. Mater.* **10**, 3611 (1998).
- <sup>11</sup>W. Cao and L. E. Cross, *Phys. Rev. B* **47**, 4825 (1993).
- <sup>12</sup>G. K. Williamson and W. H. Hall, *Acta Metall.* **1**, 22 (1953).
- <sup>13</sup>L. A. Shuvalov, *J. Phys. Soc. Jpn.* **28**, 38 (1970).

# **APPENDIX 8**

# The monoclinic phase in PZT: new light on morphotropic phase boundaries

B. Noheda<sup>1</sup>, J. A. Gonzalo

Universidad Autonoma de Madrid, Cantoblanco 28049, Spain

R. Guo, S.-E. Park, L.E. Cross

Materials Research Lab., Penn. State University, PA 16802

D.E. Cox, and G. Shirane

Physics department, Brookhaven National Lab., Upton, NY 11973

A summary of the work recently carried out on the morphotropic phase boundary (MPB) of PZT is presented. By means of x-ray powder diffraction on ceramic samples of excellent quality, the MPB has been successfully characterized by changing temperature in a series of closely spaced compositions. As a result, an unexpected monoclinic phase has been found to exist in between the well-known tetragonal and rhombohedral PZT phases. A detailed structural analysis, together with the investigation of the field effect in this region of compositions, have led to an important advance in understanding the mechanisms responsible for the physical properties of PZT as well as other piezoelectric materials with similar morphotropic phase boundaries.

## INTRODUCTION

The morphotropic phase boundary (MPB) of  $\text{PbZr}_{1-x}\text{Ti}_x\text{O}_3$  (PZT) has been finally characterized on extremely homogeneous ceramic samples by high resolution x-ray measurements. The boundary has been found to define the limit between the tetragonal phase and a new PZT phase with monoclinic symmetry. The recent work on this finding is reviewed [1,2,3,4].

The remarkable physical properties of the ferroelectric system  $\text{PbZr}_{1-x}\text{Ti}_x\text{O}_3$  (PZT) for compositions close to  $x=0.47$  have been known for many years. In particular, its high piezoelectric response has made PZT one of the most widely used materials for electromechanical applications. PZT was first studied five decades ago [5,6] and the main structural characteristics of the system were investigated at that time. At high temperatures PZT is cubic with the perovskite structure. When lowering the temperature the material becomes ferroelectric, with the symmetry of the ferroelectric phase being tetragonal ( $F_T$ ) for Ti-rich compositions and rhombohedral ( $F_R$ ) for Zr-rich compositions. Subsequent studies led to the generally accepted phase diagram after Jaffe et al. [7], which covers temperatures above 300 K. Jaffe's phase diagram is represented by open circles in Fig. 1 for  $0.33 \leq x \leq 0.63$ . A complete phenomenological theory was developed for this system that is able to calculate thermal, elastic, dielectric and piezoelectric parameters of ferroelectric single crystal states [8].

The boundary between the tetragonal and the rhom-

bohedral phases, at compositions close to  $x=0.47$ , the so-called morphotropic phase boundary (MPB) [7], is nearly vertical in temperature scale. It has been experimentally observed that the maximum values of the dielectric permittivity, as well as the electromechanical coupling factors and piezoelectric coefficients of PZT at room temperature occur on this phase boundary. However, the maximum value of the remanent polarization is shifted to smaller Ti contents [7].

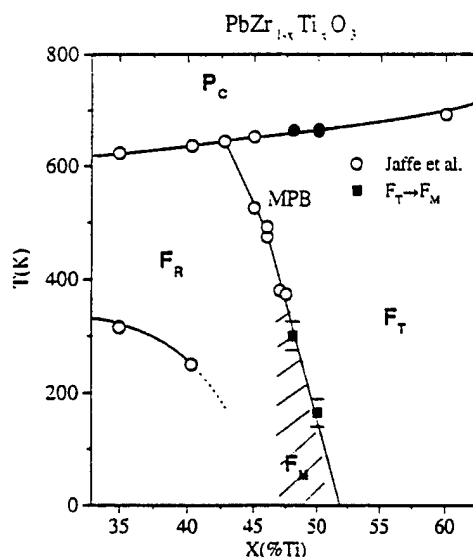


FIG. 1. Preliminary modification of the PZT phase diagram after Noheda et al. [3]. The open symbols represent the PZT phase diagram after Jaffe et al. [7].

The space groups of the tetragonal and rhombohedral phases ( $P4mm$  and  $R3m$ , respectively) are not symmetry-

\*To appear in the proceedings of the Workshop on *Fundamental Physics of Ferroelectrics* held in Aspen, Feb. 2000.

<sup>1</sup>Present address: Physics department, Brookhaven National Lab., Upton, NY 11973.

related, so a first order phase transition is expected at the MPB. However, this has never been observed and, as far as we know, only composition dependence studies are available in the literature. One of the main difficulties in the experimental approach to this problem is the lack of single crystals of PZT. Because of the steepness of the phase boundary, any small compositional inhomogeneity leads to a region of phase coexistence (see e.g. [9,10,11,12]) that conceals the tetragonal-to-rhombohedral phase transition. The width of the coexistence region has been also connected to the particle size [13] and depends on the processing conditions, so a meaningful comparison of available data in this region is often not possible.

On the other hand, the richness of phases in PZT and the simplicity of its unit cell have encouraged important theoretical efforts in recent years. So far, the first-principles studies have been successful in reproducing many of the physical properties of PZT [14,15]. But, in spite of the proven validity, these calculations had not yet accounted for the remarkable increment of the piezoelectric response observed when the material approaches its MPB.

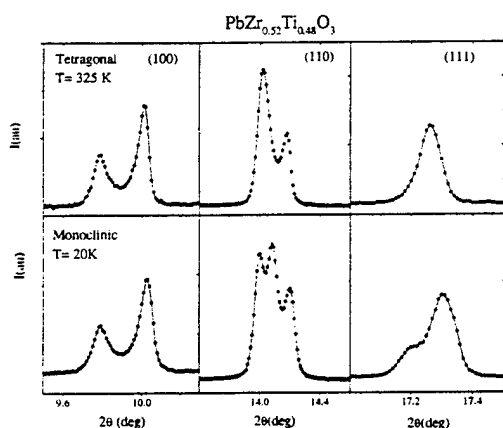


FIG. 2. Three selected peaks, (100), (110) and (111), from the diffraction profiles in the tetragonal (top) and monoclinic (bottom) PZT ( $x=0.48$ ) phases. The diffraction profiles are shown in Noheda et al. [3], Fig.6.

It was accordingly clear that there was something missing in the understanding of PZT, mainly due to experimental difficulties, and we addressed our efforts in this direction. The slight deviation from verticality of the MPB encouraged us to attempt the investigation of a temperature driven  $F_T - F_R$  phase transition knowing that only samples of exceptional quality would allow us to succeed. With this purpose such ceramics were prepared by the Penn. State group. Our collaboration has resulted in the discovery of a new monoclinic phase ( $F_M$ ) in this ferroelectric system [1,2]. The detailed structural analysis of tetragonal [3] and rhombohedral [16] phases

of PZT seemed to indicate that the local structure is different from the average one and that, in both phases, such local structure has monoclinic symmetry. This local structure would be the precursor of the observed monoclinic phase. Diffraction measurements of the effect of the electric field on ceramic samples have confirmed this model [4]. Measurements on PZT samples with  $x=0.48$  and  $x=0.50$  allowed for a modification of the PZT phase diagram as shown in Fig. 1. It should be noted that the MPB defined by Jaffe et al. is still a perfectly valid line that corresponds to the  $F_T - F_M$  phase transition.

## EXPERIMENTAL

PZT samples were prepared by conventional solid-state reaction techniques as described in refs. [1,3] at the MRL, Penn. State University, and samples with  $x=0.50$  were prepared at ICG, CSIC, Spain, as described in ref. [2]. High-resolution synchrotron x-ray powder diffraction measurements were carried out at the X7A diffractometer, at the Brookhaven National Synchrotron Light Source. Two types of experiments were done, as explained in ref. [3]. In the first one, data were collected from a disk in a symmetric flat-plate reflection geometry over selected angular regions as a function of temperature. These measurements demonstrated the high quality of the ceramic samples, whose diffraction peaks in the cubic phase have full-widths at half-maximum of  $0.02^\circ$  for  $x=0.48$ . By means of a Williamson-Hall analysis in the cubic phase, a compositional error of less than  $\Delta x = \pm 0.003$  was estimated [3] for this composition. To perform a detailed structure determination, additional measurements were made for PZT with  $x=0.48$ , at 20 and 325 K, in the monoclinic and tetragonal phases, respectively. In this case, the sample was loaded in a rotating capillary of 0.2 mm diameter to avoid texture and preferred orientation effects [3].

## THE MONOCLINIC PHASE

According to the PZT phase diagram [7], a sample with  $x=0.48$  is tetragonal just below the Curie point and rhombohedral below room temperature. The measurements on the pellets for selected diffraction peaks, with decreasing temperature from the cubic phase, showed the expected tetragonal phase down to  $\sim 300$  K. Below this temperature however new features appeared in the diffractograms, but they were not compatible with either a rhombohedral phase or with a mixture of both phases (tetragonal and rhombohedral), and they clearly corresponded to a monoclinic phase with  $b$  as a unique axis [1]. This can be observed in Figure 2 where selected parts of the diffraction profile are plotted for the monoclinic (20 K) and the tetragonal (325 K) phases.

The cell parameters of PZT ( $x=0.48$ ) are represented in Fig. 3 as a function of temperature. In the tetragonal phase (below  $T_c = 660$  K), the tetragonal strain  $c_t/a_t$ , increases as the temperature decreases. At  $T \approx 300$  K the tetragonal-to-monoclinic ( $F_T - F_M$ ) phase transition takes place and the  $c_t/a_t$  ratio starts decreasing slightly. The microstrain present in the sample during the evolution of the tetragonal phase seems to play a crucial role in the phase transition.  $\Delta d/d$  is obtained from a Williamson-Hall analysis of the diffraction line widths [3] and is shown as a function of temperature at the bottom of the plot. At high temperatures,  $\Delta d/d$  increases as the temperature decreases. At first, the increment is slow and no anomaly is observed at the cubic-to-tetragonal transition. At lower temperatures  $\Delta d/d$  shows a rapid increase that reaches a sharp maximum just at the  $F_T - F_M$  phase transition. For this amount of Zr substituted, the tetragonal phase cannot support the stress in the structure, which is to a large extent released by the onset of the monoclinic phase. Further analysis is being done in order to compare the microstrain exhibited by different compositions with that observed in pure  $\text{PbTiO}_3$ , where the tetragonal phase is stable at very low temperatures.

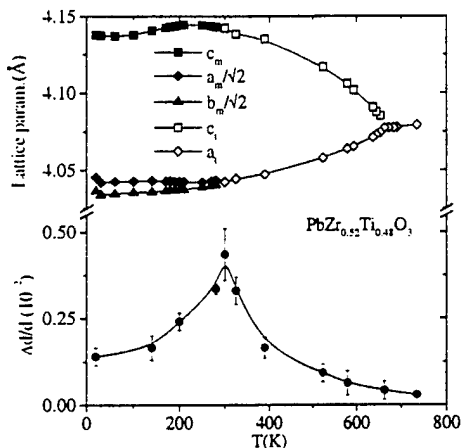


FIG. 3. Cell parameters as a function of temperature in the cubic, tetragonal and monoclinic phases for PZT  $x=0.48$ . The evolution with temperature of  $\Delta d/d$  is shown in the bottom plot. After Noheda et al. [3]

The monoclinic unit cell is doubled with respect to the tetragonal one:  $a_m$  and  $b_m$  are aligned along the  $[1\bar{1}0]$  and  $[11\bar{0}]$  directions, respectively, and  $c_m$  remains approximately equal to the tetragonal  $c_t$  but it is tilted with respect to it in the monoclinic plane, as illustrated in the inset in Fig. 4. Such a unit cell is chosen in order to have a monoclinic angle,  $\beta$ , larger than  $90^\circ$  (according to the usual convention) and  $\beta - 90^\circ$  is then defined as the order parameter of the  $F_T - F_M$  transition. Its temperature evolution is depicted in Fig. 4. The transition seems to be of second order which is allowed in this case, since  $Cm$  is a subgroup of  $P4mm$ . PZT samples with  $x=$

0.50, prepared in a slightly different way [2], showed also a monoclinic phase for temperatures below 200 K. In this case  $a_m$  is approximately equal to  $b_m$  and the monoclinic angle,  $\beta$  was found to be smaller than that observed for  $x=0.48$ . Its evolution with temperature is also plotted in Fig. 4 [2]. A direct comparison of these data for samples from different origins must be regarded with caution. Further work is being carried out in which samples with compositions in the range  $x=0.42-0.51$  processed under the same conditions are studied. However, with the data obtained so far it is already possible to represent a modification of the PZT phase diagram as the one shown in figure 1. It can be observed that the MPB established by Jaffe et al. [7] above room temperature seems to lie exactly along the  $F_T - F_M$  phase boundary.

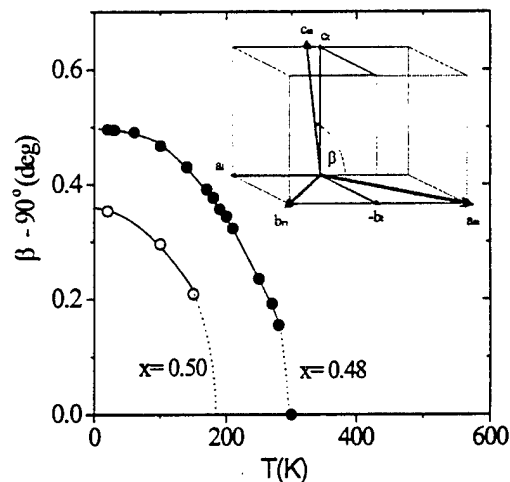


FIG. 4. Temperature evolution of the order parameter of the  $F_T - F_M$  transition for PZT with  $x=0.48$  and  $x=0.50$ . A representation of the monoclinic unit cell is included as an inset. After Noheda et al. [1,2,3].

Contrary to what occurs in the tetragonal and rhombohedral phases, in the monoclinic phase the polar axis is not determined by symmetry and could be along any direction within the monoclinic plane. To determine this direction the atom positions need to be known. A detailed structure investigation by means of a Rietveld profile analysis of the tetragonal and monoclinic phases of PZT ( $x=0.48$ ) has produced interesting results [3]. In the tetragonal phase at 325 K the unit cell has  $a_t = 4.044 \text{ \AA}$  and  $c_t = 4.138 \text{ \AA}$  and the atoms were found to be displaced in the same way as in pure  $\text{PbTiO}_3$ : Pb and Zr/Ti were shifted  $0.48 \text{ \AA}$  and  $0.27 \text{ \AA}$ , respectively, along the polar  $[001]$  axis. Anisotropic temperature factors gave a much better refinement but the resultant thermal ellipsoids were unphysically flattened perpendicularly to the polar direction. This is not a new problem in PZT: Rietveld refinement of the rhombohedral PZT

[17] structure also produced thermal disk-shaped ellipsoids flattened perpendicular to the rhombohedral polar axis [111]. This observed behavior has been previously associated with the existence of certain local ordering different from the long-range order.

The local order has been studied in rhombohedral PZT by means of the Pair Distribution Function [18] and, more recently, by modelling local disordered cation shifts by means of a Rietveld profile refinement [16]. The authors found that by considering three equivalent disordered displacements along the  $\langle 001 \rangle$  directions, superimposed on the rhombohedral cation displacement along [111] (see figure 5) the refinement produced much more reasonable temperature factors.

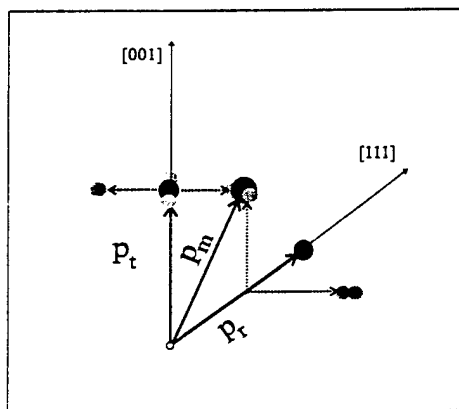


FIG. 5. Schematic view of the cation shifts in the tetragonal ( $p_t$ ), monoclinic ( $p_m$ ) and rhombohedral ( $p_r$ ) unit cells. The solid circles and the arrows represent the cation positions in each one of the three structures. In the tetragonal and rhombohedral cases, the long-range structure is an average of the short-range or local structures (three in the rhombohedral one and four in the tetragonal one) represented by smaller grey circles [3]

In the same way, for tetragonal PZT ( $x=0.48$ ) at 325 K, we can model local disordered sites for the lead atoms perpendicular to the polar axis, that is, we allow Pb to move towards the four sites allowed by symmetry, i.e. at the  $\langle xxz \rangle$  positions [3], which give an average tetragonal  $\langle 00z \rangle$  cation shift (see figure 5). Similar results are obtained if the refinement is carried out modelling local disorder shifts along the  $\langle x0z \rangle$  directions. The refinement gives local shifts of  $0.2 \text{ \AA}$  perpendicular to the polar axis in addition to the common shift of  $0.48 \text{ \AA}$  along the polar axis, which is similar to that of  $\text{PbTiO}_3$ , and gives also physically reasonable isotropic temperature factors.

The structure of the monoclinic phase at 20 K does not present this kind of problems. The refinement is very good considering isotropic temperature factors for all atoms except lead, and the resulting anisotropy for lead is not unreasonable [3]. The refined unit cell was  $a_m = 5.721 \text{ \AA}$ ,  $b_m = 5.708 \text{ \AA}$ ,  $c_m = 4.138 \text{ \AA}$  with

$\beta = 90.496^\circ$ . The results of the refinement [3] have defined the monoclinic polar axis. This lies within the monoclinic plane along a direction between the polar axes of the tetragonal and the rhombohedral phases,  $24^\circ$  away from the former (see figure 5). This value could become slightly different after the oxygen positions are more accurately determined by a neutron study that is underway. This is the first example of a ferroelectric material with  $P_x^2 = P_y^2 \neq P_z^2$ , where  $P_x, P_y$  and  $P_z$  are the Cartesian components of the spontaneous polarization.

Although this result is interesting, the striking fact about it is that the monoclinic shifts exactly corresponds to one of the four locally disordered shifts proposed for the tetragonal phase, as it can be observed in fig. 5. The monoclinic phase appears, as the temperature is lowered, by the condensation of one of the local shifts existing in the tetragonal phase. Most interesting is the fact that the monoclinic displacement also corresponds to one of the three locally disordered shifts proposed by Corker et al. [16] for the rhombohedral phase (see fig. 5), so the condensation of this particular site would also give rise to the observed monoclinic phase.

## FIELD EFFECT

Diffraction experiments with poled ceramics as well as with PZT ceramics under electric field applied *in-situ* were carried out. This measurement were taken on the flat plate on symmetric reflection, which means that only scattering vectors perpendicular to the surfaces are measured [4]. A plot of selected diffraction peaks of poled and unpoled samples (Fig. 6) shows the expected intensity differences which are attributed to differences in domain populations after poling, in both the tetragonal ( $x=0.48$ ) and a rhombohedral ( $x=0.42$ ) compositions. The behavior of the peak positions after poling was, however, unexpected. As shown in the same figure for the rhombohedral composition, the (hhh) diffraction peaks, corresponding to the polar direction, were not shifted after poling. A large shift of the (h00) peak position was observed, however, which means that the piezoelectric elongation of the unit cell is not along the polar direction, but along [001]. In a similar way, for the tetragonal composition ( $x=0.48$ ), no shift was observed along the polar [001] direction, while clear poling effects were evident in the (hhh) peaks. The explanation of this striking behavior lies in the monoclinic phase. The piezoelectric strain occurs, for compositions close to the MPB not along the polar axes but along the directions that induce the monoclinic distortion.

All these observations lead us to propose that the so-called morphotropic phase boundary is not a boundary but rather a phase with monoclinic symmetry. This new phase is intermediate between the tetragonal and rhombohedral PZT phases. Its symmetry relates both phases

(Cm being a subgroup of both P4mm and R3m) through the only common symmetry element, the mirror plane. Both, the tetragonal and rhombohedral phases (at least in the proximity of the MPB) have a local structure different from the long-range one and at low temperatures a monoclinic long range order is established by the freezing-out of one of the "local monoclinic structures" in both the rhombohedral and the tetragonal phases. Under the application of an electric field, one of the locally disordered sites becomes preferred, inducing the monoclinic distortion. This induced monoclinic phase is stable and remains after the field is removed.

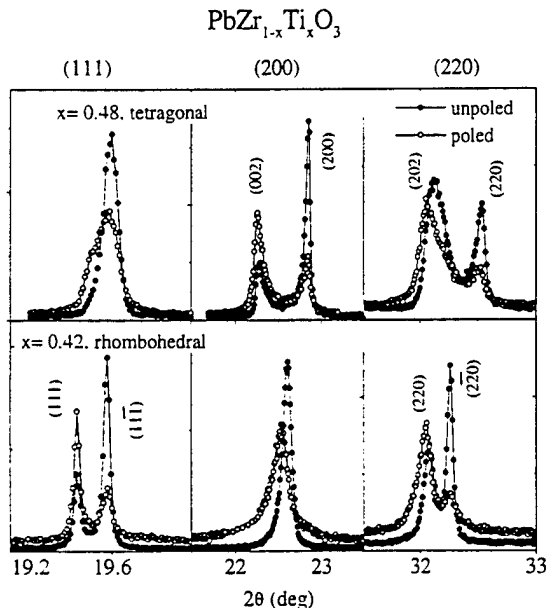


FIG. 6. (111), (200) and (220) pseudo-cubic reflections for the  $x=0.48$  (tetragonal) and  $x=0.42$  (rhombohedral) PZT compositions, before and after poling. After Guo et al. [4]

These results can explain some of the puzzles in PZT, such as the larger piezoelectric coefficient found in rhombohedral PZT along the tetragonal direction [19]. Taking into account the monoclinic phase, very recent *ab initio* calculations have been able to explain the high piezoelectric response of these materials by considering rotations of the polar axis in the monoclinic plane ( $d_{15}$ ) [20]. Indications of a phase of lower symmetry than tetragonal have been found by optical measurement on single crystals of PZN-PT close to the MPB [21]. Something similar could be true in other ferroelectric systems with similar MPBs as PMN-PT or some Tungsten-Bronzes.

We thank L. Bellaiche, T. Egami, A.M. Glazer and C. Moure for helpful discussions, B. Jones for the excellent samples, and A. Langhorn for his technical support dur-

ing the field experiments. Financial support by the U.S. Department of Energy under contract No. DE-AC02-98CH10886 and ONR under project MURI (N00014-96-1-1173) is also acknowledged.

- [1] B. Noheda, D.E. Cox, G. Shirane, J.A. Gonzalo, L.E. Cross, and S-E. Park, *Appl. Phys. Lett.* **74**, 2059 (1999).
- [2] B. Noheda, J.A. Gonzalo, A.C. Caballero, C. Moure, D.E. Cox, and G. Shirane, presented at the *9th European Meeting on Ferroelectricity*, Prague, July 1999 (to be published in *Ferroelectrics*, March 2000). e-print:cond-mat/9907286.
- [3] B. Noheda, J.A. Gonzalo, L.E. Cross, R. Guo, S-E. Park, D.E. Cox, and G. Shirane, *Phys. Rev. B* **61** (in press), 1 April (2000). e-print:cond-mat/9910066
- [4] R. Guo, L.E. Cross, S-E. Park, B. Noheda, D.E. Cox, and G. Shirane, e-print:cond-mat/9912118 (to be published).
- [5] G. Shirane and K. Suzuki, *J. Phys. Soc. Japan* **7**, 333 (1952).
- [6] E. Sawaguchi, *J. Phys. Soc. Japan* **8**, 615 (1953).
- [7] B. Jaffe, W.R. Cook, and H. Jaffe, *Piezoelectric Ceramics* (Academic Press, London, 1971). We are unable to locate the original publication that describes how the MPB was determined.
- [8] M. J. Haun, E. Furman, S.J. Jang, and L.E. Cross, *Ferroelectrics* **99**, 13 (1989).
- [9] K. Kakewaga, O. Matsunaga, T. Kato, and Y. Sasaki, *J. Amer. Ceram. Soc.* **78**, 1071 (1995).
- [10] S. K. Mishra, D. Pandey, *Appl. Phys. Lett.* **69**, 1707 (1996)
- [11] S. Zhang, X. Dong, S. Kojima, *Jpn. J. Appl. Phys.* **36**, 2994 (1997).
- [12] A.P. Wilkinson, J. Xu, S. Pattanaik and J.L. Billinge, *Chem. Mat.* **10**, 3611 (1998).
- [13] W. Cao and L.E. Cross, *Phys. Rev. B* **47**, 4825 (1993).
- [14] G. Saghi-Szabo, R. Cohen, and H. Krakauer, *Phys. Rev. B* **59**, 12771 (1999).
- [15] L. Bellaiche and D. Vanderbilt, *Phys. Rev. Lett.* **83**, 1347 (1999).
- [16] D.L. Corker, A.M. Glazer, R.W. Whatmore, A. Stallard, and F. Fauth, *J. Phys.:Condens. Matter* **10**, 6251 (1998).
- [17] A.M. Glazer and S.A. mabud, *Asta Cryst.* **B34**, 1060 (1978).
- [18] S. Teslic, T. Egami, and D. Viehland, *J. Phys. Chem. Solids* **57**, 1537 (1996); *Ferroelectrics* **194**, 271 (1997).
- [19] X-h Du, J. Zheng, U. Belegundu, and K. Uchino, *Appl. Phys. Lett.* **72**, 2421 (1998).
- [20] L. Bellaiche, A. Garcia, and D. Vanderbilt (to be published).
- [21] K. Fujishiro, R. Vlokh, Y. Uesu, Y. Yamada, J-M. Kiat, B. Dkhil, and Y. Yamashita, presented at the *9th European Meeting on Ferroelectricity*, Prague, July 1999 (to be published in *Ferroelectrics*, March 2000).

# **APPENDIX 9**

## ARTICLES

# Tetragonal-to-monoclinic phase transition in a ferroelectric perovskite: The structure of $\text{PbZr}_{0.52}\text{Ti}_{0.48}\text{O}_3$

B. Noheda\* and J. A. Gonzalo

*Departamento de Física de Materiales, UAM, Cantoblanco, 28049 Madrid, Spain*

L. E. Cross, R. Guo, and S.-E. Park

*Materials Research Laboratory, The Pennsylvania State University, Pennsylvania 16802-4800*

D. E. Cox and G. Shirane

*Department of Physics, Brookhaven National Laboratory, Upton, New York 11973-5000*

(Received 11 October 1999; revised manuscript received 27 December 1999)

The perovskitelike ferroelectric system  $\text{PbZr}_{1-x}\text{Ti}_x\text{O}_3$  (PZT) has a nearly vertical morphotropic phase boundary (MPB) around  $x=0.45-0.50$ . Recent synchrotron x-ray powder diffraction measurements by Noheda *et al.* [Appl. Phys. Lett. 74, 2059 (1999)] have revealed a monoclinic phase between the previously established tetragonal and rhombohedral regions. In the present work we describe a Rietveld analysis of the detailed structure of the tetragonal and monoclinic PZT phases on a sample with  $x=0.48$  for which the lattice parameters are, respectively,  $a_t=4.044$  Å,  $c_t=4.138$  Å, at 325 K, and  $a_m=5.721$  Å,  $b_m=5.708$  Å,  $c_m=4.138$  Å,  $\beta=90.496^\circ$ , at 20 K. In the tetragonal phase the shifts of the atoms along the polar [001] direction are similar to those in  $\text{PbTiO}_3$  but the refinement indicates that there are, in addition, local disordered shifts of the Pb atoms of  $\sim 0.2$  Å perpendicular to the polar axis. The monoclinic structure can be viewed as a condensation along one of the  $\langle 110 \rangle$  directions of the local displacements present in the tetragonal phase. It equally well corresponds to a freezing-out of the local displacements along one of the  $\langle 100 \rangle$  directions recently reported by Corker *et al.* [J. Phys.: Condens. Matter 10, 6251 (1998)] for rhombohedral PZT. The monoclinic structure therefore provides a microscopic picture of the MPB region in which one of the "locally" monoclinic phases in the "average" rhombohedral or tetragonal structures freezes out, and thus represents a bridge between these two phases.

## I. INTRODUCTION

Perovskitelike oxides have been at the center of research on ferroelectric and piezoelectric materials for the past fifty years because of their simple cubic structure at high temperatures and the variety of high symmetry phases with polar states found at lower temperatures. Among these materials the ferroelectric  $\text{PbZr}_{1-x}\text{Ti}_x\text{O}_3$  (PZT) solid solutions have attracted special attention since they exhibit an unusual phase boundary which divides regions with rhombohedral and tetragonal structures, called the morphotropic phase boundary (MPB) by Jaffe *et al.*<sup>1</sup> Materials in this region exhibit a very high piezoelectric response, and it has been conjectured that these two features are intrinsically related. The simplicity of the perovskite structure is in part responsible for the considerable progress made recently in the determination of the basic structural properties and stability of phases of some important perovskite oxides, based on *ab initio* calculations (see, e.g., Refs. 2-9). Recently, such calculations have also been used to investigate solid solutions and, in particular, PZT, where the effective Hamiltonian includes both structural and compositional degrees of freedom.<sup>10-12</sup>

The PZT phase diagram of Jaffe *et al.*,<sup>1</sup> which covers only temperatures above 300 K, has been accepted as the basic

characterization of the PZT solid solution. The ferroelectric region of the phase diagram consists mainly of two different regions: the Zr-rich rhombohedral region, ( $F_R$ ) that contains two phases with space groups  $R3m$  and  $R3c$ , and the Ti-rich tetragonal region ( $F_T$ ), with space group  $P4mm$ .<sup>13</sup> The two regions are separated by a boundary that is nearly independent of temperature, the MPB mentioned above, which lies at a composition close to  $x=0.47$ . Many structural studies have been reported around the MPB, since the early 1950's, when these solid solutions were first studied,<sup>13,14</sup> since the high piezoelectric figure of merit that makes PZT so extraordinary is closely associated with this line.<sup>1,15</sup> The difficulty in obtaining good single crystals in this region, and the characteristics of the boundary itself, make good compositional homogeneity essential if single phase ceramic materials are to be obtained. Because of this, the MPB is frequently reported as a region of phase coexistence whose width depends on the sample processing conditions.<sup>16-19</sup>

Recently, another feature of the morphotropic phase boundary has been revealed by the discovery of a ferroelectric monoclinic phase ( $F_M$ ) in the  $\text{Pb}(\text{Zr}_{1-x}\text{Ti}_x)\text{O}_3$  ceramic system.<sup>20</sup> From a synchrotron x-ray powder diffraction study of a composition with  $x=0.48$ , a tetragonal-to-monoclinic phase transition was discovered at  $\sim 300$  K. The monoclinic

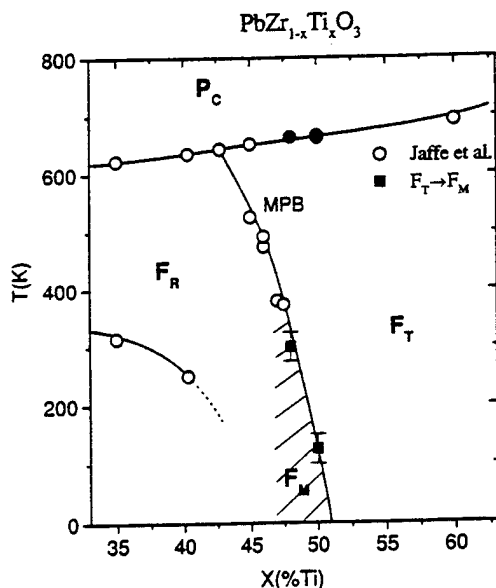


FIG. 1. Preliminary modification of the PZT phase diagram. The data of Jaffe *et al.* (Ref. 1) are plotted as open circles. The  $F_T$ - $F_M$  and  $P_C$ - $F_T$  transition temperatures for  $x=0.48$  and  $x=0.50$  are plotted as solid symbols. The  $F_T$ - $F_M$  transition for  $x=0.50$  is reported in Ref. 22.

unit cell is such that  $a_m$  and  $b_m$  lay along the tetragonal  $[1\bar{1}0]$  and  $[11\bar{0}]$  directions ( $a_m \approx b_m \approx a_t/\sqrt{2}$ ), and  $c_m$  deviates slightly from the  $[001]$  direction ( $c_m \approx c_t$ ).<sup>21</sup> The space group is  $Cm$ , and the temperature dependence of the monoclinic angle  $\beta$  gives immediately the evolution of the order parameter for the tetragonal-monoclinic ( $F_T$ - $F_M$ ) transition. The polar axis of the monoclinic cell can in principle be directed along any direction within the  $ac$  mirror plane, making necessary a detailed structural study to determine its direction.

In the present work we present such a detailed structure determination of the monoclinic phase at 20 K and the tetragonal phase at 325 K in PZT with  $x=0.48$ . The results show that the polarization in the monoclinic plane lies along a direction between the pseudocubic  $[001]_c$  and  $[111]_c$  directions, corresponding to the first example of a species with  $P_x^2 = P_y^2 \neq P_z^2$ . A tentative phase diagram is presented in Fig. 1, which includes data for the  $x=0.48$  composition together with those of the recently studied  $x=0.50$  composition.<sup>22</sup> The most striking finding, however, is that the monoclinic cation displacements found here correspond to one of the three locally disordered sites reported by Corker *et al.*<sup>23</sup> for rhombohedral compositions in the region  $x=0.1-0.4$ , and thus provide a microscopic model of the rhombohedral-to-monoclinic phase transition. This, together with the fact that the space group of the new phase,  $Cm$ , is a subgroup of both  $P4mm$  and  $R3m$ , suggests that  $F_M$  represents an intermediate phase connecting the well-known  $F_T$  and  $F_R$  PZT phases.

## II. EXPERIMENTAL

A PZT sample with  $x=0.48$  was prepared by conventional solid-state reaction techniques using appropriate amounts of reagent-grade powders of lead carbonate, zirconium

oxide, and titanium oxide, with chemical purities better than 99.9%. Pellets were pressed and heated to 1250 °C at a ramp rate of 10 °C/min, held at this temperature in a covered crucible for 2 h, and furnace cooled. During sintering,  $PbZrO_3$  was used as a lead source in the crucible to minimize volatilization of lead.

High-resolution synchrotron x-ray powder diffraction measurements were made at beam line X7A at the Brookhaven National Synchrotron Light Source. In the first set of measurements, an incident beam of wavelength 0.6896 Å from a Ge(111) double-crystal monochromator was used in combination with a Ge(220) crystal and scintillation detector in the diffraction path. The resulting instrumental resolution is about 0.01° on the  $2\theta$  scale, an order of magnitude better than that of a laboratory instrument. Data were collected from a disk in symmetric flat-plate reflection geometry over selected angular regions in the temperature range 20–736 K. Coupled  $\theta$ - $2\theta$  scans were performed over selected angular regions with a  $2\theta$  step interval of 0.01°. The sample was rocked 1–2° during data collection to improve powder averaging.

Measurements above room temperature were performed with the disk mounted on a BN sample pedestal inside a wire-wound BN tube furnace. The furnace temperature was measured with a thermocouple mounted just below the pedestal and the temperature scale calibrated with a sample of  $CaF_2$ . The accuracy of the temperature in the furnace is estimated to be within 10 K, and the temperature stability about 2 K. For low-temperature measurements, the pellet was mounted on a Cu sample pedestal and loaded in a closed-cycle He cryostat, which has an estimated temperature accuracy of 2 K and stability better than 0.1 K. The diffracted intensities were normalized with respect to the incident beam monitor.

For the second set of measurements aimed at the detailed determination of the structure, a linear position-sensitive detector was mounted on the  $2\theta$  arm of the diffractometer instead of the crystal analyzer, and a wavelength of 0.7062 Å was used. This configuration gives greatly enhanced counting rates which make it feasible to collect accurate data from very narrow-diameter capillary samples in Debye-Scherrer geometry, with the advantage that systematic errors due to preferred orientation or texture effects are largely eliminated. A small piece of the sintered disk was carefully crushed and sealed into a 0.2 mm diameter glass capillary. The latter was loaded into a closed-cycle cryostat, and extended data sets were collected at 20 and 325 K while the sample was rocked over a 10° range. With this geometry the instrumental resolution is about 0.03° on the  $2\theta$  scale. Because lead is highly absorbing, the data were corrected for absorption effects<sup>24</sup> based on an approximate value of  $\mu_r = 1.4$  determined from the weight and dimensions of the sample.

## III. PHASE TRANSITIONS

The evolution of the lattice parameters with temperature was briefly summarized in Ref. 20, and a more complete analysis is presented below. The results of the full structure analysis are described later.

A transition from the cubic to the tetragonal phase was observed at ~660 K, in agreement with the phase diagram

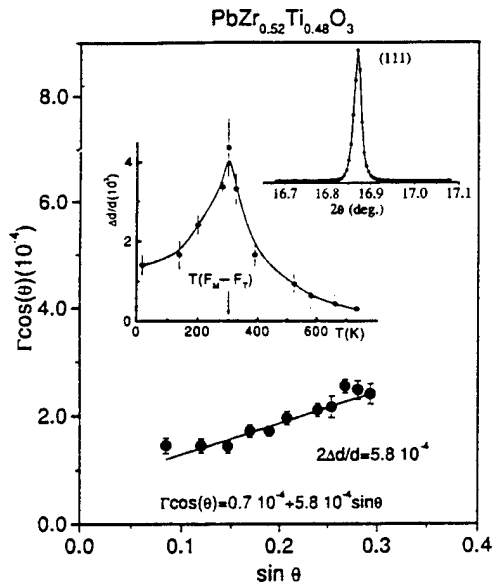


FIG. 2. The Williamson-Hall plot for PZT ( $x=0.48$ ) derived from the measured diffraction peak widths in the cubic phase ( $T=736$  K). Particle size and microstrain are estimated from a linear fit (solid line). The plot for the (111) reflection in the cubic phase demonstrates the excellent quality of the ceramic sample (peak width  $\sim 0.02^\circ$ ). The plot of  $\Delta d/d$  vs temperature is also shown as an inset.

shown in Fig. 1. The measurements made on the pellet in the cubic phase at 736 K demonstrate the excellent quality of the sample, which exhibits diffraction peaks with full-widths at half-maximum (FWHM) ranging from  $0.01^\circ$  to  $0.03^\circ$  as shown for the (111) reflection plotted as the upper-right inset in Fig. 2. The FWHM's ( $\Gamma$ ) for several peaks were determined from least-squares fits to a pseudo-Voigt function with the appropriate corrections for asymmetry effects,<sup>25</sup> and corrected for instrumental resolution. The corrected values are shown in Fig. 2 in the form of a Williamson-Hall plot<sup>26</sup>

$$\Gamma \cos \theta = \lambda/L + 2(\Delta d/d) \sin \theta, \quad (3.1)$$

where  $\lambda$  is the wavelength and  $L$  is the mean crystallite size. From the slope of a linear fit to the data, the distribution of  $d$  spacings,  $\Delta d/d$ , is estimated to be  $\sim 3 \times 10^{-4}$ , corresponding to a compositional inhomogeneity  $\Delta x$  of less than  $\pm 0.003$ . From the intercept of the line on the ordinate axis the mean crystallite size is estimated to be  $\sim 1 \mu\text{m}$ .

A tetragonal-to-monoclinic phase transition in PZT with  $x=0.48$  was recently reported by Noheda *et al.*<sup>20</sup> Additional data have been obtained near the phase transition around 300 K which have allowed a better determination of the phase transition to be made, as shown by the evolution of the lattice parameters as a function of temperature in Fig. 3. The tetragonal strain  $c_t/a_t$  increases as the temperature decreases from the Curie point ( $T \approx 660$  K), to a value of 1.0247 at 300 K, below which peak splittings characteristic of a monoclinic phase with  $a_m \approx b_m \approx a_t/\sqrt{2}$ ,  $\beta \neq 90^\circ$ , are observed (Fig. 3). As the temperature continues to decrease down to 20 K,  $a_m$  (which is defined to lie along the  $[\bar{1}\bar{1}0]$  tetragonal direction) increases very slightly, and  $b_m$  (which lies along the  $[1\bar{1}0]$  tetragonal direction) decreases. The  $c_m$  lattice parameter

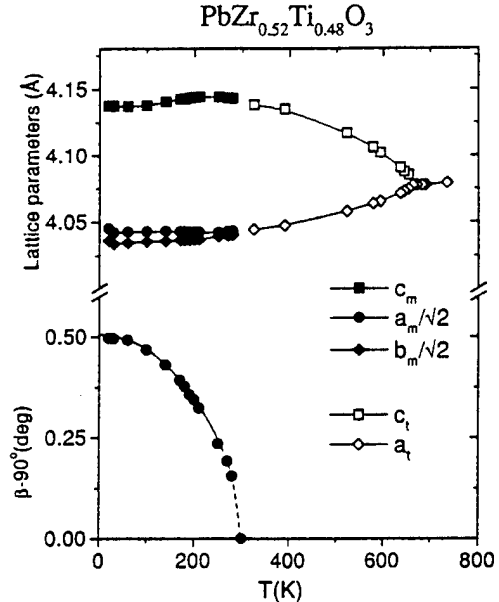


FIG. 3. Lattice parameters versus temperature for PZT ( $x=0.48$ ) over the whole range of temperatures from 20 to 750 K showing the evolution from the monoclinic phase to the cubic phase via the tetragonal phase.

reaches a broad maximum value of  $4.144 \text{ \AA}$  between 240–210 K and then reaches a shallow minimum value of  $4.137 \text{ \AA}$  at 60 K. Over the same temperature region there is a striking variation of  $\Delta d/d$  determined from Williamson-Hall plots at various temperatures, as shown in the upper-left inset in Fig. 2.  $\Delta d/d$  increases rapidly as the temperature approaches the  $F_T-F_M$  transition at 300 K, in a similar fashion to the tetragonal strain, and then decreases rapidly below this temperature in the monoclinic region. Thus the microstrain responsible for the large increase in  $\Delta d/d$  is an important feature of the phase transition, which may be associated with the development of local monoclinic order, and is very likely responsible for the large electromechanical response of PZT close to the MPB.<sup>1</sup>

The deviation of the monoclinic angle  $\beta$  from  $90^\circ$  is an order parameter of the  $F_T-F_M$  transition, and its evolution with temperature is also depicted in Fig. 3. This phase transition presents a special problem due to the steepness of the phase boundary (the MPB in Fig. 1). As shown in the previous section, the compositional fluctuations are quite small in these ceramic samples ( $\Delta x \approx \pm 0.003$ ) but, even in this case, the nature of the MPB implies an associated temperature uncertainty of  $\Delta T \approx 100$  K. There is, therefore, a rather wide range of transition temperatures instead of a single well-defined transition, so that the order parameter is smeared out as a function of temperature around the phase change, thereby concealing the nature of the transition.

Scans over the  $(220)_c$  region for several different temperatures are plotted in Fig. 4, which shows the evolution of phases from the cubic phase at 687 K (upper-left plot) to the monoclinic phase at 20 K (lower-right plot), passing through the tetragonal phase at intermediate temperatures. With decreasing temperature, the tetragonal phase appears at  $\sim 660$  K and the development of the tetragonal distortion can be observed on the left side of the figure from the splitting of

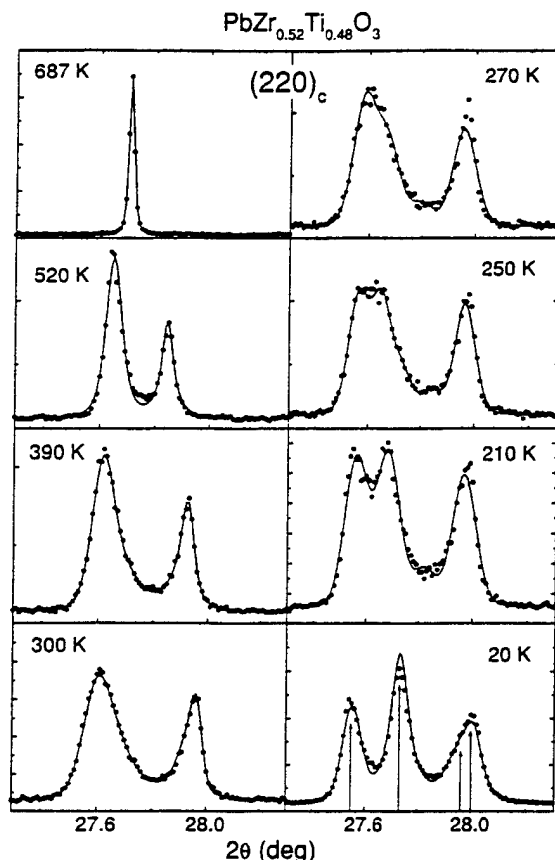


FIG. 4. Temperature evolution of the pseudocubic (220) peak from the cubic (top left) to the monoclinic (bottom right) phase.

the (202)<sub>c</sub> and (220)<sub>c</sub> reflections. On the right side of the figure, the evolution of the monoclinic phase, which appears below  $\sim 300$  K, is shown by the splitting into the (222)<sub>m</sub>, (222)<sub>m</sub>, (400)<sub>m</sub>, and (040)<sub>m</sub> monoclinic reflections. It is quite evident from Fig. 4 that the (202)<sub>c</sub> peak is much broader than the neighboring (220)<sub>c</sub> peak, for example, and this "anisotropic" peak broadening is a general feature of the diffraction data for both phases. Another feature of the patterns is the presence of additional diffuse scattering between neighboring peaks, which is particularly evident between tetragonal (00*l*) and (*h*00) pairs, and the corresponding monoclinic (00*l*) and (*h**h*0) pairs.

#### IV. STRUCTURE DETERMINATION

A detailed analysis of the 325 K tetragonal and 20 K monoclinic structures of  $\text{PbZr}_{0.52}\text{Ti}_{0.48}\text{O}_3$  was carried out by Rietveld refinement using the GSAS program package.<sup>27</sup> The pseudo-Voigt peak shape function option was chosen<sup>25</sup> and background was estimated by linear interpolation between fixed values. An important feature of the refinements was the need to allow for the anisotropic peak broadening mentioned above. This was accomplished by the use of the recently incorporated generalized model for anisotropic peak broadening proposed by Stephens,<sup>28</sup> which is based on a distribution of lattice parameters. It was also necessary to take into account some additional diffuse scattering by modeling with a second, cubic, phase with broad, predominately Gaussian,

peaks. A similar strategy has been adopted by Muller *et al.*<sup>29</sup> in a recent study of  $\text{PbHf}_{0.4}\text{Ti}_{0.6}\text{O}_3$ . Although in principle this could represent a fraction of untransformed cubic phase, we suspect that the diffuse scattering is associated with locally disordered regions in the vicinity of domain walls. The refinements were carried out with the atoms assigned fully ionized scattering factors.

##### A. Tetragonal structure at 325 K

At 325 K the data show tetragonal symmetry similar to that of  $\text{PbTiO}_3$ . This tetragonal structure has the space group  $P4mm$  with Pb in 1(*a*) sites at (0,0,*z*); Zr/Ti and O(1) in 1(*b*) sites at (1/2,1/2,*z*) and O(2) in 2(*c*) sites at (1/2, 0, *z*). For the refinement we adopt the same convention as that used in Refs. 30 and 31 for  $\text{PbTiO}_3$ , with Pb fixed at (0,0,0). However, instead of thinking in terms of shifts of the other atoms with respect to this origin, it is more physically intuitive to consider displacements of Pb and Zr/Ti from the center of the distorted oxygen cuboctahedra and octahedra, respectively. We shall take this approach in the subsequent discussion.

The refinement was first carried out with individual isotropic ( $U_{\text{iso}}$ ) temperature factors assigned. Although a reasonably satisfactory fit was obtained ( $R_F^2 = 8.9\%$ ),  $U_{\text{iso}}$  for O(1) was slightly negative and  $U_{\text{iso}}$  for Pb was very large,  $0.026 \text{ \AA}^2$ , much larger than  $U_{\text{iso}}$  for the other atoms. Similarly high values for Pb( $U_{\text{iso}}$ ) in Pb-based perovskites are well known in the literature, and are usually ascribed to local disordered displacements, which may be either static or dynamic. Refinement with anisotropic temperature factors<sup>32</sup> ( $U_{11}$  and  $U_{33}$ ) assigned to Pb (Table I, model I) gave an improved fit ( $R_F^2 = 6.1\%$ ) with  $U_{11}(=U_{22})$  considerably larger than  $U_{33}$  (0.032 and  $0.013 \text{ \AA}^2$ , respectively) corresponding to large displacements perpendicular to the polar [001] axis. A further refinement based on local displacements of the Pb from the 1(*a*) site to the 4(*d*) sites at (*x*,*x*,0), with isotropic temperature factors assigned to all the atoms, gave a small improvement in the fit ( $R_F^2 = 6.0\%$ ) with  $x = 0.033$ , corresponding to local shifts along the  $\langle 110 \rangle$  axes, and a much more reasonable temperature factor (Table I, model II). In order to check that high correlations between the temperature factor and local displacements were not biasing the result of this refinement, we have applied a commonly used procedure consisting of a series of refinements based on model II in which Pb displacements along  $\langle 110 \rangle$  were fixed but all the other parameters were varied.<sup>34,35</sup> Figure 5 shows unambiguously that there is well-defined minimum in the *R* factor for a displacement of about  $0.19 \text{ \AA}$ , consistent with the result in Table I. A similar minimum was obtained for shifts along  $\langle 100 \rangle$  directions with a slightly higher *R* factor. Thus, in addition to a shift of  $0.48 \text{ \AA}$  for Pb along the polar [001] axis towards four of its O(2) neighbors, similar to that in  $\text{PbTiO}_3$ ,<sup>30,31,36</sup> there is a strong indication of substantial local shifts of  $\sim 0.2 \text{ \AA}$  perpendicular to this axis. The Zr/Ti displacement is  $0.27 \text{ \AA}$  along the polar axis, once again similar to the Ti shift in  $\text{PbTiO}_3$ . Attempts to model local displacements along  $\langle 110 \rangle$  directions for the Zr/Ti atoms were unsuccessful due to the large correlations between these shifts and the temperature factor. Further attempts to refine the *z* parameters of the Zr and Ti atoms independently,

TABLE I. Structure refinement results for tetragonal  $\text{PbZr}_{0.52}\text{Ti}_{0.48}\text{O}_3$  at 325 K, space group  $P4mm$ , lattice parameters  $a_t = 4.0460(1)$  Å,  $c_t = 4.1394(1)$  Å. Fractional occupancies  $N$  for all atoms taken as unity except for Pb in model II, where  $N = 0.25$ . Agreement factors,  $R_{wp}$ ,  $R_F$ , and  $\chi^2$  are defined in Ref. 33.

	Model I anisotropic lead temperature factors				Model II local $\langle 110 \rangle$ lead shifts			
	$x$	$y$	$z$	$U(\text{\AA}^2)$	$x$	$y$	$z$	$U_{iso}(\text{\AA}^2)$
Pb	0	0	0	$U_{11} = 0.0319(4)$ $U_{33} = 0.0127(4)$	0.0328(5)	0.0328(5)	0	0.0127(4)
Zr/Ti	0.5	0.5	0.4517(7)	$U_{iso} = 0.0052(6)$	0.5	0.5	0.4509(7)	0.0041(6)
O(1)	0.5	0.5	-0.1027(28)	$U_{iso} = 0.0061(34)$	0.5	0.5	-0.1027(28)	0.0072(35)
O(2)	0.5	0	0.3785(24)	$U_{iso} = 0.0198(30)$	0.5	0	0.3786(24)	0.0197(30)
$R_{wp}$	4.00%				3.99%			
$R_F$	6.11%				6.04%			
$\chi^2$	11.4				11.3			

as Corker *et al.* were able to do,<sup>23</sup> were likewise unsuccessful, presumably because the scattering contrast for x rays is much less than for neutrons.

From the values of the atomic coordinates listed in Table I, it can be inferred that the oxygen octahedra are somewhat more distorted than in  $\text{PbTiO}_3$ , the O(1) atoms being displaced 0.08 Å towards the O(2) plane above. The cation displacements are slightly larger than those recently reported by Wilkinson *et al.*<sup>37</sup> for samples close to the MPB containing a mixture of rhombohedral and tetragonal phases, and in excellent agreement with the theoretical values obtained by Bellaiche and Vanderbilt<sup>38</sup> for PZT with  $x = 0.50$  from first principles calculations. As far as we are aware no other structural analysis of PZT compositions in the tetragonal region has been reported in the literature.

Selected bond distances for the two models are shown in Table II. For model I, Zr/Ti has short and long bonds with O(1) of 1.85 and 2.29 Å, respectively, and four intermediate-length O(2) bonds of 2.05 Å. There are four intermediate-length Pb-O(1) bonds of 2.89 Å, four short Pb-O(2) bonds

of 2.56 Å and four much larger Pb-O(2) distances of 3.27 Å. For model II, the Zr/Ti-O distances are the same, but the Pb-O distances change significantly. A Pb atom in one of the four equivalent  $(x, x, 0)$  sites in Table I now has a highly distorted coordination, consisting of two short and two intermediate Pb-O(2) bonds of 2.46 and 2.67 Å, and one slightly longer Pb-O(1) bond of 2.71 Å (Table II). The tendency of  $\text{Pb}^{+2}$ , which has a lone *sp* electron pair, to form short covalent bonds with a few neighboring oxygens is well documented in the literature.<sup>23,39-41</sup>

The observed and calculated diffraction profiles and the difference plot are shown in Fig. 6 for a selected  $2\theta$  range between  $7^\circ$  and  $34^\circ$  (upper figure). The short vertical markers represent the calculated peak positions. The upper and lower sets of markers correspond to the cubic and tetragonal phases, respectively. We note that although agreement between the observed and the calculated profiles is considerably better when the diffuse scattering is modeled with a cubic phase, the refined values of the atomic coordinates are not significantly affected by the inclusion of this phase. The anisotropic peak broadening was found to be satisfactorily

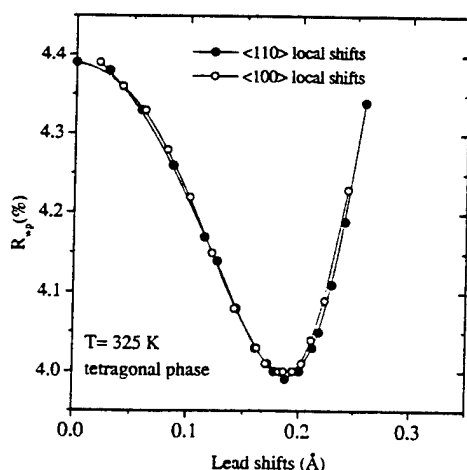


FIG. 5. Agreement factor  $R_{wp}$  as a function of Pb displacements for refinements with fixed values of  $x$  along tetragonal  $\langle 110 \rangle$  and  $\langle 100 \rangle$  directions as described in text. The well-defined minimum at  $x \sim 0.19$  Å confirms the result listed in Table I for model II.

TABLE II. Selected Zr/Ti-O and Pb-O bond lengths in the tetragonal and monoclinic structures. Models I and II refer to the refinements with anisotropic temperature factors and local  $\langle 110 \rangle$  displacements for Pb, respectively (see Table I). The standard errors in the bond lengths are  $\sim 0.01$  Å.

	Bond lengths (Å)		
	tetragonal		monoclinic
	model I	model II	
Zr/Ti-O(1)	$1.85 \times 1$	$1.85 \times 1$	$1.87 \times 1$
	$2.29 \times 1$	$2.29 \times 1$	$2.28 \times 1$
Zr/Ti-O(2)	$2.05 \times 4$	$2.05 \times 4$	$2.13 \times 2$
			$1.96 \times 2$
Pb-O(1)	$2.89 \times 4$	$2.90 \times 2$	$2.90 \times 2$
		$2.71 \times 1$	$2.60 \times 1$
Pb-O(2)	$2.56 \times 4$	$2.67 \times 2$	$2.64 \times 2$
		$2.46 \times 2$	$2.46 \times 2$

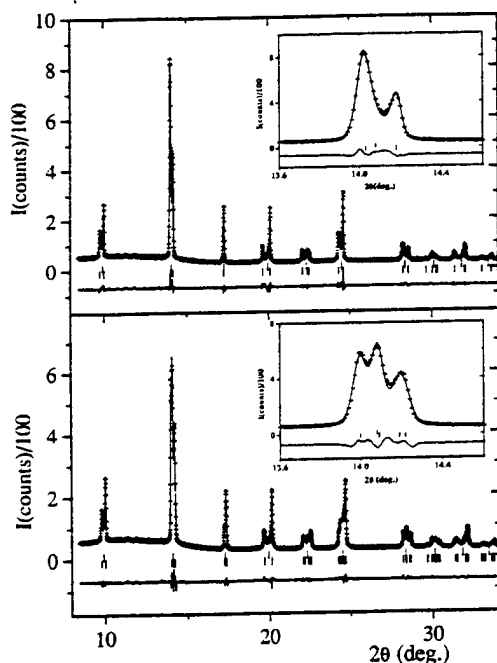


FIG. 6. Observed and calculated diffraction profiles from the Rietveld refinement of the tetragonal (top) and monoclinic (bottom) phases of PZT ( $x=0.48$ ) at 325 and 20 K, respectively. The difference plots are shown below, and the short vertical markers represent the peak positions (the upper set correspond to the cubic phase as discussed in text). The insets in each figure highlight the differences between the tetragonal and the monoclinic phase for the pseudocubic (110) reflection, and illustrate the high resolution needed in order to characterize the monoclinic phase.

described by two of the four parameters in the generalized model for tetragonal asymmetry.<sup>28</sup>

### B. Monoclinic structure at 20 K

As discussed above, the diffraction data at 20 K can be indexed unambiguously on the basis of a monoclinic cell with the space group  $Cm$ . In this case Pb, Zr/Ti, and O(1) are in  $2(a)$  sites at  $(x,0,z)$ , and O(2) in  $4(b)$  sites at  $(x,y,z)$ . Individual isotropic temperature factors were assigned, and Pb was fixed at (0,0,0). For monoclinic symmetry, the generalized expression for anisotropic peak broadening contains nine parameters, but when all of these were allowed to vary the refinement was slightly unstable and did not completely converge. After several tests in which some of the less significant values were fixed at zero, satisfactory convergence was obtained with three parameters ( $R_{wp}=0.036$ ,  $\chi^2=11.5$ ). During these tests, there was essentially no change in the refined values of the atomic coordinates. A small improvement in the fit was obtained when anisotropic temperature factors were assigned to Pb ( $R_{wp}=0.033$ ,  $\chi^2=9.2$ ). The final results are listed in Table III, and the profile fit and difference plot are shown in the lower part of Fig. 6.

From an inspection of the results in Tables I and III, it can be seen that the displacements of the Pb and Zr/Ti atoms along [001] are very similar to those in the tetragonal phase at 325 K, about 0.53 and 0.24 Å, respectively. However, in the monoclinic phase at 20 K, there are also significant shifts

TABLE III. Structure refinement results for monoclinic  $PbZr_{0.52}Ti_{0.48}O_3$  at 20 K, space group  $Cm$ , lattice parameters  $a_m=5.72204(15)$  Å,  $b_m=5.70957(14)$  Å,  $c_m=4.13651(14)$  Å,  $\beta=90.498(1)^\circ$ . Agreement factors  $R_{wp}=3.26\%$ ,  $R_F=4.36\%$ ,  $\chi^2=9.3$ .

	$x_m$	$y_m$	$z_m$	$U_{iso}(\text{\AA}^2)$
Pb	0	0	0	0.0139 <sup>a</sup>
Zr/Ti	0.5230(6)	0	0.4492(4)	0.0011(5)
O(1)	0.5515(23)	0	-0.0994(24)	0.0035(28)
O(2)	0.2880(18)	0.2434(20)	0.3729(17)	0.0123(22)

<sup>a</sup>For Pb,  $U_{iso}$  is the equivalent isotropic value calculated from the refined anisotropic values [ $U_{11}=0.0253(7)$  Å<sup>2</sup>,  $U_{22}=0.0106(6)$  Å<sup>2</sup>,  $U_{33}=0.0059(3)$  Å<sup>2</sup>,  $U_{13}=0.0052(4)$  Å<sup>2</sup>].

of these atoms along the monoclinic  $[100]$ , i.e., pseudocubic  $[110]$ , towards their O(2) neighbors in adjacent pseudocubic (110) planes, of about 0.24 and 0.11 Å, respectively, which corresponds to a rotation of the polar axis from  $[001]$  towards pseudocubic  $[111]$ . The Pb shifts are also qualitatively consistent with the local shifts of Pb along the tetragonal  $\langle 110 \rangle$  axes inferred from the results of model II in Table I, i.e., about 0.2 Å. Thus it seems very plausible that the monoclinic phase results from the condensation of the local Pb displacements in the tetragonal phase along one of the  $\langle 110 \rangle$  directions.

Some selected bond distances are listed in Table II. The Zr/Ti-O(1) distances are much the same as in the tetragonal structure, but the two sets of Zr/Ti-O(2) distances are significantly different, 1.96 and 2.13 Å, compared to the single set at 2.04 Å in the tetragonal structure. Except for a shortening in the Pb-O(1) distance from 2.71 to 2.60 Å, the Pb environment is quite similar to that in the tetragonal phase, with two close O(2) neighbors at 2.46 Å, and two at 2.64 Å.

### V. DISCUSSION

In the previous section, we have shown that the low-temperature monoclinic structure of  $PbZr_{0.52}Ti_{0.48}O_3$  is derived from the tetragonal structure by shifts of the Pb and Zr/Ti atoms along the tetragonal  $[110]$  axis. We attribute this phase transition to the condensation of local  $\langle 110 \rangle$  shifts of Pb which are present in the tetragonal phase along one of the four  $\langle 110 \rangle$  directions. In the context of this monoclinic structure it is instructive to consider the structural model for rhombohedral PZT compositions with  $x=0.08$ – $0.38$  recently reported by Corker *et al.*<sup>23</sup> on the basis of neutron powder diffraction data collected at room temperature. In this study and also an earlier study<sup>42</sup> of a sample with  $x=0.1$ , it was found that satisfactory refinements could only be achieved with anisotropic temperature factors, and that the thermal ellipsoid for Pb had the form of a disk perpendicular to the pseudocubic  $[111]$  axis. This highly unrealistic situation led them to propose a physically much more plausible model involving local displacements for the Pb atoms of about 0.25 Å perpendicular to the  $[111]$  axis and a much smaller and more isotropic thermal ellipsoid was obtained. Evidence for local shifts of Pb atoms in PZT ceramics has also been demonstrated by pair-distribution function analysis by Teslic and co-workers.<sup>39</sup>

TABLE IV. Comparison of refined values of atomic coordinates in the monoclinic phase with the corresponding values in the tetragonal and rhombohedral phases for both the "ideal" structures and those with local shifts, as discussed in text.

	tetragonal $x=0.48$ , 325 K		monoclinic $x=0.48$ , 20 K	rhombohedral (Ref. 43) $x=0.40$ , 295 K	
	ideal	local shifts <sup>a</sup>	as refined	local shifts <sup>b</sup>	ideal
$x_{\text{Zr/Ti}}$	0.500	0.530	0.523	0.520	0.540
$z_{\text{Zr/Ti}}$	0.451	0.451	0.449	0.420	0.460
$x_{\text{O(1)}}$	0.500	0.530	0.551	0.547	0.567
$z_{\text{O(1)}}$	-0.103	-0.103	-0.099	0.093	-0.053
$x_{\text{O(2)}}$	0.250	0.280	0.288	0.290	0.310
$y_{\text{O(2)}}$	0.250	0.250	0.243	0.257	0.257
$z_{\text{O(2)}}$	0.379	0.379	0.373	0.393	0.433
$a_m(\text{\AA})$	5.722		5.722	5.787	
$b_m(\text{\AA})$	5.722		5.710	5.755	
$c_m(\text{\AA})$	4.139		4.137	4.081	
$\beta(^{\circ})$	90.0		90.50	90.45	

<sup>a</sup>Tetragonal local shifts of (0.03,0.03,0).

<sup>b</sup>Hexagonal local shifts of (-0.02,0.02,0).

We now consider the refined values of the Pb atom positions with local displacements for rhombohedral PZT listed in Table IV of Ref. 23. With the use of the appropriate transformation matrices, it is straightforward to show that these shifts correspond to displacements of 0.2–0.25 Å along the direction of the monoclinic [100] axis, similar to what is actually observed for  $x=0.48$ . It thus seems equally plausible that the monoclinic phase can also result from the condensation of local displacements perpendicular to the [111] axis.

The monoclinic structure can thus be pictured as providing a "bridge" between the rhombohedral and tetragonal structures in the region of the MPB. This is illustrated in Table IV, which compares the results for PZT with  $x=0.48$  obtained in the present study with earlier results<sup>43</sup> for rhombohedral PZT with  $x=0.40$  expressed in terms of the monoclinic cell.<sup>44</sup> For  $x=0.48$ , the atomic coordinates for Zr/Ti, O(1) and O(2) are listed for the "ideal" tetragonal structure (model I) and for a similar structure with local shifts of (0.03,0.03,0) in the first two columns, and for the monoclinic structure in the third column. The last two columns describe the rhombohedral structure for  $x=0.40$  assuming local shifts of (-0.02,0.02,0) along the hexagonal axes and the as-refined "ideal" structure, respectively. It is clear that the condensation of these local shifts gives a very plausible description of the monoclinic structure in both cases. It is also interesting to note the behavior of the corresponding lattice parameters: metrically the monoclinic cell is very similar to the tetragonal cell except for the monoclinic angle, which is close to that of the rhombohedral cell.

Evidence for a tetragonal-to-monoclinic transition in the ferroelectric material  $\text{PbFe}_{0.5}\text{Nb}_{0.5}\text{O}_3$  has also been reported by Bonny *et al.*<sup>45</sup> from single crystal and synchrotron x-ray powder diffraction measurements. The latter data show a cubic-tetragonal transition at  $\sim 376$  K, and a second transition at  $\sim 355$  K. Although the resolution was not sufficient to reveal any systematic splitting of the peaks, it was concluded that the data were consistent with a very weak monoclinic

distortion of the pseudorhombohedral unit cell. In a recent neutron and x-ray powder study, Lampis *et al.*<sup>46</sup> have shown that Rietveld refinement gives better agreement for the monoclinic structure at 80 and 250 K than for the rhombohedral one. The resulting monoclinic distortion is very weak, and the large thermal factor obtained for Pb is indicative of a high degree of disorder.

The relationships between the PZT rhombohedral, tetragonal and monoclinic structures are also shown schematically in Fig. 7, in which the displacements of the Pb atom are shown projected on the pseudocubic (110) mirror plane. The four locally disordered  $\langle 110 \rangle$  shifts postulated in the present paper for the tetragonal phase are shown superimposed on the [001] shift at the left [Fig. 7(a)] and the three locally disordered  $\langle 100 \rangle$  shifts proposed by Corker *et al.*<sup>23</sup> for the rhombohedral phase are shown superimposed on the [111] shift.

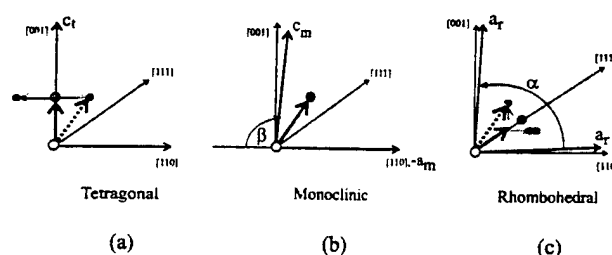


FIG. 7. Schematic illustration of the tetragonal (a), monoclinic (b), and rhombohedral (c) distortions of the perovskite unit cell projected on the pseudocubic (110) plane. The solid circles represent the observed shifts with respect to the ideal cubic structure. The light grey circles represent the four locally disordered  $\langle 100 \rangle$  shifts in the tetragonal structure (a) and the three locally disordered shifts in the rhombohedral structure (c) described by Corker *et al.* (Ref. 23). The heavy dashed arrows represent the freezing-out of one of these shifts to give the monoclinic observed structure. Note that the resultant shifts in the rhombohedral structure can be viewed as a combination of a [111] shift with local  $\langle 100 \rangle$  shifts, as indicated by the light grey arrows.

shift at the right [Fig. 7(c)]. It can be seen that both the condensation of the [110] shift in the tetragonal phase and the condensation of the [001] shift in the rhombohedral phase leads to the observed monoclinic shift shown at the center [Fig. 7(b)]. We note that although Corker *et al.* discuss their results in terms of  $\langle 100 \rangle$  shifts and a [111] shift smaller than that predicted in the usual refinement procedure, they can be equally well described by a combination of shifts perpendicular to the [111] axis and the [111] shift actually obtained in the refinement, as is evident from Fig. 7(c).

We conclude, therefore, that the  $F_M$  phase establishes a connection between the PZT phases at both sides of the MPB through the common symmetry element, the mirror plane, and suggest that there is not really a morphotropic phase boundary, but rather a "morphotropic phase," connecting the  $F_T$  and  $F_R$  phases of PZT. In the monoclinic phase the difference vector between the positive and negative centers of charge defines the polar axis, whose orientation, in contrast to the case of the  $F_T$  and  $F_R$  phases, cannot be determined on symmetry grounds alone. According to this, from the results shown in Table III, the polar axis in the monoclinic phase is found to be tilted about  $24^\circ$  from the [001] axis towards the [111] axis. This structure represents the first example of a ferroelectric material with  $P_x^2 = P_y^2 \neq P_z^2$ , ( $P_x, P_y, P_z$ ) being the Cartesian components of the polarization vector. This class corresponds to the so-called  $m3m(12)A2Fm$  type predicted by Shuvalov.<sup>47</sup> It is possible that this new phase is one of the rare examples of a two-dimensional ferroelectric<sup>48</sup> in which the unit cell dipole moment switches within a plane containing the polar axis, upon application of an electric field.

This  $F_M$  phase has important implications; for example, it might explain the well-known shifts of the anomalies of many physical properties with respect to the MPB and thus help in understanding the physical properties in this region, of great interest from the applications point of view.<sup>1</sup> It has been found that the maximum values of  $d_{33}$  for rhombohedral PZT with  $x=0.40$  are not obtained for samples polarized along the [111] direction but along a direction close to the perovskite [001] direction.<sup>49</sup> This points out the intrinsic importance of the [001] direction in perovskites, whatever the distortion present, and is consistent with Corker *et al.*'s model for the rhombohedral phase,<sup>23</sup> and the idea of the rhombohedral-tetragonal transition through a monoclinic phase.

It is also to be expected that other systems with morphotropic phase boundaries between two nonsymmetry-related phases (e.g., other perovskites or tungsten-bronze mixed systems) may show similar intermediate phases. In fact, an indication of symmetry lowering at the MPB of the PZN-PT system has been recently reported by Fujishiro *et al.*<sup>50</sup> From a different point of view, a monoclinic ferroelectric perovskite also represents a new challenge for first-principles theorists, until now used to dealing only with tetragonal, rhombohedral and orthorhombic perovskites.

A structural analysis of several other PZT compositions with  $x=0.42$ – $0.51$  is currently in progress in order to determine the new PZT phase diagram more precisely. In the preliminary version shown in Fig. 1 we have included data for a sample with  $x=0.50$  made under slightly different conditions<sup>22</sup> at the Institute of Ceramic and Glass (ICG) in Madrid, together with the data described in the present work for a sample with  $x=0.48$  synthesized in the Materials Research Laboratory at the Pennsylvania State University (PSU). As can be seen the results for these two compositions show consistent behavior, and demonstrate that the  $F_M$ - $F_T$  phase boundary lies along the MPB of Jaffe *et al.* Preliminary results for a sample from PSU with  $x=0.47$  show unequivocally that the monoclinic features are present at 300 K. However, measurements on an ICG sample with the same nominal composition do not show monoclinicity unambiguously, but instead a rather complex poorly defined region from 300–400 K between the rhombohedral and tetragonal phases.<sup>22</sup> The extension of the monoclinic region and the location of the  $F_R$ - $F_M$  phase boundary are still somewhat undefined, although it is clear that the monoclinic region has a narrower composition range as the temperature increases. The existence of a quadruple point in the PZT phase diagram is an interesting possibility.

## ACKNOWLEDGMENTS

We wish to gratefully acknowledge B. Jones for the excellent quality of the  $x=0.48$  sample used in this work, and we thank L. Bellaiche, A. M. Glazer, E. Moshopoulou, C. Moure, and E. Sawaguchi for their helpful comments. Support by NATO (Grant No. R.C.G. 970037), the Spanish CICYT (Project No. PB96-0037), and the U.S. Department of Energy, Division of Materials Sciences (Contract No. DE-AC02-98CH10886) is also acknowledged.

\*Visiting scientist at Brookhaven National Laboratory.

<sup>1</sup>B. Jaffe, W.R. Cook, and H. Jaffe, *Piezoelectric Ceramics* (Academic Press, London, 1971).

<sup>2</sup>R.E. Cohen, *Nature* (London) **358**, 136 (1992).

<sup>3</sup>R.D. King-Smith and D. Vanderbilt, *Phys. Rev. B* **49**, 5828 (1994).

<sup>4</sup>W. Zhong, D. Vanderbilt, and K. Rabe, *Phys. Rev. Lett.* **73**, 1861 (1994); *Phys. Rev. B* **52**, 6301 (1995).

<sup>5</sup>W. Zhong and D. Vanderbilt, *Phys. Rev. Lett.* **74**, 2587 (1995).

<sup>6</sup>A. Garcia and D. Vanderbilt, *Phys. Rev. B* **54**, 3817 (1996).

<sup>7</sup>K.M. Rabe and U.W. Waghmare, *Phys. Rev. B* **55**, 6161 (1997).

<sup>8</sup>K.M. Rabe and E. Cockayne, in *First-Principles Calculations for Ferroelectrics*, AIP Conf. Proc. No. 436, edited by R. Cohen (AIP, New York, 1998), p. 61.

<sup>9</sup>Ph. Ghosez, E. Cockayne, U.V. Waghmare, and K.M. Rabe, *Phys. Rev. B* **60**, 836 (1999).

<sup>10</sup>L. Bellaiche, J. Padilla, and D. Vanderbilt, *Phys. Rev. B* **59**, 1834 (1999).

<sup>11</sup>L. Bellaiche, J. Padilla, and D. Vanderbilt, *First-principles Calculations for Ferroelectrics: 5th Williamsburg Workshop*, edited by R. Cohen (AIP, Woodbury, 1998), p. 11.

<sup>12</sup>G. Soghi-Szabo and R. E. Cohen, *Ferroelectrics* **194**, 287 (1997).

<sup>13</sup>G. Shirane and K. Suzuki, *J. Phys. Soc. Jpn.* **7**, 333 (1952).

<sup>14</sup>E. Sawaguchi, *J. Phys. Soc. Jpn.* **8**, 615 (1953).

<sup>15</sup>Y. Xu, *Ferroelectric Materials and their Applications* (North Holland, Amsterdam, 1991).

<sup>16</sup>K. Kakewaga, O. Matsunaga, T. Kato, and Y. Sasaki, *J. Am. Ceram. Soc.* **78**, 1071 (1995).

- <sup>17</sup> J.C. Fernandes, D.A. Hall, M.R. Cockburn, and G.N. Greaves. Nucl. Instrum. Methods Phys. Res. B **97**, 137 (1995).
- <sup>18</sup> M. Hammer, C. Monty, A. Endriss, and M.J. Hoffmann. J. Am. Ceram. Soc. **81**, 721 (1998).
- <sup>19</sup> W. Cao and L.E. Cross. Phys. Rev. B **47**, 4825 (1993).
- <sup>20</sup> B. Noheda, D.E. Cox, G. Shirane, J.A. Gonzalo, L.E. Cross, and S.-E. Park. Appl. Phys. Lett. **74**, 2059 (1999).
- <sup>21</sup> The  $[1\bar{1}0]$  and  $[1\bar{1}0]$  directions are chosen so that the monoclinic angle  $\beta > 90^\circ$  to conform with usual crystallographic convention.
- <sup>22</sup> B. Noheda, J.A. Gonzalo, A.C. Caballero, C. Moure, D.E. Cox, and G. Shirane, cond-mat/9907286, *Ferroelectrics* (to be published).
- <sup>23</sup> D.L. Corker, A.M. Glazer, R.W. Whatmore, A. Stallard, and F. Fauth. J. Phys.: Condens. Matter **10**, 6251 (1998).
- <sup>24</sup> C.W. Diggins Jr., Acta Crystallogr., Sect. A: Cryst. Phys., Diffraction, Theor. Gen. Crystallogr. **31**, 146 (1975).
- <sup>25</sup> L.W. Finger, D.E. Cox, and A.P. Jephcoat. J. Appl. Crystallogr. **27**, 892 (1994).
- <sup>26</sup> G.K. Williamson and W.H. Hall. Acta Metall. **1**, 22 (1953).
- <sup>27</sup> A.C. Larson and R.B. Von Dreele (unpublished).
- <sup>28</sup> P.W. Stephens. J. Appl. Crystallogr. **32**, 281 (1999).
- <sup>29</sup> C. Muller, J.-L. Baudour, V. Madigou, F. Bouree, J.-M. Kiat, C. Favotto, and M. Roubin. Acta Crystallogr., Sect. B: Struct. Sci. **55**, 8 (1999).
- <sup>30</sup> A.M. Glazer and S.A. Mabud. Acta Crystallogr., Sect. B: Struct. Crystallogr. Cryst. Chem. **34**, 1065 (1978).
- <sup>31</sup> R.J. Nelmes and W.F. Kuhs. Solid State Commun. **54**, 721 (1985).
- <sup>32</sup> The structure factor correction is defined in terms of the anisotropic  $u_{ij}$  thermal factors as  $\exp\{-[2\pi^2(\sum_i j u_{ij} a_i^* a_j^*)]\}$ ,  $a_i^*$  being the lattice vectors of the reciprocal unit cell.
- <sup>33</sup> L.B. McCusker, R.B. von Dreele, D.E. Cox, D. Louër, and P. Scardi. J. Appl. Crystallogr. **32**, 36 (1999).
- <sup>34</sup> K. Itoh, L.Z. Zeng, E. Nakamura, and N. Mishima. *Ferroelectrics* **63**, 29 (1985).
- <sup>35</sup> C. Malibert, B. Dkhil, J.M. Kiat, D. Durand, J.F. Berar, and A. Spasojevic-de Bire. J. Phys.: Condens. Matter **9**, 7485 (1997).
- <sup>36</sup> G. Shirane, R. Pepinski, and B.C. Frazer. Acta Crystallogr. **9**, 131 (1956).
- <sup>37</sup> A.P. Wilkinson, J. Xu, S. Pattanaik, and J.L. Billinge. Chem. Mater. **10**, 3611 (1998).
- <sup>38</sup> L. Bellaiche and D. Vanderbilt. Phys. Rev. Lett. **83**, 1347 (1999).
- <sup>39</sup> S. Teslic, T. Egami, and D. Viehland. J. Phys. Chem. Solids **57**, 1537 (1996); *Ferroelectrics* **194**, 271 (1997).
- <sup>40</sup> D.L. Corker, A.M. Glazer, W. Kaminsky, R.W. Whatmore, J. Dec, and K. Roleder. Acta Crystallogr., Sect. B: Struct. Sci. **54**, 18 (1998).
- <sup>41</sup> S. Teslic and T. Egami. Acta Crystallogr., Sect. B: Struct. Sci. **54**, 750 (1998).
- <sup>42</sup> A.M. Glazer, S.A. Mabud, and R. Clarke. Acta Crystallogr., Sect. B: Struct. Crystallogr. Cryst. Chem. **34**, 1060 (1978).
- <sup>43</sup> A. Amin, R.E. Newnham, L.E. Cross, and D.E. Cox. J. Solid State Chem. **37**, 248 (1981).
- <sup>44</sup> The rhombohedral unit cell can be expressed in terms of a monoclinic one by  $a_m = 2a_r \cos(\alpha/2)$ ,  $b_m = 2a_r \sin(\alpha/2)$ ,  $c_m = a_r$ ,  $\beta = 180^\circ - \phi$ , where  $\cos \phi = 1 - 2\sin^2(\alpha/2)/\cos(\alpha/2)$  and  $a_r$  and  $\alpha$  are the  $R3m$  cell parameters. Note that  $a_r$  in Ref. 43 refers to the doubled cell.
- <sup>45</sup> V. Bonny, M. Bonin, P. Sciau, K.J. Schenk, and G. Chapuis. Solid State Commun. **102**, 347 (1997).
- <sup>46</sup> N. Lampis, P. Sciau, and A.G. Lehmann. J. Phys.: Condens. Matter **11**, 3489 (1999).
- <sup>47</sup> L.A. Shuvalov. J. Phys. Soc. Jpn. **28**, 38 (1970).
- <sup>48</sup> S.C. Abrahams and E.T. Keve. *Ferroelectrics* **2**, 129 (1971).
- <sup>49</sup> X.-h. Du, J. Zheng, U. Belegundu, and K. Uchino. Appl. Phys. Lett. **72**, 2421 (1998).
- <sup>50</sup> K. Fujishiro, R. Vlokh, Y. Uesu, Y. Yamada, J.-M. Kiat, B. Dkhil, and Y. Yamashita, *Ferroelectrics* (to be published).

# **APPENDIX 10**

# Origin of the high piezoelectric response in $\text{PbZr}_{1-x}\text{Ti}_x\text{O}_3$

R. Guo<sup>1</sup>, L.E. Cross<sup>1</sup>, S-E. Park<sup>1</sup>, B. Noheda<sup>2,3</sup>, D.E. Cox<sup>3</sup>, and G. Shirane<sup>3</sup>

<sup>1</sup>Mat. Res. Lab., Pennsylvania State University, PA 16802-4800

<sup>2</sup>Universidad Autonoma de Madrid, 28049-Madrid, Spain

<sup>3</sup>Brookhaven National Laboratory, Upton, NY 11973-5000

(December 7, 1999)

High resolution x-ray powder diffraction measurements on poled  $\text{PbZr}_{1-x}\text{Ti}_x\text{O}_3$  (PZT) ceramic samples close to the rhombohedral-tetragonal phase boundary (the so-called morphotropic phase boundary, MPB) have shown that for both rhombohedral and tetragonal compositions, the piezoelectric elongation of the unit cell does not occur along the polar directions but along those directions associated with the monoclinic distortion. This work provides the first direct evidence for the origin of the very high piezoelectricity in PZT.

The ferroelectric  $\text{PbZr}_{1-x}\text{Ti}_x\text{O}_3$  (PZT) system has been extensively studied because of its interesting physical properties close to the morphotropic phase boundary (MPB), the nearly vertical phase boundary between the tetragonal and rhombohedral regions of the phase diagram close to  $x=0.50$ , where the material exhibits outstanding electromechanical properties [1]. The existence of directional behavior for the dielectric and piezoelectric response functions in the PZT system has been predicted by Du *et al.* [2], [3] from a phenomenological approach [4]. These authors showed that for rhombohedral compositions the piezoelectric response should be larger for crystals oriented along the [001] direction than for those oriented along the [111] direction. Experimental confirmation of this prediction was obtained [5,6,7] for the related ferroelectric relaxor system  $\text{PbZn}_{1/3}\text{Nb}_{2/3}\text{-PbTiO}_3$  (PZN-PT), which has a rhombohedral-to-tetragonal MPB similar to that of PZT, but it has not been possible to verify similar behavior in PZT due to the lack of single crystals. Furthermore, *ab initio* calculations based on the assumption of tetragonal symmetry, that have been successful for calculating the piezoelectric properties of pure  $\text{PbTiO}_3$  [8,9,10,11], were unable to account for the much larger piezoelectric response in PZT compositions close to the MPB. Thus, it is clear that the current theoretical models lack some ingredient which is crucial to understanding the striking piezoelectric behavior of PZT.

The stable monoclinic phase recently discovered in the ferroelectric  $\text{PbZr}_{1-x}\text{Ti}_x\text{O}_3$  system (PZT) close to the MPB [12], provides a new perspective to view the rhombohedral-to-tetragonal phase transformation in PZT and in other systems with similar phase boundaries [13]. We believe that, very likely, it plays a key role in explaining some of the unsolved puzzles of PZT. The polar axis of this monoclinic phase is contained in the (110) plane along a direction between that of the tetragonal and rhombohedral polar axes [12]. An investigation of several compositions around the MPB has suggested a modification of the PZT phase diagram [1] as shown in Fig. 1(top right) [13].

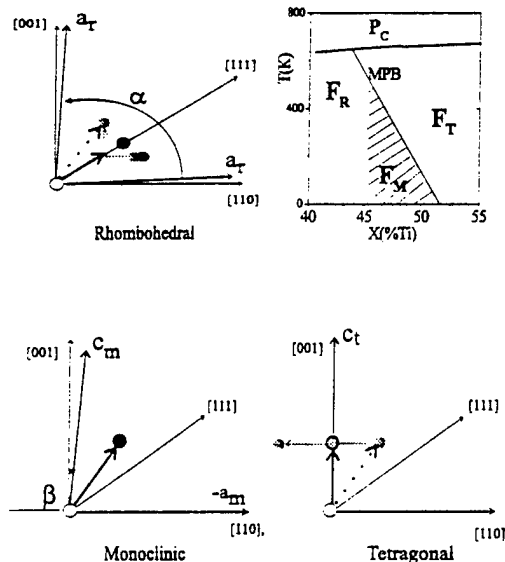


FIG. 1. Schematic view of the PZT phase diagram in the vicinity of the MPB showing the monoclinic region (top right). A projection of the rhombohedral (top left), monoclinic (bottom left) and tetragonal (bottom right) unit cells on the pseudo-cubic (110) plane is sketched. The solid circles represent the observed lead shifts with respect to the ideal cubic structure and the grey circles the locally-disordered shifts, four in the tetragonal phase and three in the rhombohedral phase. The heavy dashed arrows represent the freezing-out of one of these shifts to give the observed long-range monoclinic structure [13].

A local order different from the long-range order in the rhombohedral and tetragonal phases has been proposed from a detailed structural data analysis. Based on this, a model has been constructed in which the monoclinic distortion (Fig. 1, bottom-left) can be viewed as either a condensation along one of the  $\langle 110 \rangle$  directions of the local displacements present in the tetragonal phase [13] (Fig. 1 bottom-right), or as a condensation of the local displacements along one of the  $\langle 100 \rangle$  directions present in

the rhombohedral phase [14] (Fig. 1 top-left). The monoclinic structure, therefore, represents a bridge between these two phases and provides a microscopic picture of the MPB region [13].

In the present work experimental evidence of an enhanced elongation along [001] for rhombohedral PZT and along [101] for tetragonal PZT ceramic disks revealed by high-resolution x-ray diffraction measurements during and after the application of an electric field is presented. This experiment was originally designed to address the question whether poling in the MPB region would simply change the domain population in the ferroelectric material, or whether it would induce a permanent change in the unit cell. As shown below, from measurements of selected peaks in the diffraction patterns, a series of changes in the peak profiles from the differently oriented grains are revealed which provide key information about the PZT problem.

$\text{PbZr}_{1-x}\text{Ti}_x\text{O}_3$  ceramic samples with  $x = 0.42$ ,  $0.45$  and  $0.48$  were prepared by conventional solid-state reaction techniques using high purity (better than 99.9%) lead carbonate, zirconium oxide and titanium oxide as starting compounds. Powders were calcined at  $900^\circ\text{C}$  for six hours and recalcined as appropriate. After milling, sieving, and the addition of the binder, the pellets were formed by uniaxial cold pressing. After burnout of the binder, the pellets were sintered at  $1250^\circ\text{C}$  in a covered crucible for 2 hours, and furnace-cooled. During sintering,  $\text{PbZrO}_3$  was used as a lead source in the crucible to minimize volatilization of lead. The sintered ceramic samples of about 1 cm diameter were ground to give parallel plates of 1 mm thickness, and polished with  $1\ \mu\text{m}$  diamond paste to a smooth surface finish. To eliminate strains caused by grinding and polishing, samples were annealed in air at  $550^\circ\text{C}$  for five hours and then slow-cooled. Silver electrodes were applied to both surfaces of the annealed ceramic samples and air-dried. Disks of all compositions were poled under a DC field of  $20\ \text{kV/cm}$  at  $125^\circ\text{C}$  for 10 minutes and then field-cooled to near room temperature. The electrodes were then removed chemically from the  $x = 0.42$  and  $0.48$  samples. For the  $x = 0.45$  sample (which had been ground to a smaller thickness, about  $0.3\ \text{mm}$ ), the electrodes were retained, so that diffraction measurements could be carried out under an electric field.

Several sets of high-resolution synchrotron x-ray powder diffraction measurements were made at beam line X7A at the Brookhaven National Synchrotron Light Source. A Ge(111) double-crystal monochromator was used in combination with a Ge(220) analyser, with a wavelength of about  $0.8\ \text{\AA}$  in each case. In this configuration, the instrumental resolution,  $\Delta 2\theta$ , is an order-of-magnitude better than that of a conventional laboratory instrument (better than  $0.01^\circ$  in the  $2\theta$  region  $0-30^\circ$ ). The poled and unpoled pellets were mounted in symmetric reflection geometry and scans made over selected

peaks in the low-angle region of the pattern. It should be noted that since lead is strongly absorbing, the penetration depth below the surface of the pellet at  $2\theta = 20^\circ$  is only about  $2\ \mu\text{m}$ . In the case of the  $x = 0.45$  sample, the diffraction measurements were carried out with an electric field applied in-situ via the silver electrodes.

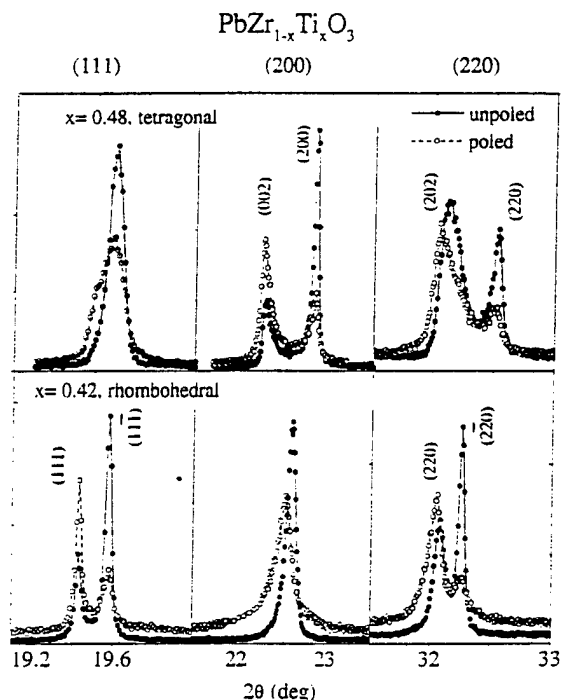


FIG. 2. Comparison of (111), (200) and (220) pseudo-cubic reflections for the  $x = 0.48$  (tetragonal), and  $x = 0.42$  (rhombohedral) PZT compositions before and after poling

Powder diffraction measurements on a flat plate in symmetric reflection, in which both the incident and the diffracted wave vectors are at the same angle,  $\theta$ , with the sample plate, ensures that the scattering vectors are perpendicular to the sample surface. Thus only crystallites with their scattering vector parallel to the applied electric field are sampled. Scans over selected regions of the diffractogram, containing the (111), (200) and (220) pseudo-cubic reflections, are plotted in Fig. 2 for poled and unpoled PZT samples with the compositions  $x = 0.48$  (top) and  $x = 0.42$  (bottom), which are in the tetragonal and rhombohedral region of the phase diagram, respectively. The diffraction profiles of the poled and unpoled samples show very distinctive features. For the tetragonal composition (top), the (200) pseudo-cubic reflection (center) shows a large increase in the tetragonal (002)/(200) intensity ratio after poling due to the change in the domain population, which is also reflected in the increased (202)/(220) intensity ratio in the right

side of the figure. In the rhombohedral composition with  $x = 0.42$  (bottom of Fig.2), the expected change in the domain population can be observed from the change of the intensity ratios of the rhombohedral (111) and (11 $\bar{1}$ ) reflections (left side) and the (220) and (2 $\bar{2}$ 0) reflections (right side).

In addition to the intensity changes, the diffraction patterns of the poled samples show explicit changes in the peak positions with respect to the unpoled samples, corresponding to specific alterations in the unit cell dimensions. In the rhombohedral case ( $x = 0.42$ ), the electric field produces no shift in the (111) peak position (see bottom-left plot in Fig.2), indicating the absence of any elongation along the polar directions after the application of the field. In contrast, the poling does produce a notable shift of the (001) reflections (center plot), which corresponds to a very significant change of d-spacing, with  $\Delta d/d = 0.32\%$ ,  $\Delta d/d$  being defined as  $(d_p - d_u)/d_u$ , where  $d_p$  and  $d_u$  are the d-spacings of the poled and unpoled samples, respectively. This provides experimental confirmation of the behavior predicted by Du *et al.* [3] for rhombohedral PZT, as mentioned above. The induced change in the dimensions of the unit cell is also reflected as a smaller shift in the (202) reflection (right side plot), corresponding to a  $\Delta d/d$  along [101] of 0.12%.

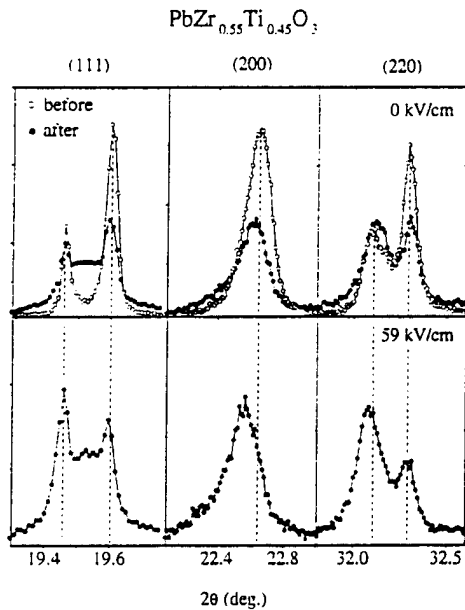


FIG. 3. (111), (200) and (220) pseudocubic reflections for PZT with  $x = 0.45$  measured on an unpoled sample (open circles) and on a similar sample after the application and removal of a field of 59 kV/cm at room temperature (solid circles) are plotted in the upper part of the figure. The scattered intensity at  $2\theta = 19.52^\circ$  from the second sample corresponds to the (111) reflection from the silver electrode. Measurements on the latter sample under an electric field of 59 kV/cm applied *in situ* are plotted in the lower part of the figure.

In the tetragonal case for  $x = 0.48$  (top of Fig.2), there is no peak shift observed along the polar [001] direction (center plot), but the (202) and the (111) reflections exhibit striking shifts (right and left sides, respectively). Furthermore, this composition, which at room temperature is just at the monoclinic-tetragonal phase boundary, shows, after poling, a clear tendency towards monoclinic symmetry, in that the (111) and (202) reflections, already noticeably broadened in the unpoled sample and indicative of an incipient monoclinicity, are split after poling. These data clearly demonstrate, therefore, that whereas the changes induced in the unit cell after the application of an electric field do not increase either the rhombohedral or the tetragonal strains, a definite elongation is induced along those directions associated with the monoclinic distortion.

In addition to the measurements on the poled and unpoled samples, diffraction measurements were performed *in situ* on the rhombohedral PZT sample with  $x = 0.45$  as a function of applied electric field at room temperature. The results are shown in Fig.3 where the (111), (200) and (220) pseudo-cubic reflections are plotted with no field applied (top) and with an applied field of 59 kV/cm field (bottom). The top part of the figure also shows data taken after removal of the field. As can be seen, measurements with the field applied show no shift along the polar [111] direction but, in contrast, there is a substantial shift along the [001] direction similar to that for the poled sample with  $x = 0.42$  shown in Fig. 2, proving that the unit cell elongation induced by the application of a field during the poling process corresponds to the piezoelectric effect induced by the in-situ application of a field. Comparison of the two sets of data for  $x = 0.45$  before and after the application of the field shows that the poling effect of the electric field at room temperature is partially retained after the field is removed, although the poling is not as pronounced as for the  $x = 0.42$  sample in Fig. 2.

A quantification of the induced microstrain along the different directions has been made by measuring the peak shifts under fields of 31 and 59 kV/cm. In Fig. 4,  $\Delta d/d$  is plotted *versus* the applied field,  $E$ , for the (200) and (111) reflections. These data show an approximately linear increase in  $\Delta d/d$  for (200) with field, with  $\Delta d/d = 0.30\%$  at 59 kV/cm, corresponding to a piezoelectric coefficient  $d_{33} \approx 500$  pm/V, but essentially no change in the d-spacing for (111).

It is interesting to compare in Fig.4 the results of dilatometric measurements of the macroscopic linear elongation ( $\Delta l/l$ ) on the same pellet, which must also reflect the effects of domain reorientation. At higher fields, this contribution diminishes and one could expect the  $\Delta l/l$  vs.  $E$  curve to fall off between those for the [100] and [111] oriented grains, typical of the strain behaviour of polycrystalline ceramics [15]. Although such a trend is seen above 30 kV/cm, it is intriguing to note that be-

low this value, the macroscopic behavior is essentially the same as the microscopic behavior for the (200) reflection.

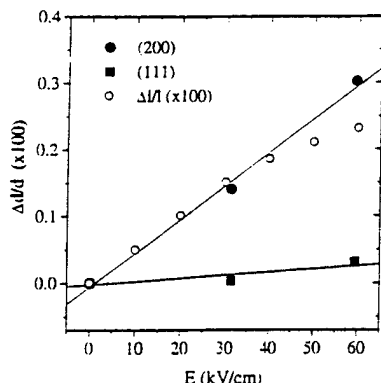


FIG. 4. Fractional change of d-spacing,  $\Delta d/d$  for PZT with  $x=0.45$  from the rhombohedral (200) and (111) reflections as a function of electric field (closed symbols). Dilatometric measurements of the macroscopic  $\Delta l/l$  for the same pellet are also shown (open circles)

We therefore conclude that the piezoelectric strain in PZT close to the morphotropic phase boundary, which produces such striking electromechanical properties, is not along the polar directions associated with the monoclinic distortion. This supports a model based on the existence of local monoclinic shifts superimposed on the rhombohedral and tetragonal displacements in PZT which has been proposed from a detailed structural analysis of tetragonal [13] and rhombohedral [14] PZT samples.

As demonstrated above, these high resolution powder data provide key information to understanding the piezoelectric effect in PZT. In particular, they allow an accurate determination of the elongation of the unit cell along the direction of the electric field, although they give no information about the dimensional changes occurring along the perpendicular directions, which would give a more complete characterization of the new structure induced by the electric field. It is interesting to note that in the case of the related ferroelectric system PZN-PT, the availability of single crystals has allowed Durbin *et al.* [7] to carry out diffraction experiments along similar lines at a laboratory x-ray source. Synchrotron x-ray experiments by the present authors are currently being undertaken on PZN-PT single crystals with Ti content of 4.5 and 8% under an electric field, and also on other ceramic PZT samples. Preliminary results on samples with  $x=0.46$  and  $0.47$ , which are monoclinic at room temperature, have already been obtained. In these cases, the changes of the powder profiles induced by poling are so drastic that further work is needed in order to achieve a proper interpretation.

We thank A. M. Glazer, J.A. Gonzalo and K. Uchino for their stimulating discussions, B. Jones and E. Alberta for assisting in the sample preparation, and A. L. Langhorn for his invaluable technical support. Financial support by the U.S. Department of Energy under contract No. DE-AC02-98CH10886, and by ONR under project MURI (N00014-96-1-1173) is also acknowledged.

- [1] B. Jaffe, W.R. Cook, and H. Jaffe, *Piezoelectric Ceramics*, Academic Press, London (1971).
- [2] X-h Du, U. Belegundu, and K. Uchino, *Jpn. J. Appl. Phys.* **36**, 5580 (1997).
- [3] X-h Du, J. Zheng, U. Belegundu, and K. Uchino, *Appl. Phys. Lett.* **72**, 2421 (1998).
- [4] M. J. Haun, E. Furman, S-J. Jang, and L.E. Cross, *Ferroelectrics* **72**, 13(1989).
- [5] J. Kuwata, K. Uchino, and S. Nomura, *Jpn. J. Appl. Phys.* **21**, 1298(1982).
- [6] S-E. Park and T. R. Shrout, *J. Appl. Phys.* **82**, 1804 (1997).
- [7] M. K. Durbin, E.W. Jacobs, J.C. Hicks, and S.-E. Parks, *Appl. Phys. Lett.* **74**, 2848 (1999).
- [8] K.M. Rabe and E. Cockayne, in *First-Principles Calculations for Ferroelectrics: Fifth Williamsburg Workshop*, edited by R.E. Cohen (AIP, Woodbury, 1998), p. 61.
- [9] G. Saghi-Szabo, R.E. Cohen, and H. Krakauer, *Phys. Rev. Lett.* **80**, 4321 (1998).
- [10] G. Saghi-Szabo, R.E. Cohen, and H. Krakauer, *Phys. Rev. B* **59**, 12771 (1999).
- [11] L. Bellaiche and D. Vanderbilt, *Phys. Rev. Lett.* **83**, 1347 (1999).
- [12] B. Noheda, D.E. Cox, G. Shirane, J.A. Gonzalo, L.E. Cross, and S-E. Park, *Appl. Phys. Lett.* **74**, 2059 (1999).
- [13] B. Noheda, J. A. Gonzalo, L.E. Cross, R. Guo, S-E. Park, D.E. Cox, and G. Shirane, (to be published), e-print: cond-mat/9910066.
- [14] D.L. Corker, A.M. Glazer, R.W. Whatmore, A. Stallard, and F. Fauth, *J. Phys.:Condens. Matter* **10**, 6251 (1998).
- [15] S.-E. Park, T.R. Shrout, P. Bridenbaugh, J. Rottenberg, and G. Loiacono, *Ferroelectrics* **207**, 519 (1998).

# **APPENDIX 11**

# Electromechanical Properties of Lead Zirconate Titanate Piezoceramics Under the Influence of Mechanical Stresses

Qiming M. Zhang, *Member, IEEE*, and Jianzhong Zhao

**Abstract**—In lead zirconate titanate piezoceramics, external stresses can cause substantial changes in the piezoelectric coefficients, dielectric constant, and elastic compliance due to nonlinear effects and stress depoling effects. In both soft and hard PZT piezoceramics, the aging can produce a memory effect that will facilitate the recovery of the poled state in the ceramics from momentary electric or stress depoling. In hard PZT ceramics, the local defect fields built up during the aging process can stabilize the ceramic against external stress depoling that results in a marked increase in the piezoelectric coefficient and electromechanical coupling factor in the ceramic under the stress. Although soft PZT ceramics can be easily stress depoled (losing piezoelectricity), a DC bias electric field, parallel to the original poling direction, can be employed to maintain the ceramic poling state so that the ceramic can be used to high stresses without depoling.

## I. INTRODUCTION

PIEZOELECTRIC ceramics, especially lead zirconate titanate ceramics (PZT), are widely used in electromechanical actuators, sensors, and transducers [1], [2]. In these applications, piezoceramics often are subjected to high mechanical stress. For instance, in high power underwater transducers, a high compressive stress is used to prestress the piezoceramic so that even at high electric driving fields, the ceramic is still in a compressive state. Because ceramics inherently have a much higher mechanical strength under compressive stresses compared with extensive stresses, prestress can improve the reliability of a ceramic transducer or actuator significantly [1]. Due to nonlinear effects, one of the direct consequences of the high mechanical stress is the change of material properties from their stress-free values [3]–[7]. In addition, the piezoelectric state in PZT ceramics is a result of poling of the ceramic. When a high mechanical stress is applied to the ceramic, it will reorient the polarization directions at each grain and may cause depoling of the piezoceramic [8]–[10]. This will certainly impose a limit on the maximum stress level that can be applied to a piezoceramic. Therefore, in order to properly utilize these piezoceramics in various actuator and transducer applications, the nonlinear behavior under stress and limiting stress field should be studied in these ceramics.

In studying the effect of mechanical stresses on the responses of PZT piezoceramics, it is also important to realize that aging and deaging processes may play a significant role in modifying the material properties [11], [12]. Aging in PZT ceramics is a process of slow and spontaneous evolution of the material properties with time after it is forced to a new state due to poling, large change of temperature, or subject to a high mechanical stress. For instance, after poling, mechanical stresses and charge imbalance at grain boundaries exist due to the redirection of the polarization at each domain to be close to the poling direction in the poling process. A slow reorientation of domains after poling will reduce the mechanical stress at grain boundaries: this plus drafting of space charges also will compensate for the charge imbalance to minimize the elastic and electric free energy in the ceramics [11], [12]. Correspondingly, there is a reduction of the piezoelectric, dielectric, and elastic compliance due to the stabilization of the domain configuration through the aging, a well-known phenomenon that occurs in both soft and hard PZT ceramics. In addition, commercial PZT piezoceramics are either acceptor (such as Fe, Co, Mn, Cr, etc.) or donor (such as La, Nb, Sb, etc.) doped to improve the material performance [2]. The dopants will induce either oxygen or lead vacancies in the lattice, forming mobile or immobile charged defects such as dipoles as well as local stress fields [2], [13]. The mobile charged defects will align themselves to the polar direction of the domain they reside to build local fields that, in turn, stabilize a domain configuration to form so-called hard PZT. Immobile defects cause frustration in the domains to form soft PZT [2], [13]. Hence, in hard PZT ceramics, there is a second aging process associated with the reorientation of the mobile charged defects. After a long time aging, a PZT ceramic will reach a state in which its properties do not show much change with time when external conditions remain unchanged and the ceramic is in an aged state (or aged). If an aged PZT ceramic is forced to change to another state by external fields (stress or electric field) or large temperature variation, a new domain configuration will form that may not be compatible with the established grain boundary conditions and local defect fields (in hard PZT). Correspondingly, the material is in a metastable state (deaged), yielding higher dielectric constant, piezoelectric coefficients, and elastic compliance.

In this paper, we report the effect of uniaxial compressive stress, applied parallel to the initial poling direction, on the piezoelectric coefficient, dielectric constant, and

Manuscript received January 8, 1999; accepted June 14, 1999. This work was supported by the Office of Naval Research.

The authors are with the Materials Research Laboratory and Department of Electrical Engineering, The Pennsylvania State University, University Park, PA 16802 (e-mail: qxz1@psu.edu).

TABLE I  
THE PROPERTIES OF PZT PIEZOCERAMICS UNDER-STRESS FREE  
CONDITION.

Material	PZT-5H	PZT-5A	PZT-4	PZT-8
$d_{33}^1$	593	374	296	225
$d_{31}$	-274	-171	-123	-97
$K_{33}$	3400	1700	1300	1000
$s_{33}$	20.7	18.8	15.5	13.9
$s_{13}$	-8.45	-7.22	-5.31	-4.6
$s_{11}$	16.5	16.4	12.3	11.1
$k_{33}$	0.75	0.7	0.7	0.64
$k_{31}$	0.39	0.34	0.33	0.3

<sup>1</sup> $d = \text{pC/N}$ ,  $s = 10^{-12} \text{ m}^2/\text{N}$ ,  $K_{33} = \epsilon_{33}/\epsilon_{01}$ ,  
where  $\epsilon_0$  is the vacuum permittivity.

elastic compliance of PZT piezoceramics. For soft PZT ceramics, the effect of limiting stress level on the piezoelectric coefficients and the DC electric bias field to stabilize the polarization against the stress depoling were also evaluated. For hard PZT ceramics, the aging of the piezoelectric coefficient under a constant stress was measured. In addition, we also compared the polarization hysteresis loops of PZT ceramics investigated here in both aged and fresh (deaged) specimens to quantify the effect of aging on these ceramics.

## II. EXPERIMENTS

The PZT ceramic samples selected for the study are PZT-5H, PZT-5A, PZT-4, and PZT-8.<sup>1</sup> PZT-5H and PZT-5A are donor doped (La in PZT-5H and Nb in PZT-5A). PZT-4 and PZT-8 are acceptor doped (Cr in PZT-4 and Fe and Mn in PZT-8). PZT-5H and PZT-5A are soft-type PZT that have high piezoelectric, dielectric, and elastic compliance. PZT-4 and PZT-8 are hard-type PZT that have relatively low piezoelectric, dielectric, and elastic compliance. For convenience, the relevant parameters for these materials (aged) at stress free conditions are listed in Table I.

For a piezoelectric ceramic material, the relevant parameters are defined by the constitutive equations<sup>2</sup>:

$$D_i = \epsilon_{ij}^T E_j + d_{im}^d T_m \quad (1a)$$

$$S_k = d_{jk}^c E_j + s_{km}^E T_m \quad (1b)$$

where  $D_i$  is the electric displacement,  $E_j$  is the applied electric field,  $S_k$  is the strain component, and  $T_m$  is the stress component ( $i, j = 1 - 3$ , and  $m, k = 1 - 6$ ). The proportional coefficients  $\epsilon_{ij}^T$ ,  $d_{im}^d$ ,  $d_{jk}^c$ , and  $s_{km}^E$  are the dielectric permittivity, the piezoelectric coefficients of the direct and converse effects, and the elastic compliance, respectively. In PZT piezoceramics, even under high external stress cycles, and for both fully poled and partially poled

ceramics the direct and converse piezoelectric coefficients are approximately equal to each other and, therefore, they will not be distinguished here [10]. As mentioned in the introduction, these parameters will change with applied mechanical stress that will be investigated.

The details of the experimental set-up that provides required uniaxial stress have been described in another publication [10]. It is a modified Universal Test Machine (UTM, Series 1101 from ATS) in which a multilayer ceramic actuator and a feedback control loop were added. The function of this added unit is to provide a precise control of the stress level on the test specimen over a broad frequency range [10]. The dimensions of the test specimen in the mechanical stress experiment were  $4.8 \times 4.8 \times 5 \text{ mm}^3$ . In order to satisfy the requirement that the length of the sample should be at least three times longer than the lateral dimension to ensure a uniaxial stress condition, three ceramic samples were stacked together to form a test sample assembly of dimensions  $4.8 \times 4.8 \times 15 \text{ mm}^3$ . To further reduce the end clamping effect in the lateral directions on the experimental result, the data were taken from the sample at the middle when all three sections were subjected to the same driving conditions. For example, for  $d_{33}$  and  $d_{31}$  measurement, the same voltage was applied to the three sections and only the strain response at the middle section was taken. An experiment also was conducted with five ceramic cubes stacked together to have a dimension of test sample assembly of  $4.8 \times 4.8 \times 25 \text{ mm}^3$ , and the strain responses from the three middle sections were measured. The results showed that, within the experimental error (5%), the field-induced strains from the three middle sections are nearly the same and are equal to that measured from the sample in the middle section of the three section stack, which indicates that the middle section sample in the three section stack can be regarded as in a uniaxial stress state.

The polarization hysteresis loop was measured by a standard Sawyer-Tower circuit at 10 Hz. The dielectric constant was measured using a multi-frequency LCR meter (HP model 4192A). The strain response of the samples was measured by a strain gauge (KYOWA KFR-02-120-C1-11). To improve the signal-to-noise ratio, the voltage signal from the strain gauge amplifier was measured by a phase-sensitive detector (a lock-in amplifier).

For the dielectric constant and  $d_{ij}$  measurement, the results did not crucially depend on the alignment of the specimen. However, for  $s_{ij}^E$  measurement, a large error may occur even for a very small misalignment of the sample (the stress was not uniformly applied to the test sample) or if the sample was not prepared properly so that the two faces that were subjected to the stress were not exactly parallel to each other. A special sample holder was designed to ensure a proper alignment of the test samples, and two strain gauges were attached to the opposite faces of the specimen to monitor the strain responses.

The results on the dielectric constant, piezoelectric coefficient, and elastic compliance were acquired at room temperature and a frequency of 10 Hz. On change of the stress

<sup>1</sup>PZT-5H, PZT-5A, PZT-4, and PZT-8 are the trade marks of Morgan Matroc, Inc., Bedford, OH, for its PZT piezoceramics.

<sup>2</sup>IEEE Standard on Piezoelectricity, ANSI/IEEE, Std. 176, 1988.

level, a finite time period is expected for the material to reach a new equilibrium state (aging). Most of the changes of the data occurred during the first 5 minutes after the change of the DC stress level. We also examined several samples under a longer waiting period and found that there was not marked change in the weak signal properties between the data taken after 10 minutes and after 1 day. This relatively fast aging is associated with the change due to the grain boundary stress and charge imbalance, and it occurs in both soft and hard PZT ceramics. For hard PZT, there is an additional aging process that takes a much longer time associated with the reorientation of local defect dipoles (several weeks or longer). Hence, in order to carry out a meaningful measurement within a reasonable time frame, except otherwise stated, the data were taken 10–15 minutes after the change of the stress level. To illustrate the effect of aging of hard PZT under stress on the properties measured, a long-time aging experiment (1 month) also was carried out, and the results are reported. The results reported here on the dielectric constant, piezoelectric coefficient, and elastic compliance were taken from the first stress cycle.

### III. RESULTS AND DISCUSSION

#### A. The Polarization Hysteresis Loops in Soft and Hard PZT Ceramics

To a large extent, the properties of PZT piezoceramics are determined by the state of the ceramic after poling. Aging results in a change in electromechanical properties of PZT ceramics after poling [11]. Thus, poled states of aged and fresh (deaged) specimens were first investigated in terms of their polarization hysteresis loops.

Fig. 1 presents the polarization hysteresis loops for aged PZT ceramics recorded from the first few cycles. These are the samples obtained from the manufacturer and are aged for more than 6 months. One interesting feature common to all the specimens, both soft and hard PZT, is that the switching field back to the original poling direction in aged samples after field depoling is zero, indicating a memory effect in these ceramics. For soft PZT ceramics, it took several hundred cycles to remove this memory effect; for hard PZT, it took many more cycles due to the inherent stability of the local defect fields developed during the aging [14]. We did not pursue this beyond a thousand cycles for hard PZT: after that the ceramic remained in a strongly internal biased state. In addition, the depoling field for these aged hard PZT ceramics is much higher than that of soft PZT, a manifestation of the existence of local bias fields to stabilize the domain orientation against external fields to depole the ceramic.

In contrast, the polarization hysteresis loops for the same PZT ceramics but deaged exhibit a symmetric loop as shown in Fig. 2. The deaged (fresh) samples were prepared by heating the aged PZT ceramic to above 400°C, which is above the Curie point of all the ceramics, for more

TABLE II  
COERCIVE FIELD OF THERMALLY DEAGED PZT CERAMICS.

Material	PZT-5H	PZT-5A	PZT-4	PZT-8
$E_c$ (kV/cm)	9	14	12	15

than 1 day. As shown in Table II, the coercive field  $E_c$  of hard PZT in these deaged specimens is not higher than that in soft PZT.

Compared with the data in Figs. 1 and 2, the depoling field in aged soft PZT ceramics is nearly equal to the coercive field in deaged samples that result in a much narrower hysteresis loop in aged samples compared with deaged samples. For aged hard PZT ceramics, the depoling field is not well defined, and there are no sharp switching field, indicating a broad distribution of the local defect field strength.

Therefore, aged PZT piezoceramic can be depoled electrically or mechanically momentarily without losing substantially the polarization and piezoelectric activity after removing these fields. The observed "hard" PZT behavior in aged samples is mainly due to the alignment of local charged defects within grains that apparently have a much stronger effect on the material responses than that caused by the space charge accumulated and stress compatibility established at the grain boundaries through the aging.

#### B. The Compressive Stress $T_3$ on the Electromechanical Properties of Soft PZT Ceramics

The stress dependence of  $d_{33}$  and  $d_{31}$ ,  $K_{33}$  (dielectric constant =  $\epsilon_{33}^T/\epsilon_0$ , where  $\epsilon_0$  is the vacuum permittivity) is shown in Fig. 3 and 4, and  $s_{33}^E$  and  $s_{31}^E$  for PZT-5H and PZT-5A (the data were acquired when the stress was maintained). A one-stress cycle (from 0 to 150 MPa and back to 0) took about 8 to 10 hours. Apparently, for soft PZT there is a large drop of the piezoelectric coefficients with stress at a stress level above about 50 MPa. As the field is reduced to zero after reaching 150 MPa, the piezoelectric coefficients become much smaller than those in the originally aged samples, indicating a partial depoling in these ceramics [9]. Similarly, in these partially depoled samples, the elastic compliance also becomes smaller, and the dielectric constant does not show much change.

The experimental results reveal that soft PZT ceramics can be depoled easily by the compressive mechanical stress  $T_3$ . However, soft PZT ceramics are important piezoelectric materials for actuator and transducer applications. Therefore, the question is, what is the limiting stress level which can be applied to a soft PZT without causing a substantial depoling of the ceramic after the stress is reduced to zero. To answer this question, the piezoelectric coefficient  $d_{33}$  was measured on PZT-5H and PZT-5A at a stress-free state after the specimens were subject to a  $T_3$  (peak stress, denoted as  $T_{3,M}$ ) stress for 10 minutes. Data presented in Fig. 5 are  $d_{33}$  thus obtained (after the stress was removed) versus the applied maximum stress

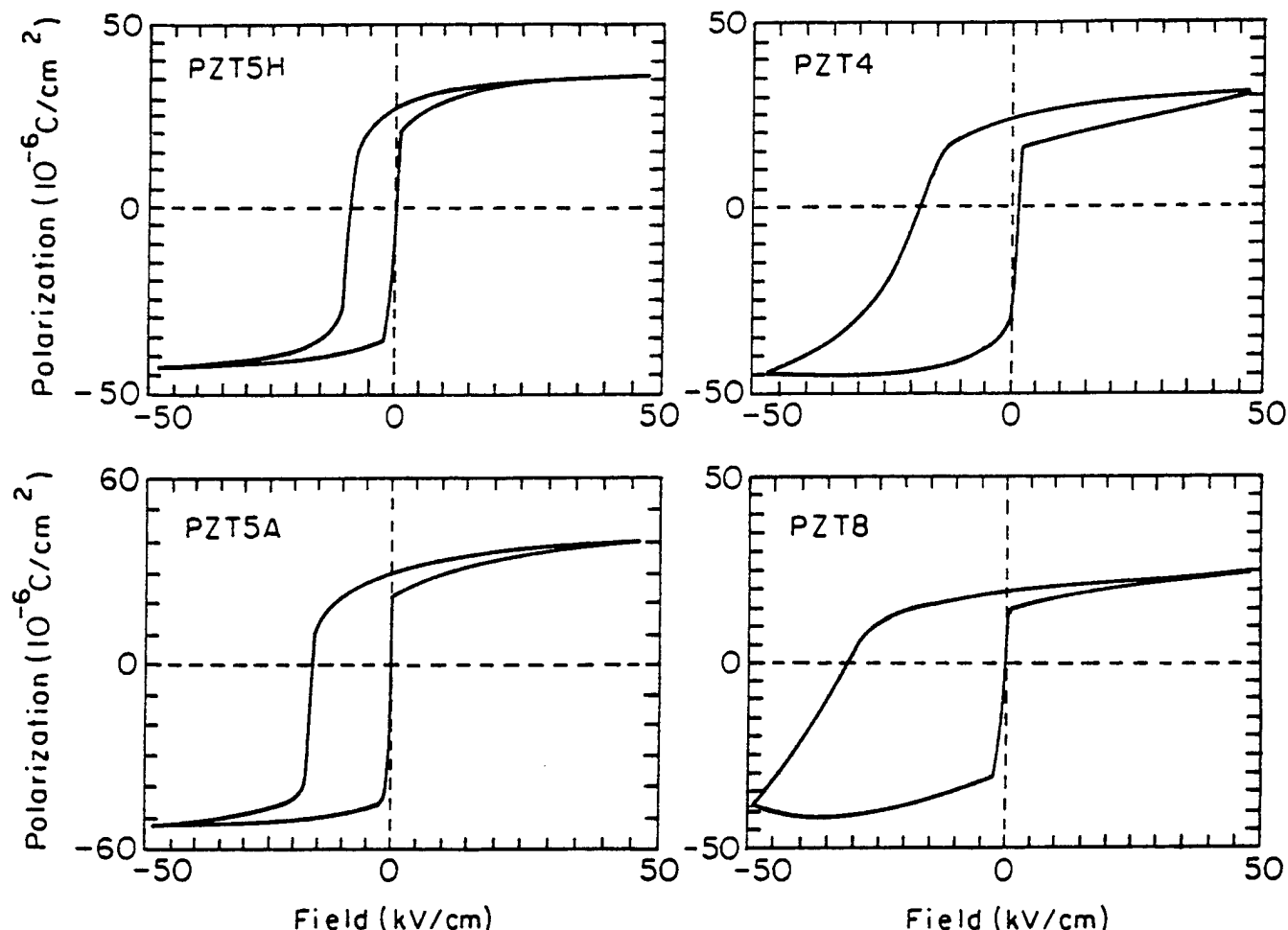


Fig. 1. The polarization hysteresis loops of aged PZT piezoceramics measured at 10 Hz.

$T_{3M}$ . To show the depoling effect due to the stress, the data are presented in the reduced unit, i.e.,  $d_{33}(\text{after the stress } T_{3M})/d_{33}(\text{sample from manufacturer})$ . In this experiment, each data point was acquired from a specimen not subjected to a stress prior to the measurement to ensure the same initial condition for each data point. In addition, each data point was repeated by a new specimen, and the difference between the two sets of data is less than 10% over the whole experimental range. If we define the stress  $T_{3M}$  that results in a reduction of  $d_{33}$  by 10% is as the limiting stress, for PZT-5H,  $T_{3M}$  is at about 50 MPa, and for PZT-5A, it is near 60 MPa. In addition, the data also reveals that, for PZT-5A, it can retain more than 70% of  $d_{33}$  even after subjected to more than 100 MPa stress. This is consistent with the fact that PZT-5A has a higher coercive field than that of PZT-5H and, hence, is more difficult to be stress depoled.

Although soft PZT can be stress depoled easily, by applying a DC bias electric field, these ceramics can be used to high stress levels without being depoled. Fig. 6 shows the change of  $d_{33}$  of PZT-5H with stress up to 150 MPa. The difference between the data in Figs. 3 and 6 is that here a DC electric field of 5 kV/cm, which is parallel to the

original poling direction, is applied to the ceramic. Apparently, after a 150 MPa stress cycle, the ceramic still can retain 90% of the original piezoelectricity. The coercive field  $E_c$  for deaged PZT-5H ceramic is at 9 kV/cm, so the result in Fig. 6 indicates that a field at below  $E_c$  can be used to stabilize a ceramic from the stress depoling. The results given here are consistent with those in Fig. 1 in aged soft PZT ceramics. There is a memory of the original poling direction and, hence, a small electric field parallel to the original poling direction can repole the ceramic back to a high polarization level.

### C. The Compressive Stress $T_3$ on the Electromechanical Properties of Hard PZT Ceramics

The stress dependence of  $d_{33}$  and  $d_{31}$ ,  $K_{33}$ , and  $s_{33}$  and  $s_{31}$  for PZT-4 and PZT-8 are shown in Figs. 7 and 8. Quite different from soft PZT ceramics, hard PZTs exhibit a large increase of piezoelectric coefficients and dielectric constant with stress. For both PZT-4 and PZT-8, the piezoelectric coefficients reach more than 40% higher than those of the aged samples measured before the stress. After a stress cycle of 150 MPa, the piezoelectric coeffi-

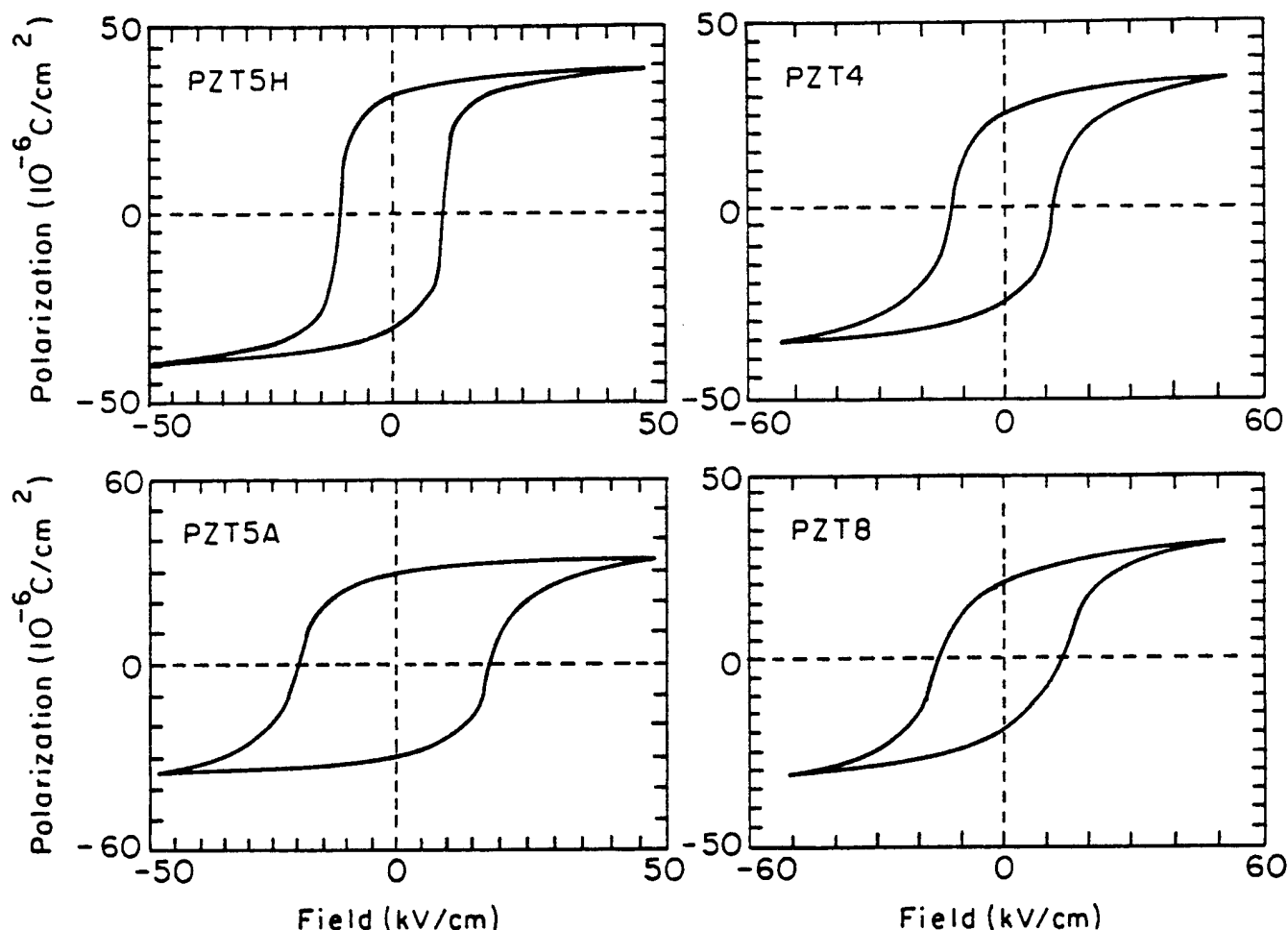


Fig. 2. The polarization hysteresis loops of thermally deaged (fresh) PZT ceramics measured at 10 Hz.

cients and dielectric constant return to the zero stress state with higher values. For PZT-8, even after a stress cycle to 280 MPa, the ceramic still can retain a  $d_{33}$  equal to the value of the aged sample before stress. This large increase in the piezoelectric coefficients also results in an increase of the electromechanical coupling factor with stress as shown in Fig. 9. And apparently, a longitudinal electromechanical coupling factor  $k_{33}$  higher than 0.85 can be obtained in hard PZT: this is far above the value, even in soft PZT.

The observed increase in the electromechanical responses in hard PZT ceramics as revealed in Figs. 7–9 is caused partially by the deaging effect. The high applied stress changes the domain orientation with respect to the local field built up by oxygen vacancies and dopants through the aging process, and this change causes the responses of the material toward soft PZT. Here, the question is whether the increased activity is caused solely by this deaging effect. In order to answer this question, an aging experiment was conducted. As shown in Fig. 10, even after a long time aging, the piezoelectric coefficient  $d_{31}$  of PZT-8 under a 90 MPa stress is still far above the value obtained under the stress free condition taken before the application of stress, which is consistent with an early ex-

perimental result [4]. The result indicates that the large increase of the piezoelectric activity observed in hard PZT ceramics under stress is more than a deaging effect. In addition, the data in Fig. 10 also show that the depoling stress for PZT-8 is higher than 90 MPa.

In fact, an increase of the piezoelectric coefficients and coupling factor with  $T_3$  stress also was observed in soft PZT, as shown in Figs. 3 and 4. Careful inspection of the figures reveals that, at stress level before depoling occurs (50 MPa), there is a slight increase of piezoelectric coefficients and coupling factor (becomes larger than 0.8). These results indicate that, by moving the polarization direction of the domains locally away from the averaged poling direction, increased non-180° domain wall motions in PZT ceramics (under  $T_3$  stress) can result in an increase in piezoelectric activity and coupling factor. This observation may resemble the experimental results on  $\text{Pb}(\text{Zn}_{1/3}\text{Nb}_{2/3})\text{O}_3$ - $\text{PbTiO}_3$  relaxor single crystals in which a high piezoelectric response and coupling factor were observed when the crystal was poled along [001] direction which is not the direction of the spontaneous polarization [15], [16].

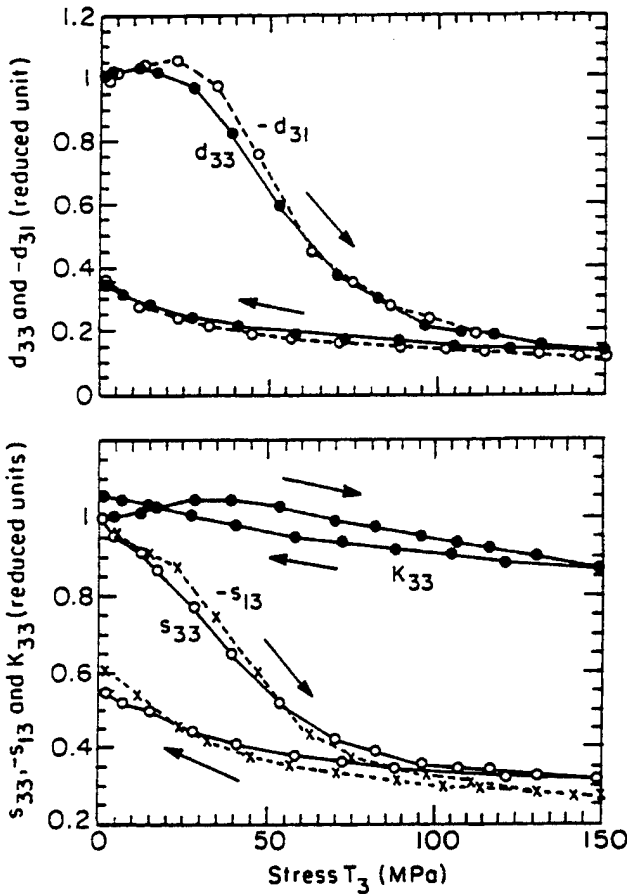


Fig. 3. The dependence of the weak signal piezoelectric coefficients ( $d_{33}$  and  $d_{31}$ ), dielectric constant  $K_{33}$ , and elastic compliance ( $s_{33}$  and  $s_{13}$ ) of PZT-5H on the compressive uniaxial stress  $T_3$ . Solid and dashed lines are drawn to guide the eyes.

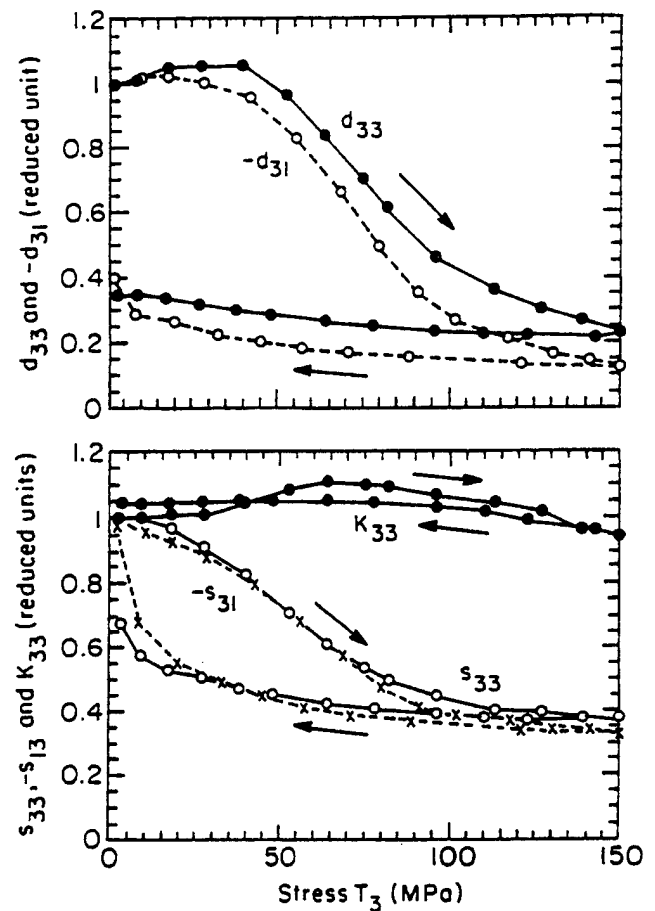


Fig. 4. The dependence of the weak signal piezoelectric coefficients ( $d_{33}$  and  $d_{31}$ ), dielectric constant  $K_{33}$ , and elastic compliance ( $s_{33}$  and  $s_{13}$ ) of PZT-5A on the compressive uniaxial stress  $T_3$ . Solid and dashed lines are drawn to guide the eyes.

#### D. Load Curves for PZT Piezoceramics

The load curves for PZT-5H, a soft PZT, and PZT-8, a hard PZT, were measured under different DC electric bias fields, and the results are presented in Fig. 11. Several features are revealed in this figure. In PZT-5H, there is a large nonlinearity in both the strain-DC applied electric field relationship and in the strain-stress relationship. In PZT-8, the nonlinear effect is much smaller. These results are consistent with the results of early publications [7], [9]. The compliance  $s_{33}^E$  measured here (under near DC condition) is more than twice that measured at 10 Hz (from the load curves under a small DC field, 1 kV/cm,  $s_{33}^E = \Delta S_3 / \Delta T_3$  is about  $40 \times 10^{-12} \text{ m}^2/\text{N}$  for PZT-5H and  $30 \times 10^{-12} \text{ m}^2/\text{N}$  for PZT-8), indicating a strong frequency dependence at very low frequency region. For hard PZT, for the DC bias fields studied, there is no large change of compliance with DC bias field. For PZT-5H, at low stress region (stress near zero), there is a slight increase of the compliance with DC electric bias field. However, the slope for the load curve under 6 kV/cm at near 20 MPa stress level becomes near half of that at low stress level (from  $47 \times 10^{-12}$  to  $23 \times 10^{-12} \text{ m}^2/\text{N}$ ).

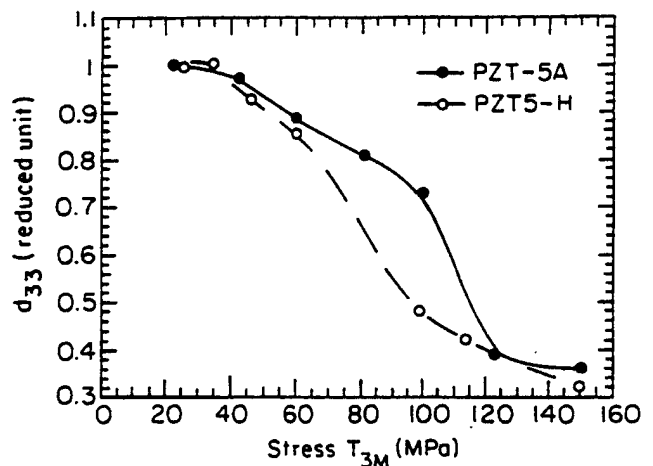


Fig. 5. The piezoelectric coefficient  $d_{31}$  retained (compared with the initial value in aged sample) after the specimen is subjected to a  $T_3$  stress and then back to stress-free state for PZT-5H. Solid and dashed lines are drawn to guide the eyes.

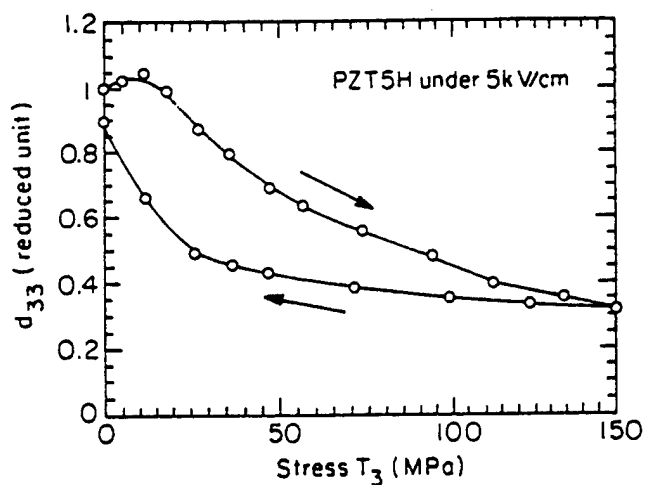


Fig. 6. The dependence of  $d_{33}$  on the compressive  $T_3$  stress while under a 5 kV/cm DC electric bias field that is parallel to the original poling direction for PZT-5H. Solid line is drawn to guide the eyes.

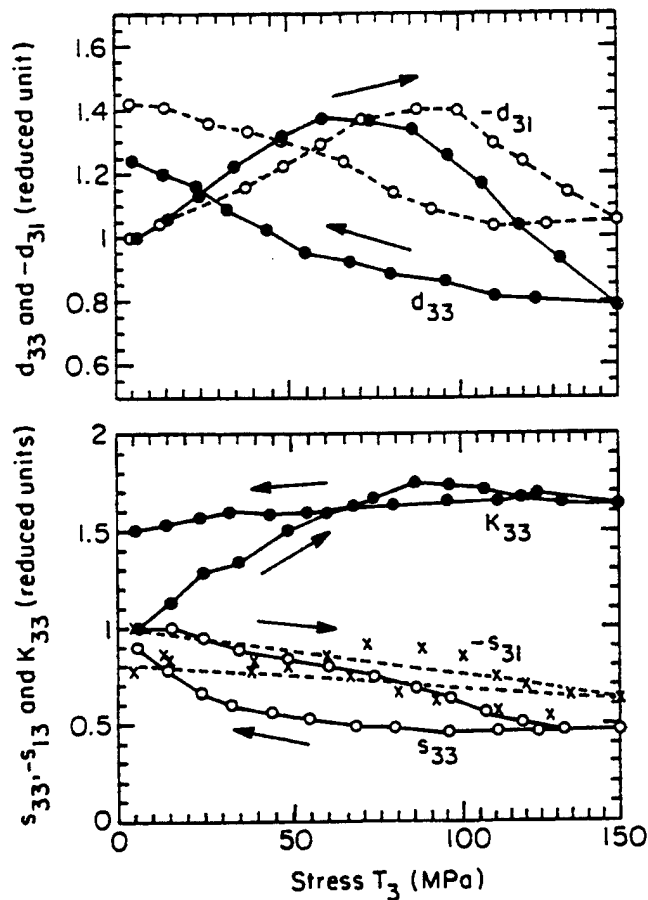


Fig. 7. The dependence of the weak signal piezoelectric coefficients ( $d_{33}$  and  $d_{31}$ ), dielectric constant  $K_{33}$ , and elastic compliance ( $s_{33}$  and  $s_{13}$ ) of PZT-4 on the compressive uniaxial stress  $T_3$ . Solid and dashed lines are drawn to guide the eyes.

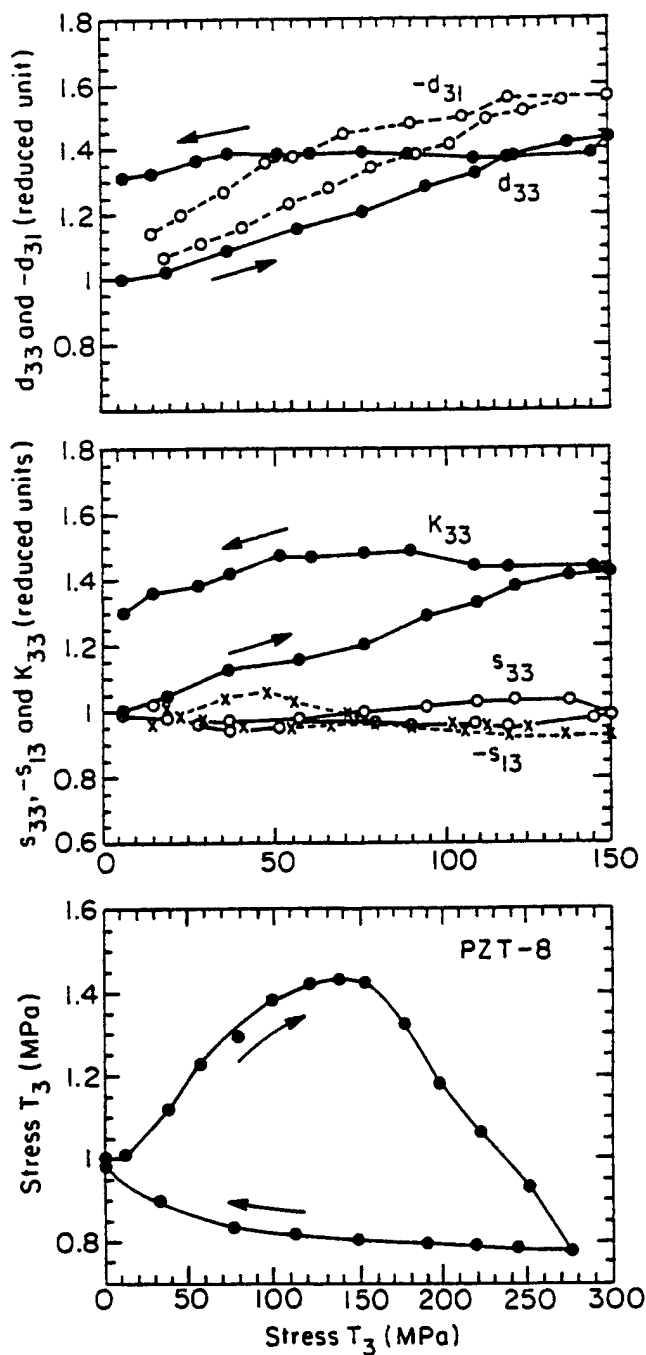


Fig. 8. The dependence of the weak signal piezoelectric coefficients ( $d_{33}$  and  $d_{31}$ ), dielectric constant  $K_{33}$ , and elastic compliance ( $s_{33}$  and  $s_{13}$ ) of PZT-8 on the compressive uniaxial stress  $T_3$ . Solid and dashed lines are drawn to guide the eyes.

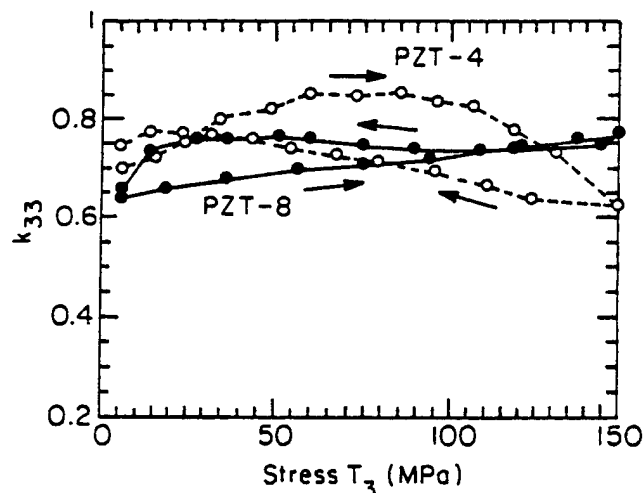


Fig. 9. The dependence of the longitudinal electromechanical coupling factor  $k_{33}$  on the compressive uniaxial stress  $T_3$  for PZT-4 and PZT-8 piezoceramics. Solid and dashed lines are drawn to guide the eyes.

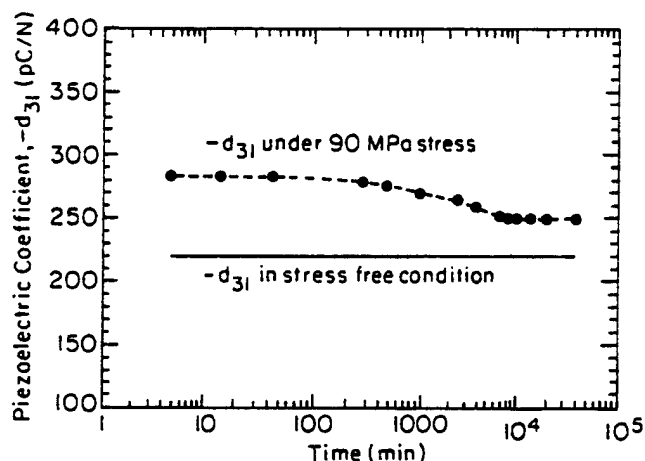


Fig. 10. Aging of  $d_{31}$  of PZT-8 over 1 month's time under a constant stress of 90 MPa.  $d_{31}$  aged after 1 month aging under stress is still higher than that under stress-free condition. Dashed line is drawn to guide the eyes.

#### IV. SUMMARY

There is a large difference in the polarization hysteresis loops and other material properties in aged and fresh samples. In fresh samples, the coercive field for hard PZT may not be higher than those in soft PZT. In aged PZT ceramics, there is no well defined coercive field. For hard PZT ceramics, local fields stabilize the poling state against electric field and stress depoling. There is a near zero coercive field in returning to the original poling direction of the hysteresis loop for both hard and soft PZT ceramics.

There is a large change of the material properties with stress due to nonlinear effects and the stress depoling. The material properties at stress-free state cannot reflect the properties under stress. Furthermore, it also can be in-

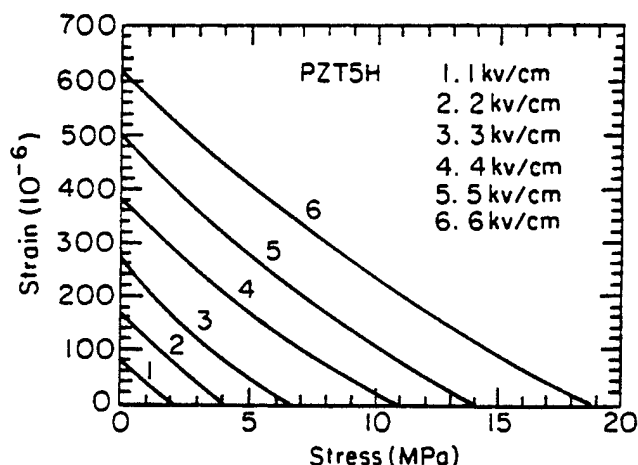
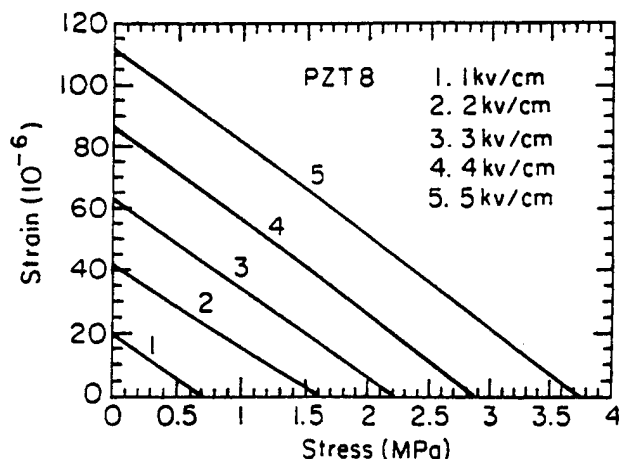


Fig. 11. Load curves of longitudinal strain versus  $T_3$  for PZT-5H and PZT-8 piezoceramics. The applied DC electric fields are indicated.

ferred that the nonlinear effects due to stress alone, due to applied electric field alone, and due to combined stress and electric field, will produce quite different material responses.

Soft PZT ceramics can be stress easily depoled, and the limiting stress  $T_3$  for PZT-5H and PZT-5A is at about 50 MPa level. A DC electric field can be used to stabilize soft PZT to against the stress depoling. The DC bias field used to stabilize the polarization in an aged sample can be smaller than the coercive field measured from deaged samples.

Compressive stress  $T_3$  can significantly increase the piezoelectric activity and coupling factor in hard PZT ceramics. This increase is not an effect of deaging alone, but rather involves a change of domain orientations with respect to the external field and applied stress and the coupling of the local polarization to the local defect fields.

The data presented suggest that the time scale is important in the results of the electric and mechanical load experiments. Although for hard PZT, no stress depoling was observed in the time scale of the current experiment, a much longer time scale experiment on hard PZT will pro-

duce a stress depoling. As shown in Fig. 10, the depoling stress is higher than 90 MPa for PZT-8.

#### ACKNOWLEDGMENT

The authors thank Dr. Z.-Y. Cheng for valuable discussions.

#### REFERENCES

- [1] J. M. Herbert, *Ferroelectric Transducers and Sensors*. New York: Gordon and Breach, 1982.
- [2] B. Jaffe, W. R. Cook, and H. Jaffe, *Piezoelectric Ceramics*. New York: Academic, 1971.
- [3] D. Berlincourt and H. Krueger, "Domain processes in lead titanate zirconate and barium titanate ceramics," *J. Appl. Phys.*, vol. 30, pp. 1804-1810, 1959.
- [4] H. Krueger and D. Berlincourt, "Effects of high static stress on the piezoelectric properties of transducer materials," *J. Acoust. Soc. Amer.*, vol. 33, pp. 1339-1344, 1961.
- [5] H. Krueger, "Stress sensitivity of piezoelectric ceramics: Part 1. Sensitivity to compressive stress parallel to the polar axis," *J. Acoust. Soc. Amer.*, vol. 42, pp. 636-646, 1967.
- [6] R. Y. Nishi, "Effects of one-dimensional pressure on the properties of several transducer ceramics," *J. Acoust. Soc. Amer.*, vol. 40, pp. 486-495, 1966.
- [7] V. Mueller and Q. M. Zhang, "Shear response of lead zirconate titanate piezoceramics," *J. Appl. Phys.*, vol. 83, pp. 3754-3760, 1998.
- [8] A. G. Luchaninov, A. V. Shil'nikov, L. A. Shuvalov, and V. A. Malyshev, "The effect of mechanical stress on the properties of electrically depolarized piezoelectric ceramics," *Ferroelectrics*, vol. 145, pp. 235-239, 1993.
- [9] H. Cao and A. Evans, "Nonlinear deformation of ferroelectric ceramics," *J. Am. Ceram. Soc.*, vol. 76, pp. 890-896, 1993.
- [10] Q. M. Zhang, J. Zhao, K. Uchino, and J. Zheng, "Change of weak field properties of Pb(ZrTi)O<sub>3</sub> piezoceramics with compressive uniaxial stress and its links to the effect of dopants on the stability of the polarization in the materials," *J. Mater. Res.*, vol. 12, pp. 226-234, 1997.
- [11] W. A. Schulze and K. Ogino, "Review of literature on aging of dielectric," *Ferroelectrics*, vol. 87, pp. 361-377, 1988.
- [12] W. Wersing, "On the stabilization field of lead-titanate-zirconate ceramics doped with transition metal ions," *Ferroelectrics*, vol. 12, pp. 143-145, 1976.
- [13] M. E. Lines and A. M. Glass, *Principles and Applications of Ferroelectrics and Related Materials*. Oxford: Clarendon Press, 1977.
- [14] M. Takahashi, "Space charge effect in lead zirconate titanate ceramics caused by the addition of impurities," *Jpn. J. Appl. Phys.*, vol. 9, pp. 1236-1246, 1970.
- [15] S. E. Park and T. R. Shrout, "Ultrahigh strain and piezoelectric behavior in relaxor based ferroelectric single crystals," *J. Appl. Phys.*, vol. 82, pp. 1804-1811, 1997.
- [16] J. Kawata, K. Uchino, and S. Nomura, "Dielectric and piezoelectric properties of 0.9Pb(Zn<sub>1/3</sub>Nb<sub>2/3</sub>)O<sub>3</sub>-0.09PbTiO<sub>3</sub> single crystals," *Jpn. J. Appl. Phys.*, vol. 21, pp. 1298-1302, 1982.

**Qiming M Zhang** (M'97) was born in Zeijian, China, in 1957. He received the B.S. degree in electron physics from Nanjing University, China, in 1981 and a Ph.D. degree in solid state physics from the Pennsylvania State University, University Park, in 1986.

From 1986 to 1988, he was a post-doctor at Materials Research Laboratory of Penn State. From 1988 to 1991, he was a research scientist at Brookhaven National Laboratory, NY, conducting research on interface, surface, and thin films with neutron and synchrotron X-ray scattering techniques. He currently is an associate professor of electrical engineering at the Materials Research Laboratory and Department of Electrical Engineering of the Pennsylvania State University. His research interests involve ferroelectric polymer, ceramic, and composite and their actuator, sensor, and transducer applications: characterization of piezoelectricity and electrostriction and constitutive relations in ferroelectrics; smart materials and structures; dielectric materials and capacitors; novel, artificial, and nano-composite materials; effects of defect structure on the dielectric, piezoelectric; and elastic properties of ferroelectric materials.

Dr. Zhang is a member of IEEE, American Physical Society, Materials Research Society, and American Ceramic Society.

# **APPENDIX 12**

# Characterization of lead zirconate titanate piezoceramic using high frequency ultrasonic spectroscopy

Haifeng Wang, Wenhua Jiang,<sup>a)</sup> and Wenwu Cao<sup>b)</sup>

*Materials Research Laboratory, National Resource Center for Medical Ultrasonic Transducer Engineering, The Pennsylvania State University, University Park, Pennsylvania 16802*

(Received 4 November 1998; accepted for publication 9 March 1999)

Doped piezoceramic lead zirconate titanate has been characterized in the frequency range of 20–60 MHz using ultrasonic spectroscopy. Theoretical analyses were performed for the reflection and refraction of acoustic waves at the interface of water-piezoelectric ceramic. The incident directions of the wave were chosen to be appropriate for ultrasonic spectroscopy measurements. Shear wave spectrum was obtained through mode conversion using a pair of longitudinal transducers submerged in water. The phase velocity shows linear dependence on frequency while the attenuation may be described by a second order polynomial of frequency in the frequency range investigated. The Kramers–Kronig relation between ultrasonic phase velocity and attenuation was compared to measured results. © 1999 American Institute of Physics. [S0021-8979(99)00412-0]

## I. INTRODUCTION

Application of higher frequency broadband ultrasonic transducer results in the improvement of the axial and lateral resolutions in medical imaging. Design high frequency transducer requires better knowledge of material properties since the ultrasonic dispersion becomes important for frequencies above 50 MHz. The dispersions of velocity and attenuation may deform the acoustic pulse and cause inappropriate interpretation of the pulse acoustic signal. Hence, knowing the properties of the transducer materials at high frequencies is important for designing high frequency transducers. Currently, there are very limited experimental data available in the literature on high frequency properties of piezoelectric materials due to many technical difficulties.<sup>1</sup> Reported in this article are results of velocity and attenuation for doped lead zirconate titanate (PZT-5H) in the frequency range of 20–60 MHz measured by using an ultrasonic spectroscopy method. The experimental results were also used to verify the Kramers–Kronig relations.<sup>2</sup>

The ultrasonic spectroscopy method has been widely used in the characterization of solid materials. With angular incidence, mode conversion effect was used to investigate shear wave properties of porous materials and polymeric materials.<sup>3–8</sup> If such a method is generalized to characterize piezoelectric materials, one needs to deal with the problem of plane wave propagation through an interface between an isotropic medium and an anisotropic piezoelectric material. Since the propagation velocity of waves varies with propagation direction in an anisotropic material, the refraction becomes complicated when the ultrasonic wave is obliquely incident onto the interface. Generally speaking, the refraction coefficient cannot be given in an explicit analytic form. For poled PZT ceramics the symmetry is  $\infty m$ , which has the

same number of independent physical constants as that of 6 mm symmetry, i.e., five independent elastic constants, three independent piezoelectric coefficients, and two independent dielectric permittivities. Because of the reasonably high symmetry, the situation may be simplified in some special incident angles. The present article is divided into two parts: first, we discuss the refraction of a plane wave at the interface of water-PZT ceramic. Based on the theoretical analysis, an ultrasonic spectroscopy technique suitable for characterization of PZT ceramic was developed and used to characterize PZT-5H samples. Second, the measured results were compared with those predicted by the Kramers–Kronig relations.

## II. THE REFLECTION AND REFRACTION OF A LONGITUDINAL WAVE AT THE WATER-PIEZOCERAMIC INTERFACE

Based on the principle described by Rokhlin,<sup>8</sup> we have derived the reflection/refraction of acoustic wave at the interface of water and a PZT ceramic plate. The poling direction of a plate PZT sample is either perpendicular or parallel to the large surface of the plate. As shown in Fig. 1, the plate sample with the poling direction perpendicular to its large surface is referred as PZT<sub>z</sub>, whereas the plate with poling direction parallel to its large surface is referred as PZT<sub>x</sub>.

### A. Reflection/refraction of a longitudinal wave at the interface of water and PZT<sub>z</sub>

When a longitudinal wave is incident upon the interface of water and PZT<sub>z</sub>, we choose the coordinate system to make the incident plane coincident with either the  $x$ - $z$  or the  $y$ - $z$  plane of PZT since the plane perpendicular to the  $z$  axis is acoustically isotropic for PZT with  $\infty m$  symmetry. If the  $x$ - $z$  plane is a wave propagation plane as shown in Fig. 1(a), the incident longitudinal wave in water can be expressed as

$$U_i = U_{0i} \exp[j(\omega t - k_w x_1 \sin \theta_i - k_w x_3 \cos \theta_i)]$$

$$(i = 1, 2, 3) \quad (1)$$

<sup>a)</sup>Present address: Institute of Acoustics and State Key Laboratory of Modern Acoustics, Nanjing University, Nanjing 210093, People's Republic of China.

<sup>b)</sup>Electronic mail: cao@math.psu.edu

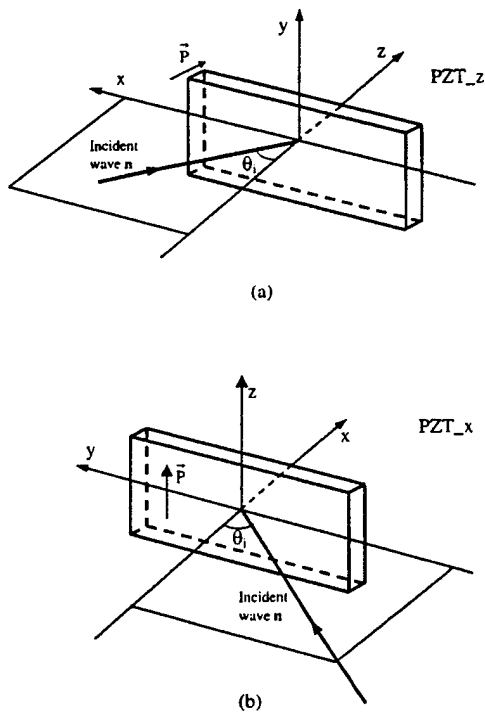


FIG. 1. (a) Incidence of a wave in the x-z plane of a PZT sample. (b) Incidence of a wave in the x-y plane of a PZT sample.

or

$$U_i = U_{0i} \exp[j\omega(t - m_1^w x_1 - m_3^w x_3)], \quad (1')$$

where  $k_w = \omega/v_w$ ,  $v_w$  is sound velocity of water,  $\theta_i$  is incidence angle

$$m_1^w = \frac{n_1}{v_w} = \frac{\sin \theta_i}{v_w} \quad \text{and} \quad m_3^w = \frac{n_3}{v_w} = \frac{\cos \theta_i}{v_w}.$$

The unit vector  $\vec{n}$  represents the wave propagation direction.

Similarly, the refractive waves propagating in the PZT sample are expressed as

$$u_i = u_{0i} \exp[j(\omega t - kn_1 x_1 - kn_3 x_3)] \quad (i=1,2,3,4), \quad (2)$$

where  $u_4$  stands for electric potential wave with the electric field given by  $E_i = \partial u_4 / \partial x_i$ . For convention we rewrite Eq. (2) as

$$u_i = u_{0i} \exp[j\omega(t - m_1 x_1 - m_3 x_3)] \quad (2')$$

with  $m_i = n_i/v$  ( $i=1$  or  $3$ ). Substituting the wave solutions into the equation of motion  $\rho \ddot{u}_i = \partial T_{ij} / \partial x_j$  and considering the constitutive equation  $T_{ij} = c_{ijkl} \partial u_k / \partial x_l - e_{mij} E_m$ , the amplitude  $u_{0i}$  ( $i=1-4$ ) in Eq. (2) will be governed by the following equations:

$$\left[ \frac{1}{\rho} (c_{11} m_1^2 + c_{44} m_3^2 - 1) u_{01} + \frac{1}{\rho} (c_{13} + c_{44}) m_1 m_3 u_{03} + \frac{1}{\rho} (e_{31} + e_{15}) m_1 m_3 u_{04} \right] = 0, \quad (3a)$$

$$\left\{ \frac{1}{\rho} \left[ \frac{1}{2} (c_{11} - c_{12}) m_1^2 + c_{44} m_3^2 \right] - 1 \right\} u_{02} = 0, \quad (3b)$$

$$\frac{1}{\rho} (c_{13} + c_{44}) m_1 m_3 u_{01} + \left[ \frac{1}{\rho} (c_{44} m_1^2 + c_{33} m_3^2) - 1 \right] u_{03} + \frac{1}{\rho} (e_{15} m_1^2 + e_{33} m_3^2) u_{04} = 0, \quad (3c)$$

$$(e_{15} + e_{31}) m_1 m_3 u_{01} + (e_{15} m_1^2 + e_{33} m_3^2) u_{03} - (\epsilon_{11} m_1^2 + \epsilon_{33} m_3^2) u_{04} = 0, \quad (3d)$$

where  $\rho$  is the density,  $c_{ij}$  are the elastic stiffness constants,  $e_{ij}$  are the piezoelectric stress constants, and  $\epsilon_{ij}$  are the dielectric constants for the poled PZT ceramic. Short notation for the elastic constants,  $\bar{c}$ , and the piezoelectric coefficients,  $\bar{e}$ , have been used; their definition could be found in Ref. 9.

From Eq. (3) it is seen that  $u_{02}$  representing the amplitude of a shear wave does not couple with  $u_{01}$  and  $u_{03}$ . Hence, this wave cannot be generated through mode conversion effect in this incidence arrangement. In other words, the particle displacement of the refractive waves in the PZT ceramic has only  $u_1$  and  $u_3$  components.

From Eq. (3d)

$$u_{04} = \frac{(e_{15} + e_{31}) m_1 m_3 u_{01} + (e_{15} m_1^2 + e_{33} m_3^2) u_{03}}{\epsilon_{11} m_1^2 + \epsilon_{33} m_3^2}. \quad (4)$$

Substituting Eq. (4) into Eqs. (3a) and (3c) gives

$$\left[ \frac{1}{\rho} \left( c_{11} m_1^2 + c_{44} m_3^2 + \frac{(e_{31} + e_{15})^2 m_1^2 m_3^2}{\epsilon_{11} m_1^2 + \epsilon_{33} m_3^2} \right) - 1 \right] u_{01} + \frac{1}{\rho} \left[ c_{13} + c_{44} + \frac{(e_{33} m_3^2 + e_{15} m_1^2)(e_{31} + e_{15})}{\epsilon_{11} m_1^2 + \epsilon_{33} m_3^2} \right] \times m_1 m_3 u_{03} = 0, \quad (5a)$$

$$\frac{1}{\rho} \left[ c_{13} + c_{44} + \frac{(e_{33} m_3^2 + e_{15} m_1^2)(e_{31} + e_{15})}{\epsilon_{11} m_1^2 + \epsilon_{33} m_3^2} \right] m_1 m_3 u_{01} + \left[ \frac{1}{\rho} \left( c_{44} m_1^2 + c_{33} m_3^2 + \frac{(e_{15} m_1^2 + e_{33} m_3^2)^2}{\epsilon_{11} m_1^2 + \epsilon_{33} m_3^2} \right) - 1 \right] u_{03} = 0. \quad (5b)$$

The propagation directions of the refractive waves allowed in the PZT ceramic are determined by the coefficient determinate of Eq. (5), i.e.,

$$\begin{vmatrix} \frac{1}{\rho} \left( c_{11} m_1^2 + c_{44} m_3^2 + \frac{(e_{31} + e_{15})^2 m_1^2 m_3^2}{\epsilon_{11} m_1^2 + \epsilon_{33} m_3^2} \right) - 1 & \frac{1}{\rho} \left( c_{13} + c_{44} + \frac{(e_{33} m_3^2 + e_{15} m_1^2)(e_{31} + e_{15})}{\epsilon_{11} m_1^2 + \epsilon_{33} m_3^2} \right) m_1 m_3 \\ \frac{1}{\rho} \left( c_{13} + c_{44} + \frac{(e_{33} m_3^2 + e_{15} m_1^2)(e_{31} + e_{15})}{\epsilon_{11} m_1^2 + \epsilon_{33} m_3^2} \right) m_1 m_3 & \frac{1}{\rho} \left( c_{44} m_1^2 + c_{33} m_3^2 + \frac{(e_{15} m_1^2 + e_{33} m_3^2)^2}{\epsilon_{11} m_1^2 + \epsilon_{33} m_3^2} \right) - 1 \end{vmatrix} = 0. \quad (6)$$

It is known that the phase matching condition at the interface, or the Snell's law, demands  $m_1^{\text{incident}} = m_1^{\text{reflective}} = m_1^{\text{refractive}}$ , or  $m_1^w = m_1^{\text{PZT}}$ . Since  $m_1^w$  is known for a given incident wave, one can determine  $m_3^{\text{PZT}}$  of refractive waves propagating in the PZT from Eq. (6).

There are two solutions of  $m_3^{\text{PZT}}$  from Eq. (6) corresponding to two refracted waves in PZT. Substituting the two roots of Eq. (6) back into Eq. (5), two eigenvectors with two components can be obtained, which provides the polarization directions of the two refracted waves. In more general cases, one of them is a quasilongitudinal wave and the other is a quasishear wave. Thus, when a longitudinal wave is incident from water upon PZT ceramic, there are incident and refracted waves in the water medium; both are longitudinal waves with amplitudes given by  $u_0$  and  $u_r$ , respectively. In the PZT ceramic there are refracted quasilongitudinal and quasishear waves. Their propagation direction and polarization direction are determined by Eqs. (5) and (6) to be  $\mathbf{m}^L$ ,  $\mathbf{l}^L$  and  $\mathbf{m}^S$ ,  $\mathbf{l}^S$ , respectively. Their amplitudes  $u_L$  and  $u_S$  are related to that of the incident wave  $u_0$  through the boundary conditions at the interface of  $x_3 = 0$

$$u_3(\text{water}) = u_3(\text{PZT}), \quad (7a)$$

$$T_{13} = 0, \quad (7b)$$

$$T_{33}(\text{water}) = T_{33}(\text{PZT}). \quad (7c)$$

The above equations may be rewritten as

$$u_r \cos \theta + l_3^L u_L + l_3^S u_S = u_0 \cos \theta, \quad (8a)$$

$$r u_L + s u_S = 0, \quad (8b)$$

$$Z_w u_r - p u_L - q u_S = -Z_w u_0, \quad (8c)$$

where  $Z_w$  is the acoustic impedance of water and

$$r = c_{44}(m_3^L l_1^L + m_1 l_3^L) + e_{15}(A^L l_1^L + B^L l_3^L), \quad (9a)$$

$$s = c_{44}(m_3^S l_1^S + m_1 l_3^S) + e_{15}(A^S l_1^S + B^S l_3^S), \quad (9b)$$

$$p = c_{13} m_1 l_1^L + c_{33} m_3^L l_1^L + e_{33} m_3^L (A^L l_1^L + B^L l_3^L), \quad (9c)$$

$$q = c_{13} m_1 l_1^S + c_{33} m_3^S l_1^S + e_{33} m_3^S (A^S l_1^S + B^S l_3^S), \quad (9d)$$

with

$$A^{L,S} = \frac{(e_{15} + e_{31}) m_1 m_3^{L,S}}{\epsilon_{11} m_1^{L,S} + \epsilon_{33} m_3^{L,S}}, \quad B^{L,S} = \frac{e_{15} m_1 + e_{33} m_3^{L,S}}{\epsilon_{11} m_1^{L,S} + \epsilon_{33} m_3^{L,S}}.$$

From Eq. (8) the ratios of  $u_r/u_0$ ,  $u_L/u_0$ , and  $u_S/u_0$ , i.e. the reflection and refraction coefficients, can be determined. Using this procedure, one can determine the amplitude and propagation direction of the refractive waves.

In ultrasonic spectroscopy technique, however, one can use slightly different ways to solve the problem. As mentioned above,  $m_1^w$  is known for a given incident wave, i.e.,

$$m_1^w = \frac{n_1}{v_w} = \frac{\sin \theta_i}{v_w}.$$

From Snell's law it is given that  $m_1^{\text{PZT}} = \sin \theta_i / v_w = \sin \theta_p / v_p$ , where  $\theta_p$  and  $v_p$  ( $p = L$  or  $S$ ) are the refractive angle and velocity of longitudinal (L) or shear (S) wave. If the velocity  $v_p$  has been determined by spectroscopy

method, one can simply calculate  $\theta_p$  through Snell's law. Obviously,  $m_3^{\text{PZT}}$  can be found by the relation of  $m_3^{\text{PZT}} = \cos \theta_p / v_p$ .

Using Eq. (6) the longitudinal and shear velocities can be correlated to appropriate elastic constants. In what follows we discuss three special cases to illustrate the procedure.

Case 1. Normal incidence

In this case  $m_1^{\text{water}} = 0$ , therefore,  $m_1^{\text{PZT}} = 0$ ,  $\theta_p = 0$  and

$$m_3^S = \frac{1}{v_S} \quad (10a)$$

or

$$m_3^L = \frac{1}{v_L}. \quad (10b)$$

Substituting these results into Eq. (5) results in the following simple relations:

$$v_S = \sqrt{\frac{c_{44}}{\rho}} \quad \text{and} \quad v_L = \sqrt{\frac{c_{33}}{\rho}} = \sqrt{\frac{c_{33} + \frac{e_{33}^2}{\epsilon_{33}}}{\rho}} \quad (10c,d)$$

which are the velocities of the shear wave and the stiffened longitudinal wave, respectively.

From Eq. (6), two eigenvectors are obtained

$$\mathbf{l}^S = [1, 0, 0] \quad \text{and} \quad \mathbf{l}^L = [0, 0, 1]. \quad (11a,b)$$

This means that one of the possible refracted waves is a pure shear wave with polarization direction along the  $x$  axis and another is a pure longitudinal wave. Substituting these results into Eqs. (8) and (9), one can obtain the reflection and refraction ratios

$$R = \frac{u_r}{u_0} = \frac{Z_L - Z_w}{Z_L + Z_w}, \quad (12a)$$

$$T = \frac{u_L}{u_0} = \frac{2Z_L}{Z_L + Z_w}, \quad (12b)$$

$$u_S = 0. \quad (12c)$$

Equation (12c) implies that mode conversion does not exist in normal incidence, and reflection coefficient  $R$  and transmission coefficient  $T$  of the longitudinal wave are the same as for an interface of water and an isotropic solid. In the expressions Eqs. (12a,b),  $Z_L$  is the acoustic impedance of the longitudinal wave in PZT.

Case 2. Incidence at the critical angle of the longitudinal wave.

When a longitudinal wave is obliquely incident from water upon PZT, mode conversion takes place. In PZT medium there are, in general, refractive quasilongitudinal and quasishear waves. If the wave is incident at the critical angle of longitudinal wave, the refractive longitudinal wave becomes an evanescent wave. This means that  $m_3^L$  is equal to zero ( $\theta_i = \text{critical angle}$ ) or complex ( $\theta_i > \text{critical angle}$ ). The vector  $\mathbf{m}^S$  representing the propagation direction of the refractive quasishear wave can be determined by the following expressions:

$$m_1^S = \frac{\sin \theta_i}{v_w} = \frac{\sin \theta_S}{v_S}, \quad (13a)$$

$$m_3^S = \frac{\cos \theta_S}{v_S}. \quad (13b)$$

If the velocity  $v_S$  is determined from the ultrasonic spectroscopy method,  $\theta_S$  can be calculated from Eq. (13a), therefore  $\mathbf{m}^S$  is totally determined. Knowing  $\mathbf{m}^S$ , the polarization direction can be determined by Eq. (5) and the transmission coefficient can be calculated from Eq. (8). The velocity of the quasishear wave is related to a combination of elastic constants of PZT by

$$v_S = \sqrt{\frac{c^*}{\rho}}, \quad (14)$$

where

$$2c^* = c_{11} \sin^2 \theta_S + c_{33} \cos^2 \theta_S + c_{44} + p_1 + p_2 + \{[(c_{11} - c_{44}) \sin^2 \theta_S + (c_{44} - c_{33}) \cos^2 \theta_S + p_1 - p_2]^2 + (c_{13} + c_{44} + p_3)^2 \sin^2 2\theta_S\}^{1/2} \quad (15a)$$

and

$$p_1 = \frac{(e_{31} + e_{15})^2 \sin^2 \theta_S \cos^2 \theta_S}{\epsilon_{11} \sin^2 \theta_S + \epsilon_{33} \cos^2 \theta_S}, \quad (15b)$$

$$p_2 = \frac{(e_{33} \cos^2 \theta_S + e_{15} \sin^2 \theta_S)^2}{\epsilon_{11} \sin^2 \theta_S + \epsilon_{33} \cos^2 \theta_S}, \quad (15c)$$

$$p_3 = \frac{(e_{33} \cos^2 \theta_S + e_{15} \sin^2 \theta_S)(e_{31} + e_{15})}{\epsilon_{11} \sin^2 \theta_S + \epsilon_{33} \cos^2 \theta_S}, \quad (15d)$$

are terms associated with piezoelectric coupling.  $\theta_S$  is the refractive angle of the quasishear wave in PZT ceramic.

### B. Reflection/refraction of a longitudinal wave at the interface of water and PZT<sub>x</sub>

Assuming the plate normal direction is along the  $x$  axis and the poling direction is parallel to the  $z$  direction of the PZT plate as shown in Fig. 1(b), the incident plane of the ultrasonic wave has three independent orientations: (1)  $x$ - $y$  plane; (2)  $y$ - $z$  plane, and (3) incident in a plane that rotates around the  $y$  axis at an arbitrary angle. Since the last case makes the problem more complicated, it will not be discussed here. The second option is actually equivalent to the Case 2 of Sec. II A, therefore we only need to discuss the first option which we call Case 3, as described below.

The plane perpendicular to the  $z$  axis of PZT is an acoustically isotropic plane as mentioned above. When an incident wave is in the  $x$ - $y$  plane, as shown in Fig. 1(b), the reflection/refraction of a longitudinal wave at the interface of water and PZT ceramic is the same as at the interface of water and an isotropic solid. In this case, the particle displacement  $\mathbf{u}$  of the refractive waves has only components in the  $x$  and  $y$  directions. When a wave is normally incident, the only refractive wave is a pure longitudinal wave with the velocity given by

$$v_L = \sqrt{\frac{c_{11}}{\rho}}. \quad (16a)$$

When a wave is obliquely incident, one of the two refractive waves is a pure longitudinal wave with the same velocity as Eq. (16a), another refractive wave is a pure shear wave with the velocity of

$$v_S = \sqrt{\frac{1/2(c_{11} - c_{12})}{\rho}} = \sqrt{\frac{c_{66}}{\rho}}. \quad (16b)$$

This shear wave polarizes in the  $x$ - $y$  plane.

Other cases of reflection/refraction of a plane wave at the interface of PZT ceramic water can be discussed by using the same procedure. However, pure modes do not exist for general cases.

In summary, by using angular incidence of a longitudinal wave from water to two PZT plates we can determine the elastic constants and their dispersion from dispersion of velocity and attenuation in the following acoustic modes:

(A). For a PZT<sub>z</sub> sample:

- (1) Longitudinal wave propagating along the poling direction with the wave normal incident upon the plate. From the velocity dispersion of this wave, the frequency dependence of elastic constant  $c_{33}^D$  can be determined.
- (2) Quasishear wave propagating in the  $x$ - $z$  plane with the wave obliquely incident at the critical angle of the longitudinal wave. From its velocity dispersion one can determine an elastic constant combination  $c^*$  and its frequency dependence.

(B). For a PZT<sub>x</sub> sample:

- (1) Longitudinal wave propagating perpendicular to the poling direction. From its velocity dispersion one can determine the elastic constant  $c_{11}$  and its frequency dependence.
- (2) Shear wave with directions of propagation and polarization normal to the poling direction when the wave is incident at the critical angle of the longitudinal wave. From the velocity dispersion of this wave one can determine the elastic constant  $c_{66}$  and its frequency dependence.

### III. PRINCIPLES OF MEASUREMENTS

The basic principle of the ultrasonic spectroscopy method used to determine the velocity and attenuation of materials is shown in Fig. 2. A pair of aligned transmitting and receiving transducers are immersed in water with an adjustable separation between them. When the transmitting transducer is driven by an electric pulse signal, an acoustic broadband signal is produced at  $x=0$ , noted as  $u(t)$ . Its Fourier transform is  $\bar{u}(f)$ . For a linear and causal acoustic system shown in Fig. 2(a), the transfer function of the medium for the wave to propagate can be expressed as

$$H(f) = \exp[-\alpha_w(f)L] \exp\{-j[2\pi fL/v_w(f)]\}, \quad (17)$$

where  $L$  is the distance between the transmitting and receiving transducers,  $v_w$  and  $\alpha_w$  are the wave velocity and attenuation of water, respectively. When the medium is considered

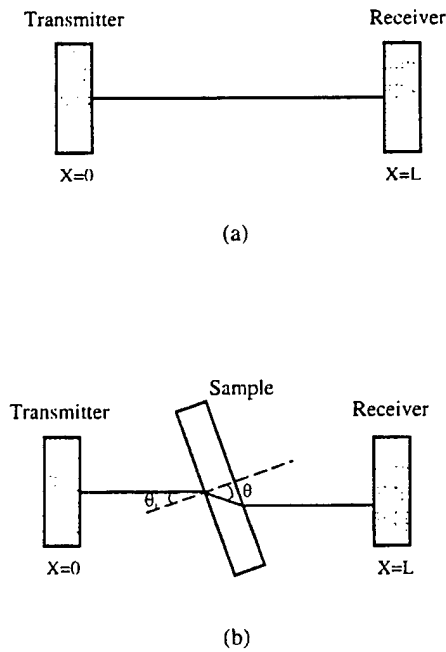


FIG. 2. Principle of ultrasonic spectroscopy technique: (a) without sample, (b) with sample placed in a rotated position.

to be dispersive and dissipative, both  $\alpha_w$  and  $v_w$  are frequency dependent. The spectrum of the output signal from the receiving transducer is

$$\bar{u}_w(f) = \bar{u}(f) \exp[-\alpha_w(f)L] \times \exp[-j(2\pi fL/v_w(f))\bar{u}'(f)], \quad (18)$$

where  $\bar{u}'(f)$  is the transfer function of the receiving transducer. Thus, the amplitude and phase spectra of the output signal can be expressed as

$$A_w(f) = |\bar{u}(f)| \exp[-\alpha_w(f)L] |\bar{u}'(f)|, \quad (19a)$$

$$\varphi_w(f) = 2\pi fL/v_w(f) + \phi_u + \phi_u', \quad (19b)$$

where  $\phi_u$  and  $\phi_u'$  are the phase angles of the two transducers, respectively. They will not enter the calculations below since the spectroscopic method depends only on the relative phase shift.

When the sample to be measured is inserted between the transmitting and receiving transducers, the transfer function of the system as shown in Fig. 2(b) becomes

$$H_S(f) = T\bar{u}(f) \exp\left\{-\alpha_w(f)\left[L - \frac{d}{\cos \theta_i} - d(tg \theta - tg \theta_i)\right] \times \sin \theta_i\right\} \exp\left[-\alpha(f)\frac{d}{\cos \theta}\right] \times \exp\left\{-j\left[2\pi f\left(L - \frac{d}{\cos \theta_i} - d(tg \theta - tg \theta_i)\right) \times \sin \theta_i\right] / v_w(f) + 2\pi f\frac{d}{\cos \theta} / v(f)\right\} \bar{u}'(f), \quad (20)$$

where  $d$  is the thickness of the sample,  $\alpha$  and  $v$  are attenuation coefficient and phase velocity in the sample, respec-

tively,  $\theta_i$  and  $\theta$  are the incident and the refractive angles of the wave at the interface, respectively,  $T$  is the total transmission coefficient which is equal to the product of the transmission coefficients of the wave from water to sample and from sample to water.

Thus, the amplitude and phase spectra of the output signal for the system shown in Fig. 2(b) can be written as

$$A(f) = T|\bar{u}(f)| \exp\left\{-\alpha_w(f)\left[L - \frac{d}{\cos \theta_i} - d(tg \theta - tg \theta_i)\right] \times \sin \theta_i\right\} \exp\left[-\alpha(f)\frac{d}{\cos \theta}\right] |\bar{u}'(f)|, \quad (21a)$$

and

$$\varphi = 2\pi f\left[L - \frac{d}{\cos \theta_i} - d(tg \theta - tg \theta_i)\sin \theta_i\right] / v_w(f) + \frac{2\pi fd}{v(f)\cos \theta} + \phi_u + \phi_u'. \quad (21b)$$

From Eqs. (19) and (21) the phase velocity and attenuation coefficients in the sample are given by

$$v = \frac{v_w}{\sqrt{\sin^2 \theta_i + \left[\frac{(\varphi - \varphi_w)v_w}{2\pi fd} + \cos \theta_i\right]^2}}, \quad (22)$$

$$\alpha = \alpha_w \cos(\theta - \theta_i) + \left(\ln \frac{TA_w}{A}\right) \cos \theta / d. \quad (23)$$

If the values of  $A_w$ ,  $A$ ,  $\varphi_w$ , and  $\varphi$  can be measured, the attenuation and phase velocity dispersion of the sample can be determined.

When the wave is normally incident to the sample,  $\theta_i = \theta = 0$ , the above equations give the velocity and attenuation of the longitudinal wave in the case discussed in Sec. II for the longitudinal wave propagating in either  $x$ - $z$  plane or  $x$ - $y$  plane as shown in Figs. 1(a) and 1(b), respectively

$$v_L = \frac{v_w}{1 + \frac{(\varphi - \varphi_w)v_w}{2\pi fd}}, \quad (24)$$

and

$$\alpha_L = \alpha_w + \ln\left(\frac{TLA_w}{A}\right) / d, \quad (25)$$

where

$$T_L = \frac{4\rho_0 v_w \rho v_L}{(\rho_0 v_w + \rho v_L)^2} = \frac{4z_w z_L}{(z_L + z_w)^2} \quad (26)$$

and  $\rho_0$  and  $\rho$  are the mass density of water and sample, respectively, and  $v_L$  is the longitudinal wave velocity in the sample.

If the wave is obliquely incident at the critical angle of the longitudinal wave shear wave will be generated through mode conversion effect. The velocity and attenuation of the shear wave can be calculated by the following expressions:

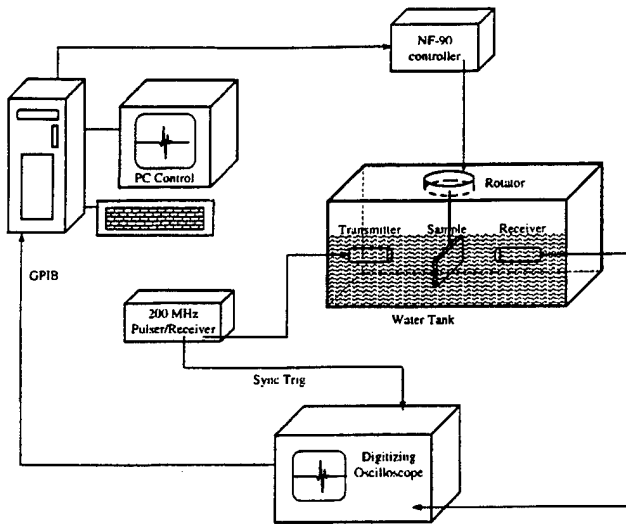


FIG. 3. Experiment setup.

$$v_S = \frac{v_w}{\sqrt{\sin^2 \theta_i + \left[ \frac{(\varphi - \varphi_w) v_w}{2\pi f d} + \cos \theta_i \right]^2}}, \quad (27)$$

$$\alpha_S = \alpha_w \cos(\theta_S - \theta_i) + \left( \ln \frac{T_S A_w}{A} \right) \cos \theta_S / d, \quad (28)$$

where  $T_S$  and  $\theta_S$  are transmission coefficient and refractive angle of the shear wave. The transmission coefficients for fluid-isotropic solid interface are simply given by

$$T_1 = - \left( \frac{\rho_0}{\rho} \right) \frac{2z_{Sn} \sin(2\theta_S)}{z_{Ln} \cos^2(2\theta_S) + z_{Sn} \sin^2(2\theta_S) + z_{wn}}, \quad (29a)$$

$$T_2 = \frac{\tan \theta_i}{2 \sin^2 \theta_S} \left( 1 - \frac{z_{Ln} \cos^2(2\theta_S) - z_{Sn} \sin^2(2\theta_S) + z_{wn}}{z_{Ln} \cos^2(2\theta_S) + z_{Sn} \sin^2(2\theta_S) + z_{wn}} \right), \quad (29b)$$

$$T_S = T_1 T_2, \quad (29c)$$

where  $T_{12}$  and  $T_{21}$  stand for the transmission coefficients of a wave from water to PZT and from PZT to water, respectively;  $z_{wn} = z_w / \cos \theta_i$ ,  $z_{Ln} = z_L / \cos \theta_L$ ,  $z_{Sn} = z_S / \cos \theta_S$ , and  $v_S$  is the shear wave velocity in the sample. The refractive angles  $\theta_L$  and  $\theta_S$  are calculated from Snell's law

$$\frac{\sin \theta_i}{v_w} = \frac{\sin \theta_L}{v_L} = \frac{\sin \theta_S}{v_S}, \quad (30)$$

where the incident angle  $\theta_i$  is controlled by a computerized rotating table in our experiments. For the quasishear wave propagating in the  $x$ - $z$  plane of a PZT ceramic. The transmission coefficient can be calculated from Eq. (8).

#### IV. EXPERIMENT RESULTS FOR PZT-5H AND DISCUSSIONS

The experimental setup is shown in Fig. 3. A pair of transducers with a center frequency of 50 MHz and bandwidth of 80% were used. Without sample, the spectra of the output signal from the receiving transducer are shown in Fig. 4. Since the ultrasonic attenuation of water is about 6 dB/cm

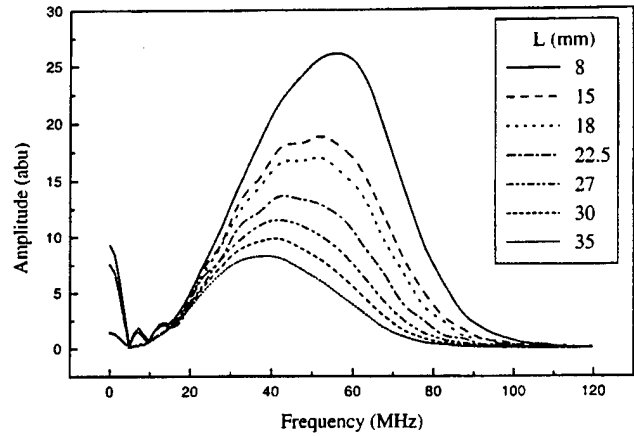


FIG. 4. The variation of amplitude spectrum with propagation distance in water.

at 50 MHz the high frequency components of the Fourier spectrum are decayed when the distance between the transmitter and receiver increases, as indicated in Fig. 4. The interval between transmitter and receiver should be selected in such a way that the high frequency components are preserved as much as possible, and at the same time leaving enough room for the sample to be rotated. In our experiments, the distance  $L$  is set at about 3 cm.

The output waveform was sampled by a digital oscilloscope (Tektronix TDS 460A) at a sampling rate of 10 Gs/s. The data were transferred into computer via a general purpose interface bus (GPIB) interface. The total recording length for a waveform was 2500 points. The amplitude  $A_w$  and the phase spectra  $\varphi_w$  were obtained through fast Fourier transform (FFT) of the output signal from the configuration in Fig. 2(a). When the sample was put in place, the trigger delay time was adjusted so that the shifting of the waveform caused by putting in the sample can be compensated. Using the same procedure, the amplitude  $A$  and the phase  $\varphi$  of the output signal from the configuration Fig. 2(b) were obtained. [Note: the velocity calculation must take into account the trigger time delay,  $\tau$ ]

$$v_L = \frac{v_w}{1 + \frac{(\varphi - \varphi_w + 2\pi f \tau) v_w}{2\pi f d}}, \quad (31a)$$

$$v_S = \frac{v_w}{\sqrt{\sin^2 \theta_i + \left[ \frac{(\varphi - \varphi_w + 2\pi f \tau) v_w}{2\pi f d} + \cos \theta_i \right]^2}}. \quad (31b)$$

The attenuation of the longitudinal and shear waves can be calculated from Eqs. (23) and (25), respectively. Here the attenuation of water was given by  $0.000271 f^2$  (dB/mm), ( $f$  in MHz). The measured velocity and attenuation for piezoceramic PZT-5H are given in Figs. 6–9. It was observed that velocity dispersion exists for both the longitudinal and shear waves in the frequency range of the measurement and it is nearly linear, but the attenuation exhibits nonlinear frequency dependence. The attenuation of the shear wave is an order of magnitude higher than that of the longitudinal wave.

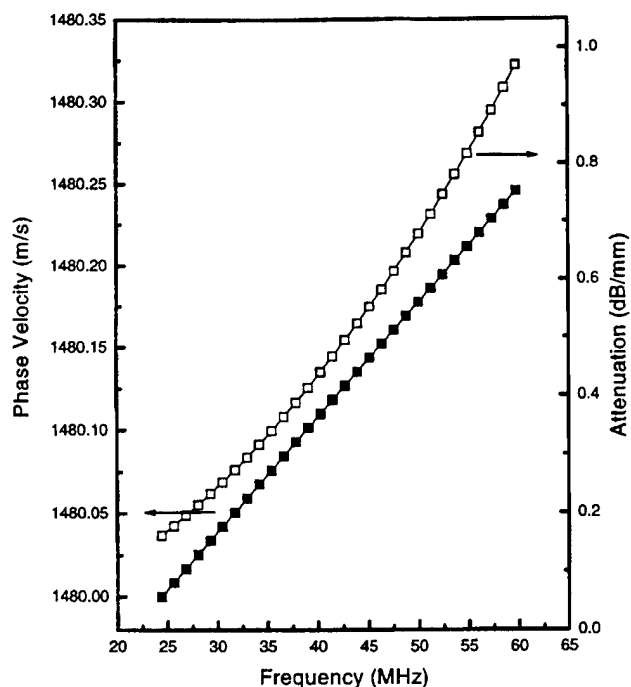
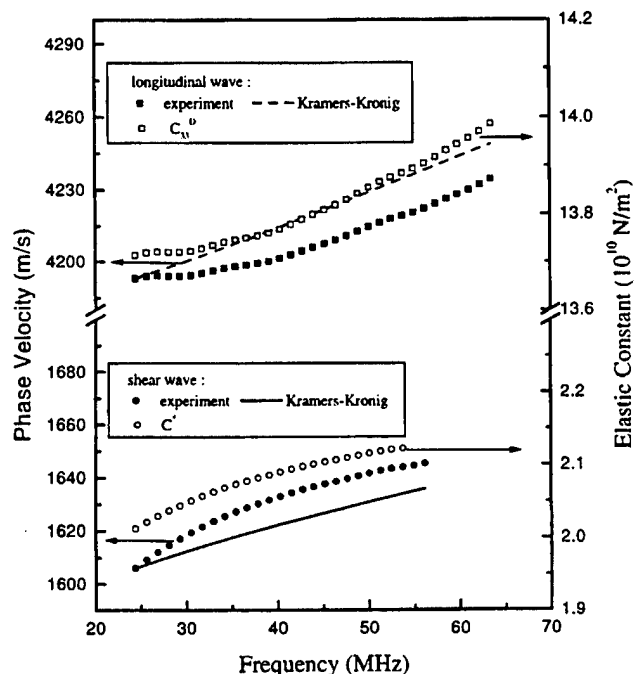
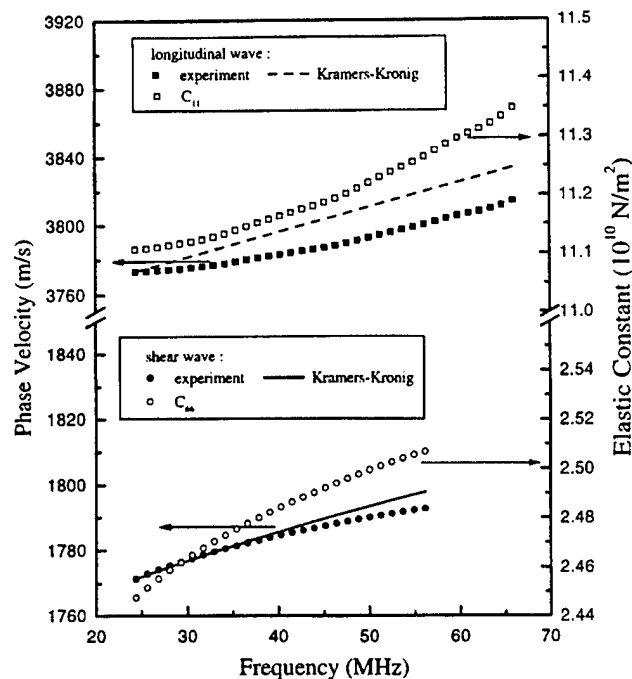


FIG. 5. Dispersion relationship of the velocity and attenuation for water.

Usually, the wave number of a decay wave is considered to be a complex number. Therefore, if the frequency is taken as real, the velocity becomes complex and is associated with the complex elastic modulus in the following fashion:

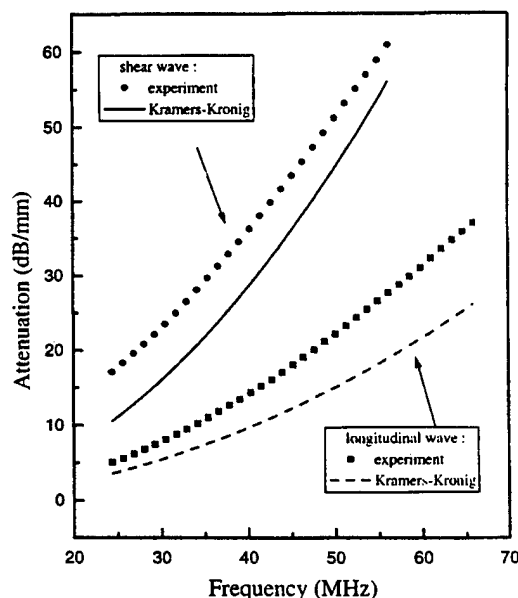
$$\bar{v} = \sqrt{\frac{\bar{C}}{\rho}} = \sqrt{\frac{C + jC'}{\rho}}. \quad (32)$$

FIG. 6. The phase velocity dispersion measured by experiment and derived by Kramers-Kronig relationship for a wave propagating in the  $x$ - $z$  plane of a PZT sample and the corresponding elastic constants.FIG. 7. The phase velocity dispersion measured by experiment and derived by Kramers-Kronig relationship for wave propagating in the  $x$ - $y$  plane of a PZT sample and the corresponding elastic constants. The longitudinal and shear velocities were fitted to linear curves:  $v_L = 3744.4 + 1.00e - 6 * f$  (Hz) and  $v_S = 1762.5 + 5.47e - 7 * f$  (Hz).

In general, it is true that  $|C'|/|C| \ll 1$ , we may write the above equation as

$$\bar{v} \approx \sqrt{\frac{C}{\rho}} \left( 1 + j \frac{C'}{2C} \right). \quad (33)$$

The complex wave number can be expressed as

FIG. 8. The attenuation measured by experiment and derived by Kramers-Kronig relationship for a wave propagating in the  $x$ - $z$  plane of a PZT sample. The longitudinal and shear velocities were fitted to linear curves:  $v_L = 4156.8 + 1.44e - 6 * f$  (Hz) and  $v_S = 1597 + 8.67e - 7 * f$  (Hz).

$$\bar{k} = k - j\alpha, \quad (34)$$

where  $k = \omega/v$  and  $\alpha$  is the attenuation coefficient. Thus, the real and imaginary parts of the elastic modulus can be derived from the phase velocity and attenuation measurements

$$C = \rho v^2, \quad (35a)$$

$$\tan \delta = \frac{C'}{C} = \frac{2\alpha v}{\omega}. \quad (35b)$$

If a medium in which an acoustic wave propagates can be considered as a linear and causal system, its attenuation, which is associated with the imaginary part of the elastic modulus, and velocity dispersion, which is associated with the real part of elastic modulus, are related by the Kramers-Kronig relations. The approximation forms of the nearly local relationships can be expressed as<sup>10,11</sup>

$$v(\omega) = v(\omega_0) + \frac{2v^2(\omega_0)}{\pi} \int_{\omega_0}^{\omega} \frac{\alpha(\omega')}{\omega'^2} d\omega', \quad (36a)$$

$$\alpha(\omega) = \frac{\pi\omega^2}{2v^2(\omega_0)} \frac{dv(\omega)}{d\omega}, \quad (36b)$$

where  $\omega_0$  is the starting frequency at which  $v(\omega_0)$  and  $\alpha(\omega_0)$  are known. In our experiment,  $\omega_0 = 2\pi \cdot 20$  MHz.

The ultrasonic spectroscopy technique is inherently based on the assumption of linearity. Thus, the velocity dispersion and attenuation obtained from the technique are expected to satisfy the above Kramers-Kronig relations. To verify the validity of these relations, the measured attenuation for the PZT-5H samples was fitted as a polynomial of frequency and the phase velocity dispersion was derived by the first Kramers-Kronig relation Eq. (36a), then these calculated results were compared to measured results. As shown in Figs. 6 and 7 that the agreement is quite acceptable. The maximum deviation is less than 0.6% and the trend is correct. We have also performed the reverse checking, i.e., using the measured velocity dispersion to calculate the dispersion of the attenuation based on the local approximation Eq. (36b). We found that this relation is extremely sensitive to the curvature of the velocity dispersion. Higher order polynomial fitting of the velocity curve gives unreasonable results. Because the velocity dispersion is fairly small, we decided to use a linear approximation to these velocity data, which created error less than the experimental uncertainty for the velocity fitting but gave good agreement to the measured attenuation dispersion. The results are shown in Figs. 8 and 9 for the two different cut PZT samples. Owing to this sensitivity, one should be really careful when using the second Kramers-Kronig relation Eq. (36b). One may have problems using this relation if the velocity dispersion has a downward curvature, such as the shear velocity measured in this work, since it will lead to a decrease of the attenuation at higher frequencies. The measured attenuation seems to always increase with frequency. Our experience is that a linear fitting of the velocity dispersion could provide a much better prediction of the attenuation dispersion using the Kramers-

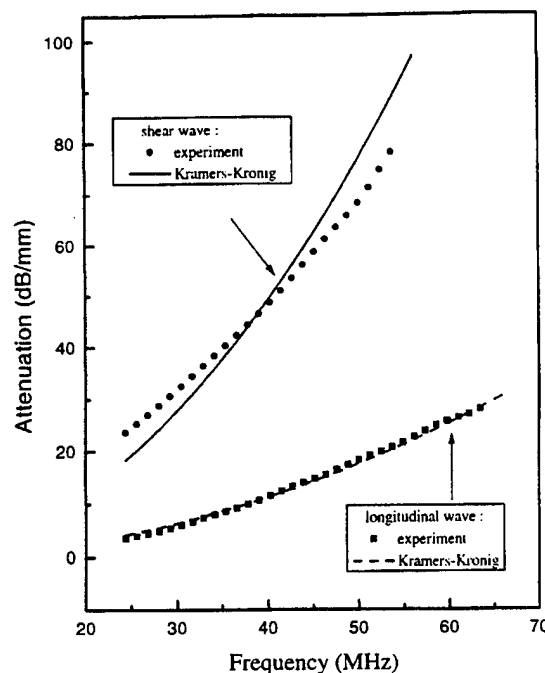


FIG. 9. The attenuation measured by experiment and derived by Kramers-Kronig relationship for a wave propagating in the  $x$ - $y$  plane of a PZT sample.

Kronig relations. This linear fitting, of course, must be piece wise since the relationship is not linear in general for all frequency ranges.

## V. CONCLUSION

The dispersions of velocity and attenuation for piezoelectric PZT-5H were investigated by using ultrasonic spectroscopy at the frequency range of 20–60 MHz. In the investigated frequency range, velocity dispersion of 1–3 m/s per MHz was observed. The attenuation depends nonlinearly on frequency and the shear wave exhibited an order of magnitude larger attenuation than the longitudinal wave.

We showed that the Kramers-Kronig relations between velocity dispersion and attenuation dispersion are satisfied for the longitudinal waves. However, for the shear waves, the agreement between experiments and theory was not satisfactory, indicating the nonlinear origin of the shear wave attenuation. Based on these results, we conclude that the Kramers-Kronig relation may be safely applied to longitudinal waves, which provides us with a convenient way to measure the velocity dispersion. It is difficult to be accurate with such measurement using other available techniques since the dispersion is quite small. By using the Kramers-Kronig relations, one can derive the velocity dispersion from the velocity measurement at one frequency plus the attenuation spectrum.

## ACKNOWLEDGMENTS

This research was sponsored by the NIH under Grant No. P41-RR11795-01 A1 and the ONR under Grant No. N00014-98-1-0527.

- <sup>1</sup>A. R. Selfridge, IEEE Trans. Sonics Ultrason. **SU-32**, 3, 381 (1985).
- <sup>2</sup>M. O'Donnell, E. T. Jaynes, and J. G. Miller, J. Acoust. Soc. Am. **63**, 1935 (1978).
- <sup>3</sup>W. Sachse and Y. H. Pao, J. Appl. Phys. **49**, 4320 (1978).
- <sup>4</sup>R. A. Kline, J. Acoust. Soc. Am. **76**, 498 (1984).
- <sup>5</sup>S. Baudouin and B. Hosten, Ultrasonics **34**, 379 (1996).
- <sup>6</sup>T. J. Plona, R. D'Angelo, and D. L. Johnson, Proceedings of the IEEE 1990 Ultrasonics Symposium, 1990, p. 1233.
- <sup>7</sup>J. Wu, J. Acoust. Soc. Am. **99**, 2871 (1996).
- <sup>8</sup>S. I. Rokhlin, T. K. Balland, and L. Adler, J. Acoust. Soc. Am. **79**, 906 (1986).
- <sup>9</sup>J. F. Nye, in *Physical Properties of Crystals* (Clarendon, Oxford, 1985).
- <sup>10</sup>M. O'Donnell, E. T. Jaynes, and J. G. Miller, J. Acoust. Soc. Am. **69**, 696 (1981).
- <sup>11</sup>D. Zellouf, Y. Jayet, N. Saint-Pierre, J. Tatibouet, and J. C. Baboux, J. Appl. Phys. **80**, 2728 (1996).

# **APPENDIX 13**

# The influence of the external stress on the electromechanical response of electrostrictive $0.9\text{Pb}(\text{Mg}_{1/3}\text{Nb}_{2/3})\text{O}_3-0.1\text{PbTiO}_3$ in the dc electrical field-biased state

J. Zhao, Volkmar Mueller, and Q. M. Zhang<sup>a)</sup>

Materials Research Laboratory and Electrical Engineering Department, The Pennsylvania State University, University Park, Pennsylvania 16802

(Received 16 January 1998; accepted 22 July 1998)

The influence of uniaxial compressive stress,  $T_3$ , applied parallel to the electrical field, on the electromechanical parameters of  $0.9\text{Pb}(\text{Mg}_{1/3}\text{Nb}_{2/3})\text{O}_3-0.1\text{PbTiO}_3$  ceramics in the dc electrical field-biased state and at temperatures near the dielectric constant maximum  $T_m$  was investigated. It was found that  $T_3$  reduces both the dielectric constant and polarization level, which results in a reduction of the piezoelectric coefficient with stress. However, the compliance of the material does not show much change with stress. As a consequence, the coupling factor  $k_{33}$  is also reduced with stress. On the other hand, the existence of the local micropolar region in the material causes anomalous changes in the aforementioned properties when the material is subjected to a high electric field, which induces a macropolar state. The transformation of this macropolar state back to a micropolar state under stress involves a large volume strain and results in an enhancement of the hydrostatic piezoelectric response.

## I. INTRODUCTION

Lead magnesium niobate-lead titanate (PMN-PT) based electrostrictive materials exhibit many attractive features such as high dielectric constant, high electrical and elastic energy density, and low hysteresis, for actuator and transducer applications. In these applications, the materials are often subjected to high external stresses due to a prestress or high external load. In order to properly use the materials under different external conditions, it is necessary to understand how the electromechanical properties are influenced by those conditions.

In PMN-PT used in the electrostrictive regions (at temperatures near or above the dielectric constant maximum  $T_m$ ), the material is composed of two phases: micropolar regions embedded in a nonpolar matrix.<sup>1,2</sup> And as has been demonstrated in a recent study, the polarization response, and hence the dielectric and electric field induced strain behaviors, at temperatures near  $T_m$  are mainly controlled by the response of the micropolar regions, rather than by the so-called "intrinsic" contribution from the change of the unit cell dimension and polarization level.<sup>1,3</sup> This is somewhat similar to another widely used electromechanical material, the piezoceramic lead zirconate titanate (PZT), where the material properties are largely controlled by the macrodomain configuration and the movements of the domain boundaries.<sup>4</sup> One difference between the two systems is that in PMN-PT the response of the micro-

polar region exhibits only weak hysteresis while in PZT, large irreversibility occurs when external fields cause depoling of the piezoceramic.<sup>5</sup> The influence of external stresses on the response of micropolar region is still unclear at this stage.

In this paper, we report the results of an experimental investigation on the effect of uniaxial compressive stress ( $T_3$ ), which is parallel to the applied electric field direction (defined as the 3-direction), on various electromechanical parameters of PMN-PT with the composition of 10% PT ( $0.9\text{PMN}-0.1\text{PT}$ ). As has been demonstrated by many early studies, for electrostrictive applications at near room temperature, the composition of PMN-PT is near  $0.9\text{PMN}-0.1\text{PT}$  whose weak field dielectric constant is presented in Fig. 1.<sup>6-8</sup> In addition, by applying a dc bias electric field to the material, an effective piezoelectric state can be induced, as shown schematically in Fig. 2. For an electrostrictive material such as the one investigated here, the material is often operated in the field-biased state. In this investigation, therefore, all the parameters are also characterized under different dc electric bias fields to simulate this operation mode.

## II. EXPERIMENTAL

All the specimens used in this investigation were made using conventional mixed oxides processing following the columbite B-site precursor method.<sup>9</sup> Most of the specimens were sintered at a temperature of 1250 °C for 2–6 h followed by annealing in an oxygen-rich

<sup>a)</sup>Address all correspondence to this author.

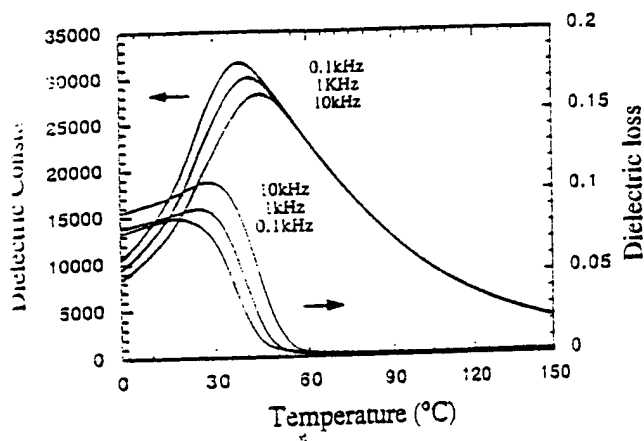


FIG. 1. The dielectric constant  $K$  and dielectric loss  $D$  as a function of temperature for 0.9PMN-0.1PT ceramics without external stress. The measuring frequency is 0.1, 1, and 10 kHz.

atmosphere at 900 °C for 6–24 h. The typical dielectric constant of the specimens is shown in Fig. 1.

In this investigation, the uniaxial stress applied to specimens is provided by an apparatus developed recently which has been described in an early publication.<sup>5</sup> Making use of this apparatus, the effective piezoelectric coefficient, the elastic compliance, and the dielectric constant in the dc electric field-biased state can be characterized under well-defined boundary conditions.

In this apparatus, the strain response was measured by a strain gauge (KYOWA KFR-02-120-C1-11). In the dc electric field-biased state, the strain response of the specimen is described by<sup>10</sup>

$$S_3 = d_{33}E_3 - s_{33}^E T_3 \quad \text{and} \quad S_1 = d_{31}E_3 - s_{13}^E T_3.$$

Hence, in the dc electric field-biased state, a weak ac electric field  $E_{ac}$  ( $< 100$  V/cm) induces ac strains  $S_3$  and  $S_1$  (under constant stress condition), parallel and perpendicular to  $E_{ac}$ , respectively, from which the piezoelectric coefficients  $d_{33}$  ( $= S_3/E_{ac}$ ) and  $d_{31}$  ( $= S_1/E_{ac}$ ) can be determined (see Fig. 2). In analogy, by measuring the

$S_3$  and  $S_1$  induced by a weak ac stress field  $T_{ac}$  (about 0.1 MPa) under constant electric field condition, the elastic compliance  $s_{33}^E$  and  $s_{13}^E$  can be determined. In this investigation, the strain was acquired at a frequency of 10 Hz. In order to improve the signal-to-noise ratio, the voltage signal from the strain gauge amplifier was measured by a lock-in amplifier. Furthermore, to ensure that  $T_3$  was uniformly applied to the specimen, two strain gauges attached to opposite faces of the specimen were utilized. Adjustment was made before the data acquisition so that the strain readings from the two strain gauges were the same within 5%. From repeated measurements, it was found that this adjustment was not very crucial to the determination of piezoelectric coefficients. However, for the elastic compliance, any nonuniformity in  $T_3$  can result in a large error. Hence, the

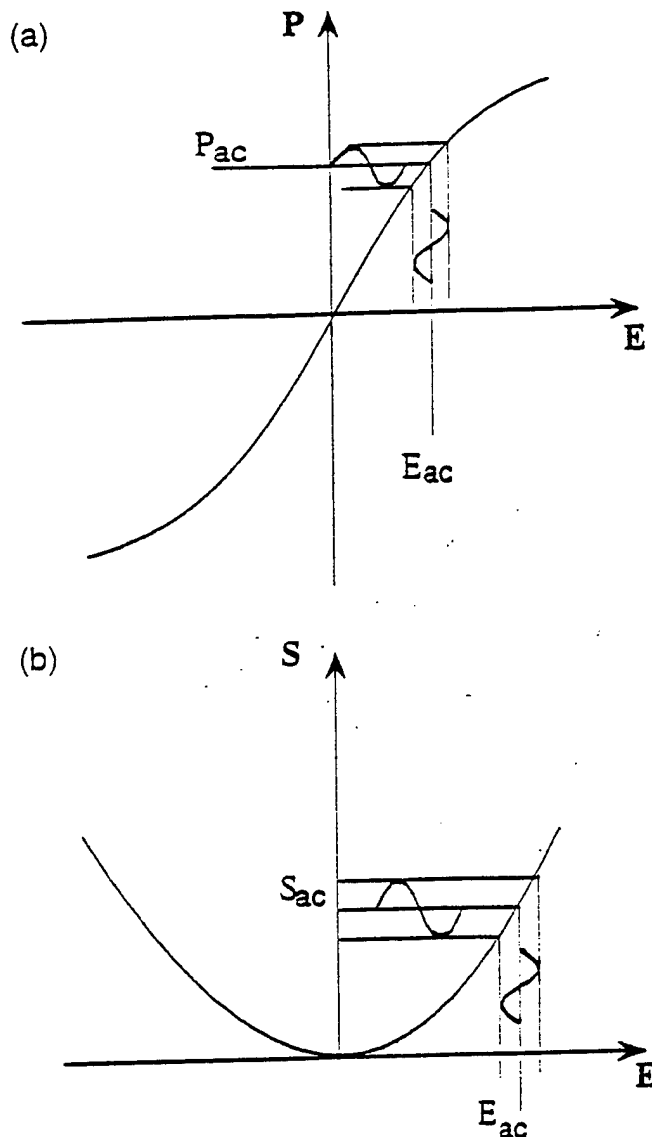


FIG. 2. Schematic drawing of (a) the polarization  $P$  and (b) strain  $S$  responses of 0.9PMN-0.1PT in the dc electric field-biased state where the effective dielectric constant is defined as  $P_{ac}/E_{ac}$  and the effective piezoelectric coefficient as  $S_{ac}/E_{ac}$ , respectively.  $S_{ac}$  can be  $S_1$  and  $S_3$ , and  $E$  is the electric field.

error in the piezoelectric coefficient determined is within 5% while error in the elastic compliance is about 10%.

The dielectric constant was determined using either a multifrequency LCR meter (HP model 4192A), or a calibrated small resistor in series with the specimen. In the later method, the voltage across the resistor, which is directly proportional to the current flowing through the specimen, was measured using a lock-in amplifier. From the data, the complex dielectric constant can be determined. The frequency range for the dielectric constant measurement is from 10 Hz to 1 MHz. The polarization level at each electric bias field and dc stress state was measured by a Sawyer-Tower circuit.

Since the material is operated at a temperature near the dielectric constant maximum  $T_m$  where there is a large change in the dielectric constant (see Fig. 1) and the polarization level in the field biased state, it is necessary to characterize the electromechanical parameters over a temperature region about  $T_m$ . In this investigation, three temperatures were chosen: 25 °C ( $< T_m$ ), 50 °C (near above  $T_m$ ), and 80 °C ( $> T_m$ ).

### III. THE DIELECTRIC RESPONSES

Presented in Fig. 3 is the dielectric constant acquired at 25 °C, which is below the dielectric constant maximum ( $T_m = 37$  °C at 1 kHz). Without dc electric bias fields, the data in Fig. 3 show that the dielectric constant decreases as the compressive stress  $T_3$  increases, a trend generally expected for a dielectric material with a positive electrostrictive coefficient  $Q_{11}$ .<sup>11,12</sup> On the other hand, at high dc bias fields, for instance, at 5 kV/cm, an increase of the dielectric constant with the compressive stress was observed. For the pressure range investigated, a dielectric maximum was observed near 60 MPa, which seems to be inconsistent with conventional electrostrictive behavior. This could be understood from the fact that because of the existence of micropolar regions, a high dc bias field can induce a macropolar state in the material. As the compressive stress increases, which tends to reduce the macropolarization level in the material, a "transformation" of the macropolar domain state to micropolar state occurs, resulting in the observed broad dielectric constant anomaly.<sup>13</sup>

It is well known that for a dielectric material, the change of the dielectric constant  $K$  with external stress can be a result of the electrostrictive coupling in the material. In fact, for many nonferroelectric materials, the electrostrictive coefficient can be determined conveniently from the slope of  $1/K$  versus the applied stress  $T$ .<sup>11,12</sup> However, for a ferroelectric based electrostrictive material such as PMN-PT, the change in the dielectric constant can also be a result of the changes in the local polarization state as has been pointed out in an early publication (shifting of the local Curie temperatures).<sup>12</sup> Moreover, the polarization response near  $T_m$  is mainly from the reorientation process of the micropolar regions to the external electric field. These so-called "extrinsic" contributions to the dielectric response can be affected by external stress. As a consequence, the  $1/K$  versus  $T_3$  relation even for the data without dc electric field exhibits a strong nonlinear behavior and the slope of the curve is far below  $Q_{11}$  measured directly from the strain-polarization relationship.

For the data at temperatures above the dielectric constant maximum, the dielectric constants all show monotonic decrease with the compressive stress for the dc bias fields investigated (up to 5 kV/cm), although at

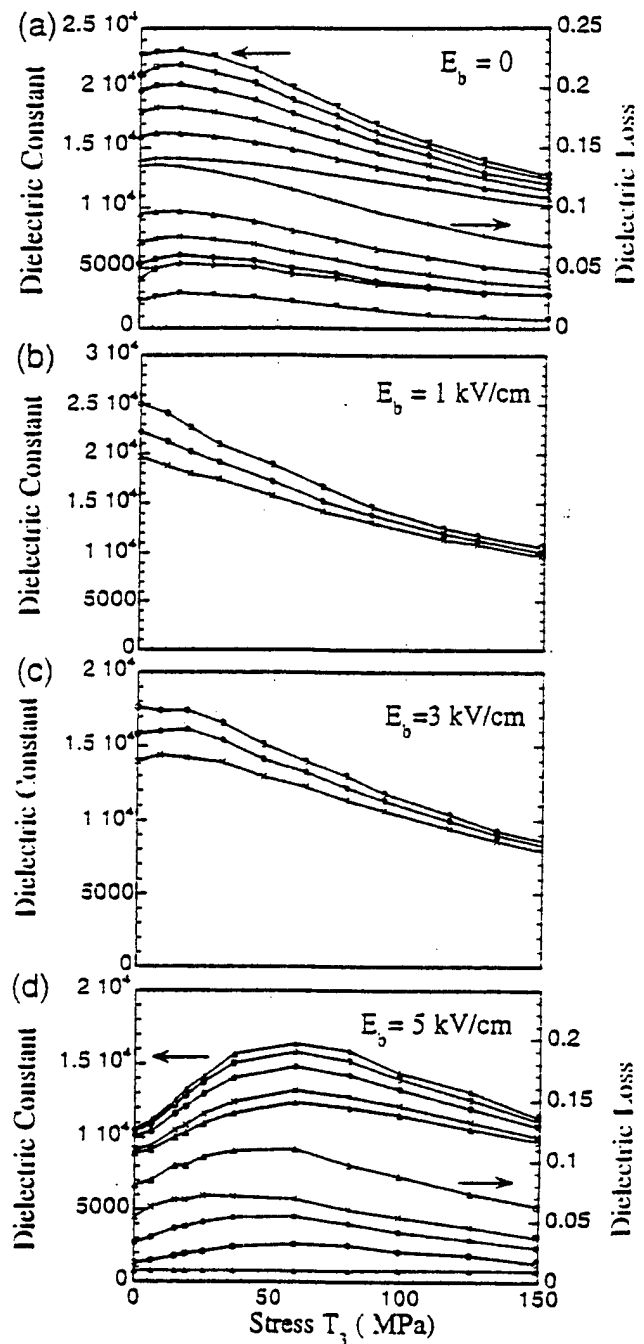


FIG. 3. The dielectric constant  $K$  and dielectric loss  $D$  as a function of the compressive stress  $T_3$  measured at 25 °C and different dc bias electric fields: (a)  $E_b = 0$ , (b)  $E_b = 1$  kV/cm, (c)  $E_b = 3$  kV/cm, and (d)  $E_b = 5$  kV/cm. The measuring frequency of the data: 10 Hz (▲), 0.1 kHz (○), 1 kHz (●), 10 kHz (×), 100 kHz (Δ), and 1 MHz (—).

50 °C, the dielectric constant under 5 kV/cm dc electric bias field exhibits a plateau at  $T_3 < 50$  MPa, which is presented in Fig. 4. The existence of this plateau is reminiscent of the transformation of the material from a macropolar state to a micropolar state, analogous to that observed at 25 °C. Because of the existence of the micropolar regions, even for the data at 80 °C (shown in Fig. 5), the slope of the dielectric stiffness versus stress

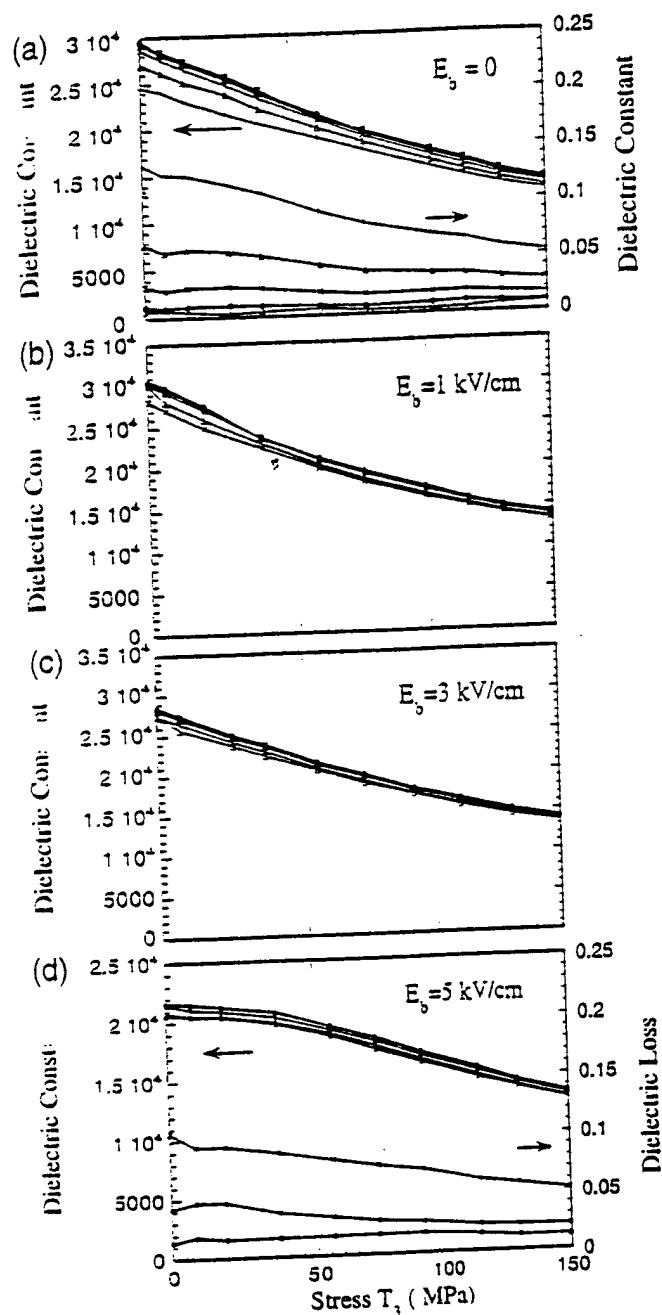


FIG. 4. The dielectric constant and dielectric loss as a function of the compressive stress  $T_3$  measured at 50 °C. (a)  $E_b = 0$ , (b)  $E_b = 1$  kV/cm, (c)  $E_b = 3$  kV/cm, and (d)  $E_b = 5$  kV/cm. The measuring frequency: 10 Hz (▲), 0.1 kHz (○), 1 kHz (●), 10 kHz (×), 100 kHz (□), and 1 MHz (+).

is still far below that determined by the electrostrictive coefficient despite the curve of  $1/K$  versus  $T_3$  exhibiting a nearly linear relationship in the stress range investigated. In addition, the slope of the curve decreases as the dc bias field increases, a signature of increased ferroelectric activity in the material when subjected to high electric fields.

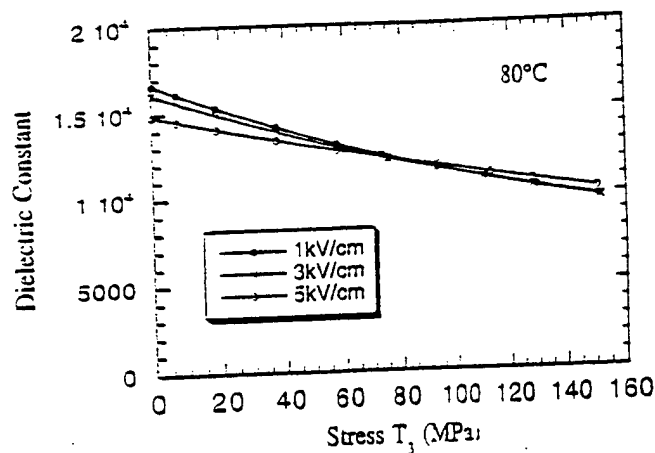


FIG. 5. The dielectric constant as a function of the compressive  $T_3$  at 30 °C, 1 kHz, and under different dc bias fields. The dielectric constant at this temperature exhibits very little dispersion.

At 25 and 50 °C, the dielectric data exhibit strong frequency dispersion. For that reason the data were collected at frequencies from 10 Hz to above 100 kHz to probe the influence of this dispersion by the applied stress  $T_3$ . Apparently, the external stress  $T_3$  reduces the dielectric dispersion significantly, and accompanying this reduction in the dispersion the dielectric loss is also reduced. The results reveal that the compressive stress  $T_3$  reduces the response of the micropolar regions and hence the degree of the relaxor behavior in the material. The data at 30 °C were acquired at a single frequency of 1 kHz because of a very weak frequency dispersion at the temperature.

#### IV. THE ELASTIC COMPLIANCE AS A FUNCTION OF THE COMPRESSIVE STRESS AT DIFFERENT BIAS FIELDS

Elastic compliances  $s_{33}^E$  and  $s_{11}^E$  were characterized as a function of compressive stress at different electric bias fields and temperatures are presented in Figs. 6 and 7, respectively. The general features revealed from the data are as follows: (i) the elastic compliance increases with dc bias fields and, hence, the polarization level in the material; (ii) the compliance exhibits a slight decrease with the compressive stress; (iii) the compliance decreases with temperature for the three temperatures measured. For the data at 25 °C under 5 kV/cm, an anomaly is observed which is apparently related to the phase transformation from a macropolar state to a micropolar state as has been discussed in the dielectric data. In the temperature and stress range investigated, the ratio of  $-s_{11}^E/s_{33}^E$  remains near 1/3.

In an early investigation by Cao and Evans,<sup>14</sup> it was found that in soft PZT, Poisson's ratio can reach near 0.5 when there is a stress depoling of the samples which is a direct consequence of the domain reorientation during

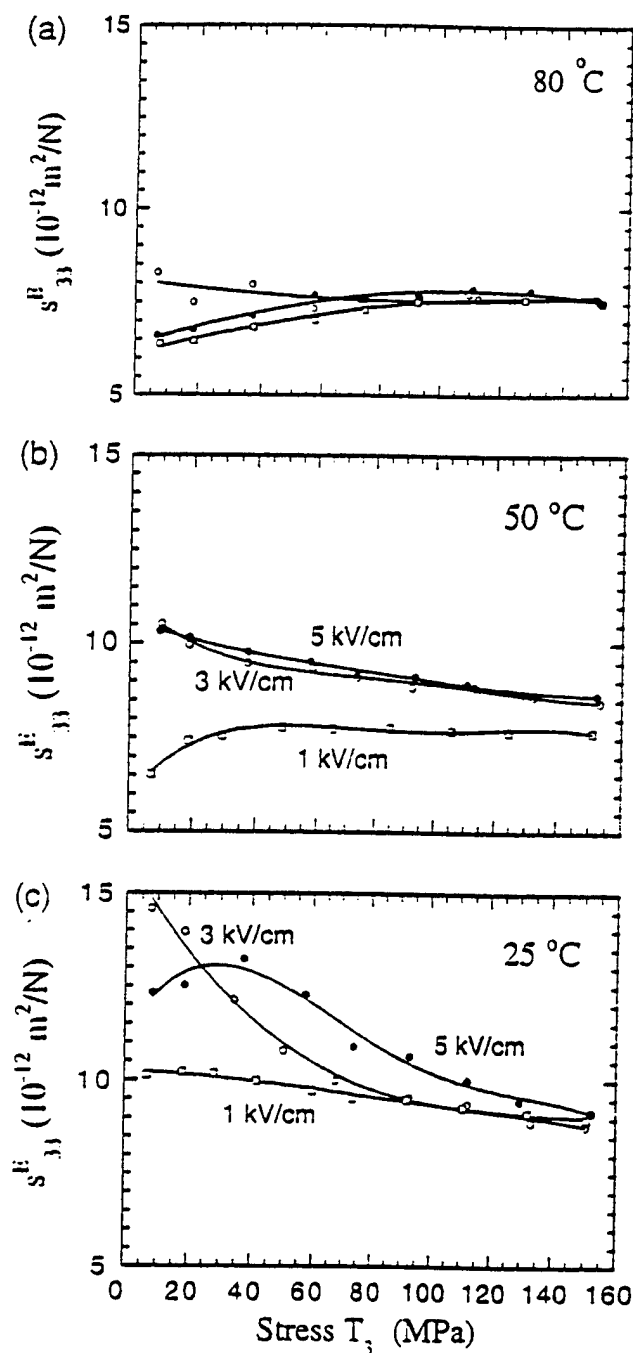


FIG. 6. The elastic compliance  $s_{33}^E$  as a function of the compressive  $T_3$  at different temperatures: (a)  $80^\circ\text{C}$ , (b)  $50^\circ\text{C}$ , and (c)  $25^\circ\text{C}$ ; and dc electric bias fields: 1 kV/cm ( $\square$ ), 3 kV/cm ( $\circ$ ), and 5 kV/cm ( $\bullet$ ).

the depoling process. If there is a significant contribution from the reorientation of the micropolar regions to the elastic process in the material, one would expect similar results, since this process will not generate volume strain. Therefore, the relatively small ratio of  $-s_{13}^E/s_{33}^E$  implies that the reorientation process of micropolar regions, which is responsible for the large dielectric constant near  $T_m$ , is not contributing significantly to the elastic process.

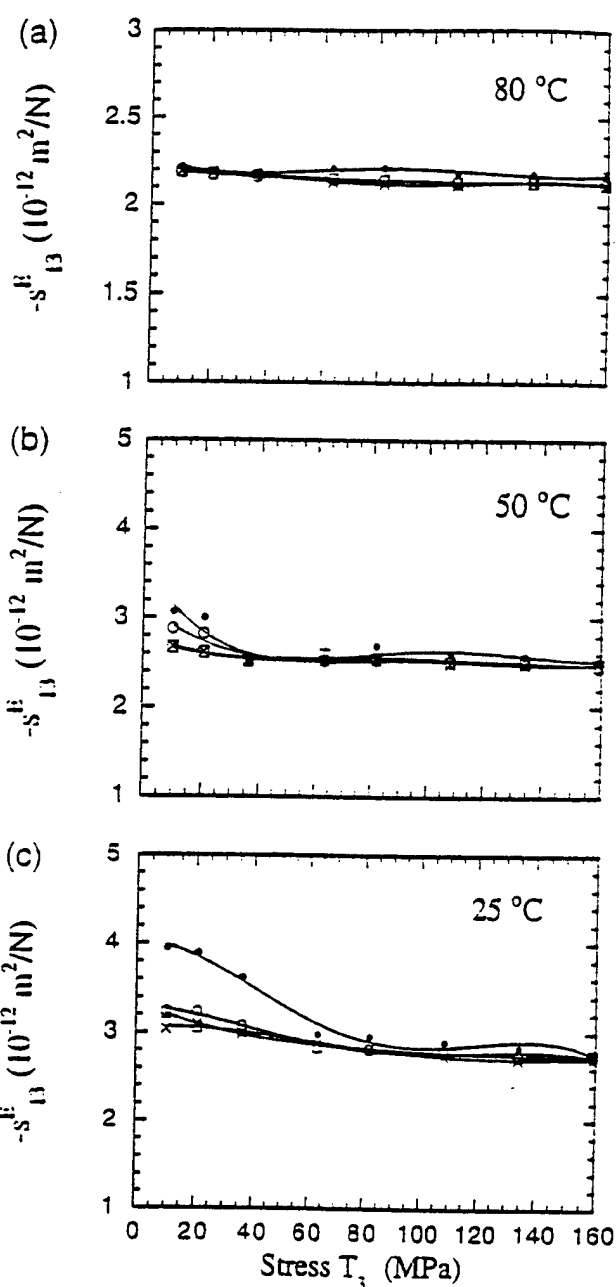


FIG. 7. The elastic compliance  $s_{13}^E$  as a function of the compressive  $T_3$  at different temperatures: (a)  $80^\circ\text{C}$ , (b)  $50^\circ\text{C}$ , and (c)  $25^\circ\text{C}$ ; and dc electric bias fields: zero bias ( $\times$ ), 1 kV/cm ( $\square$ ), 3 kV/cm ( $\circ$ ), and 5 kV/cm ( $\bullet$ ).

Indeed, there is only a very weak elastic compliance peak at temperatures near  $T_m$ .<sup>15</sup>

## V. THE EFFECTIVE PIEZOELECTRIC RESPONSES IN DC FIELD-BIASED STATES

The effective piezoelectric coefficients  $d_{33}$  and  $d_{31}$  in the electric field-biased state were characterized and are presented in Figs. 8 and 9. Analogous to the dielectric

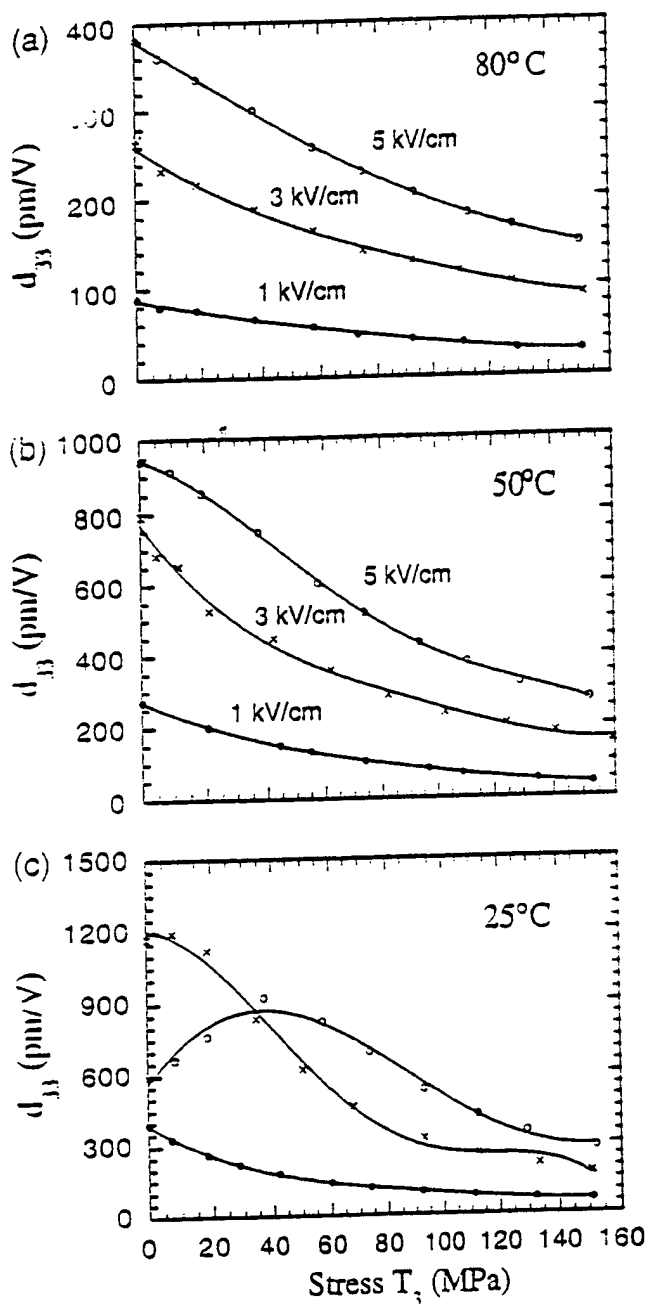


FIG. 8. The effective piezoelectric coefficient  $d_{33}$  at the dc field-biased states as a function of the compressive  $T_3$  at different temperatures: (a) 80 °C, (b) 50 °C, and (c) 25 °C; and dc electric bias fields: 1 kV/cm (●), 3 kV/cm (×), and 5 kV/cm (○).

constant and elastic compliance data, a broad peak of  $d_{33}$  at the bias field of 5 kV/cm data was observed. In addition, there is also a weak peak at 3 kV/cm, while at 1 kV/cm  $d_{33}$  decreases monotonically with the stress. As pointed out earlier, this anomalous behavior observed at 3 and 5 kV/cm bias fields is associated with the phase transformation in the material in the dc field-biased state from a macropolar state to a micropolar

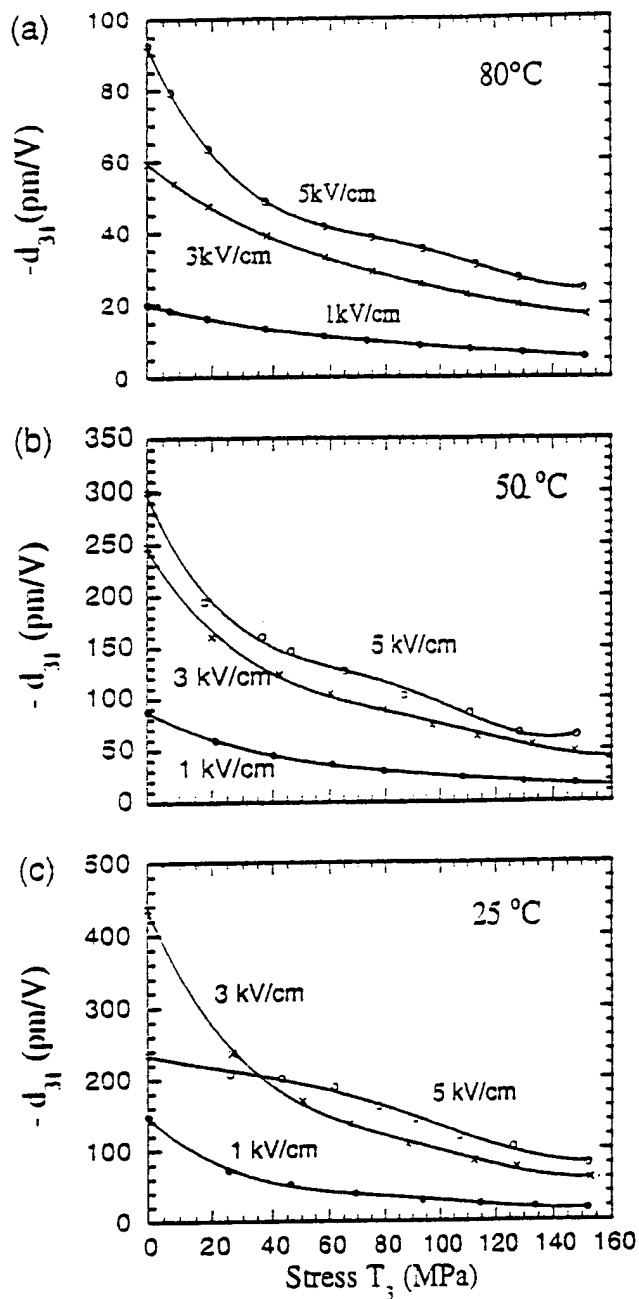


FIG. 9. The effective piezoelectric coefficient  $d_{31}$  at the dc field-biased states as a function of the compressive  $T_3$  at different temperatures: (a) 80 °C, (b) 50 °C, and (c) 25 °C; and dc electric bias fields: 1 kV/cm (●), 3 kV/cm (×), and 5 kV/cm (○).

state. The peak is much less pronounced in the data of  $d_{31}$ . At higher temperatures, both  $d_{33}$  and  $d_{31}$  exhibit a monotonic decrease with the compressive stress. The decrease of  $d_{33}$  and  $d_{31}$  with the compressive stress at higher temperatures is a result of the reduction of the polarization level  $P_3$  and the dielectric constant  $K$  at the dc field-biased state with the stress. In fact, the ratio of  $d_{33}$  (or  $d_{31}$ ) to  $P_3K$ , which is directly proportional to

the effective electrostrictive coefficients of the ceramic sample, does not show marked change with stress.

Based on  $d_{33}$  and  $d_{31}$  data, the hydrostatic piezoelectric coefficient  $d_h$  ( $d_h = d_{33} - 2d_{31}$ ) in the dc field biased state is evaluated and presented in Fig. 10. One of the interesting features of the data in Fig. 10 is that a very pronounced peak in  $d_h$  is observed at 25 °C under a 5 kV/cm bias field. For the data at higher temperatures, a weaker but clear peak is observed under 5 kV/cm bias

field. This is in sharp contrast to the dielectric, elastic compliance, and piezoelectric  $d_{33}$  and  $d_{31}$  coefficients where the peak associated with the anomaly is much weaker. As has been pointed out, the anomaly is due to the transformation from a macropolar state to a micropolar state due to the applied stress. The result reveals that this transformation involves a large volume change which yields a large change in  $d_h$  in the broad transition region.

In a recent study of the electrostrictive coefficients of prototype cubic phase of PMN, it was found that the hydrostatic electrostrictive coefficient is about  $0.08 \text{ m}^2/\text{C}^2$ .<sup>3</sup> This value is more than 10 times higher than that determined directly from a field-induced strain measurement.<sup>2</sup> The difference between the two results lies in the fact that at temperatures near  $T_m$ , the material has a high population of micropolar regions and the reorientation of these polar regions does not generate volume change. Consequently, the  $Q_h$  measured from the volume strain-polarization relationship at temperatures near  $T_m$  has a much smaller value than the intrinsic  $Q_h$  value of the material. ( $Q_h$  for the prototype cubic phase of  $0.9\text{PMN}-0.1\text{PT}$  is nearly the same as that of PMN.) In this paper, this low value of  $Q_h$  measured from field-induced volume strain  $S_v$  at temperatures near  $T_m$  is named as the apparent  $Q_h$  ( $Q_h^a$ ) of the material to distinguish it from the intrinsic  $Q_h$  which is determined from the change in the lattice constant of the unit cell due to the change in polarization.

For  $0.9\text{PMN}-0.1\text{PT}$ ,  $Q_h^a = 0.006 \text{ m}^2/\text{C}^2$  at room temperature without external field. From the electrostrictive relation  $S_v = Q_h^a P^2$ , where  $P$  is the total polarization response in the sample, and also  $S_v = Q_h P_v^2$ , where  $P_v$  is the polarization response which generates volume strain, the ratio  $P_v/P = \sqrt{Q_h^a/Q_h}$  can be determined. For PMN-PT near  $T_m$ , this ratio is about 0.27, which implies that about 70% of the weak field polarization response in  $0.9\text{PMN}-0.1\text{PT}$  at temperatures near  $T_m$  is due to the reorientation of the micropolar regions, which does not generate the volume change of the material.

This observation raises an interesting issue on how to improve the hydrostatic response of the material, which is important for many underwater applications. By reducing the polarization response related to the micropolar region reorientation, even if this may not increase  $d_h$  in the case that  $P_v$  in the material does not change (from the electrostrictive relation,  $d_h = 2Q_h P_v \Delta P_v$  in the field biased state), the reduction of the dielectric constant will improve the hydrostatic figure of merit  $d_h g_h$  since  $g_h$  is equal to  $d_h/K$ . The  $d_h g_h$  for the samples investigated is presented in Fig. 11. As can be seen from the figure, in spite of the fact that the material possesses a relatively high  $d_h$  ( $> 400 \text{ pm/V}$ , about 10 times higher than that of PZT piezoceramics), the relatively high dielectric constant due to the micropolar region reori-

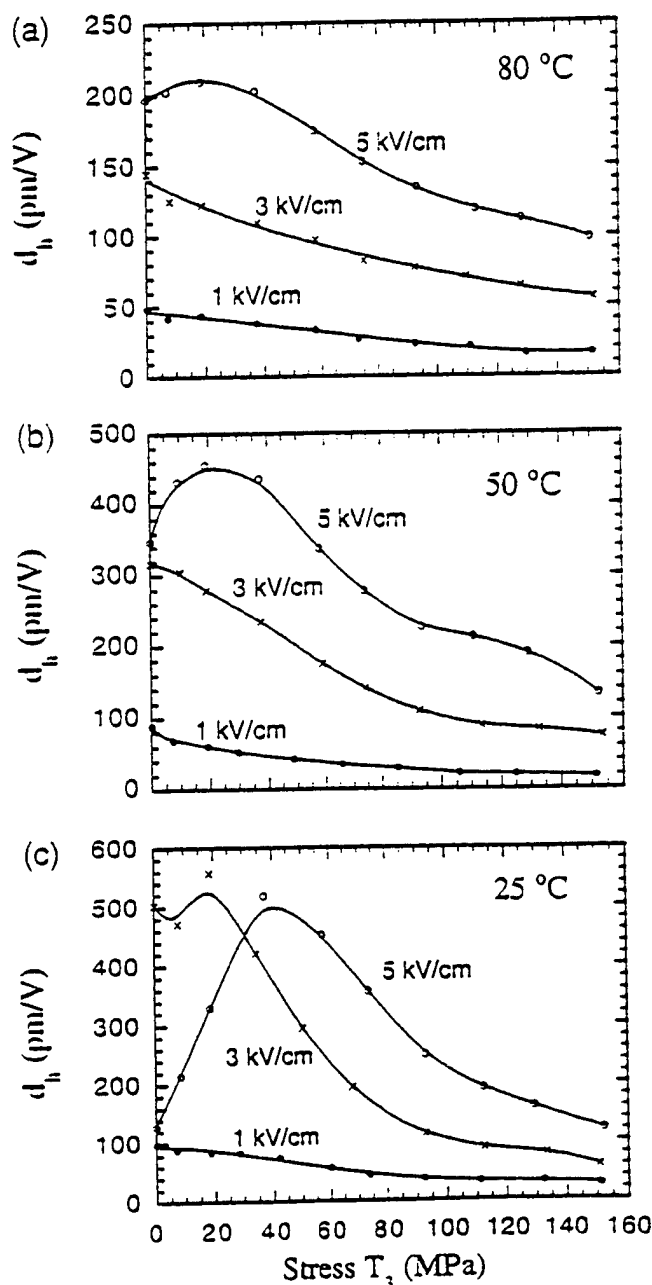


FIG. 10. The effective hydrostatic piezoelectric coefficient  $d_h$  at the dc field-biased states as a function of the compressive  $T_3$  at different temperatures: (a) 80 °C, (b) 50 °C, and (c) 25 °C; and dc electric bias fields: 1 kV/cm (●), 3 kV/cm (×), and 5 kV/cm (○).

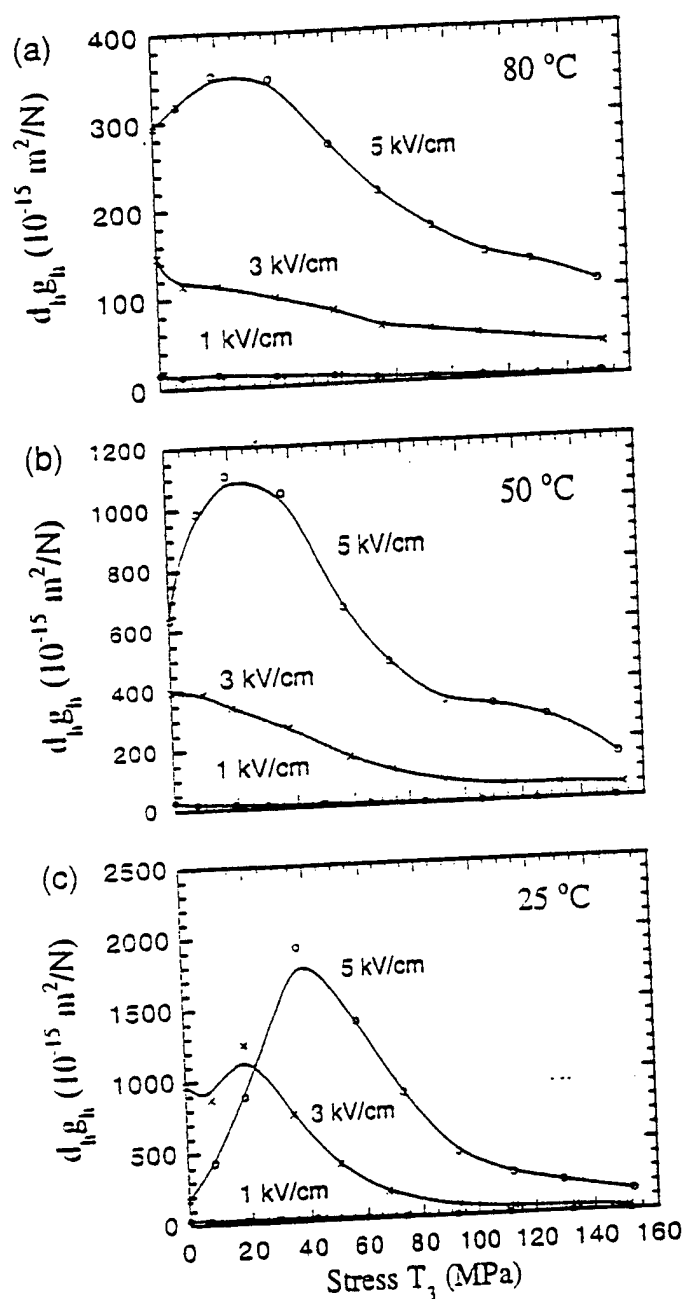


FIG. 11. The hydrostatic figure of merit  $d_h g_h$  at the dc field-biased states as a function of the compressive  $T_3$  at different temperatures: (a) 80 °C, (b) 50 °C, and (c) 25 °C; and dc electric bias fields: 1 kV/cm (●), 3 kV/cm (×), and 5 kV/cm (○).

entation results in a figure of merit which is only about 20 times higher than that of PZT piezoceramics and is nearly the same as that of the piezopolymer PVDF.<sup>16</sup>

## VI. THE ELECTROMECHANICAL COUPLING FACTOR $k_{33}$ UNDER UNIAXIAL STRESS $T_3$

From the data presented in the preceding sections, the electromechanical coupling factor  $k_{33}$ , defined as

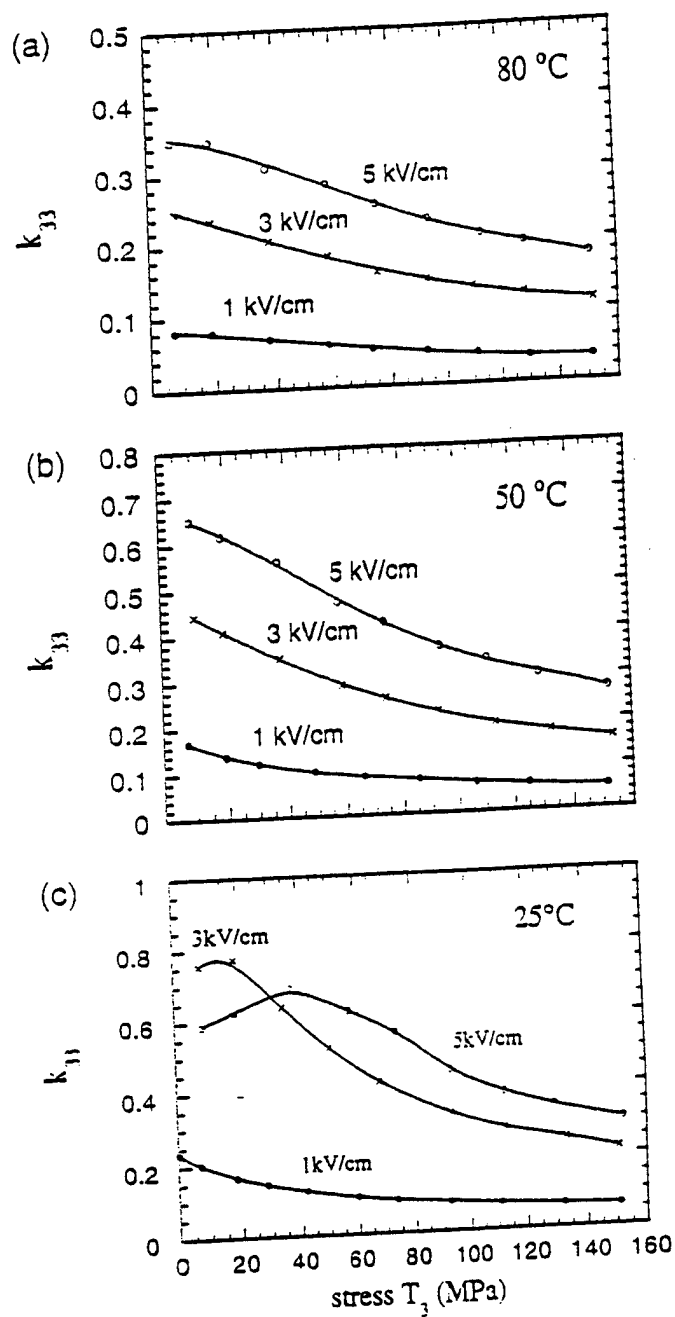


FIG. 12. The electromechanical coupling factor  $k_{33}$  (calculated at 10 Hz) as a function of the compressive  $T_3$  at different temperatures: (a) 80 °C, (b) 50 °C, and (c) 25 °C; and dc electric bias fields: 1 kV/cm (●), 3 kV/cm (×), and 5 kV/cm (○).

$k_{33}^2 = d_{33}^2 / (K \epsilon_0 \epsilon_{33}^E)$ , where  $\epsilon_0$  is the vacuum permittivity, can be derived.<sup>10</sup> The coupling factor as a function of  $T_3$  is presented in Fig. 12. Apparently, at high dc bias electric fields and without external stress,  $k_{33}$  of 0.9PMN-0.1PT at temperatures near  $T_m$  is near that of soft PZT, i.e., above 0.7. A disappointing feature of this material is that  $k_{33}$  drops quite significantly as the material is subjected to external compressive stress. This seems inevitable from the data presented in the

preceding sections since the reduction of the piezoelectric coefficients with stress is due to the reduction in both the dielectric constant and the polarization level in the field-biased state while the elastic compliance does not show a marked reduction with stress. As a result,  $k_{33}$  is reduced with stress. In order to improve the material performance with stress, one may need to develop materials with a broader dielectric peak so that the reduction of the polarization and dielectric constant with stress can be reduced.

## VII. SUMMARY

The influence of uniaxial compressive stress on the electromechanical behavior of  $0.9\text{PMN}-0.1\text{PT}$  ceramics under dc bias electric fields at temperatures near  $T_m$  was investigated. The compressive stress  $T_3$  reduces the responses of the micropolar regions, which results in a decrease in the dielectric constant, dielectric dispersion, dielectric loss, and effective piezoelectric coefficients. Our results also show that the response of the micropolar regions contributes far less to the elastic process compared with the dielectric process. Hence, the elastic compliance does not exhibit a marked change with stress and the ratio of  $-s_{13}^E/s_{33}^E$  remains near  $1/3$ . By combining the data of the piezoelectric coefficient, the dielectric constant, and elastic compliance, the longitudinal electromechanical coupling factor  $k_{33}$  was derived and was shown to decrease with the compressive stress  $T_3$ .

For electrostrictive PMN-PT at temperatures near  $T_m$ , the material can be converted into a macropolar state by applying a high dc electric field. Compressive stress will force the material back into a micropolar state, and the experimental results reveals that there is a broad transformation region between the two states instead of a smooth process. This transformation involves a change in part of the material between a rhombohedral phase and a cubic phase which involves a large volume strain as revealed by a pronounced peak in the hydrostatic

piezoelectric coefficient  $d_4$ . This phenomenon could be used to enhance the hydrostatic piezoelectric response of the material if the bias stress level is properly adjusted. Furthermore, for a given external prestress level, the material composition may be adjusted so that this transformation will occur at the given stress.

## ACKNOWLEDGMENT

This work was supported by the Office of Naval Research.

## REFERENCES

1. L. E. Cross, *Ferroelectrics* **76**, 241-257 (1987).
2. Q. M. Zhang and J. Zhao, *Appl. Phys. Lett.* **71** (12), 1649-1651 (1997).
3. J. Zhao, A. E. Glazounov, and Q. M. Zhang, *Appl. Phys. Lett.* (1998, in press).
4. Q. M. Zhang, H. Wang, N. Kim, and L. E. Cross, *J. Appl. Phys.* **75**, 454 (1994).
5. Q. M. Zhang, J. Zhao, K. Uchino, and J. Zheng, *J. Mater. Res.* **12**, 225-234 (1997).
6. J. Zhao, Q. M. Zhang, N. Kim, and T. Shrout, *Jpn. J. Appl. Phys.* **34** (10), 5658-5663 (1995).
7. S. M. Pilgrim, M. Massuda, J. D. Procey, and A. P. Ritter, *J. Am. Ceram. Soc.* **75** (7), 1964-1969 (1992).
8. C. L. Hom, S. M. Pilgrim, N. Shankar, K. Bridger, M. Massuda, and S. R. Winzer, *IEEE Trans. Ultrason., Freq. Contr.* **41** (4), 542-551 (1994).
9. S. L. Swartz and T. R. Shrout, *Mater. Res. Bull.* **17**, 1245-1250 (1982).
10. *IEEE Standard on Piezoelectricity*, IEEE, Ultrason., Ferroelect., and Freq. Contr. Soc., ANSI/IEEE Std. 176-1897 (1987).
11. V. Sundar and R. E. Newnham, *Ferroelectrics* **135**, 431-446 (1992).
12. Q. M. Zhang, W. Y. Pan, S. J. Jang, and L. E. Cross, *Ferroelectrics* **88**, 147-154 (1988).
13. G. A. Samara, *Phys. Rev. Lett.* **77**, 314-317 (1996).
14. H. Cao and A. G. Evans, *J. Am. Ceram. Soc.* **76** (4), 890-896 (1993).
15. D. D. Viehland, Ph.D. Thesis, The Pennsylvania State University (1991).
16. H. Wang, Ph.D. Thesis, The Pennsylvania State University (1994).

# **APPENDIX 14**

# Change in electromechanical properties of 0.9PMN:0.1PT relaxor ferroelectric induced by uniaxial compressive stress directed perpendicular to the electric field

J. Zhao, A. E. Glazounov, and Q. M. Zhang<sup>a)</sup>

*Materials Research Laboratory, The Pennsylvania State University, University Park, Pennsylvania 16802*

(Received 12 October 1998; accepted for publication 11 November 1998)

It was shown that the uniaxial compressive stress applied perpendicular to the electric field strongly changes the dielectric and electromechanical properties of relaxor ferroelectric 0.9PMN:0.1PT at temperatures around its dielectric constant maximum,  $T_m$ . This includes: (i) a shift of the temperature of the electric field induced phase transition into the ferroelectric state and a depoling temperature to higher values which brings a large hysteresis in the material response to the electric field, and (ii) the symmetry breaking in the plane perpendicular to the direction of the electric field (3-axis). Using this symmetry breaking, from the ratio of the effective piezoelectric coefficients in the field biased state,  $d_{32}/d_{31}$ , the size of the micropolar regions at temperatures near  $T_m$  was estimated. © 1999 American Institute of Physics. [S0003-6951(99)04503-9]

In recent years, the electrostrictive properties of relaxor ferroelectrics (relaxors) have been the focus of intensive studies in view of their application in actuators and transducers. This is because at temperatures around the dielectric constant maximum,  $T_m$ , relaxors exhibit large electrostrictive strain, the strain-field relationship is practically free of hysteresis,<sup>1</sup> and the effective piezoelectric coefficient can be tuned by changing the magnitude of the dc bias field.<sup>2</sup> These features are highly desirable for actuators used in precise micropositioning and for applications in smart structures.

The material selected for this study was solid solution (1-x)PMN:xPT, with  $x=0.10$ , because it exhibits the highest strain around room temperature among other relaxor compositions. The goal was to characterize the change in its electromechanical properties with external stress, since in most actuator and transducer applications, the material is often subjected to high external mechanical load. In addition to these purely practical issues, we also demonstrate results which are of interest from a fundamental point of view. It is shown that by using the stress dependence of the piezoelectric coefficients of 0.9PMN:0.1PT one can deduce the size of the micropolar regions.

The ceramic samples were fabricated using a route described in Ref. 3. The uniaxial stress was applied to the specimen using an apparatus developed recently.<sup>4</sup> In the studied temperature range around  $T_m$ , the electric field induced strain of 0.9PMN:0.1PT is electrostrictive,<sup>1,2</sup> and therefore, a direct current (dc) electric bias field was applied in order to characterize the stress dependence of the effective piezoelectric coefficients of this material.

During the experiments, the induced strain was measured using a strain gauge ("KYOWA").<sup>4</sup> In the dc electric field biased state, the longitudinal,  $S_3$ , and transverse,  $S_j$  ( $j=1,2$ ), strain responses of the material can be described by<sup>5</sup>

$$S_3 = d_{33}E_3 + s_{31}^E\sigma_1 \quad \text{and} \quad S_j = d_{3j}E_3 + s_{1j}^E\sigma_1, \quad (1)$$

where  $d_{ij}$  is the effective piezoelectric coefficient,  $s_{ij}^E$  is the elastic compliance, and the coordinate system is chosen such that the 3-axis is parallel to the applied electric field, the 1-axis is along the compressive stress, and the 2-axis is perpendicular to the 1- and 3-axes, respectively. Under the constant stress condition, we apply a weak alternating current (ac) electric field  $E_{ac}$  ( $<100$  V/cm) to induce ac strains  $S_3$ ,  $S_1$ , and  $S_2$ , parallel and perpendicular to  $E_{ac}$ , from which the effective piezoelectric coefficients  $d_{33}(=S_3/E_{ac})$  and  $d_{3j}(=S_j/E_{ac}, j=1,2)$  can be determined. In order to ensure that  $\sigma_1$  was uniformly applied to the specimen, two strain gauges attached to opposite faces of the specimen were utilized. Adjustments were made before acquiring the data so that the strain readings from the two strain gauges were the same within 5%. The dielectric constant,  $\epsilon$ , was measured by using a calibrated small resistor connected in series with the specimen, and monitoring the voltage drop across the resistor, which is related with the current flowing through the specimen. The polarization level at each electric bias field and constant stress state was measured by a Sawyer-Tower circuit. All the measurements of  $d_{ij}$ ,  $\epsilon$  and the polarization were performed using a frequency of 10 Hz.

Since the material is operated at temperatures near the dielectric constant maximum, where there is a large change in material properties with temperature, it is necessary to characterize them over the temperature range around  $T_m$ . In stress-free conditions and without a dc bias 0.9PMN:0.1PT has  $T_m \approx 35^\circ\text{C}$  at 10 Hz. Thus to have a systematic picture, three points were chosen:  $25^\circ\text{C}$  (below  $T_m$ ),  $50^\circ\text{C}$  (slightly above  $T_m$ ), and  $80^\circ\text{C}$  (above  $T_m$ ).

Unlike normal ferroelectrics, in relaxors the maximum in  $\epsilon(T)$  at  $T_m$  does not correspond to the spontaneous structural phase transition to the polar state.<sup>6,7</sup> In the (1-x)PMN:xPT system, with  $x<0.3$ , the phase transition occurs at lower temperatures and only under a large electric field,<sup>8-10</sup> which is represented by the electric field-temperature phase diagram.<sup>3</sup> Once induced, the macropolar state will remain stable at temperatures below  $T_d$ , above

<sup>a)</sup>Corresponding author; electronic mail: qxz1@psu.edu

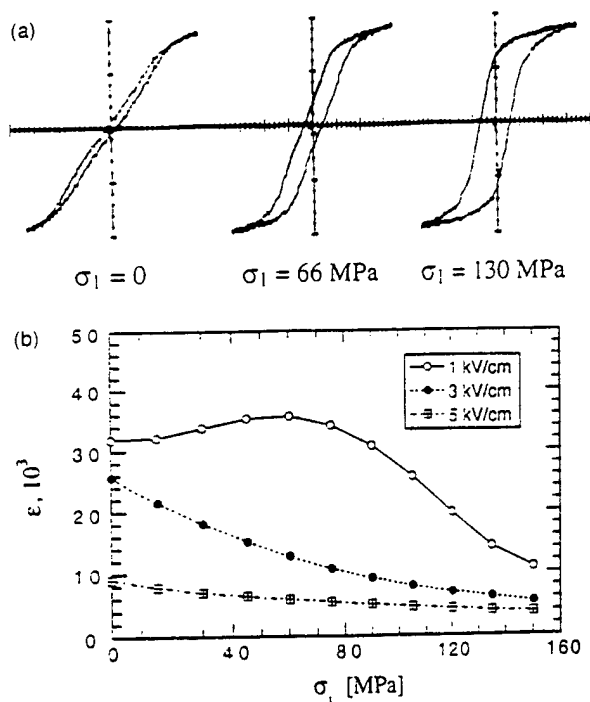


FIG. 1. Polarization and dielectric data measured at 25 °C at frequency 10 Hz. (a) Change in the polarization-electric field hysteresis loop with the compressive stress  $\sigma_1$  from slim loop (micropolar state) to square loop characteristic of regular ferroelectric state. The axis scale is 1.5 kV/cm per division for electric field and 0.14 C/m<sup>2</sup> per division for polarization. (b) Stress dependence of small-signal dielectric constant measured at different dc bias field. Symbols show experimental data and the lines are drawn to guide the eye.

which the thermal depoling of the material occurs. According to the phase diagram, the depoling temperature,  $T_d$ , shifts to higher values under the dc bias field. The thermal depoling of the material above  $T_d$  manifests itself, for example, in the change of the shape of the polarization-field dependence from a rectangular loop below  $T_d$  to the so-called slim loop without hysteresis around  $T_m$ .<sup>6,7</sup> On a microscopic level, the depoling is described as breaking of the macropolar state into small, nanometer scale size, regions with the local spontaneous polarization (micropolar state).<sup>7</sup>

In a normal ferroelectric the electrostrictive coupling in the material shifts the Curie temperature,  $T_c$ , under the external stress according to<sup>5,11</sup>

$$\Delta T = 2\epsilon_0 C Q_{11}\sigma_3 \quad \text{and} \quad \Delta T = 2\epsilon_0 C Q_{12}\sigma_1, \quad (2)$$

where  $\Delta T = T_c(\sigma_1) - T_c(0)$ ,  $\epsilon_0 = 8.854 \times 10^{-12}$  F/m,  $C$  is the Curie-Weiss constant,  $Q_{11}$  and  $Q_{12}$  are the longitudinal and transverse electrostrictive coefficients, respectively, and we use a conventional sign notation that the compressive stress is of negative sign. The trend should be the same for relaxor 0.9PMN:0.1PT, where one should expect that the depoling temperature will be shifted by the external stress. For example, a compressive  $\sigma_1$  stress should shift  $T_d$  to higher values, since in 0.9PMN:0.1PT  $Q_{12} < 0$ .<sup>11</sup>

Indeed, as shown in Fig. 1(a), at 25 °C, there is a transformation of the polarization-field dependence from a slim loop under the stress free condition to a nearly square hysteresis loop under a high compressive stress,  $\sigma_1$ . This implies that the macropolar state induced by the electric field becomes stable at room temperature after the field is turned

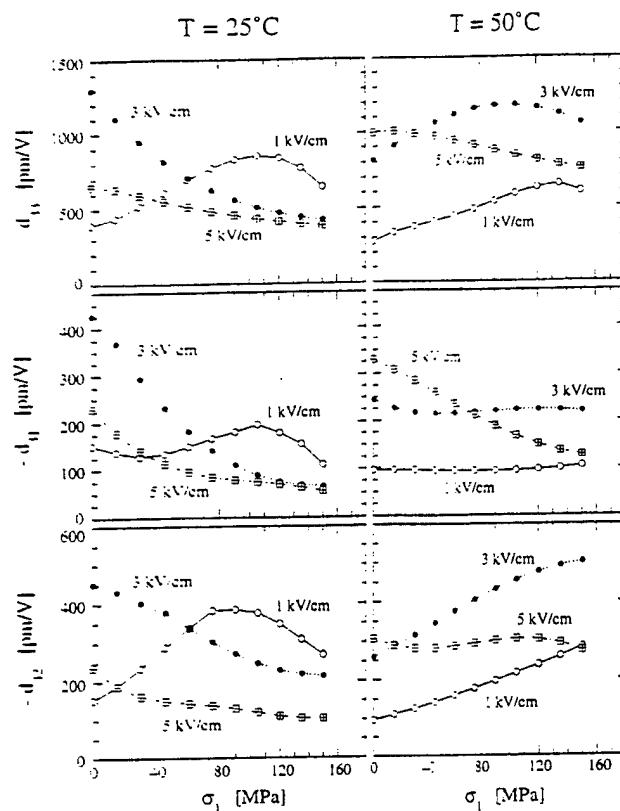


FIG. 2. Effective piezoelectric coefficients,  $d_{33}$ ,  $d_{31}$ , and  $d_{32}$ , of 0.9PMN:0.1PT in the electric field biased state measured as a function of compressive stress,  $\sigma_1$ , and dc bias at two temperatures: 25 °C (left column) and 50 °C (right column). The frequency of small ac probing field is 10 Hz. Symbols show experimental data, and the lines are drawn to guide the eye.

off. In other words, the compressive stress shifted the depoling temperature from  $T_d \approx 10$  °C, Ref. 2, to higher values so that now  $T_d(\sigma_1) > 25$  °C.

The stress dependence of the dielectric constant measured at different dc bias fields at 25 °C also presents evidence that the external stress,  $\sigma_1$ , moves the depoling temperature to higher values, only that now  $T_d$  is a function of both the dc bias field,  $E_b$ , and  $\sigma_1$ . In the plot in Fig. 1(b), the anomalous change in  $\epsilon$  measured at  $E_b = 1$  kV/cm around  $\sigma_1 = 80$  MPa can be explained in terms of the phase transition from the micropolar state to the macropolar state. This corresponds to the shift in the depoling temperature from  $T_d \approx 15$  °C at the stress free condition,<sup>12</sup> to 25 °C at  $\sigma_1 = 80$  MPa, at the same value of the dc bias,  $E_b = 1$  kV/cm. Furthermore, since  $T_d$  increases with increasing dc bias,<sup>8</sup> one should expect that at larger  $E_b$ , a lower stress level will be required to induce the macropolar state. Indeed, this can be seen in Fig. 1(b), where at  $E_b = 3$  and 5 kV/cm, the gradual decrease in  $\epsilon(\sigma_1)$  indicates that the material is in the macropolar state already at  $\sigma_1 = 0$ . Similar gradual change is also observed in  $\epsilon(\sigma_1)$  measured at 1 kV/cm at high stress levels, Fig. 1(b).

For the effective piezoelectric coefficients, the phase transition to macropolar state manifests itself in the form of the maximum in  $d_{ij}(\sigma_1)$ , as shown in Fig. 2 at 25 °C at  $E_b = 1$  kV/cm. Using the equation for the effective piezoelectric coefficients of the electrostrictive material, for example,<sup>2</sup>  $d_{33} = 2Q_{11}\epsilon_0\epsilon P(E_b)$ , the maximum can be explained as a result of competition between the increase in the macro-

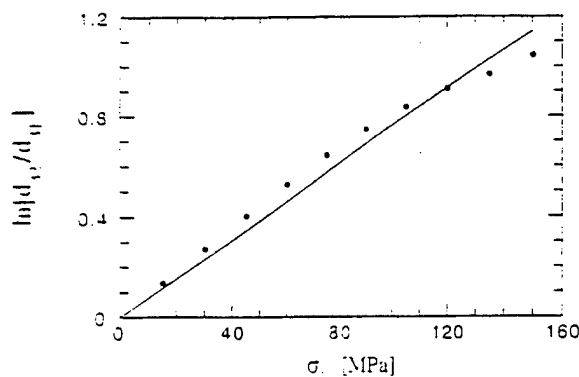


FIG. 3. Stress,  $\sigma_1$ , dependence of  $\ln(d_{32}/d_{31})$  calculated from the data measured at 50 °C at dc bias field of 1 kV/cm. In these conditions, the effective piezoelectric coefficients represent the strain response of the material due to reorientation of the micro-polar regions. Closed circles show the experimental data, and the solid line corresponds to the fit of Eq. (3) to the data.

scopic polarization,  $P(E_b)$ , during the phase transformation and the drop of the dielectric constant, shown in Fig. 1(b).

Besides the fundamental interest that an external stress can affect the electric field-temperature phase diagram of relaxors,<sup>13</sup> the results presented in Fig. 1(a) raise an important issue for practical application of these materials. Namely, even though at zero stress the material does not exhibit hysteresis in the polarization-field and strain-field relationships, application of high mechanical load can transform it into a state with a large hysteresis, which will significantly affect the performance of the device.

Another interesting issue revealed by this study is a large difference between  $d_{31}$  and  $d_{32}$ , which means that the external stress  $\sigma_1$  breaks the symmetry between the 1- and 2-axes. The difference includes numerical values and even the shape of the stress dependence (at 50 °C) of both coefficients, Fig. 2. For the piezoelectric response from the intrinsic contribution, i.e., from the induced lattice strain, based on the phenomenology and known experiment data, one would not expect such a large difference between  $d_{32}$  and  $d_{31}$ . On the other hand, for extrinsic contributions, such as domain wall motion or reorientation of the micropolar regions, which are thermally activated processes, the stress  $\sigma_1$  can induce a large difference between  $d_{31}$  and  $d_{32}$ .

We can demonstrate that using the data measured at  $E_b = 1$  kV/cm at 50 °C. At 1 kV/cm, no evidence for the phase transition to the macropolar state was observed within the whole studied range of stress  $\sigma_1$ . Therefore, the material can be described as an ensemble of the micropolar regions, and for temperatures near  $T_m$  its response to small ac field is dominated by their reorientation.<sup>14</sup> Since these regions are also ferroelastic and generate strain response, the measured  $d_{31}$  and  $d_{32}$  represent the strain related with the reorientation of the polar regions in the direction of ac probing field, i.e., along 3-axis. In (1-x)PMN:xPT family, the micropolar regions have a rhombohedral structure,<sup>15</sup> and therefore, the measured strain is related with the polar vector reorientation on 71° and 109°. For a ceramic specimen consisting of randomly oriented crystallites, the largest contribution to the strain  $S_1$  and  $S_2$  will be from the polar regions whose polar axis is initially close to 1- and 2-axes, respectively.

When an external static stress is applied to the specimen,

the initial orientation of individual micropolar region will depend also upon extra energy term  $\sigma_1 S_1 V_r$ , resulting from the coupling of stress  $\sigma_1$  to the local strain  $S_1$  in the polar region ( $V_r$  is the volume of the polar region). Thus, the difference between the population of the polar regions oriented along 1- and 2-axes will depend upon the elastic energy difference between these two orientation states. Therefore, one can write

$$\frac{d_{32}}{d_{31}} = \exp\left(\frac{\Delta S_1 V_r}{k_B T} \sigma_1\right), \quad (3)$$

where  $k_B$  is the Boltzmann constant, and  $\Delta S_1$  is the difference in the strain  $S_1$  for polar region oriented along 1-axis and 2-axis, respectively. We stress again that we assume that all the strain response of 0.9PMN:0.1PT is from the micropolar region reorientation, which is a good approximation for the relaxor ferroelectric at temperatures near  $T_m$ .<sup>14</sup>

Indeed, as shown in Fig. 3, the plot of  $\ln(d_{32}/d_{31})$  vs  $\sigma_1$  yields nearly a straight line, as predicted by Eq. (3). From the average slope of the line, we evaluated the volume  $V_r$  of a single micropolar region, using  $\Delta S_1 = 0.1\%$  based on the lattice constant data of the rhombohedral polar phase for close composition, PMN, which were obtained using a high-resolution neutron powder diffraction.<sup>16</sup> The estimate yielded  $V_r \approx 100 \times 10^3 \text{ \AA}^3$ , which corresponds to the size of the polar region approximately equal to 46 Å, assuming that the region has a spherical shape. This estimate is consistent with the value of 100 Å derived using other experimental techniques,<sup>15,17</sup> indicating that the polar regions existing in the material indeed have a nanometer scale size.

The authors wish to thank the Office of Naval Research for the financial support of this work.

- <sup>1</sup> K. Uchino, S. Nomura, L. E. Cross, R. E. Newnham, and S. J. Jang, *J. Mater. Sci.* **16**, 569 (1981).
- <sup>2</sup> J. Zhao, Q. M. Zhang, N. Kim, and T. Shrout, *Jpn. J. Appl. Phys., Part 1* **34**, 5658 (1995).
- <sup>3</sup> S. L. Swartz and T. R. Shrout, *Mater. Res. Bull.* **17**, 1245 (1982).
- <sup>4</sup> Q. M. Zhang, J. Zhao, K. Uchino, and J. Zheng, *J. Mater. Res.* **12**, 225 (1997).
- <sup>5</sup> F. Jona and G. Shirane, *Ferroelectric Crystals* (Dover, New York, 1993).
- <sup>6</sup> G. A. Smolensky, *J. Phys. Soc. Jpn.* **28**, 26 (1970).
- <sup>7</sup> L. E. Cross, *Ferroelectrics* **76**, 241 (1987).
- <sup>8</sup> R. Sommer, N. K. Yushin, and J. J. van der Klink, *Phys. Rev. B* **48**, 13230 (1993).
- <sup>9</sup> O. Noblanc, P. Gaucher, and G. Calvarin, *J. Appl. Phys.* **79**, 4291 (1996).
- <sup>10</sup> E. V. Colla, N. K. Yushin, and D. Viehland, *J. Appl. Phys.* **83**, 3298 (1998).
- <sup>11</sup> V. Sundar and R. E. Newnham, *Ferroelectrics* **135**, 431 (1992).
- <sup>12</sup> D. J. Taylor, D. Damjanovic, and A. Bhalla, *Ferroelectrics* **118**, 143 (1991).
- <sup>13</sup> G. A. Samara, *Phys. Rev. Lett.* **77**, 314 (1996).
- <sup>14</sup> Q. M. Zhang and J. Zhao, *Appl. Phys. Lett.* **71**, 1649 (1997).
- <sup>15</sup> N. de Mathan, E. Husson, C. Calvarin, J. Gavarrin, A. Hewat, and A. Moreil, *J. Phys.: Condens. Matter* **3**, S159 (1991).
- <sup>16</sup> J. Zhao, A. E. Glazounov, Q. M. Zhang, and B. Toby, *Appl. Phys. Lett.* **72**, 1048 (1998).
- <sup>17</sup> S. B. Vakhruшев, B. E. Kvyatkovsky, A. Naberezhnov, N. Okuneva, and B. P. Toperverg, *Ferroelectrics* **90**, 173 (1989).

# **APPENDIX 15**

## Large Hydrostatic Piezoelectric Constant and Temperature Dependence of the Piezoelectric Properties of $\text{Bi}(\text{NiTi})_{1/2}\text{O}_3$ : $\text{PbTiO}_3$ Ceramics

EDWARD F. ALBERTA<sup>a\*</sup>, AMAR S. BHALLA<sup>a</sup> and T. TAKENAKA<sup>b</sup>

<sup>a</sup>*Materials Research Laboratory, The Pennsylvania State University, University Park, Pennsylvania, USA and* <sup>b</sup>*Faculty of Science and Technology, Science University of Tokyo, Noda, Chiba-ken, 278 JAPAN.*

(Received July 15, 1998)

Large hydrostatic piezoelectric coefficient,  $d_h \sim 111$  pC/N, for compositions in the system  $(1-x) \text{Bi}(\text{NiTi})_{1/2}\text{O}_3$ :  $(x) \text{PbTiO}_3$  [BPNT] has been reported in this paper. Temperature dependencies of the dielectric, elastic, and piezoelectric properties of two compositions,  $x = 0.40$  and  $x = 0.50$ , around the morphotropic phase boundary of  $\text{Mn}^{+2}$  doped BPNT ceramics have been studied. Room temperature dielectric hysteresis loops with  $P_r = 37.86$   $\mu\text{C}/\text{cm}^2$  and  $E_c = 25.75$  kV/cm were observed for  $x = 0.40$ . Electromechanical coupling factors,  $k_p = 32.5\%$ ,  $k_{31} = 19.7\%$ , and  $k_t = 57.1\%$  and piezoelectric constants,  $d_{33} = 250$  pC/N,  $d_{31} = -67$  pC/N, and  $d_h = 111$  pC/N were measured in the BPNT-40 composition. The hydrophone figure of merit,  $d_h g_h \approx 1055 \times 10^{-15} \text{ m}^2/\text{N}$  was calculated from these measurements.

### INTRODUCTION

The solid solution bismuth nickel titanate - lead titanate,  $(1-x) \text{Bi}(\text{NiTi})_{1/2}\text{O}_3$ :  $(x) \text{PbTiO}_3$  [BPNT- $x$ ], system has a morphotropic phase boundary at  $x = 0.445$ .<sup>1</sup> BPNT compositions have high Curie temperatures on the order of 400°C and have shown high mechanical strength ( $\sigma = 170$  MPa). These features, as well as, the large remanent polarization values ( $30 \mu\text{C}/\text{cm}^2$ ) make BPNT- $x$  ceramics attractive for high temperature sensor applications. However, the large coercive fields ( $>45$  kV/cm) and low breakdown strength could limit the ability to fully pole the ceramics. Takenaka, et al. has proposed  $\text{MnCO}_3$  additions to increase the breakdown strength and enhance the poling efficiency of these materials.<sup>2,3,4</sup>

\* Communicated by Dr. George W. Taylor

In our earlier work large hydrostatic  $d_h$  values have been reported on these materials.<sup>5</sup> In this paper we report various ferroelectric and piezoelectric properties for these high temperature - low lead content - piezoelectric compositions. To enhance poling, 0.02 wt%  $\text{MnCO}_3$  was added to these compositions. Temperature dependencies of two selected BPNT-(x) compositions with  $x = 0.40$  and  $x = 0.50$  were measured. Hydrostatic piezoelectric coefficient,  $d_h$ , and hydrophone figure of merit,  $d_h g_h$  were determined on these samples.

### EXPERIMENTAL PROCEDURE

Ceramics were prepared using the conventional mixed-oxide method. The milled powders were calcined at 800°C for one hour and then re-milled. Pellets were then pressed and sintered at 1100°C for two hours in air. After polishing, fired-on silver-paste electrodes were applied to the ceramic samples.

The dielectric constant and loss were measured using a computer-controlled multifrequency LCR meter (HP 4174A, Hewlett-Packard, Inc.). The temperature dependence of the dielectric constant and loss was also measured using a liquid nitrogen fed furnace with a working range of -150°C to 500°C. Dielectric hysteresis measurements were made using a modified Sawyer-Tower circuit.

Piezoelectric measurements were made on samples poled at 42 kV/cm while cooling from 100°C to room temperature in a silicone oil bath. After aging for 24 hours,  $d_{33}$  was measured using a Berlincourt  $d_{33}$  meter. The rest of the piezoelectric and elastic constants were determined using the fundamental resonance and first overtone frequencies, as described in the IEEE standards on piezoelectricity.<sup>6</sup> Hydrostatic piezoelectric measurements were made using a hydraulic pump and pressure vessel. An actuator within the pressure vessel was used to apply a small dynamic hydrostatic pressure at a frequency of 30 Hz. The voltages produced by both the test specimen and a standard (PZT-5A) were measured with a spectrum analyzer. These voltages were then used to calculate the value of  $d_h$ .

The temperature dependence of the piezoelectric coefficients was evaluated using an impedance analyzer (HP-4194A, Hewlett-Packard, Inc.) and a nitrogen-fed furnace (DD-2300, Delta Design, Inc.). The same method previously mentioned was

used to calculate these coefficients between  $-150^\circ\text{C}$  and  $100^\circ\text{C}$ . After cycling through the temperature runs,  $d_{33}$  was re-measured.

### RESULTS AND DISCUSSION

Figure 1 shows the temperature dependence of the dielectric constant for the two compositions. The room temperature dielectric constant (measured at 1 kHz) is 860 and the dissipation factor 0.047 for BPNT-50 the values of 1289 and 0.084 are measured respectively for BPNT-40. At the transition temperature for BPNT-50,  $\sim 375^\circ\text{C}$ , the dielectric constant value of 30500 is measured as shown in the figure. Another weak anomaly can be seen near  $-25^\circ\text{C}$  in this composition. The transition temperature for BPNT-40 occurs at  $\sim 340^\circ\text{C}$  and corresponds to a maximum dielectric constant of 17000. The second, or lower temperature, anomaly for this composition occurs at the relatively higher temperature  $\sim 230^\circ\text{C}$ .

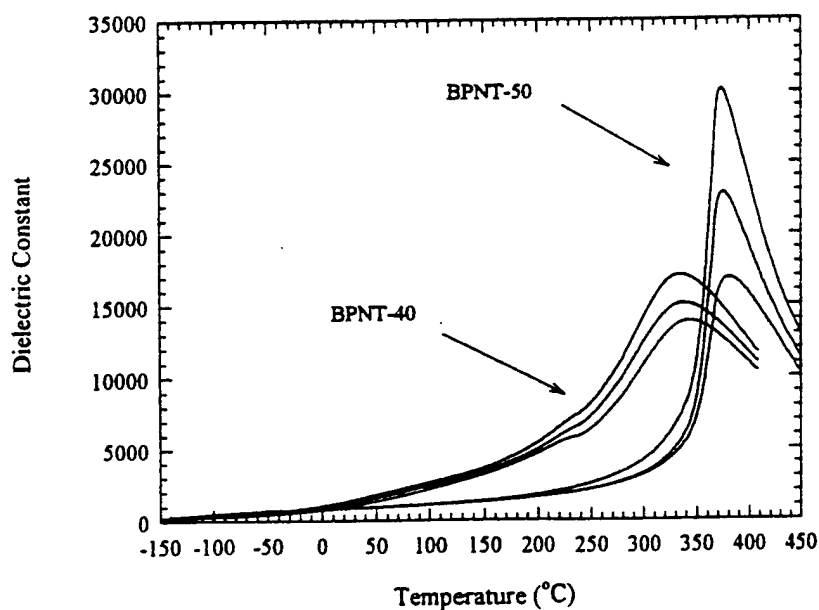


Figure 1. Variation of the dielectric constant with temperature for BPNT-40 and BPNT-50 ceramics measured at 1, 10, and 100 kHz.

Well-defined dielectric hysteresis loops are observed at room temperature for these compositions (figure 2). The saturation and remanent polarization values are on the order of  $50 \mu\text{C}/\text{cm}^2$  and  $37 \mu\text{C}/\text{cm}^2$ , respectively and are in the same range for both BPNT-40 and BPNT-50, in spite of the fact that the magnitudes of the coercive fields for these compositions are quite different. The composition on the rhombohedral side of the morphotropic phase boundary (BPNT-40) gives a typical value for the coercive field,  $\sim 26 \text{ kV}/\text{cm}$ , nearly half the value obtained for the composition on tetragonal side, (BPNT-50).

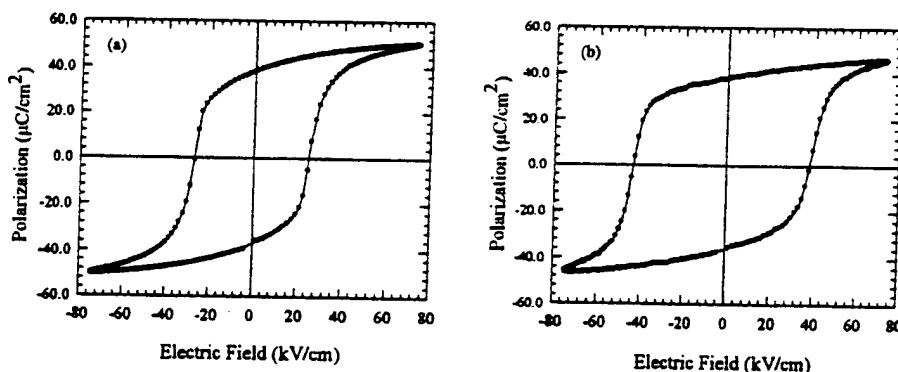


Figure 2. Dielectric hysteresis loops for: (a) BPNT-40 and (b) BPNT-50 ceramics.

Samples (of both compositions) were poled with a field of  $42 \text{ kV}/\text{cm}$  at  $100^\circ\text{C}$ . After allowing the samples to age for 24 hours, the measured  $d_{33}$  was in the range of  $250 \text{ pC}/\text{N}$  for BPNT-40 and  $105 \text{ pC}/\text{N}$  for BPNT-50. Resonance measurements at room temperature yield the coupling coefficients,  $k_p$ ,  $k_{31}$ , and  $k_t$  of: 32.5 %, 19.7 %, and 57.1 % for BPNT-40 and 20.1 %, 12.1 %, and 46.6 % for BPNT-50. The piezoelectric coefficient,  $d_{31}$ , is of the order  $-67 \text{ pC}/\text{N}$  and  $-35 \text{ pC}/\text{N}$  for BPNT-40 and BPNT-50, respectively.

The large anisotropy between  $d_{33}$  and  $d_{31}$  makes these compositions attractive for hydrophone applications. The hydrostatic piezoelectric coefficient for the poled ceramics was calculated using the relationship:  $d_h = d_{33} + 2d_{31}$ . High  $d_h$  values on the order of  $116 \text{ pC}/\text{N}$  were calculated for BPNT-40. Direct measurements of  $d_h$  were undertaken and the results show high  $d_h$  values of  $111 \text{ pC}/\text{N}$  for BPNT-40 and a

moderate  $d_h$  of 34 pC/N for BPNT-50. The hydrophone figure of merit,<sup>7</sup>  $d_h g_h$ , (as calculated from the measured  $d_h$  and  $g_h$ ) gives the values of  $1055 \times 10^{-15} \text{ m}^2/\text{N}$  for BPNT-40 and  $150 \times 10^{-15} \text{ m}^2/\text{N}$  for BPNT-50. For composites, much higher values of  $d_h g_h$  have been reported<sup>7</sup> but for a monolithic compound these values of  $d_h$  and  $d_h g_h$  are very attractive. The  $d_h g_h$  value for BPNT-40 compares well with  $\text{PbTiO}_3$  ( $d_h = 48 \text{ pC/N}$  and  $d_h g_h = 1248 \times 10^{-15} \text{ m}^2/\text{N}$ ) and is significantly larger than the value reported for PZT-5 ( $d_h = 21 \text{ pC/N}$  and  $d_h g_h = 42 \times 10^{-15} \text{ m}^2/\text{N}$ ).<sup>6</sup>

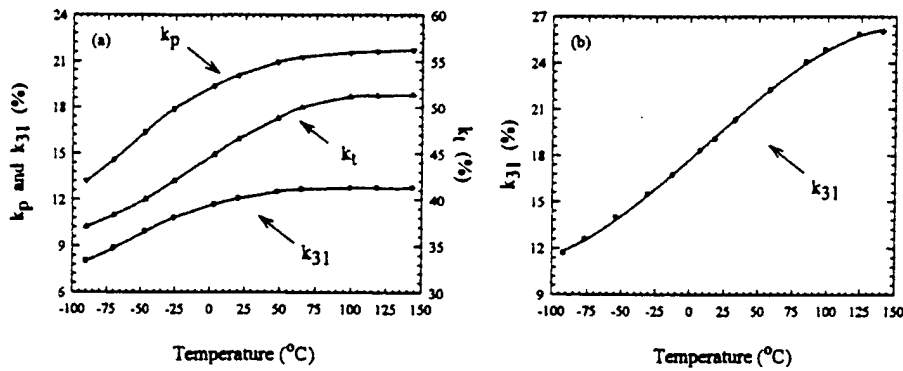


Figure 3. Variation of the coupling coefficients, ( $k_p$ ,  $k_{31}$ , and  $k_t$ ) with temperature for: (a) BPNT-40 and (b) BPNT-50 ceramics.

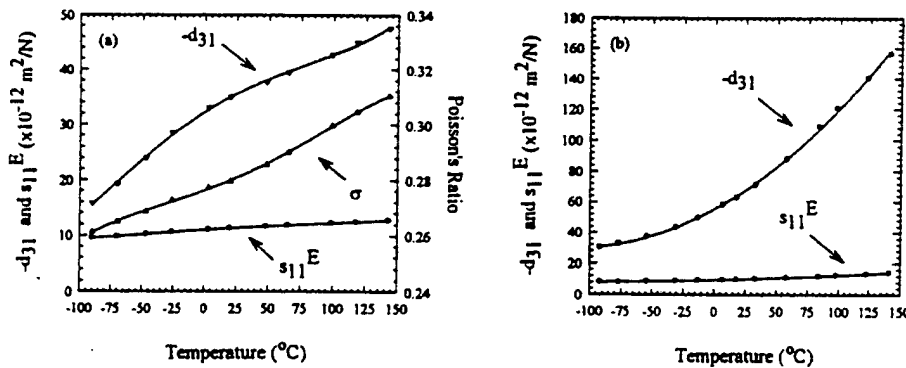


Figure 4. Variation of  $d_{31}$ ,  $s_{11}^E$ , and Poisson's ratio with temperature for: (a) BPNT-40 and (b) BPNT-50 ceramics.

The temperature dependence of various piezoelectric characteristics of BPNT-50 is shown in figures 3(a), 4(a), and 5(a). All of the property coefficients increase with temperature, with the exception of the mechanical quality factor,  $Q_m$ . All of the plots show some change in slope near  $-25^\circ\text{C}$ . This could probably be due to a slight curvature in the morphotropic phase boundary (which is located at  $x = 0.445$ ). During heating cycles the three coupling factors,  $k_p$ ,  $k_{31}$ , and  $k_t$ , attain nearly constant values (21.7 %, 12.8 %, and 51.3 %, respectively) at  $\sim 125^\circ\text{C}$ . The elastic compliance  $s_{11}^E$  is less dependent on temperature and reaches a maximum value of  $12.71 \times 10^{-12} \text{ m}^2/\text{N}$  at  $150^\circ\text{C}$ , the upper temperature at which the measurements were made. The piezoelectric constant,  $d_{31}$ , approaches  $-47.6 \text{ pC/N}$  at  $150^\circ\text{C}$ .

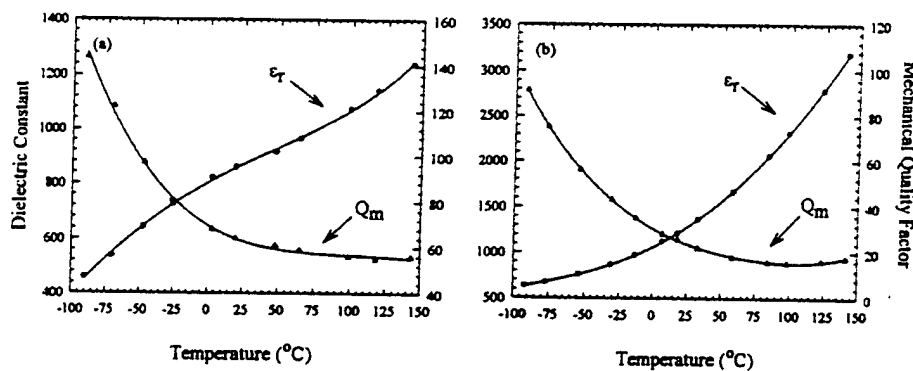


Figure 5. Variation of the dielectric constant and mechanical quality factor with temperature for: (a) BPNT-40 and (b) BPNT-50 ceramics.

The temperature dependence of the piezoelectric coefficients for BPNT-40 is shown in figures 3(b), 4(b) and 5(b). Unlike the case of BPNT-50, the effect of the morphotropic phase boundary cannot be detected, as the temperature of the second dielectric anomaly shifts from  $25^\circ\text{C}$  to  $230^\circ\text{C}$  in this composition. The coefficients  $k_{31}$ ,  $d_{31}$  and  $s_{11}^E$  and the dielectric constant all increase with temperature to maximum values of:  $k_{31} = 25.8 \%$ ,  $d_{31} = 156.6 \text{ pC/N}$ ,  $s_{11}^E = 14.2 \times 10^{-12} \text{ m}^2/\text{N}$ , and  $\epsilon_r = 3179$ . The mechanical quality factor,  $Q_m$ , decreases to a value of 18. After the temperature cycling, between  $-100^\circ\text{C}$  and  $150^\circ\text{C}$ , the room temperature piezoelectric coefficients return to their original values.

Table 1. Property coefficients for BPNT-40 and BPNT-50 ceramics.

$\text{Bi}(\text{NiTi})_{1/2}\text{O}_3$ / $\text{PbTiO}_3$	(40/60)	(50/50)
Dielectric:		
K at 1 kHz	1289	856
D at 1 kHz (%)	8.40	4.70
Transition temperatures:		
$T_c$ ( $^{\circ}\text{C}$ )	340	375
$T_c'$ ( $^{\circ}\text{C}$ )	230	-25
Dielectric Hysteresis:		
$P_r$ ( $\mu\text{C}/\text{cm}^2$ )	37.86	37.17
$E_c$ (kV/cm)	25.75	41.14
$P_{\max}$ ( $\mu\text{C}/\text{cm}^2$ )	50.35	46.73
Coupling factors:		
$k_p$ (%)	32.50	20.08
$k_{31}$ (%)	19.68	12.05
$k_t$ (%)	57.05	46.55
Piezoelectric constants:		
$d_{33}$ (pC/N)	250	105
$d_{31}$ (pC/N)	-67	-35
$d_h$ (pC/N) (calc.)	116	35
$d_h$ (pC/N) (meas.)	111	34
$d_h g_h$ ( $\times 10^{-15} \text{ m}^2/\text{N}$ )	1055	150
Frequency constants:		
$N_p$ (Hz m)	2526	2351
$N_t$ (Hz m)	2077	1924
Elastic compliance:		
$s_{11}^E$ ( $\times 10^{-12} \text{ m}^2/\text{N}$ )	10.18	11.34
Mechanical quality factor:		
$Q_m$	24	64
Poisson's ratio:		
$\sigma$	0.2669	0.2796

### CONCLUSIONS

Table 1 summarizes all the property coefficients measured on the Mn doped BPNT-40 and BPNT-50 compositions. The high transition temperatures (400°C) and large remanent polarizations (37  $\mu\text{C}/\text{cm}^2$ ), look promising for high temperature piezoelectric applications. BPNT ceramics have also shown a high mechanical strength and a nominal temperature dependence in the range of experimental measurement. Large and attractive  $d_h \sim 111$  pC/N and  $d_{hg} \sim 1055 \times 10^{-15}$  m<sup>2</sup>/N in BPNT-40 are also promising for hydrostatic sensor applications. Further studies are underway to improve upon  $d_{hg}$  values on these compositions.

### *References*

- [1] T. Takenaka and M. Yamada, *Jpn. J. Appl. Phys.*, Vol. 32, pp. L928-L931 (1993).
- [2] T. Takenaka and M. Yamada, *Jpn. J. Appl. Phys.*, Vol. 32, pp. 4218-4222 (1993).
- [3] T. Takenaka, M. Yamada, and T. Okuda, *Ferroelectrics*, Vol. 154, pp. 259-264 (1994).
- [4] T. Okuda, M. Yamada, and T. Takenaka, *Jpn. J. Appl. Phys.*, Vol. 33, pp. 5356-5360 (1994).
- [5] A.S. Bhalla, et al., Office of Naval Research review meeting, September 1995, Naval Research Laboratory, Washington DC.
- [6] "IRE Standards on Piezoelectric Crystals: Measurement of Piezoelectric Ceramics", *Proceedings of the IRE*, Vol. 49, p 1161 (1961).
- [7] A.S. Bhalla and R.Y. Ting, *Sensors and Materials*, Vol. 4, pp. 181-185 (1988).

# **APPENDIX 16**



ELSEVIER

August 1999

Materials Letters 40 (1999) 114–117

**MATERIALS  
LETTERS**

www.elsevier.com/locate/matlet

## Investigation of the lead indium niobate–lead magnesium niobate solid solution

Edward F. Alberta, Amar S. Bhalla \*

*Materials Research Laboratory, The Pennsylvania State University, University Park, PA 16802, USA*

Received 27 October 1998; received in revised form 17 January 1999; accepted 29 January 1999

### Abstract

This paper describes the first study on processing and electrical properties of ceramics in the  $(x)\text{Pb}(\text{In}_{1/2}\text{Nb}_{1/2})\text{O}_3 \cdot (1-x)\text{Pb}(\text{Mg}_{1/3}\text{Nb}_{2/3})\text{O}_3$  [PIMN( $x/100-x$ )] solid solution system with  $x=50$  mol%. Pellets were sintered at  $1100^\circ\text{C}$  resulting in phase-pure perovskite ceramics with 98% theoretical density. These ceramics displayed typical relaxor ferroelectric behavior with a maximum dielectric constant of 8056 at  $26^\circ\text{C}$ . A slight polarization hysteresis was observed at  $25^\circ\text{C}$ . A maximum induced polarization of  $23.95 \mu\text{C}/\text{cm}^2$  and remanent polarization of  $1.2 \mu\text{C}/\text{cm}^2$  at the peak field level of  $48 \text{ kV}/\text{cm}$  was measured. The strain and electrostriction coefficient were measured, the values were in the range of  $x_{33} = 8.12 \times 10^{-4}$  and  $Q_{33} = 1.42 \times 10^{-2} \text{ m}^4/\text{C}^2$ , respectively. The low hysteresis in  $x_{33}$  and low values of  $P_r$  make this solid solution attractive for further study. © 1999 Elsevier Science B.V. All rights reserved.

**Keywords:** Solid solutions; Relaxor ferroelectrics; Lead indium niobate; Lead magnesium niobate; Dielectric properties; Electrostrictive properties

### 1. Introduction

Lead magnesium niobate  $\text{Pb}(\text{Mg}_{1/3}\text{Nb}_{2/3})\text{O}_3$  [PMN] is probably the most widely studied relaxor ferroelectric known. A maximum dielectric constant of nearly 18 000 at its transition temperature,  $T_m$ , of approximately  $-15^\circ\text{C}$  has been reported at a measurement frequency of 1 kHz [1]. There are also several reports on the properties of PMN:PbTiO<sub>3</sub> [PMN:PT] solid solution with various concentrations of PbTiO<sub>3</sub> [PT]. The PMN:PT solid solution also

shows a morphotropic phase boundary at which further enhancement in some properties has been measured. PMN:PT compositions are highly promising for electrostrictive and piezoelectric devices. The composition (0.93)PMN:(0.07)PT has been shown to have a large piezoelectric effect under electrical field [2]. This composition, as well as others in this solid solution system appear to be promising candidates for some smart ferroic systems such as vibration control and actuators.

Lead indium niobate  $\text{Pb}(\text{In}_{1/2}\text{Nb}_{1/2})\text{O}_3$  [PIN] is an interesting order–disorder type relaxor. In its disordered state PIN is a relaxor ferroelectric with a pseudo cubic perovskite structure and a dielectric constant maximum ( $T_m$ ) of  $66^\circ\text{C}$  [3]. Annealing PIN

\* Corresponding author. Tel.: +1-814-8659931; Fax: +1-814-8652326; E-mail: piezo@psu.edu

at a suitable temperature causes the material to order into an antiferroelectric orthorhombic phase. This phase, which is isostructural with lead zirconate, has a transition temperature of 190°C [4]. Another important and well-studied order–disorder relaxor is  $\text{Pb}(\text{Sc}_{1/2}\text{Ta}_{1/2})\text{O}_3$  [PST]. Its solid solution with PT has shown a variable order–disorder region as well as a morphotropic phase boundary [5].

To our knowledge there are no reports so far on the PIMN solid solution. This system is expected to show some unique and unexplored characteristics. There is a possibility that additions of PMN may alter the order–disorder behavior of PIN such that it may fully disorder and display its relaxor ferroelectric behavior, or to produce ordering over a limited compositional range, and thereby transforming the composition into an antiferroelectric. The obvious stoichiometric differences between PIN and PMN may lead to other ordering phenomena, and even the existence of morphotropic phase boundaries. In order to study this interesting solid solution system this study has been undertaken and the first results on the PIN:PMN (50/50) compositions are reported here.

## 2. Experimental procedures

Ceramics with the composition PIMN(50/50) were fabricated using vibratory milled PIN and PMN

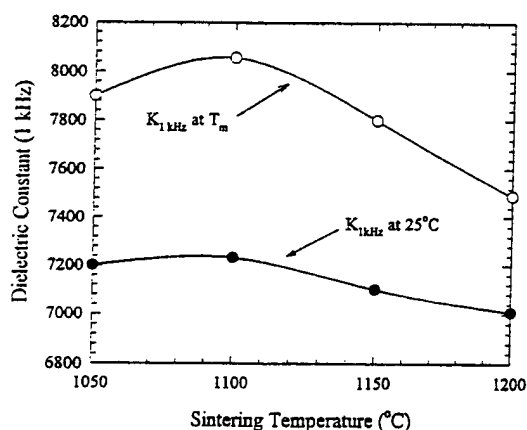


Fig. 1. Dielectric constant at room temperature and at  $T_m$  as a function of sintering temperature.

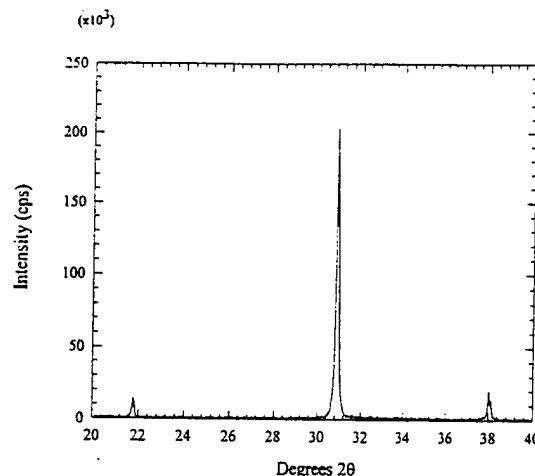


Fig. 2. X-ray diffraction pattern for PIMN(50/50) ceramic sintered at 1100°C.

powders. Stoichiometric PIN and PMN powders were prepared using the Columbite precursor method [3,6]. The precursor materials were synthesized using  $\text{In}_2\text{O}_3$ ,  $\text{Nb}_2\text{O}_5$  and  $\text{MgCO}_3$  to form stoichiometric  $\text{InNbO}_4$  and  $\text{MgNb}_2\text{O}_6$ .  $\text{PbO}$  was added to each precursor to form PIN and PMN, respectively. After calcining, the powders were mixed and milled for 24 h in acetone with  $\text{ZrO}_2$  media. The powders were then dried for another 24 h and then mixed with 3 wt.% binder.

Pellets from the mixture were pressed and the binder removed. The green ceramics were sintered at various temperatures between 1050°C and 1200°C. Following the sintering step, X-ray diffraction was used to determine the concentration of the unwanted pyrochlore phase. For the electrical measurements the ceramic disks were polished using 1  $\mu\text{m}$   $\text{Al}_2\text{O}_3$ . Finally, the samples were cleaned in an ultrasonic bath, dried, and sputtered with gold.

Dielectric constant and loss measurements were made using an automated measurement system. This system consisted of an LCR meter (HP-4174A, Hewlett-Packard), a nitrogen-fed furnace (Model-9023, Delta Design), and a desktop computer (HP-200 series, Hewlett-Packard). Hysteresis measurements were made using a modified Sawyer-Tower circuit controlled by a PC. This system is also capable of simultaneous measurement of strain using an

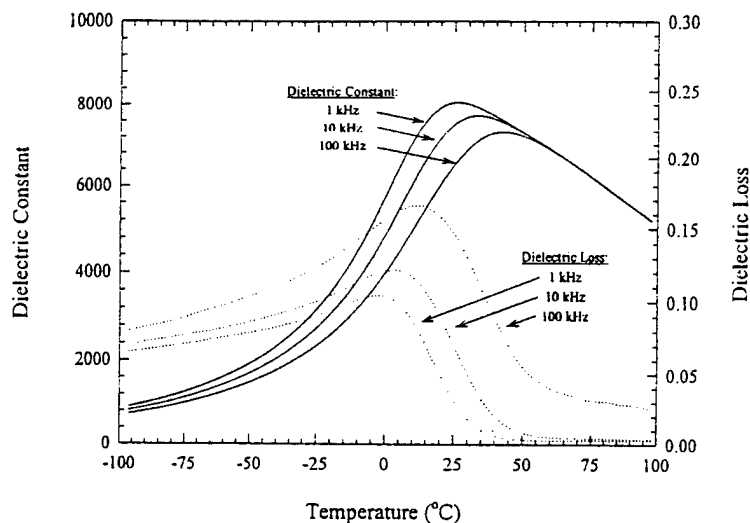


Fig. 3. Temperature dependence of the dielectric constant and loss for PIMN(50/50). (Measurement made while heating at 2°C/min).

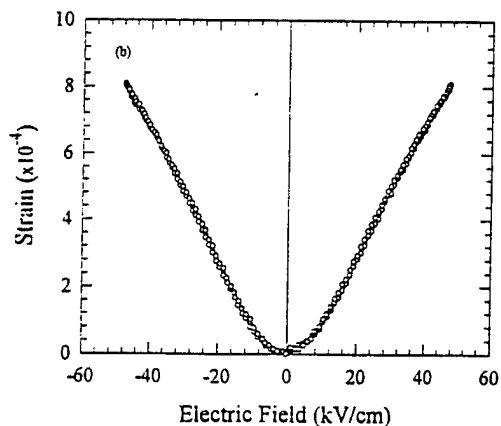
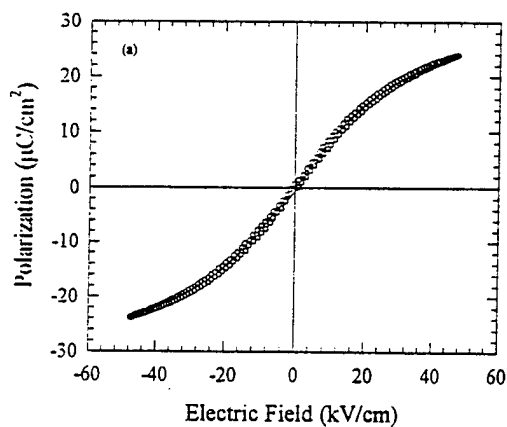


Fig. 4. (A) Room temperature dielectric hysteresis loop and (B) strain for PIMN(50/50).

LVDT and lock-in amplifier (SR830 DSP, Stanford Research).

### 3. Results and discussion

Sintered densities of the PIMN(50/50) ceramics were found to vary between 8.13 and 8.18 g/cm<sup>3</sup>. Weight loss was limited to less than 1 wt.% between the sintering temperatures of 1050°C and 1200°C. At a sintering temperature of 1100°C both dielectric constant and density were found to be optimized

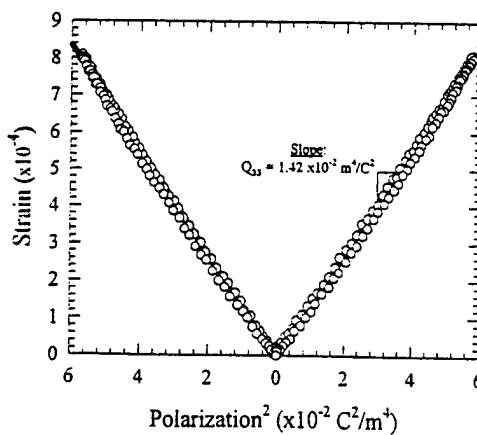


Fig. 5. Calculation of the electrostriction coefficient,  $Q_{33}$ , for PIMN(50/50).

Table 1  
Physical and electric properties of PIMN(50/50) ceramics

Property	PIN:PMN (50/50)
Sintering temperature (°C)	1100
Density (g/cm <sup>3</sup> )	8.18
Perovskite concentration (%)	100
Dielectric constant	
at 25°C	7233
at $T_m$	8056
Dielectric loss	
at 25°C	0.020
at $T_m$	0.027
Transition temperature (°C)	26
Hysteresis	
$E_{max}$ (kV/cm)	48.00
$P_{max}$ (μC/cm <sup>2</sup> )	23.95
$P_r$ (μC/cm <sup>2</sup> )	1.19
$Q_{33}$ ( $\times 10^{-2}$ m <sup>4</sup> /C <sup>2</sup> )	1.42

(Fig. 1). Ceramics were determined, by X-ray diffraction, to be single-phase perovskite (Fig. 2).

Electrical measurements were made on samples sintered at 1100°C. The temperature dependence of the dielectric constant and loss of PIMN(50/50) shows typical relaxor ferroelectric behavior (Fig. 3). The maximum dielectric constant, measured at 1 kHz, is 8056 at 26°C and it shifts towards higher temperatures with increasing frequency. The maximum loss measured at 1 kHz is 0.1043 at -4°C and also shifts towards higher temperatures with increasing frequency.

Dielectric hysteresis behavior of PIMN(50/50) resembles that of a typical electrostrictive relaxor ferroelectric (Fig. 4). At room temperature, the maximum polarization,  $P_s$ , was 23.95 μC/cm<sup>2</sup> at an applied field of 48 kV/cm and the remanent polarization,  $P_r$ , was in the range of 1.2 μC/cm<sup>2</sup>. Electrostrictive measurements were made and the resulting strain was found to be non-hysteretic in nature with a maximum strain value of 0.0812% at a field of 48 kV/cm.  $Q_{33}$  as calculated from the strain data was on the order of  $1.42 \times 10^{-2}$  m<sup>4</sup>/C<sup>2</sup> (Fig. 5).

As expected from the hysteresis data, the sample was difficult to pole near or above room temperature. However, a remanent polarization of about 12 μC/cm<sup>2</sup> was observed at -75°C using a 20 kV/cm poling field (applied while cooling). With increasing

temperature the remanent polarization decreased to 1 μC/cm<sup>2</sup> at room temperature and decreases to zero at approximately 90°C. Table 1 summarizes the electrical measurements on the PIMN(50/50) samples.

#### 4. Conclusions

The composition  $(x)\text{Pb}(\text{In}_{1/2}\text{Nb}_{1/2})\text{O}_3:(1-x)\text{Pb}(\text{Mg}_{1/3}\text{Nb}_{2/3})\text{O}_3$ ,  $x = 0.5$ , was synthesized for studying its relaxor behavior and electrical properties. A maximum dielectric constant of 8056 was observed at 26°C for the samples sintered at 1100°C. Only a slight dielectric hysteresis was observed at 25°C ( $P_r < 1.2$  μC/cm<sup>2</sup>) for these samples which showed a maximum induced polarization of approximately 23.95 μC/cm<sup>2</sup> at 48 kV/cm. The strain levels and resulting electrostrictive coefficient,  $Q_{33}$ , were determined to be  $8.12 \times 10^{-4}$  and  $1.42$  m<sup>4</sup>/C<sup>2</sup> at 48 kV/cm, respectively. No room temperature piezoelectric activity was detected under zero bias conditions as the material is near  $T_m$ .

The solid solution compositions of PIN:PMN appear to be promising for electrostrictive devices. Further work is currently underway on both temperature and biasing effects on these materials and other compositions across the PIN:PMN phase diagram.

#### References

- [1] Z.-G. Ye, H. Schmid, Optical, dielectric and polarization studies of the electric field-induced phase transition in  $\text{Pb}(\text{Mg}_{1/3}\text{Nb}_{2/3})\text{O}_3$  [PMN], *Ferroelectrics* 145 (1993) 83.
- [2] D.J. Taylor, Electric and elastic coefficients of lead magnesium niobate-based ceramics under DC bias for active smart sensor applications, PhD Thesis, The Pennsylvania State University, 1992.
- [3] E.F. Alberta, A.S. Bhalla, Preparation of phase-pure perovskite lead indium niobate ceramics, *Materials Letters* 29 (1996) 127.
- [4] P. Groves, Fabrication and characterization of ferroelectric perovskite lead indium niobate, *Ferroelectrics* 65 (1985) 67.
- [5] J.R. Giniewicz, An investigation of the lead scandium tantalate-lead titanate solid solution system, PhD Thesis, The Pennsylvania State University, 1991.
- [6] S.L. Swartz, T.R. Shrout, Fabrication of perovskite lead magnesium niobate, *Mater. Res. Bull.* 17 (1982) 1245.

# **APPENDIX 17**

## Electrical Property Diagram and Morphotropic Phase Boundary in the $\text{Pb}(\text{In}_{1/2}\text{Ta}_{1/2})\text{O}_3 - \text{PbTiO}_3$ Solid Solution System

EDWARD F. ALBERTA and AMAR S. BHALLA

*Materials Research Laboratory, The Pennsylvania State University,  
University Park, Pennsylvania, USA*

Communicated by Dr George W. Taylor

(Received March 25, 1999)

Dielectric, pyroelectric and piezoelectric properties of the solid solution:  $(1-x)\text{Pb}(\text{In}_{1/2}\text{Ta}_{1/2})\text{O}_3 - (x)\text{PbTiO}_3$  [PIT : PT] have been investigated. High dielectric constant of 2300 at room temperature and 13000 at approximately 248°C, remnant polarization of approximately  $26 \mu\text{C}/\text{cm}^2$ , and coercive field of 11 kV/cm were measured for compositions near the morphotropic phase boundary [MPB] at  $x = 38 \text{ mol\% PT}$ . Poled ceramics of this composition gave a piezoelectric coefficient,  $d_{33}$ , of 302 pC/N and piezoelectric coupling coefficients,  $k_p$  and  $k_{31}$ , of 37% and 20%, respectively.

### INTRODUCTION

Perovskite lead indium tantalate (PIT) was first prepared, in crystalline form, by Kania [1,2] and Bokov [3]. This material displays typical relaxor behavior, with a maximum in the dielectric constant of 900 occurring at approximately 100°C. Several other groups [4-7] have attempted the preparation of ceramic PIT. However, due to the persistence of an undesirable pyrochlore phase, these studies have had limited success. The groups reporting the synthesis of PIT also report dielectric properties inferior to reported by Kania and Bokov.

In this work, the solid solution system  $\text{Pb}(\text{In}_{1/2}\text{Ta}_{1/2})\text{O}_3$  (PIT) :  $\text{PbTiO}_3$  (PT) is explored. Lead titanate was chosen for two reasons: (1) to stabilize the perovskite phase of PIT, and (2) to identify the morphotropic phase boundary (MPB) in this system. This paper reports on the compositional dependence of the dielectric, pyroelectric, and piezoelectric properties of the  $(1-x)$  PIT :  $(x)$  PT system, with emphasis on those compositions near the morphotropic phase boundary.

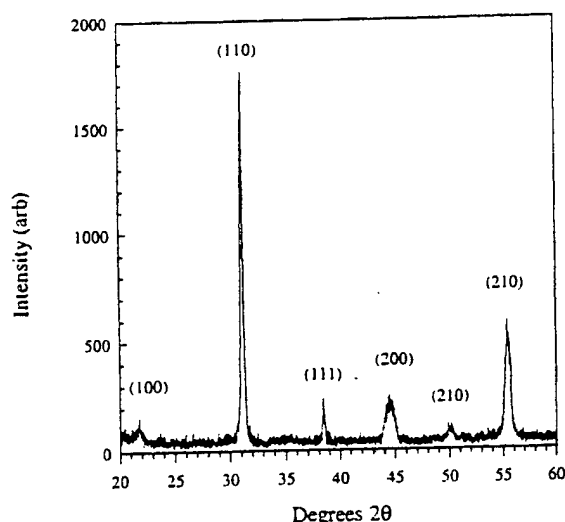


Figure 1. X-Ray diffraction pattern for a (0.64) PIT : (0.36) PT ceramic at room temperature.

#### EXPERIMENTAL PROCEDURE

The Columbite precursor method was used to prepare the ceramics for this study[8]. First, the  $\text{InTaO}_4$  precursor phase was prepared by ball milling  $\text{In}_2\text{O}_3$  and  $\text{Ta}_2\text{O}_5$  using  $\text{ZrO}_2$  Balls. The slurry was then dried and calcined in an  $\text{Al}_2\text{O}_3$  crucible at  $1100^\circ\text{C}$  for 4 hours. The resulting  $\text{InTaO}_4$  was then mixed in stoichiometric proportions with  $\text{PbO}$  and  $\text{TiO}_2$  and re-milled. The dried powder was calcined at  $900^\circ\text{C}$  for 4 hours. After an additional milling step, the powder was pressed into disks and sintered between  $1000^\circ\text{C}$  and  $1300^\circ\text{C}$ . Both calcined powders and sintered ceramics were analyzed for phase purity using X-ray diffraction (Pad V, Sintag Inc.). The sintered ceramics were found to be at least 95 % theoretical density.

The sintered ceramics were polished and then coated with sputtered-gold electrodes. The temperature dependence of the dielectric properties was measured using a multifrequency LCR meter (HP4274A, Hewlett Packard Co.) and computer controlled oven (Delta Design, Inc.). Pyroelectric measurements were made using a similar system including a picoammeter (HP4140B, Hewlett Packard Co.). The ceramics were poled in a high-temperature stirred silicone bath (DC-200, Dow Corning,

Inc. and EX-250 HT, Exacal, Inc.). Piezoelectric measurements were then made using an impedance analyzer (HP4194A, Hewlett Packard Co.) following the IEEE resonance method.

## RESULTS AND DISCUSSION

The addition of PT to the PIT:PT system was found to stabilize to perovskite phase. Using X-Ray diffraction, it was found that the calcined powders of PIT:PT with PT concentrations of at least 30 mol% were phase-pure. After sintering, only traces of the pyrochlore phase were present in these compositions, figure 1.

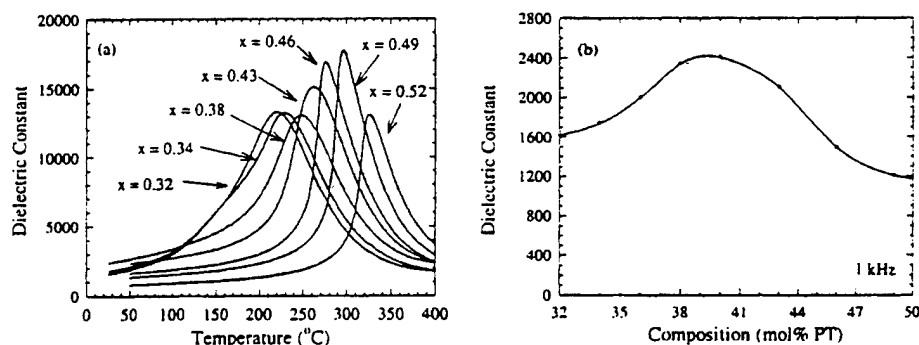


Figure 2. Compositional dependence of the dielectric constant for poled ceramics in the  $(1-x)$  PIT :  $(x)$  PT system measured at 1 kHz: (a) temperature dependence and (b) room temperature values.

The temperature dependence of the dielectric constant (measured at 1 kHz) for various poled ceramics with  $0.30 \leq x \leq 0.48$  is shown in figure 2(a). As expected, the addition of PT the system shifts the Curie temperature from 200°C to 300°C. Careful examination of the curves in figure 2(a) shows an additional anomaly in the dielectric constant for compositions with  $x < 0.38$ . These anomalies indicate a transition between the pseudo-cubic and tetragonal phases. The temperature at which this anomaly occurs was found to decrease with the addition of PT. The compositional dependence of the dielectric constant, figure 3(a), also indicates the MPB in the PIT:PT system. From these observations, the phase boundary was determined to be at  $x = 0.38$ . Figure 3(a)

shows the temperature dependence of the dielectric constant and loss for this composition.

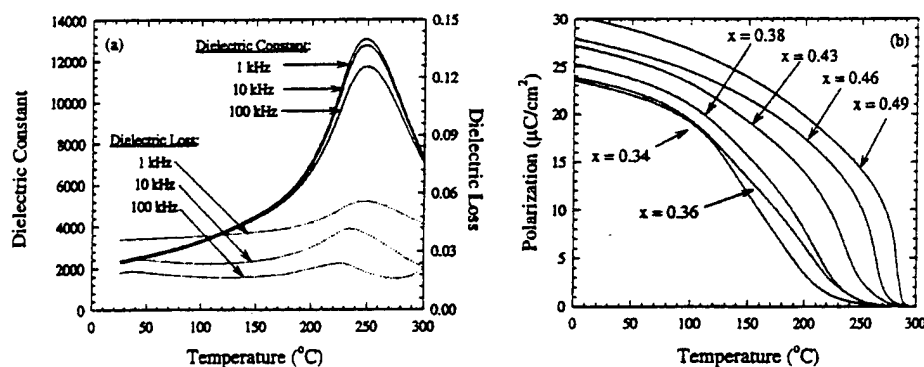


Figure 3. Temperature dependence of (a) the dielectric constant for poled ceramics with  $x = 0.38$  and (b) the polarization for ceramics with  $0.34 < x < 0.49$ .

The temperature dependence of the remnant polarization in the  $(1-x)$  PIT :  $(x)$  PT solid solution system was determined from pyroelectric measurements, figure 3(b). Again, the transition temperature increased, as expected, with increasing  $x$ . The polarization also increased with the addition of PT. As with the dielectric data, the pseudo-cubic to tetragonal phase boundary was identified by the slope changes that occur in the data for compositions with  $x < 0.40$ .

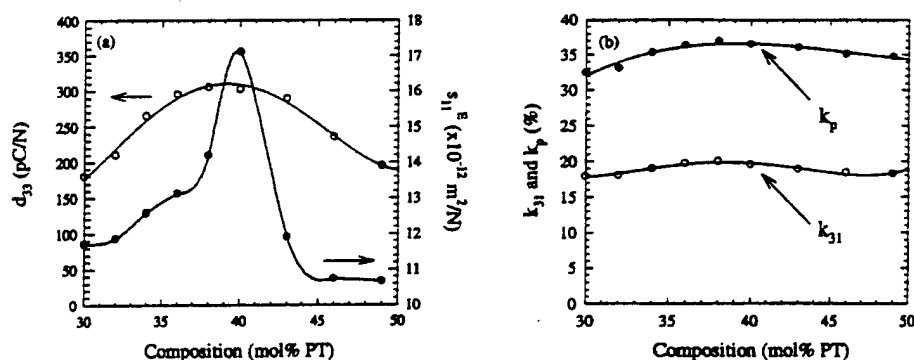


Figure 4. Compositional dependence of the piezoelectric properties for PIT:PT ceramics: (a) the piezoelectric constant,  $d_{33}$ , and elastic compliance,  $s_{11}^E$ , and (b) the electromechanical coupling factors,  $k_p$  and  $k_{31}$ .

The piezoelectric properties of the  $(1-x)$  PIT :  $(x)$  PT solid solution system are shown in figure 4. The samples were poled in a stirred silicone bath at  $25^\circ\text{C}$  for 30 min, using a field of  $30 \text{ kV/cm}$ . After allowing the sample to age 24 hours, the piezoelectric coefficient,  $d_{33}$ , was measured and found to be on the order of  $302 \text{ pC/N}$  for the composition  $x = 0.38$ . The piezoelectric coupling factors ( $k_p$  and  $k_{31}$ ) are also maximized in this composition, with values of 37% and 20%, respectively. The elastic compliance was found to increase to a maximum of  $-17 \times 10^{-12} \text{ m}^2/\text{N}$  at  $x = 0.40$ .

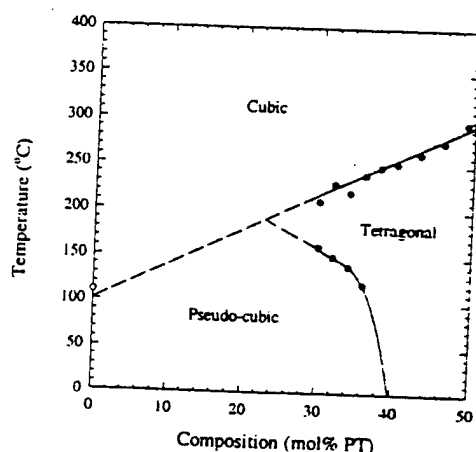


Figure 5. Phase diagram for  $(1-x)$  PIT :  $(x)$  PT ceramics based on dielectric data.

Finally, a phase diagram based on dielectric data was constructed (figure 5). It was rather difficult to obtain phase-pure perovskite samples for compositions with PT content less than 30%. This coexistence region, between the pyrochlore and perovskite phases, is shown by the dashed line between  $x = 0.00$  and  $0.36$ . The temperature of the ferroelectric to paraelectric phase transition for each composition was determined from the maximums in the dielectric constant (figure 2). The pseudo-cubic to tetragonal phase boundary was identified from the lower temperature anomalies in the dielectric data.

Table 1. Electrical properties of (1-x) PIT : (x) PT ceramics.

Property:	PIT:PT
Composition (mol% PT)	38.0
Dielectric constant:	
at 25°C (unpoled)	1900
at 25°C (poled)	2300
at $T_c$	13000
Dielectric Loss:	
at 25°C (unpoled)	0.021
at 25°C (poled)	0.019
at $T_c$	0.025
Transition temperature (°C)	248
Piezoelectric:	
$\sigma$	0.41
$s_{11}E$ ( $\times 10^{-12}$ m <sup>2</sup> /N)	14.08
$d_{33}$ (pC/N)	302
$d_{31}$ (pC/N)	-114
$k_p$ (%)	37
$k_{31}$ (%)	20

## CONCLUSIONS

This paper reports the first successful study of the preparation of single-phase perovskite (1-x) PIT : (x) PT ceramics. Based on anomalies in the dielectric data, a phase diagram was constructed. Piezoelectric, pyroelectric and dielectric data suggests the presence of a morphotropic phase boundary in this system at  $x \sim 0.38$  mol% PT.

## References

- [1] Kania, A., "A New Perovskite  $\text{Pb}(\text{In}_{0.5}\text{Ta}_{0.5})\text{O}_3$  (PIT)," *Ferroelectric Letters*, Vol. 11, pp. 107-110, (1990).
- [2] Kania, A. and M. Pawelczyk, "Order-Disorder Aspects in  $\text{PbIn}_{0.5}\text{Ta}_{0.5}\text{O}_3$  Crystals," *Ferroelectrics*, Vol. 124, pp. 261-264, 1991.
- [3] Bokov, A.A., I.P. Rayevsky, V.V. Neprin and V.G. Smotrakov, "Investigation of Phase Transitions in  $\text{Pb}(\text{In}_{0.5}\text{Ta}_{0.5})\text{O}_3$  Crystals," *Ferroelectrics*, Vol. 124, pp. 271-273, (1990).
- [4] Jones, F.G., C.A. Randall, S.J. Jang, and T.R. Shrout, "Preparation and Characterization of Indium Based Complex Perovskites -  $\text{Pb}(\text{In}_{1/2}\text{Nb}_{1/2})\text{O}_3$  (PIN),  $\text{Ba}(\text{In}_{1/2}\text{Nb}_{1/2})\text{O}_3$  (BIN), and  $\text{Ba}(\text{In}_{1/2}\text{Ta}_{1/2})\text{O}_3$  (BIT)," *Ferroelectrics Letters*, Vol. 12, pp. 55-62, (1990).
- [5] Yasuda, N., S. Imamura, "Diffuse Phase Transition in A New Perovskite  $\text{Pb}(\text{In}_{1/2}\text{Ta}_{1/2})\text{O}_3$ ," *Appl. Phys. Lett.*, Vol. 59, No. 26, pp.3493-3495, (1991).
- [6] Yasuda, N., H., Inagaki, and S. Imamura, "Dielectric Properties of Perovskite Lead Indium Niobate and Tantalate Prepared by Fast Firing Technique," *Jpn. J. Appl. Phys.*, Vol. 31, pp. L 574 - L 575, (1992).
- [7] Yasuda, N., and S. Imamura, "Preparation and Characterization of Perovskite Lead Indium Tantalate", *Ferroelectrics*, Vol. 126, pp. 109-114. (1992).

- [8] Alberta, E.F., and A.S. Bhalla, "Preparation of Phase-Pure Lead Indium Niobate," *Mater. Lett.*, Vol. 29, pp. 127-129, (1996).
- [9] Alberta, E.F., and A.S. Bhalla, "Piezoelectric Properties of  $\text{Pb}(\text{In}_{1/2}\text{Nb}_{1/2})\text{O}_3$ - $\text{PbTiO}_3$  Solid Solution Ceramics," *J. Korean Phys. Soc.*, Vol. 32, pp. S 1265 - S 1267, (1998).

# **APPENDIX 18**

## Piezoelectric and Dielectric Properties of $\text{Fe}_2\text{O}_3$ -Doped $0.57\text{Pb}(\text{Sc}_{1/2}\text{Nb}_{1/2})\text{O}_3$ – $0.43\text{PbTiO}_3$ Ceramic Materials

Jin-Soo KIM, So-Jung KIM<sup>1</sup>, Ho-Gi KIM<sup>1</sup>, Duck-Chool LEE<sup>2</sup> and Kenji UCHINO<sup>3</sup>

Department of Technology Education, Korea National University of Education, Chungbuk 363-791, Korea

<sup>1</sup>Department of Material Science and Engineering, KAIST, Daejeon 305-701, Korea

<sup>2</sup>Department of Electrical Engineering, Inha University, Incheon 402-751, Korea

<sup>3</sup>Materials Research Laboratory, The Pennsylvania State University, University Park, PA 16802, USA

(Received September 7, 1998; accepted for publication November 27, 1998)

High-power piezoelectric materials are presently being extensively developed for applications such as ultrasonic motors and piezoelectric transformers. In this study, the piezoelectric and dielectric properties of  $\text{Fe}_2\text{O}_3$ -doped  $0.57\text{Pb}(\text{Sc}_{1/2}\text{Nb}_{1/2})\text{O}_3$ – $0.43\text{PbTiO}_3$  (hereafter 0.57PSN–0.43PT), which is the morphotropic phase boundary composition of the PSN–PT system, were investigated. The maximum dielectric constant ( $\epsilon_{33}/\epsilon_0 = 2551$ ) and the minimum dielectric loss ( $\tan\delta = 0.51\%$ ) at room temperature were obtained at  $\text{Fe}_2\text{O}_3$  additions of 0.1 wt% and 0.3 wt%, respectively. The temperature dependence of the dielectric constant and the dielectric loss was measured between room temperature and 350°C. With the addition of  $\text{Fe}_2\text{O}_3$ , the piezoelectric constant  $d_{33}$  and electromechanical coupling factor  $k_p$  were slightly decreased, but the mechanical quality factor  $Q_m$  was significantly increased. The highest mechanical quality factor ( $Q_m = 297$ ) was obtained at 0.3 wt%  $\text{Fe}_2\text{O}_3$ , which is 4.4 times higher than that of nondoped 0.57PSN–0.43PT ceramics. The  $P$ – $E$  and  $S$ – $E$  loops of the samples at room temperature and at 1.0 Hz were measured at the same time using an automated polarization measuring system.

KEYWORDS: lead scandium niobate, dielectric properties,  $P$ – $E$  loops and  $S$ – $E$  loops, mechanical quality factor, PSN–PT

### 1. Introduction

Lead scandium niobate,  $\text{Pb}(\text{Sc}_{1/2}\text{Nb}_{1/2})\text{O}_3$  (PSN), is a typical relaxor dielectric material which has a Curie temperature of 90°C.<sup>1)</sup> With the addition of  $\text{PbTiO}_3$  (PT), which has a Curie temperature of 490°C, the composition of PSN–PT solid solutions exhibits a morphotropic phase boundary (MPB) between the rhombohedral and tetragonal phases at 42.5 mol% PT.<sup>2)</sup> Only five studies of the PSN–PT system have been carried out.<sup>2,6)</sup> In 1968, Tennery *et al.* initially reported on the ferroelectric and structural properties of solid solutions of the  $\text{Pb}(\text{Sc}_{1/2}\text{Nb}_{1/2})\text{O}_3$ – $\text{PbTiO}_3$  system.<sup>2)</sup> In the PSN–PT system, a two-phase region between the rhombohedral and tetragonal phases was observed between 0.425 and 0.45PT at room temperature. Also, at the MPB composition of the 0.575PSN–0.425PT system, the electromechanical radial coupling factor  $k_p$  of 46% was reported. In 1993, Yamashita reported on the effect of  $\text{Nb}_2\text{O}_5$  addition to 0.575PSN–0.425PT ceramics, where a large electromechanical coupling factor  $k_p$  of 69% was obtained.<sup>3)</sup> The structural and electrical properties of niobium-doped  $(1-x)\text{PSN}$ – $x\text{PT}$  ( $x = 0.4$ – $0.45$ ) ceramics near the MPB were also investigated by Yamashita.<sup>4,5)</sup> At  $x = 0.435\text{PT}$ , the maximum dielectric constant  $\epsilon_{33}/\epsilon_0 = 3200$  and piezoelectric constant  $d_{33} = 590\text{ pC/N}$  were found; also,  $k_p$  and the mechanical quality factor  $Q_m$  were 67% and 70, respectively. Adachi *et al.* reported the dielectric and piezoelectric properties of 0.575PSN–0.425PT ceramics, and determined  $k_p$  to be 51%.<sup>6)</sup> For high-power piezoelectric actuator devices such as ultrasonic motors and piezoelectric transformers, it is necessary to have a high  $Q_m$  and low dielectric loss  $\tan\delta$ .  $Q_m$  is increased by the addition of acceptor dopants, such as  $\text{Fe}_2\text{O}_3$  or  $\text{Cr}_2\text{O}_3$ , but it is decreased by the addition of donor dopants such as  $\text{Nb}_2\text{O}_5$ .<sup>3,7)</sup>

In this study, the addition of  $\text{Fe}_2\text{O}_3$  to the 0.57PSN–0.43PT MPB composition was carried out to improve the value of  $Q_m$  for high-power device applications, and the resulting piezoelectric and dielectric properties of the sintered ceramics were investigated.

### 2. Experimental Procedure

#### 2.1 Sample preparation

The samples were prepared from high-purity  $\text{PbO}$  (99.9%),  $\text{Sc}_2\text{O}_3$  (99.9%),  $\text{Nb}_2\text{O}_5$  (99.9%) and  $\text{TiO}_2$  (99 + %). The additive was chemical reagent grade ferric oxide ( $\text{Fe}_2\text{O}_3$ ). Six compositions of 0.57PSN–0.43PT +  $x$  wt%  $\text{Fe}_2\text{O}_3$  ( $x = 0, 0.1, 0.3, 0.5, 0.7, 0.9$ ) were selected. Mixtures of the raw materials of a given composition were ball-milled for 24 h with zirconia grinding media and distilled water. Dried powders were crushed and calcined at 850°C for 2 h. The calcined powders were granulated using an 80 mesh sieve and then mixed with 5 wt% polyvinyl alcohol binder. The powder was next cold-pressed with a steel mold into disks 14.63 mm in diameter and 1 mm in thickness at a pressure of 1000 kg/cm<sup>2</sup>. The binder was decomposed by heating at 600°C for 2 h. The samples were sintered at 1250°C for 3 h, and the heating and cooling rates were both 5°C/min. The sintered samples were polished to a thickness of about 0.84 mm using 400 grit (22  $\mu\text{m}$ ) SiC powder. Electrodes were applied by painting both sides of the samples with silver paste and firing at 650°C for 30 min. Before measuring the piezoelectric properties, the samples were poled in a silicone oil bath at 120°C by applying a DC electric field of 2.5 kV/mm for 15 min. The piezoelectric properties were measured 24 h after poling. The final sample dimensions were 12.9 mm in diameter and 0.84 mm in thickness.

#### 2.2 Measurement

Dielectric constant and dielectric loss of samples at 1 kHz were measured before and after poling with a LCR meter (SR715). The temperature dependence of the dielectric constant and the dielectric loss at 0.1, 1, 10 and 100 kHz was measured using a computer-controlled system consisting of a temperature controller (Delta9010), a multifrequency LCR meter (HP4274A) and a personal computer (HP9121). The heating rate for the samples was 2°C/min between 20°C and 350°C. The resonance and antiresonance frequencies of planar and thickness modes were measured using an impedance/gain-phase analyzer (HP4194A) and a plotter (HP ColorPro). Elec-

mechanical coupling factors,  $k_p$ ,  $k_t$ , and  $Q_m$  were calculated by the resonance-antiresonance method. Ferroelectric hysteresis  $P$ - $E$  loops and strain  $S$ - $E$  loops were examined using an automated polarization measuring system with a DSP lock-in amplifier (SR830), a high-voltage DC amplifier (TREK 609C-6) and an IBM personal computer. After poling, a piezo  $d_{33}$  meter (ZJ-2) was used to measure the piezoelectric constant  $d_{33}$  and the voltage constant  $g_{33}$ .

### 3. Results and Discussion

#### 3.1 Dielectric properties

Figure 1 shows the X-ray diffraction patterns for pure and iron-doped 0.57PSN-0.43PT calcined powders. The ratio of pyrochlore phase to perovskite phase decreased with iron doping until 0.5 wt% and then increased with increasing amount of  $\text{Fe}_2\text{O}_3$  added.

Figure 2 shows the dielectric constant and the dielectric loss before and after poling of 0.57PSN-0.43PT ceramics as a function of the amount of  $\text{Fe}_2\text{O}_3$  added. The dielectric constant after poling showed a maximum value (2551) at 0.1 wt%  $\text{Fe}_2\text{O}_3$  addition, and then decreased with a further increase in the amount of  $\text{Fe}_2\text{O}_3$  added. The decrease of the dielectric constant for the  $\text{Fe}_2\text{O}_3$ -doped samples suggests an acceptor effect of the Fe atoms.<sup>8,9)</sup> Dielectric loss ( $\tan \delta$ ) after poling of iron-doped samples is decreased and is less than 0.7% at room temperature. In the case of 0.3 wt%  $\text{Fe}_2\text{O}_3$  addition, the dielectric loss is 0.51%. The acceptor dopant  $\text{Fe}_2\text{O}_3$  decreases the dielectric loss ( $\tan \delta$ ) of 0.57PSN-0.43PT ceramics; on the other hand, the donor dopant,  $\text{Nb}_2\text{O}_5$ , increases it.<sup>3)</sup>

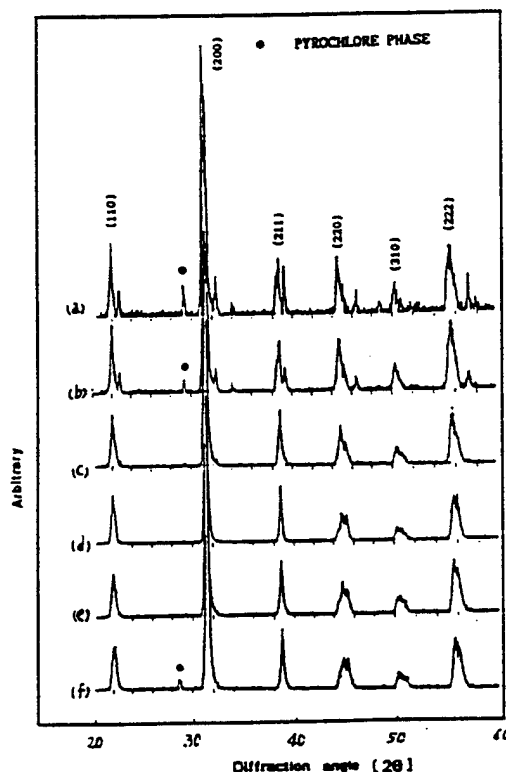


Fig. 1. X-ray diffraction patterns of 0.57PSN-0.43PT  $x$  wt%  $\text{Fe}_2\text{O}_3$  samples with (a)  $x = 0$ , (b)  $x = 0.1$ , (c)  $x = 0.3$ , (d)  $x = 0.5$ , (e)  $x = 0.7$  and (f)  $x = 0.9$ . The samples were calcined at 850°C for 2 h.

Figure 3 shows typical plots of the dielectric constant and the dielectric loss as a function of temperature and various frequencies for (a) non-doped, (b) 0.1 wt%, (c) 0.3 wt% and (d) 0.7 wt%  $\text{Fe}_2\text{O}_3$ -doped samples with composition 0.57PSN-0.43PT. The Curie temperature  $T_c$  of the non-doped sample is at 271.5°C. The maximum dielectric constant of the non-doped sample at  $T_c$  is 32680. For both non-doped and iron-doped samples,  $T_c$  did not depend on the measuring frequency. Above  $T_c$ , the dielectric constant of iron-doped samples [Figs. ??(b)-3(d)] is the highest at a low frequency of 0.1 kHz. This high dielectric constant may be attributed to the high electrical conductivity due to iron doping.<sup>10)</sup> For each iron-doping level, the dielectric properties exhibited typical ferroelectric behavior, with a distinct anomaly in the dielectric constant at  $T_c$ .<sup>11)</sup> The maximum of the dielectric constant decreased with increasing frequency. When the amount of  $\text{Fe}_2\text{O}_3$  was increased,  $T_c$  was slightly decreased, but maximum values of dielectric constant at the Curie temperature were increased. The dielectric loss at room temperature was less than 0.7% for all iron-doped samples. The maximum of the dielectric loss increased with increasing frequency, as shown in Fig. 3. The temperature of the maximum dielectric loss can be attributed to the ferroelectric-paraelectric phase transition. With increasing temperature above the Curie point, the dielectric loss was observed to be dispersive. Higher amounts of iron dopant in the samples resulted in slightly higher dielectric loss. The highly dispersive dielectric loss at  $T > T_c$  originates from either increasing electronic or ionic conduction.<sup>11)</sup>

#### 3.2 $P$ - $E$ and $S$ - $E$ properties

Figure 4 shows the  $P$ - $E$  and  $S$ - $E$  hysteresis loops of non-doped and iron-doped samples at room temperature and at 1.0 Hz, which were measured at the same time using an automated polarization measuring system. This measurement was performed under the condition that samples were poled to full saturation under electric fields without electrical breakdown of the samples.<sup>12)</sup> By applying a maximum electric field, a remanent polarization  $P_r$  of 36.8  $\mu\text{C}/\text{cm}^2$ , a saturation polarization  $P_s$  of 42.7  $\mu\text{C}/\text{cm}^2$  and a coercive field  $E_c$  of 10.47 kV/cm were obtained for nondoped 0.57PSN-0.43PT ceramics. Most of the ferroelectric compositions showed a large remanent polarization  $P_r$  and a small coercive field  $E_c$ .

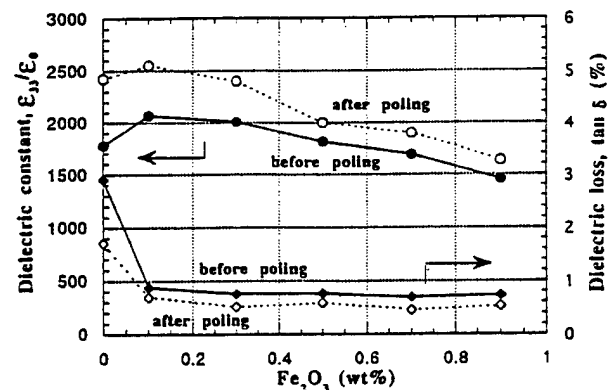


Fig. 2. Dielectric constant and dielectric loss before and after poling of 0.57PSN-0.43PT ceramics as a function of the amount of  $\text{Fe}_2\text{O}_3$  added.

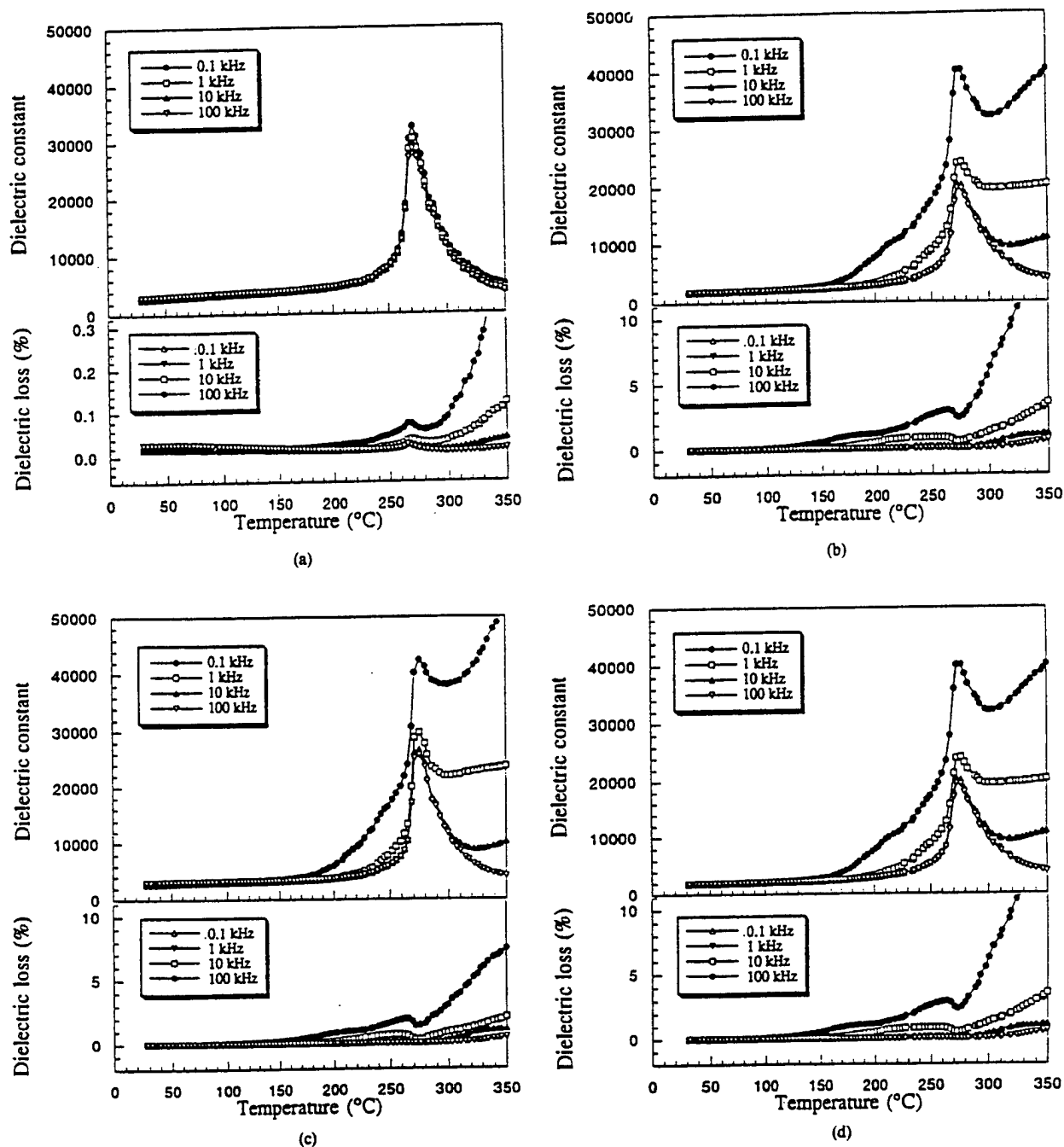


Fig. 3. Temperature dependence of the dielectric constant and the dielectric loss as a function of  $\text{Fe}_2\text{O}_3$  content in  $0.57\text{PSN}-0.43\text{PT}+x\text{wt}\%\text{Fe}_2\text{O}_3$  samples. Samples were measured while being heated to  $350^\circ\text{C}$ . (a)  $x = 0$  without  $\text{Fe}_2\text{O}_3$  (b)  $x = 0.1$  with  $\text{Fe}_2\text{O}_3$  (c)  $x = 0.3$  with  $\text{Fe}_2\text{O}_3$  (d)  $x = 0.7$  with  $\text{Fe}_2\text{O}_3$

The shape of the  $P$ - $E$  hysteresis became more rectangular with decreasing amount of  $\text{Fe}_2\text{O}_3$ . Domain wall mobility depends on the type of dopant and lattice defect. By doping of  $\text{Fe}_2\text{O}_3$  acceptors, oxygen vacancies are introduced into the  $0.57\text{PSN}-0.43\text{PT}$  ceramics. The introduction of oxygen vacancies decreased the domain wall mobility, which subsequently decreased the hysteresis loss.<sup>13)</sup> This is confirmed by the  $P$ - $E$  hysteresis loops of iron-doped PSN-PT ceramics shown in Fig. 4.

Figure 4 also shows the  $S$ - $E$  curve of strain versus electric field for  $\text{Fe}_2\text{O}_3$ -doped  $0.57\text{PSN}-0.43\text{PT}$  samples. The to-

tal strain, whose definition is given in the paper of Li and Haertling,<sup>14)</sup> was evaluated for each composition. The total field-induced strain resulted from domain wall motion and domain switching. We are currently studying the strain properties of these samples in greater detail. The magnitude of strain in  $\text{Fe}_2\text{O}_3$ -doped  $0.57\text{PSN}-0.43\text{PT}$  samples is presented in Table I.

Figure 5 shows the remanent polarization  $P_r$  and the coercive field  $E_c$  of  $0.57\text{PSN}-0.43\text{PT}$  ceramics as determined from  $P$ - $E$  hysteresis loops at room temperature as a function of the amount of  $\text{Fe}_2\text{O}_3$  added. Remanent polariza-

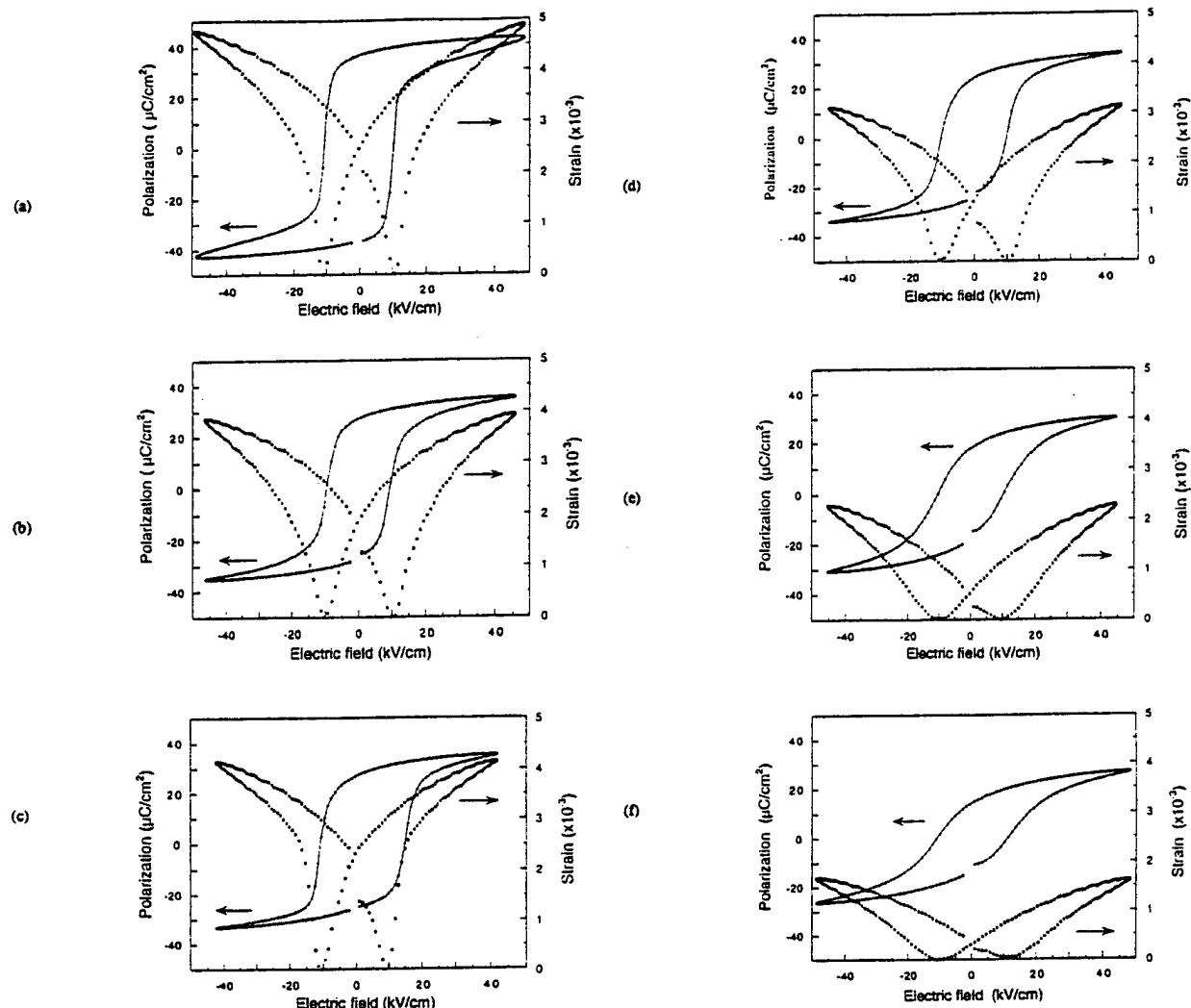


Fig. 4.  $P$ - $E$  and  $S$ - $E$  hysteresis loops (a)  $x = 0$ , (b)  $x = 0.1$ , (c)  $x = 0.3$ , (d)  $x = 0.5$ , (e)  $x = 0.7$  and (f)  $x = 0.9$  in 0.57PSN-0.43PT+ $x$  wt%  $\text{Fe}_2\text{O}_3$  samples at room temperature and at 1.0 Hz.

Table 1. Dielectric and piezoelectric properties of 0.57PSN-0.43PT ceramics as a function of the amount of  $\text{Fe}_2\text{O}_3$  added.

$\text{Fe}_2\text{O}_3$ (wt%)	$\epsilon_{33}/\epsilon_0$	$\tan \delta$ (%)	$d_{33}$ (pC/N)	$g_{33}$ ( $10^{-3}$ Vm/N)	$k_p$ (%)	$k_t$ (%)	$N_p$ (Hz·m)	$N_t$ (Hz·m)	$Q_m$	$S_{101}$ ( $\times 10^{-3}$ )
0	2422	1.71	380	17.7	50.0	54.3	2007	1785	68	4.883
0.1	2551	0.69	390	17.3	55.9	51.3	2009	1830	201	3.9381
0.3	2401	0.51	370	17.4	57.7	47.1	2138	1899	297	4.1535
0.5	2001	0.58	365	20.6	53.7	47.2	2151	1916	272	3.1403
0.7	1897	0.45	338	20.1	50.6	47.0	2289	2027	255	2.3010
0.9	1630	0.53	282	19.5	42.9	44.0	2331	1946	234	1.7145

tion  $P_r$  values gradually decrease with increasing amount of  $\text{Fe}_2\text{O}_3$  added. Coercive field  $E_c$  reached a maximum value of 12.83 kV/cm at 0.3 wt%  $\text{Fe}_2\text{O}_3$ , after which it decreased and slightly increased with further increase in the amount of  $\text{Fe}_2\text{O}_3$  added.

### 3.3 Piezoelectric properties

Figure 6 shows the electromechanical coupling factors for planar mode  $k_p$  and thickness mode  $k_t$ , and the mechanical quality factor  $Q_m$  of 0.57PSN-0.43PT ceramics as a func-

tion of  $\text{Fe}_2\text{O}_3$  content. The largest value of  $k_p$ , 57.5%, was observed at 0.3 wt%  $\text{Fe}_2\text{O}_3$  addition.  $Q_m$  reached a maximum value of 297 at 0.3 wt%  $\text{Fe}_2\text{O}_3$ ; this leads us to conclude that this particular PSN-PT composition is suitable for high-power applications. Acceptor dopants, such as  $\text{Fe}^{3+}$ , induce the formation of oxygen vacancies since charge neutrality must be maintained. The distortion and shrinkage of unit cells by oxygen vacancies might contribute to the increase of the mechanical quality factor  $Q_m$ , and the coercive field  $E_c$ .<sup>15)</sup> It is well known that the addition of acceptor dopants, such as

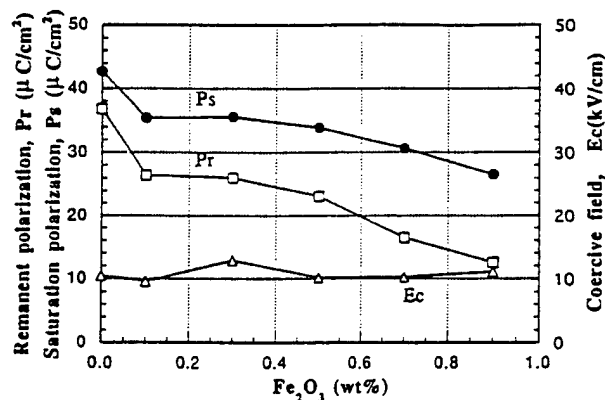


Fig. 5. Remanent and saturation polarization and coercive field of 0.57PSN–0.43PT ceramics as a function of the amount of Fe<sub>2</sub>O<sub>3</sub> added.

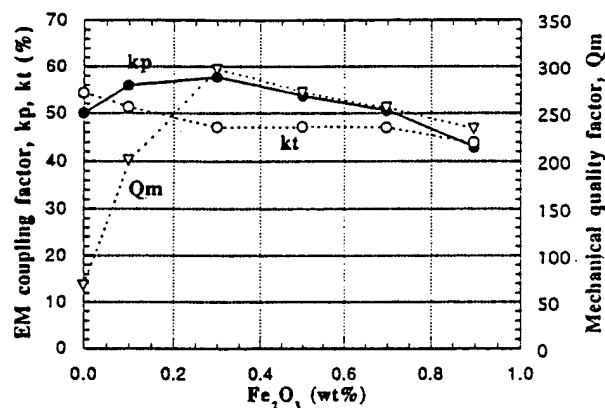


Fig. 6. Electromechanical coupling factor for planar and thickness modes and mechanical quality factor of 0.57PSN–0.43PT ceramics as a function of the amount of Fe<sub>2</sub>O<sub>3</sub> added.

Fe<sub>2</sub>O<sub>3</sub> improves  $Q_m$ , while decreasing  $d_{33}$  and  $k_p$ .<sup>13,16</sup> Fe<sup>3+</sup> ions occupy the B sites of the ABO<sub>3</sub> perovskite structure. The charge deficit of Fe<sup>3+</sup> ions at B sites is compensated by oxygen vacancies. The presence of iron oxide during sintering leads to the formation of oxygen vacancies. Oxygen vacancies inhibit the movement of domain walls, and therefore decrease the piezoelectric constant, the dielectric constant and the electromechanical coupling factor. The effects of domain wall motion on nondoped and iron-doped PSN–PT ceramics

will be studied using a charge coupled device (CCD) microscope system, and will be reported in detail in the near future, along with the high-power characteristics of these ceramics.

Table I summarizes the dielectric and piezoelectric properties of pure and Fe<sub>2</sub>O<sub>3</sub>-doped 0.57PSN–0.43PT ceramics.

#### 4. Conclusion

The piezoelectric and dielectric properties of nondoped and iron-doped 0.57Pb(Sc<sub>1/2</sub>Nb<sub>1/2</sub>O<sub>3</sub>)–0.43PbTiO<sub>3</sub> ceramics were investigated. The dielectric constant after poling increased for both nondoped and iron-doped 0.57PSN–0.43PT ceramics. The dielectric loss ( $\tan \delta$ ) for poled, iron-doped samples is less than 0.7%. The dielectric constant after poling showed a maximum value (2551) at 0.1 wt% Fe<sub>2</sub>O<sub>3</sub> addition, and then decreased with further increase in Fe<sub>2</sub>O<sub>3</sub> addition. The Curie temperature of nondoped 0.57PSN–0.43PT ceramics is 271.5°C. For the sample with 0.3 wt% Fe<sub>2</sub>O<sub>3</sub> addition, an electromechanical coupling factor  $k_p$  of 57.7% and a mechanical quality factor  $Q_m$  of 297 were observed. It was determined that the 0.3 wt% iron-doped 0.57PSN–0.43PT is the most suitable composition for high-power applications.

#### Acknowledgements

Jin-Soo Kim would like to acknowledge financial support of the Korea Science and Engineering Foundation (KOSEF) and his university (KNUE) for research at The Pennsylvania State University from Jan. 1996 to Jan. 1997.

- G. A. Smolenskii, V. A. Isupov and A. I. Agranovskaya: *Sov. Phys. Solid State* **1** (1959) 150.
- V. J. Tennery, K. W. Hang and R. E. Novak: *J. Am. Ceram. Soc.* **51** (1968) 671.
- Y. Yamashita: *Jpn. J. Appl. Phys.* **32** (1993) 5036.
- Y. Yamashita: *Jpn. J. Appl. Phys.* **33** (1994) 4652.
- Y. Yamashita: *Jpn. J. Appl. Phys.* **33** (1994) 5328.
- M. Adachi, E. Miyabukuro and A. Kawabata: *Jpn. J. Appl. Phys.* **33** (1994) 5420.
- F. Kulscar: *J. Am. Ceram. Soc.* **42** (1959) 343.
- X. Wang and X. Yao: *Ferroelectrics* **154** (1994) 307.
- J. H. Moon and H. M. Jang: *J. Mater. Res.* **8** (1993) 3184.
- N. Ichinose and N. Kato: *Jpn. J. Appl. Phys.* **33** (1994) 5423.
- W. R. Xue, P. W. Lu and W. Huebner: *Proc. IEEE* (1995) 101.
- J. S. Kim, Y. H. Chen and K. Uchino: *9th Int. Meet. Ferroelectricity* (1997) p. 54.
- S. Takahashi and S. Hirose: *Jpn. J. Appl. Phys.* **32** (1993) 2422.
- G. Li and G. Haertling: *Ferroelectrics* **166** (1995) 31.
- K. Uchino: *Piezoelectric Actuators and Ultrasonic Motors* (Kluwer Academic, Boston, 1997) Chap. 2.
- H. Ouchi, M. Nishida and S. Hayakawa: *J. Am. Ceram. Soc.* **49** (1966) 577.